DISSERTATION

UNDERSTANDING THE AMIDE-ASSISTED SYNTHESIS AND OLIVINE STRUCTURE-DIRECTED TWINNING OF Fe_2GeS_4 NANOPARTICLES

Submitted by

Rebecca Caroline Miller

Department of Chemistry

In partial fulfillment of the requirements

For the Degree of Doctor of Philosophy

Colorado State University

Fort Collins, Colorado

Summer 2020

Doctoral Committee:

Advisor: Amy L. Prieto

Matthew P. Shores
Christopher J. Ackerson
James R. Sites

ABSTRACT

UNDERSTANDING THE AMIDE-ASSISTED SYNTHESIS AND OLIVINE STRUCTURE-DIRECTED TWINNING OF Fe_2GeS_4 NANOPARTICLES

The reality of detrimental anthropogenic effects on the environment requires the development of a number of sustainable practices and technologies. The Prieto Group strives to advance the synthesis and understanding of materials for use in energy conversion and storage. Advances in computational solid-state chemistry have resulted in the identification of a number of earth-abundant, relatively non-toxic compounds as promising photovoltaic absorber materials. However, the synthesis of solids remains a step behind, requiring empirical exploration of precursors and conditions. As reaction intermediates and mechanisms are discovered, general synthetic strategies can be translated from one material system to the next. Inorganic nanoparticle (NP) syntheses rely on the interdisciplinary expertise of solid-state, organometallic, and organic chemistry and show interesting complexity. The work herein has advanced the understanding of amide-assisted NPs syntheses and examined the microstructure of twinned Fe_2GeS_4 NPs.

Chapter 1 presents a history of solution-based, amide-assisted NP reactions. As scientists understand the in situ speciation of precursors, more efficient reactions can be designed. This understanding allows the use of more benign and safe (both in terms of human and environmental) precursors and provides higher synthetic control over the end products. The presence of amide bases has generally provided access to higher NP nucleation rates and accessed smaller, more monodisperse particles. The increased monomer reactivity has also allowed the formation of ternary NPs free from binary or unary impurities by balancing the reactivity of cations of different valency. The most common amide base is $LiN(SiMe_3)_2$, and I relate this field to the use of its conjugate acid, hexamethyldisilazane or HMDS, in NP syntheses. Its addition has aided the production of NPs, but its chemical role remains unclear. This chapter was written utilizing a portion of an invited review paper written by myself, Jennifer M. Lee, Lily J. Moloney, and Amy L. Prieto

in the Journal of Solid State Chemistry (**2019**, *273*, 243-286.). Section 2.2 of the review outlined the evolution of understanding of amide-assisted NP syntheses and was adapted and expanded upon herein.

In Chapter 2, I report the redesign of a Fe_2GeS_4 NP synthesis. In 2013, the Prieto group was the first to report a NP synthesis for the compound, which had been predicted to be a promising photovoltaic absorber material in 2011. The original reaction relied on HMDS as an additive and employed the highly-reactive S precursor, hexamethyldisilathiane. Herein, I speculate on these precursors' roles and exchange their use for $LiN(SiMe_3)_2$ and S powder, eliminating the formation of an $Fe_{1-x}S$ intermediate and reducing the growth time from 24 h to 10 min. I thoroughly map the reaction landscape of this system and provide structural, compositional, and optical characterization of the particles. This work was published in the Journal of the American Chemical Society (*J. Am. Chem. Soc.* **2020**, *142* (15), 7023–7035.).

The Fe_2GeS_4 NPs show an interesting star-shaped morphology, so I examine the microstructure via electron microscopy and identify the presence of crystal twinning in Chapter 3. The particles exist as three sets of stacked nanoplates intersecting at 60˚ angles, which forms a triplet of twins or trillings. In the products, 98% of the particles are twinned. Because crystal twinning, and especially trilling formation, in macroscopic crystals is rare, a synthetic route to a massive collection of twinned particles stands as a valuable resource for understanding the fundamentals of crystal twinning in olivine compounds. I relate the twinning to the underlying hexagonal pseudosymmetry of the orthorhombic, olivine crystal structure. Because of the ratio of the unit cell dimensions ($a_{Pnma}/b_{Pnma} \approx \sqrt{3}$), the compound is susceptible to forming twins with growth of the [010] direction off the {310} faces. This can occur for other olivine compounds of similar unit cell dimension ratios, so I rank all of the olivine compounds listed in the Inorganic Crystal Structure Database according to this metric in Appendix A. This chapter is a manuscript prepared for submission.

Finally, Chapter 4 outlines our recommendations for future work to advance the understanding of amide-assisted NP syntheses and translate this synthetic system to other compounds. I suggest the systematic development of SnS NP reactions utilizing each of the precursors: Sn silylamide, alkali silylamides, and HMDS. I outline a set of complementary techniques to characterize the reaction

intermediates and mechanisms. This type of investigation has been done by the Kovalenko group for the formation of unary Sn^0 NPs, but the interaction of the chalcogen species remains unknown. Further, no systematic mechanistic study exists for the use of HMDS in NP synthesis. This work would advance the understanding and use of amide-assisted syntheses for all metal chalcogenide compounds.

In addition, I present preliminary data in our extrapolation of the Fe_2GeS_4 NP synthesis to the following solid solutions: $Fe_2GeS_{4-x}Se$ (including the end member Fe_2GeSe_4) and $Fe_{2-x}Mn_xGeS_4$. One composition of each solid solution was formed and characterized by powder X-ray diffraction, and I present electron microscopy to show twinning in the $Fe_2GeS_{4-x}Se_x$ (x = 0.96, 24 mol% Se) NPs. Lastly, I consider the possibility for twinning in an important olivine compound for battery science, $LiFePO_4$, which is a common cathode material. The crystal structure shows a high degree of hexagonal pseudosymmetry, indicating that the energetics of forming twin domains may be favorable. I discuss the possible ramifications this may have on battery cycling performance.

Thus, the scope of this work focuses on one compound, Fe_2GeS_4, but investigation into its synthesis and microstructure has opened a number of avenues for promising research. This compound itself presents a promising material for both photovoltaic and thermoelectric energy conversion, and the syntheses herein provide a launching point for property measurement and application evaluation. Further, the general examination of twinning in olivine compounds identifies questions for evaluating the function of other compounds useful for a number of applications. Lastly, analogous calculations to the geometrical evaluation done for orthorhombic olivine compounds could be carried out for other crystal structure types with unit cells that exist close to higher orders of symmetry. The advances presented herein on understanding the reactivity and roles of NP precursors are fundamental for progressing the field of NP synthesis. The reproducible formation and structural characterization of these twinned NPs provide a promising system for future explorations in crystal twinning and its effect on material properties.

ACKNOWLEDGEMENTS

I am extremely grateful to all those who have supported, encouraged, and impacted me throughout my time at Colorado State University. I'm thankful I was given the opportunity to join the chemistry department and am very proud to have an advisor as inspiring and understanding as Prof. Amy L. Prieto. Thank you for encouraging me to explore the facets of nanoparticle synthesis and crystallography that most intrigued me. Your enthusiasm for uncovering trends, coming up with clever strategies, and examining beautiful microscopy is contagious. Whenever I expressed doubt about myself or my capability, your gentle guidance and confidence were crucial for my development.

I feel so lucky to have been able learn from and work with Dr. Roy H. Geiss on the transmission electron microscope. Your depth of knowledge and insight were invaluable in our pursuit to use almost every possible microscopy technique to characterize and understand the microstructure of the twinned Fe_2GeS_4 nanoparticles. I truly appreciate the priority you placed on building my skillset and having me, a graduate student, run demonstrations on the TEM for prospective students. I am also indebted to the other folks of the Central Instrument Facility, the chemistry department administration, and my professors and committee members for taking the time to help me whenever I was in need. I especially admire professors Jamie Neilson and Matt Shores for their curiosity and intellect. I will fondly remember their engaging classes and open doors for research discussions.

As for the Prieto Group, I have had so much fun learning with and from all of you. Sarah, Dan, Max and Lasantha, thank you for teaching me laboratory skills and being just as excited about our exploratory science as our lab music choices (Poppy Tunes, Space Jam soundtrack…). Leslie, I loved our tradition of going to the library book sales each year, and I hope we continue to recommend books to one another. Jen and Lily, I'm so proud to have both of you as coauthors and friends, and hold dear those days spent in our room at the library. Jake and Cogell, thanks for being your jovial selves, both in the lab and on bicycles. Chris, your enthusiasm for science and impromptu whiteboard research discussions can only be

matched by your thoughtfulness; thank you. Max, Amy, Andy, Ethan, and Paul, I always enjoyed asking about your research and discussing my own puzzles with you. Our lunchtime hacky sack sessions were absolutely liberating, especially at a time when I was confined to crutches and a boot.

I have felt so supported by my friends and family outside of graduate school, especially Sarah, Magon, and Cami as well as Elena and Simon. I'm thankful for the friends I've gained through ultimate frisbee, including my Iowa State, CLX, CSU Hell's Belles, and Molly Brown teammates. You all have brought me so much joy. I'm especially grateful that this sport connected me with my partner, Ben, and to him I am eternally grateful. Your understanding, support, and endless playfulness has meant the world to me. I love you. To all of the Lohres and Bennetts, I have loved becoming part of the family here in Colorado. And finally, I want to thank my parents and my siblings. I am so grateful to have loved and learned from each of your as long as I've known you. Sabina and Peter, you each have a powerful drive to pursue your passions, and I'm so inspired by you. Mom, I love how you submerge yourself in undaunted curiosity whenever you find something new to ponder, learn, or practice. Dad, I have always looked up to your methodical and utterly ingrained work ethic, and only through interaction with other solid state chemists did I learn of your intense humility, seeing your work and intellect through their eyes. Being able to ask each of you questions about the gritty details of my research and puzzling over crystallography problems at the dining room table are fond memories of mine. I strive to be like both of you in whatever I do in the future. Thank you for your unending support and encouragement.

TABLE OF CONTENTS

CHAPTER 1

THE EVOLUTION OF UNDERSTANDING THE ROLES OF AMIDE BRØNSTED BASES AND CONJUGATE ACIDS IN AMIDE-ASSISTED NANOPARTICLE SYNTHESES[†]

1. Introduction

The field of solid-state chemistry is often motivated by understanding and employing interesting structure-property relationships. Scientists are advancing in the ability to computationally predict useful compounds with desired properties, but synthesis development generally exists in a realm of experimental exploration rather than theoretical prediction.[1] This is especially true for the production of colloidal nanoparticles (NPs) which requires cross-disciplinary expertise, including that of solid-state, organometallic, and organic chemistry.[2–4] Solution-based NP syntheses are complex but offer access to a variety of compounds for which composition, phase, size, and morphology can be tuned. In solution, these reactions involve lower temperatures than typical bulk solid state reactions and shorter growth times. Because of the small dimensions and high surface area to volume ratios, NPs often exhibit interesting physical properties in comparison to the extended structure in bulk. For example, in quantum-confined NPs, band gap tuning and multiple exciton generation are possible.[5] If single-particle measurements can be done, NP syntheses may present massive sample sizes in just one reaction batch.

Developing NP syntheses requires careful design of conditions to target the desired end products. The strategies outlined in the literature are aided by a knowledge of the reaction mechanisms and evolution of solid products present in the system. This involves understanding both the roles (possibly multifold) of each reagent whether precursor, additive, or solvent as well as the effects of the various

[†] This chapter is adapted from section 2.2 of a review article published (*J. Solid State Chemistry*, **2019**, *273*, 243-286) by Rebecca C. Miller, Jennifer M. Lee, Lily J. Moloney, and Amy L. Prieto. Rebecca C. Miller was the primary author for section 2.2, which highlighted careful synthetic reports employing amide bases in NP syntheses. Here, Rebecca C. Miller expanded that section to include the HMDS-based NP synthetic literature and provided analysis comparing both areas of synthetic literature to one another. Amy L. Prieto provided guidance on this chapter.

synthetic parameters possible (i.e. concentrations, temperature, time, and order of precursor introduction). As the field progresses, the state of innovation progresses from the realm of trial and error, i.e. characterizing only the final NP products to characterization of the reaction solutions, byproducts, and in situ processes. Capturing signatures of reaction intermediates is inherently difficult due to their transience and because the solvent system often plays a non-innocent role in monomer speciation. Detection of these complex and dynamic systems has spurred the development of in situ techniques, but these are quite recent and employ model NP materials such as cadmium chalcogenides[6–9]. Further, the logistical requirements of characterization techniques introduce the question of whether the measured sample is representative of the speciation and processes present in the standard reaction. For example, capillary work alters precursor and solvent concentrations and eliminates the headspace. Many NP synthetic systems have advanced via ex situ characterization of aliquots extracted at early growth times and through clever control reactions to eliminate alternate hypotheses. Furthering these advances relies on the consideration of a wide range of possible reaction mechanisms and intermediates.

In Fig. 1.1, we have outlined a simplistic overview of possible routes for reaction pathways in solution-phase syntheses of colloidal NPs, viewed from left to right. As the top arrow suggests, we typically think of the precursors dissolving into solution as monomers and directly nucleating the end product. However, many dynamic components and multiple pathways are possible. The solvent system and additives may play crucial roles in coordinating the monomers, affecting their reactivity. As monomers react to form intermediates or end products, the solvated ligand molecules fluctuate in concentration and can play a role at different stages of NP evolution or growth. As depicted, if solid intermediates form, they may be crystalline or amorphous as well as composed of an number of different phases. We have defined three possible transformations to the end products: conversion, consumption, and coalescence. For conversion, the intermediates incorporate and/or expel elemental species to transition into the end phase. In consumption, the solid intermediates dissolve back into solution, providing active monomers in solution, usually at different conditions (temperature, coordination,

concentration, etc.) compared to the conditions during the intermediates' initial nucleation. Lastly, coalescence may occur by adhesion of solid intermediates, merging to form the end product.

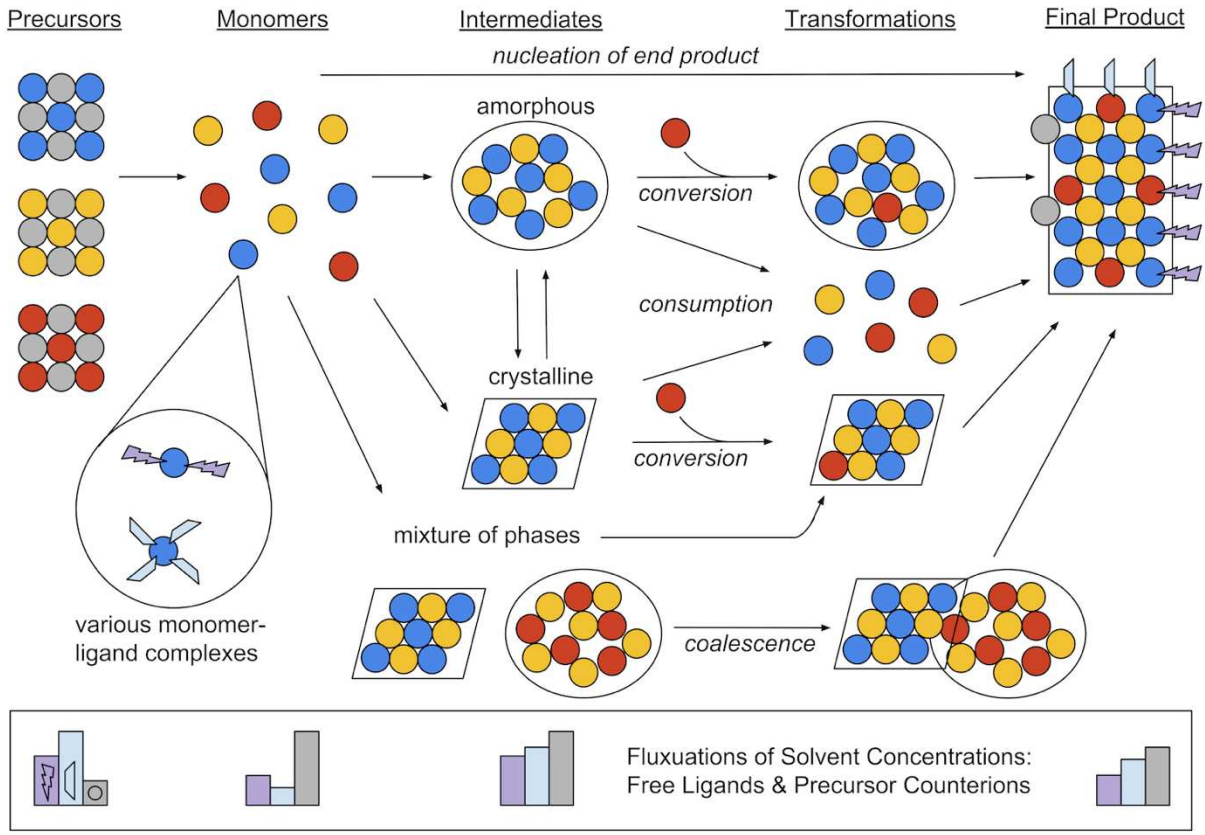

Fig. 1.1. A general depiction of the transformation from NP precursors to end products, with possible reaction routes identified. Generally, syntheses follow the evolution of the underlined components, but may involve multiple simultaneous processes, and are inherently dynamic, complex systems. Constituent elements of the end product are depicted as red, yellow, and blue circles. Solvent molecules capable of complexation to the constituent elements (ligands) are depicted in purple lightning bolts and light blue trapezoids. Processes labeled between components are italicized. A simplistic description of the dynamic nature of the solvent system is shown in bar graphs at the bottom, with exaggerated concentration changes of the two ligands and the precursor material counterions.

1.1 Select Lessons from the Cadmium Chalcogenide Literature

Classic examples from the Cd chalcogenide literature show how understanding NP reaction systems informs the development of more efficient NP syntheses and design of interesting morphologies. Traditionally in early NP syntheses, highly reactive precursors amenable to forming a supersaturation of active species for swift nucleation were targeted.[2] As understanding in the field has progressed, simpler metal salts have been more commonly employed. A major factor in this shift comes from a better

identification of the active species, specifically how the metal atoms are complexed in solution prior to nucleation. Often, some form of solvent molecules exists as the ultimate metal complexing agent(s) during reaction, and advances in cation precursor selection have occurred via achieving these intermediates from more benign starting precursors. This change usually accompanies additional benefits with the use of relatively safer (regarding both human use and environmental impact) and more economical precursors.

Early work on Cd chalcogenide NP syntheses, including the influential study by Murray et al., employed the use of highly reactive dimethylcadmium, targeting swift nucleation for monodisperse particles via pyrolysis of this organometallic compound.[10] In following works, Cd was found to complex with strong ligands, such as hexylphosphonic acid, prior to NP formation.[11] This prompted skepticism of the need for the sensitive, reactive dimethylcadmium precursor. Indeed, syntheses with $CdCl_2$ and CdO were explored, identifying high quality NPs formed from CdO alongside the use of phosphonic acids. Thus, the initial choice of a highly reactive compound targeting rapid nucleation was replaced by simpler, more stable precursors that afforded the same, or similar, important reactive species.

Understanding the evolution of precursors in NP syntheses allows for the development of specific NP phases and morphologies. If crystallographic facets of a compound exhibit different surface energies and sufficiently high growth rates are achieved, the NPs should grow in the direction of the high energy facets than the lower energy ones resulting in anisotropic morphologies. A classic example employs this in combination with the zincblende/wurtzite polymorphism possible for Cd chalcogenides. In 2004, Milliron et al. reported syntheses for linear and branched heterostructures.[12] Sequential growth regimes of either linear nanorods or branched tetrapods allowed the formation of four different NP morphologies. Because the cubic zincblende ABCABC stacking is slightly higher in energy than the ABAB stacking of the hexagonal wurtzite polymorph, the reaction conditions could be altered to transition from forming one polymorph to the other. Thus, tetrapods can be formed by nucleation of higher energy zincblende cores in a pyramidal morphology followed by a drop in monomer concentration and growth on the shared (111) facet switching to the [1000] direction of the hexagonal wurtzite phase. Milliron et al. tuned reaction

temperatures and carried out secondary precursor injections to create various heterostructures that exhibited polytypism and different Cd chalcogenide compositions (CdQ, Q = S, Se, Te).

These two NP synthetic themes exist in the work presented here. This introductory chapter outlines the evolution of understanding in amide-assisted NP synthesis, i.e. those containing either amide Brønsted bases such as metal or alkali silylamides (i.e. $LiN(SiMe_3)_2$) or the conjugate acid, $HN(SiMe_3)_2$ (HMDS). This body of literature inspired the work presented in Chapter 2, an investigation and redesign of the complex and poorly-understood HMDS-based synthesis of Fe_2GeS_4 NPs.[13] The unique morphology of the resultant Fe_2GeS_4 nanostars was characterized as crystal twinning in Chapter 3. We relate the origin of the twinning to the underlying pseudo-hexagonal symmetry of the orthorhombic olivine Fe_2GeS_4 crystal structure and predict other olivine compounds for which twinning should be probable. Following, in Chapter 4, we outline our outlook for future research directions for this material and the field of amide-assisted NP syntheses as a whole.

1.2 The Hard-Soft Acid-Base Principle

To preface a history of metal amide understanding in NP syntheses, the Hard-Soft Acid-Base (HSAB) principle provides a framework for interpreting some of the observations covered in the upcoming discussion. Introduced by Pearson in 1963, its ideas inform many aspects of NP systems: precursor decomposition or stability, reactive monomer complexation, surface-ligand interactions, cation-exchange mechanisms, and ligand exchange mechanisms, etc.[14–16] Within the HSAB principle, chemical groups are categorized as Lewis acids (electron acceptors) and Lewis bases (electron donors) each on a scale between hard and soft. Hard acids usually exhibit high positive charge and small size with paired valence electrons, while soft acids show the opposite: low positive charge, large size, and often unshared valence electron pairs. Hard bases have tightly held electrons, while soft bases' electron clouds are easily deformed and oxidation is less difficult. In general, polarizability of components underscores the main difference, with low polarizability in hard acids and bases and high polarizability in soft ones. The key HSAB principle then follows that hard acids prefer to coordinate with hard bases and soft acids with soft bases. Common NP synthetic acids and bases are organized along a hard/soft scale in Fig. 1.2.[3]

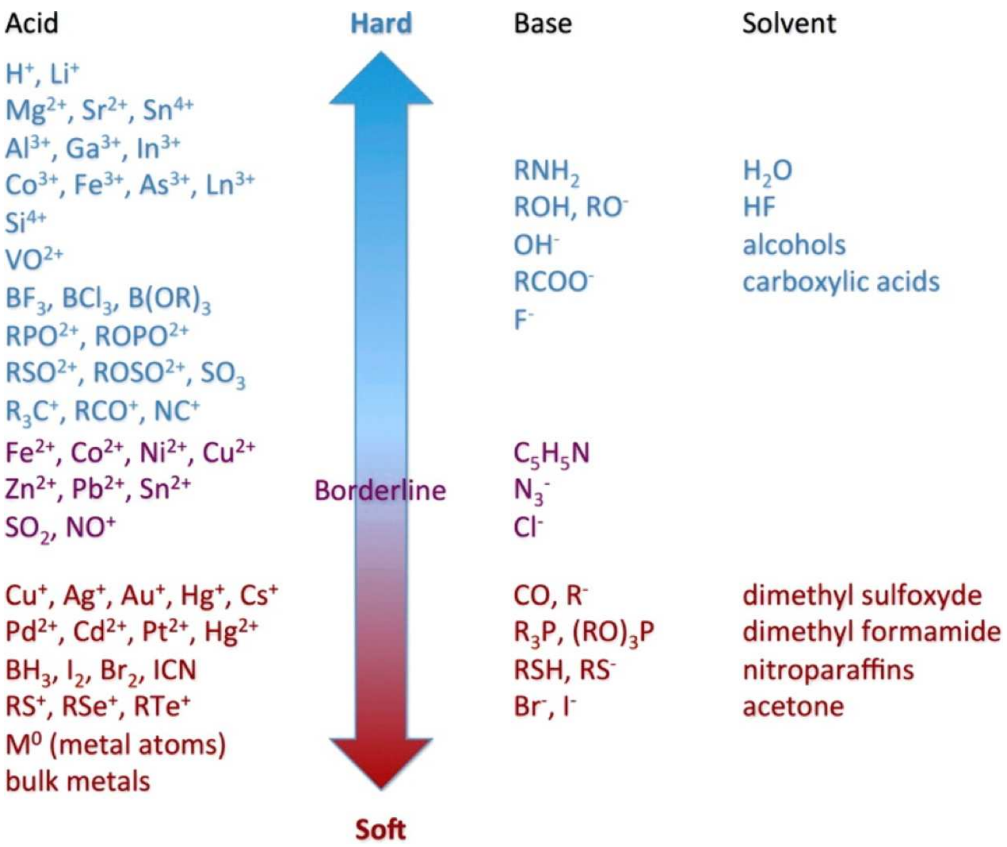

Fig. 1.2. Common NP synthetic components categorized as Lewis acids and bases on a qualitative scale of hard to soft, based on the Pearson HSAB principle. Reproduced with permission from ref.[3] Copyright 2016 American Chemical Society.

Of course, solution-based NP synthetic systems are inherently complex with many interacting components. Relying on standard, quantitative properties of atoms and compounds may aid explanation of empirical synthetic observations, but syntheses are hardly carried out at standard conditions, and extrapolating to NP synthetic conditions degrades the standard properties' reliability for this use. Thus, the strength of relying on Pearson's HSAB principle may lie in its empirical basis. It suggests how components might interact, but it is not a quantitative law. Within the principle itself (outside of the world of NP synthesis), Pearson acknowledges there exist important chemical factors determining bond energies that must be taken into account beyond the HSAB principle, such as orbital overlap and steric repulsions, for example. Nonetheless, scientists have benefited in NP synthetic explorations guided by the general trends of the HSAB principle, which is featured in a few examples in this section.

2. Use and Understanding of $LiN(SiMe_3)_2$ and HMDS in NP Syntheses

Metal amide precursors and related in situ formed species have been used for the synthesis of metal, metalloid, binary, and multinary nanoparticles. Relative to common NP conditions (metal salts in high boiling point solvents), the introduction of a metal amide species often enhances reactivity of the involved components which can alter nucleation rates. Strategically, this has been used as a handle for forming smaller, more monodisperse NPs or for balancing the reactivity of multiple cationic components. The most commonly employed amide Brønsted base is lithium bis(trimethylsilyl)amide ($LiN(SiMe_3)_2$). Interestingly, the conjugate acid, $HN(SiMe_3)_2$ or HMDS, has been employed as an additive in NP syntheses without a clear understanding of its role. To our knowledge, no study has experimentally attempted to contrast the effects of these additives in NP syntheses. In part, some of the isolation of HMDS and Brønsted base-containing NP syntheses in the literature may stem from potential confusion in syntax. The descriptors hexamethyldisilazane, bis(trimethylsilyl)amine, and HMDS all refer to the conjugate acid, $HN(SiMe_3)_2$. Similarly, lithium hexamethyldisilazide, bis(trimethylsilyl)amide, and LiHMDS can all correspond to the base, $LiN(SiMe_3)_2$. Further, the term amide holds two definitions in terms of functional groups: the conjugate base of ammonium (R_2N^-) and a carbonyl carbon linked to nitrogen. However, we have adapted a complex, HMDS-based Fe_2GeS_4 NP synthesis to a $LiN(SiMe_3)_2$-based synthesis that directly forms the phase-pure targeted ternary product (Chapter 2). In this chapter, we outline and analyze the evolution of scientists' understanding of amide- and HMDS-assisted NP syntheses. Increased identification of important intermediates and chemical reactions has resulted in greater synthetic control for a range of materials with a broad set of functionalities.

2.1 Metal Amide Complex Precursors

These sections cover the initial work in amide-assisted NP syntheses in which metal amides have been used directly as highly-reactive NP precursors. While useful for swift nucleation of NPs to provide monodisperse products, these compounds require elaborate synthetic, isolation, and handling procedures and can be flammable[17]. This is analogous to the initial use of dialkyl cadmium precursors for their reactivity in early cadmium chalcogenide syntheses.

2.1.1 Early Use of Metal Amides for Metal and Metalloid NP Syntheses

Early work employing metal amide precursors for metal NPs was pioneered by Chaudret et al. starting in the late '90s and Buhro et al. in the early '00s. Chaudret et al. formed nanostructures of many metals and metalloids (Fig. 1.3), including but not limited to Sn/SnO_2[18], Ni[19], Ru[20], Fe[21], Fe-Co[22], and Co[23]. The synthetic approach generally involved the use of an organometallic precursor (e.g. metal silylamides) in the presence of ligand solvent molecules used to direct various morphologies. Reduction of the metal centers was commonly induced by reaction with hydrogen under temperature and pressure. Metal oxide nanostructures were formed either by a secondary oxidation reaction step or direct hydrolysis of the organometallic precursors.[24–27] A perspective article from Amiens et al. depicts the breadth of materials the authors were able to form via this general scheme.[28]

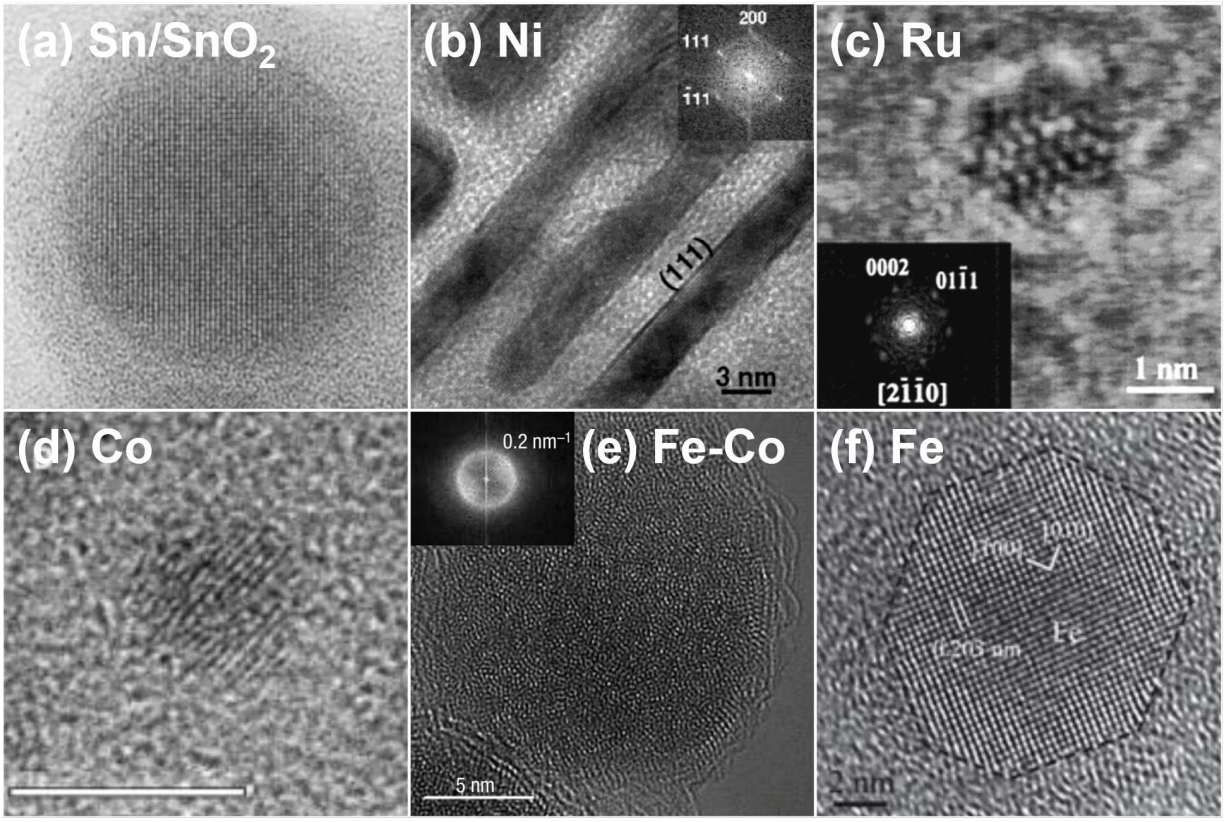

Fig. 1.3. Electron micrographs of various nanostructures formed by an organometallic approach from the group of Chaudret et al. **a,** Sn/SnO_2, adapted with permission from ref [18]. Copyright 1999 Wiley-VCH Verlag GmbH, Weinheim, Fed. Rep. of Germany. **b,** Ni nanorods, adapted with permission from ref [19]. Copyright 2001 American Chemical Society. **c,** Ru, adapted with permission from ref [20]. Copyright 2001 American Chemical Society. **d,** Co, adapted from ref [23]. Copyright 2002 Wiley-VCH Verlag GmbH & Co. KGaA, Weinheim. **e,** Fe-Co, adapted from ref [22]. Copyright 2005 Springer Nature. **f,** Fe, adapted from ref [21]. Copyright 2011 Royal Society of Chemistry.

Buhro et al. developed syntheses for small, monodisperse Bi NPs via the reported thermal decomposition of $Bi[N(SiMe_3)_2]_3$ in the presence of $NaN(SiMe_3)_3$ and polymer stabilizers.[29–32] The authors found the Bi NPs to be useful for diameter-controlled solution-liquid-solid (SLS) growth of semiconductor nanowires. In 2010, the authors published an advancement of their Bi NP synthesis avoiding the meticulous and sensitive synthesis of $Bi[N(SiMe_3)_2]_3$, stating it formed in situ from $BiCl_3$ and $NaN(SiMe_3)_2$; however, direct characterization of the transient Bi silylamide was not presented.[32]

2.1.2 Small, Monodisperse IV-VI NPs via IV-$[N(SiMe_3)_2]_2$

In 2007, Kovalenko et al. first extended the use of the metal silylamide, $Sn[N(SiMe_3)_2]_2$, to the synthesis of small, monodisperse tin monochalcogenide NPs.[33] The precursor was chosen for its increased reactivity compared to other Sn salts (oleate, acetate, and chloride) that did not produce small, monodisperse NPs. The synthesis of SnTe was reported specifically, and it was also stated the procedure could be adapted to form both SnSe and SnS. In 2008 and 2010, Hickey et al.[34] and Baumgardner et al.[35] extended the use of $Sn[N(SiMe_3)_2]_2$ to the formation of SnS and SnSe NPs, respectively. These studies observed dependencies of NP size and morphology on parameters such as reaction temperature and the amount of alkylamine solvent. Specifically, Hickey et al. found manipulation of the solvent system affected the morphology of the SnS NPs; a higher OLA amount resulted in smaller, spherical particles and a higher oleic acid (OA) amount gave larger, angular ones.

In 2011, GeTe NPs of different sizes (8, 17, and 100 nm) with the two smaller sizes relying on $Ge[N(SiMe_3)_2]_2$ as the germanium precursor were formed by Polking et al.[36] This Ge compound was observed to yield NP nuclei much faster than $GeCl_2$-dioxane, which was used for the 100 nm-sized NPs. The authors acknowledged the reaction mechanism was not fully understood but associated the smaller NP sizes with an increased reduction rate of Ge^{2+} in the silylamide as opposed to the halide salt. For further discussion of Sn and Ge monochalcogenide nanostructures, we refer the reader to a review compiled by Antunez et al. in 2011.[37] This sampling of IV-VI NP syntheses stood as one of the early examples of the versatility of a metal silylamide precursor for rapid development of small, monodisperse NPs in related material systems.

2.1.3 Proposed Cation-Exchange Mediated Nucleation Mechanism for PbSe NPs

An interesting early study from Kovalenko et al. in 2008 employed $Sn[N(SiMe_3)_2]_2$ for the formation of Pb chalcogenides and suggested a cation-exchange-mediated nucleation.[38] Inclusion of the Sn silylamide compound with $PbCl_2$, TOP–Se, and OLA resulted in small, monodisperse PbSe NPs, as opposed to the large, elongated particles observed without the Sn compound. Additionally, size tuning of the PbSe NPs was observed to be dependent on the concentration of the Sn compound. Via in situ infrared photoluminescence (IR PL) measurements, luminescent PbSe was detected within the first second after injection. The authors suggested the reaction scheme outlined in Fig. 1.4. Assuming the initial formation of SnSe, the system seemed to display "an unusually fast cation-exchange reaction." While the lattice free energies of PbSe and SnSe could not provide an explanation, two factors were offered in support of the suggested pathway. These included both the small size of the NPs, being comparable to solid state reaction widths (4-5 nm), and the favored interaction of the harder acid, Sn^{2+}, with the solvent, OLA, relative to softer Pb^{2+}. This study stands as an example in which the SnSe NP intermediates were suggested without their detection, and the reaction system was not analyzed for potential byproducts to test the validity of the proposed reaction pathway.

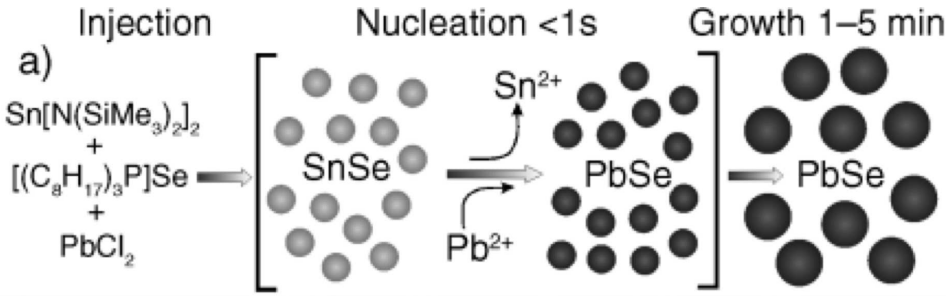

Fig. 1.4. Proposed reaction mechanism for the formation of PbSe NPs via cation-exchange-mediated-nucleation and subsequent growth. Adapted with permission from ref [38]. Copyright 2008 Wiley-VCH Verlag GmbH & Co. KGaA, Weinheim.

2.2 Alkali Amide Brønsted Base Precursors

The next sections detail NP syntheses that have replaced metal amide precursors with metal salts and alkali amide Brønsted bases. As detailed in the following reports, the use of alkali amides has provided in situ access to high monomer reactivity from more benign precursors. This provided the ability

to balance the reactivities of cation precursors of varied valency resulting in the incorporation of both species in ternary NPs.

2.2.1 Proposed Silylamide Metathesis Reaction Mechanism

The above described PbSe NP reaction mechanism inspired M. Yarema et al. to adapt the synthesis for the formation of luminescent Ag_2Se NPs in 2011.[39] Unlike the PbSe system, altering the Sn silylamide amount was not observed to induce Ag_2Se NP size tuning. Thus, $LiN(SiMe_3)_2$ was substituted for the Sn analogue, and improved NPs were formed with respect to colloidal stability, photoluminescence, quantum efficiency, and synthetic yield. Different from the quasi-seeded cation exchange mechanism proposed in the PbSe work, a metathesis-based reaction mechanism (Fig. 1.5) was offered. A short-lived Ag silylamide complex was thought to form before decomposing to a Ag^0 species followed by reaction with the phosphine chalcogenide. To support this suggested route, the higher ionization potential of Ag relative to Li was cited as a driving force for their exchange. Additionally, a control experiment (synthesizing the Ag silylamide) was carried out in order to probe its solubility and decomposition in similar solvent systems. While it was found to be thermally robust up to 275 °C and not soluble in hydrocarbons, it underwent reduction to Ag^0 in either hot tetrahydrofuran or pyridine, which was reported to exemplify its possible reactivity in the Ag_2Se formation.

$$CF_3COOAg + Li[N(SiMe_3)_2] \rightleftharpoons \{Ag[N(SiMe_3)_2]\} + CF_3COOLi$$

$$\{Ag[N(SiMe_3)_2]\} \xrightarrow[\text{-byproducts}]{\text{in OLA}} [Ag^0] \xrightarrow{+TOPX} Ag_2X$$

Fig. 1.5. Proposed reaction mechanism for the formation of Ag_2E NPs via a metathesis exchange, reduction of Ag^+, and reaction with phosphine chalcogenides. Reproduced with permission from ref [39]. Copyright 2011 American Chemical Society.

The authors additionally carried out a synthesis identical to that of the Ag_2Se NPs but without Se, noting the formation of metallic Ag NPs and stating this proved the hypothesis of the reaction mechanism outlined in Fig. 1.5. Given the aforementioned Bi NP literature precedence that had cited the speculation of in situ formation of $Bi[N(SiMe_3)_2]_3$ from $BiCl_3$ and $NaN(SiMe_3)_2$,[32] the reaction mechanism proposed here seems plausible. However, the control reactions of testing the solubility and reactivity of ex situ

synthesized Ag silylamide alongside the results of the Ag_2Se reaction performed without Se only demonstrated the ability of Ag, potentially with different coordination, to react in those solvents and at those temperatures. This was already demonstrated to an extent by the formation of Ag_2Se in the original synthesis, and, in our opinion, isn't conclusive evidence for the reaction mechanism. Experiments designed to identify the presence or lack of expected byproducts might provide more convincing evidence of the proposed reaction mechanisms. It might be worth attempting to isolate the Ag silylamide complex upon mixture of the Ag precursor, $LiN(SiMe_3)_2$ and OLA, potentially carried out at lower temperatures to avoid reduction to Ag^0. Examining the reaction solution post-synthesis might highlight an unexpected byproduct that could illuminate the reaction mechanisms taking place during NP formation.

Further, applying scrutiny to otherwise overlooked aspects of the system might be useful specifically in the case of understanding the dependence and independence of various parameters on Ag_2Se NP size. The authors described NP size to be independent of parameters including concentration of the silylamide salt, reaction temperature, and growth time but dependent on the Ag:Se precursor molar ratio. This was offered with few synthetic details. The amounts of the lithium silylamide salt tested when varied were not reported, but it was stated the "amount of silylamide does not essentially influence the final size of the NPs." Experimental amounts of the Ag and Se precursors for the Ag to Se ratios probed were absent; this information might be useful for the consideration of the possible effect of the presumed innocent conjugate components of the precursors, TOP from TOP-Se and trifluoroacetate from Ag trifluoroacetate. Based on the growing understanding in the composition of the solvent system playing a larger role than expected in many NP systems, it would be of interest to more closely examine the possible effect of these unintended changes on the NP size variation reactions. A second area of interest would be the effect of reaction temperature and growth time on NP size and size dispersion. Despite the report of NP size independence from these parameters, these reactions required unspecified, varied temperatures (RT - 100 ºC) with highly temperature-dependent growth times (2 min - several days) in order to attain optimal size dispersion. Overall, the odd nature of size tuning in the Ag_2Se NP system,

requiring multiple changes to commonly important parameters, could be indicative of the proposed reaction mechanism being blind to unknown, important processes.

2.2.2 First Use of Metal Silylamides for Ternary NPs and Syntheses of I-III-VI NPs

The first silylamide-promoted synthesis for a ternary NP system was published by O. Yarema of the Wood group in the development of Cu-In-Se NP syntheses in 2013.[40] Based on previous success in similar systems, oleylamine-based reactions were explored. While small Cu-In-Se NPs could be formed, they lacked photoluminescence. The authors attributed this to the alkylamine's reported role in catalyzing oxidation of NP surfaces.[41] Thus, altered reactions combined Cu and In halide salts in trioctylphosphine (TOP), and injected $LiN(SiMe_3)_2$ and Se dissolved in TOP. Generally, as the silylamide amount was decreased, the NP size was found to increase, with a lessened number of nucleation events offered as an explanation. This work was later extended to the Ag-In-Se system,[42] utilizing an analogous reaction system; however, metal chlorides could be used in the copper-based system but iodides were necessary in the silver-based system due to the observed decomposition of AgCl in TOP at >100 °C. Within this reaction space, manipulating the amount of $LiN(SiMe_3)_2$ and the ratio of the metal precursors lent control over the NP composition (Fig. 1.6), while both the silylamide amount and the growth time were the key parameters for NP size control (Fig. 1.7).

Interestingly, the authors observed dependence of the Ag:In composition in the NPs on the $LiN(SiMe_3)_2$ amount. When the molar amount of silylamide relative to iodide anions was in excess, the NPs displayed Ag:In molar ratios that reflected the molar ratios of the starting metal precursors. Alternatively, when the silylamide molar amount was deficient relative to the iodide amount, the particles are In-rich, as shown in Fig. 1.6. To explain this observation, the authors suggest the following reaction scheme, depicted in Fig. 1.8. Upon interaction of the metal iodide precursors with the Li silylamide, metal amide complexes form. These active species then react with TOPSe in order to form the Ag-In-Se NPs. The key factor here lies in their suggestion of the In-amide having a much higher rate of formation compared to the Ag-amide ($r_{In} >> r_{Ag}$). When the silylamide amount is low, the difference between r_{Ag} and r_{In} is inferred by the In-rich NP compositions. When the silylamide is present in excess, the NP rate

of formation is proposed to be the limiting step, and the NPs exhibit Ag:In ratios as supplied in the reaction solution.

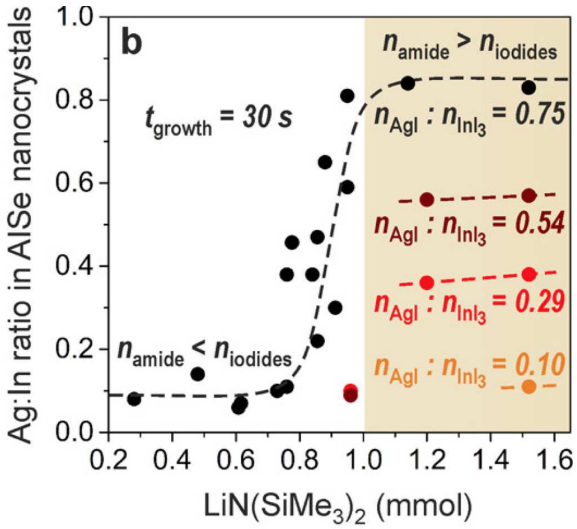

Fig. 1.6. Compositions of Ag-In-Se NPs as a function of variable LiN(SiMe$_3$)$_2$ amounts and AgI:InI$_3$ ratios while the growth time was maintained at 30 s. At high molar LiN(SiMe$_3$)$_2$ amounts relative to the counter I^- ions, the NP compositions reflected the starting metal stoichiometries. At low LiN(SiMe$_3$)$_2$ amounts, the NPs were In-rich. Adapted with permission from ref [42]. Copyright 2015 American Chemical Society.

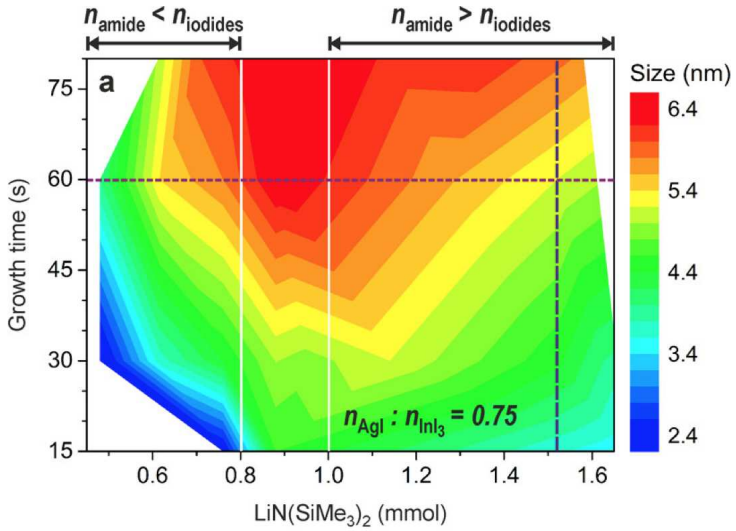

Fig. 1.7. Sizes of the Ag-In-Se NPs displayed as a function of the LiN(SiMe$_3$)$_2$ amount and growth time. The AgI:InI$_3$ molar ratio was held constant at 0.75. Adapted with permission from ref [42]. Copyright 2015 American Chemical Society.

The authors connect these observations with the HSAB principle, as the hard base, $[N(SiMe_3)_2]^-$ should preferentially coordinate with the hard acid, In^{3+}, relative to the soft Ag^+. Additionally, we offer

support of this connection considering the metal precursors used here are iodides. The soft base, iodide, would preferentially dissociate from In^{3+} over the Ag^{+}, which could be an additional factor in the speculated differences in the metal amide rates of formation. This work exemplifies the potential for amide-assisted NP syntheses to not only be useful for forming smaller, more monodisperse NPs via enhanced nucleation but also as a possible handle for balancing the reactivities of multiple cations of varying HSAB character in a ternary compound.

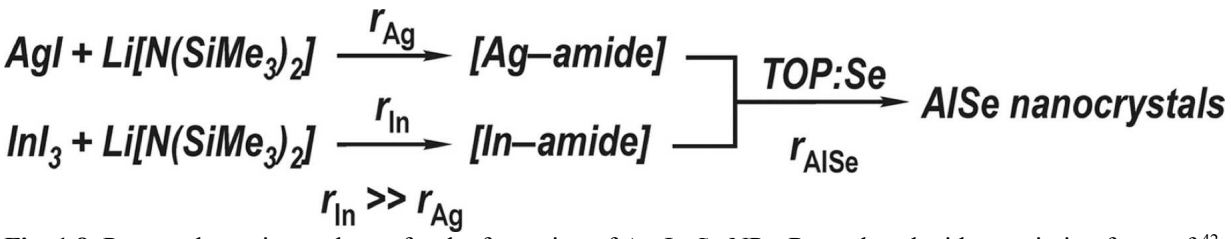

Fig. 1.8. Proposed reaction pathway for the formation of Ag-In-Se NPs. Reproduced with permission from ref [42]. Copyright 2015 American Chemical Society.

Following, the amide-assisted approach was also applied to attain size and compositional control over the Cu-In-Te and Ag-In-Te NP systems in 2016.[43] In translating the principles of the selenide system by substituting TOPTe for TOPSe, a difference in the reactivity of the two phosphine chalcogenides was found to be the major factor in the outcome of the reaction. Initially, a bimodal distribution of Cu-In-Te NPs was observed and attributed to TOPTe reacting with both metal amides and unconverted metal halides. The authors cited the higher reactivity of TOPTe relative to TOPSe. In order to promote the transformation of the metal halides to amides and push the NP formation to be the rate limiting step, the Li silylamide amount was increased. This demonstrated the utility of the proposed reaction mechanism from the Ag-In-Se study. Hypothesizing differences in the reaction rates based on the use of TOPTe, the authors were able to apply a straightforward adaptation and achieve size control over the Te-based NPs.

Additionally, these systems exemplify the sensitivity of NP syntheses in terms of controlling aspects such as composition and size dispersion. In the Cu-In-Te reactions, temperatures of 280 ˚C or greater resulted in uncontrollable compositions; however, too low of a reaction temperature can also be detrimental for the same parameter, as observed in the Ag-In-Te system. The inactivity of the In-amide

complex below 220 °C resulted in Ag-rich ternary NPs as well as the side product, Ag_2Te. Compositional control was achieved in these syntheses by using slightly lower temperatures for the Cu system and by decreasing the initial amount of the Ag precursor for the Ag system. The reaction temperatures also influenced both systems in terms of size distribution. In the Cu system, temperatures at 240 °C or lower gave broad size distributions and featureless absorption spectra, while the NP nucleation rate in the Ag system was so swift that reducing the reaction temperatures narrowed size distributions. The variations in optimization of these parameters within these two highly related NP reaction systems displays the sensitivity and complex nature of rational design in NP synthesis. It can be highly difficult to tease out direct trends based on one synthetic parameter, and extrapolating the knowledge to other material systems does not often result in predictable effects. For a broader scope on the synthesis and compositional control of I-III-VI NPs, we refer the reader to the comprehensive review by O. Yarema et al.[44]

2.2.3 Metal-Oleylamide Detection & Synthesis of Metal and Metalloid NPs

In 2013, pivotal work by Kravchyk et al. in the formation of Sn/SnO_2 NPs was inspired by the success of systems employing the high reactivity of metal amide compounds to induce swift nucleation.[45] Indeed, the authors were able to produce small, monodisperse Sn NPs, but, more importantly, a better understanding of the active Sn species was achieved, suggesting a new reaction mechanism. Key methodology for this work was ^{119}Sn NMR, identifying the formation of a Sn-oleylamido complex upon the combination of a tin precursor salt, alkylamine solvent, and a Brønsted base. Instead of the previously proposed metal silylamide metathesis reaction mechanism, a new role for the base was suggested. It was thought to deprotonate the alkylamine solvent, forming oleylamide which could then coordinate the metal cation. Instead of $Sn[N(SiMe_3)_2]_2$ as the active species for NP nucleation, Sn-oleylamido would then have been reduced by diisobutylaluminum hydride to form Sn NPs.

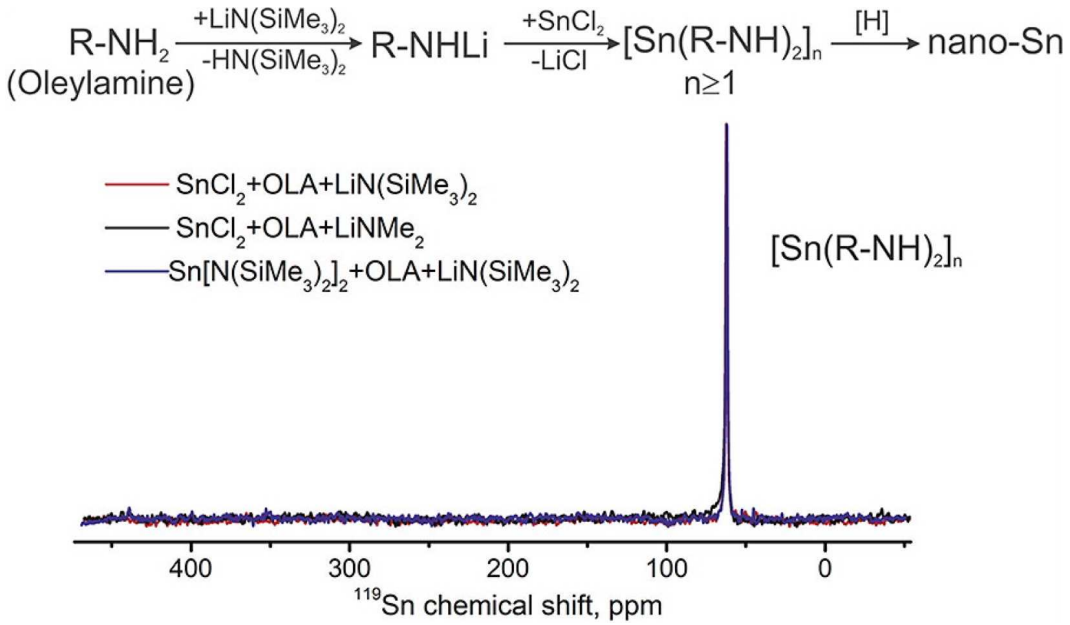

Fig. 1.9. Proposed reaction mechanism for the formation of Sn/SnO_2 NPs through the in situ formation of a Sn-oleylamido intermediate. Accompanying ^{119}Sn NMR data for solutions combining Sn precursors, OLA, and Brønsted bases. Reproduced with permission from ref [45]. Copyright 2013 American Chemical Society.

Fig. 1.9 depicts the proposed reaction mechanism and shows the ^{119}Sn NMR spectra for different combinations of Sn precursors, OLA, and Brønsted bases, each resulting in a single, equivalent Sn species. Based on the reaction mechanism proposed, the authors assign this signal ($\delta(^{119}Sn)$ = 62.5 ppm, to the Sn-oleylamido species. In order to eliminate alternative hypotheses for the speciation of Sn in these solutions, various other Sn compounds were characterized. The pure, liquid form of $Sn[N(SiMe_3)_2]_2$, the literature-predicted intermediate, gave a signal at $\delta(^{119}Sn)$ = 772 ppm. Further, solvation effects were ruled out as a possible hypothesis for a shift to 62.5 ppm. The relatively non-coordinating solvent, squalene, with $Sn[N(SiMe_3)_2]_2$ gave a signal at $\delta(^{119}Sn)$ = 779 ppm, while the combination of $Sn[N(SiMe_3)_2]_2$ and OLA gave signal at $\delta(^{119}Sn)$ = 646 ppm. The control solution of $SnCl_2$ in OLA gave a peak at $\delta(^{119}Sn)$ = -420 ppm. Finally, the addition of a Brønsted base to either of the last two solutions, $Sn[N(SiMe_3)_2]_2$/OLA or $SnCl_2$/OLA, resulted in conversion to the Sn-oleylamido (Fig. 1.10). The strength of this work is demonstrated in the experimental evidence eliminating the possibility of the literature-

predicted $Sn[N(SiMe_3)_2]_2$ intermediate and in support of a new reaction mechanism possible for amide-assisted NP syntheses.

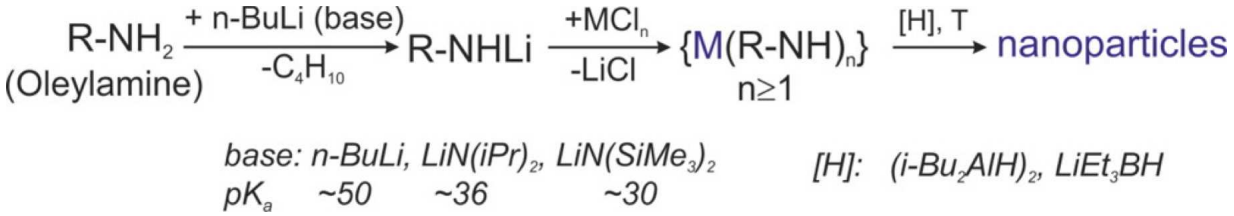

Fig. 1.10. General synthetic route proposed by He et al. via the combination of metal and metalloid salts, alkylamines, and Brønsted bases. Metal-oleylamido intermediates are proposed to form which may then be reduced to metal and metalloid NPs. Reproduced with permission from ref [46]. Copyright 2015 American Chemical Society.

Understanding a step in the transformation of the reaction components prior to NP nucleation and growth aided the authors' ability to extend this reaction scheme to the use of various other Sn salts, organometallic bases, and reducing agents.[45] Further, an impressive collection of metal and metalloid NP syntheses were developed and characterized by He et al., extending this general reaction scheme, seen in Fig. 1.10 to materials including In, Bi, Sn, Sb, Cu, Zn, Ga, and some alloys such as Bi_xSb_{1-x}, Cu_6Sn_5, and Cu_2Sb.[46] This development relied on consideration of the stability of the M–N bond. Most of the elements formed relatively unstable metal oleylamide intermediates (Bi, Sb, Cu, Zn) and could be directly decomposed to unary or binary M^0 NPs by simply combining the metal salts and Brønsted base in OLA. Conversely, Sn and In formed more stable metal oleylamide intermediates and required the use of a reducing agent to induce M^0 formation. Also, the Ga oleylamide system did not provide Ga^0 NPs. A higher reactivity was found by adaptation to use the secondary amine, dioctylamine, instead of OLA. The versatility of this NP synthetic strategy emphasizes the necessity for the consideration of this possible reaction mechanism, or a related process, in future studies of NPs developed with similar constituent reagents.

2.3 Post-Metal Oleylamide Formation Mechanistic Studies

The following studies highlight investigations of amide-assisted NP syntheses after metal oleylamides have formed. These three studies highlight the versatility of amide-assisted syntheses but

point to the careful investigation required for individual systems. The following studies involved the examination of the role of various reducing agent additives,[47] determination of the reaction mechanism for the formation of Ni NPs from Ni dioleylamide precursors and the effects of oligomerization,[48] and, lastly, the reactivity of oleylamide in the formation of InN NPs.[49]

2.3.1 Role of the Reducing Agent for Amide-Assisted InAs QD Synthesis

In amide-assisted syntheses, the metal-amide bond may be strong enough to require a reducing agent for optimized NP formation. A report in 2018 from the Talapin group introduced a study focused on identifying the role of the reducing agent in the reaction of $InCl_3$ and $As(NMe_2)_3$ in OLA to produce more monodisperse InAs QDs.[47] Depending on the strength of the reductant, quantified by its hydride donating ability, varying QD products resulted. Outlined in Fig. 1.11, the weakest reducing power produced no reaction while slightly increasing the reductant's ability gave InAs products but with a broad size distribution. As the reducing ability of the reductant was increased and the precursor conversion rate increased, the size distribution narrowed, which was explained within the LaMer model of nucleation and growth[50]. The fast precursor conversion rate allows a swift monomer supersaturation, causing a short nucleation burst. A shorter nucleation time period results in comparable growth times for the collection of particles and a smaller size distribution. Thus, increasing the power of the reductant exhibited a more monodisperse collection of InAs QDs. Using a reductant of greater strength ($LiEt_3BH$) than the optimal reductant identified in this study, Alane *N,N*-dimethylethylamine complex (DMEA-AlH_3), initiated an unwanted side-reaction, reducing some In^{3+} to In^0 NPs. Depending on the reactivities and stabilities of the metals involved, the reducing agent provides a handle for monodisperse NP formation.

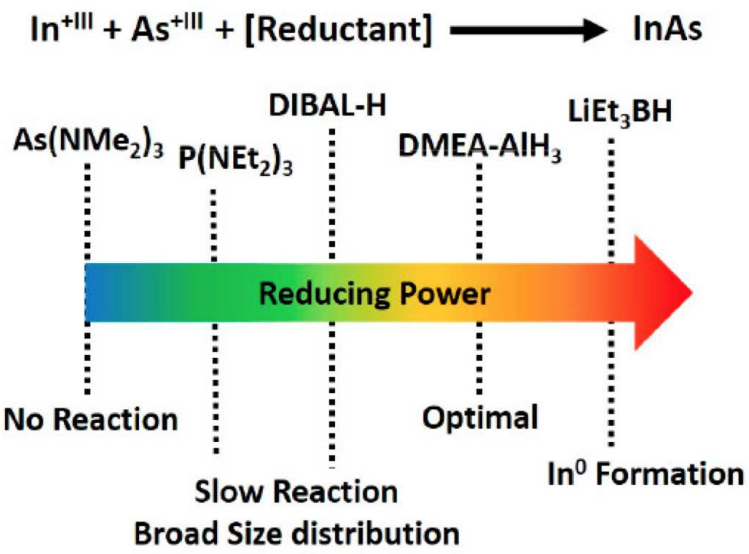

Fig. 1.11. General reaction equation for the formation of InAs QDs. Scaled description of reducing agents used in this work ranked in terms of reducing power alongside the observed effects on the NP reaction products. Adapted with permission from ref [47]. Copyright 2018 American Chemical Society.

The authors investigated the reducing ability of the compounds experimentally by introduction to the precursor solution at RT, and observed the solutions' color slowly change to red, proposed to be the formation of amorphous InAs clusters. The absorption spectra of the solutions were monitored over time, and a clear difference in precursor conversion rates could be identified, as depicted in Fig. 1.12. This study stands as a good example of examining the role of one synthetic parameter, the reducing agent. Beyond simply connecting the synthetic variations with their respective reaction outcomes, the authors experimentally tested the hypothesis of the reductant strength affecting the precursor conversion kinetics. The authors discussed a standard property of the reductants, the hydride donor ability, but did not rely on it alone to explain the observed trends. Monitoring the evolution of precursor conversion via absorption spectroscopy provides some empirical evidence of how well the hydride donor ability stands as a predictive scale. An important strength of this test involved its inclusion of the NP reaction solvent system. Hopefully, in the development of other NP syntheses involving reducing agents, the hydride donor ability values could inform a mindful exploration of NP syntheses accompanied with kinetic studies via spectroscopy. This study's system benefited from the precursor conversion kinetics existing on

a suitably extended time scale when carried out at RT and from the signature red color of the conversion products. Generally, beyond the scope of this specific example, it would be beneficial for NP synthetic studies to search for identifying, dynamic characteristics of precursor conversion and other processes during NP synthesis for empirical evidence of proposed reaction schemes.

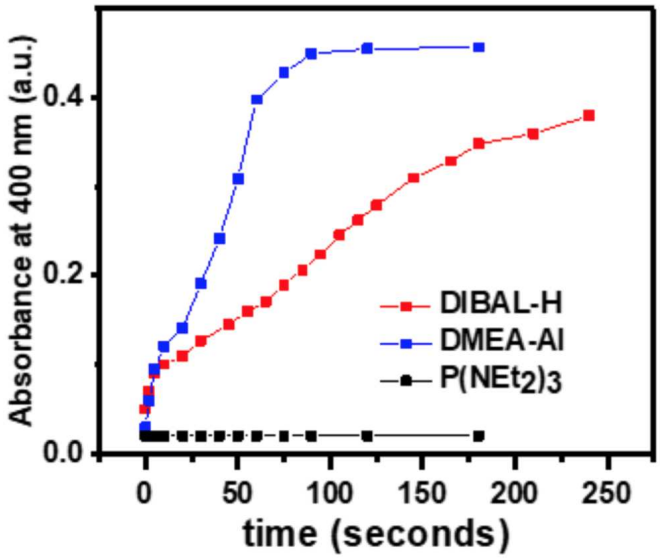

Fig. 1.12. The temporal evolution of absorption at 400 nm for solutions of various reducing agents following injection into the reaction mixture at RT. Reproduced with permission from ref [47]. Copyright 2018 American Chemical Society.

2.3.2 Water-Free Synthesis of Ni NPs & Metal Amide Oligomerization

In 2012, Carenco and coworkers examined the reduction of $Ni(acac)_2$ by OLA to form Ni^0 NPs[51]. Through complementary characterization of reaction byproducts, the authors proposed possible reaction schemes. These were evaluated with density functional theory (DFT) calculations, and the reaction was identified to occur via condensation of an acetylacetonate ligand followed by β-H abstraction from a coordinated primary alkylamide to the remaining acetylacetonate ligand. The group was motivated to alter this reaction mechanism to avoid the production of H_2O and achieved this through a Ni(II)-dioleylamide intermediate (Fig. 1.13)[48]. Drawing inspiration from the Kovalenko group's general synthetic strategy[46], *n*-BuLi and OLA reacted to form oleylamide species which could be introduced to a Ni halide precursor

to attain the desired intermediate. The authors suggested that β-H transfer could occur from one alkylamide ligand to the other, generating the active monomer for the formation of Ni NPs.

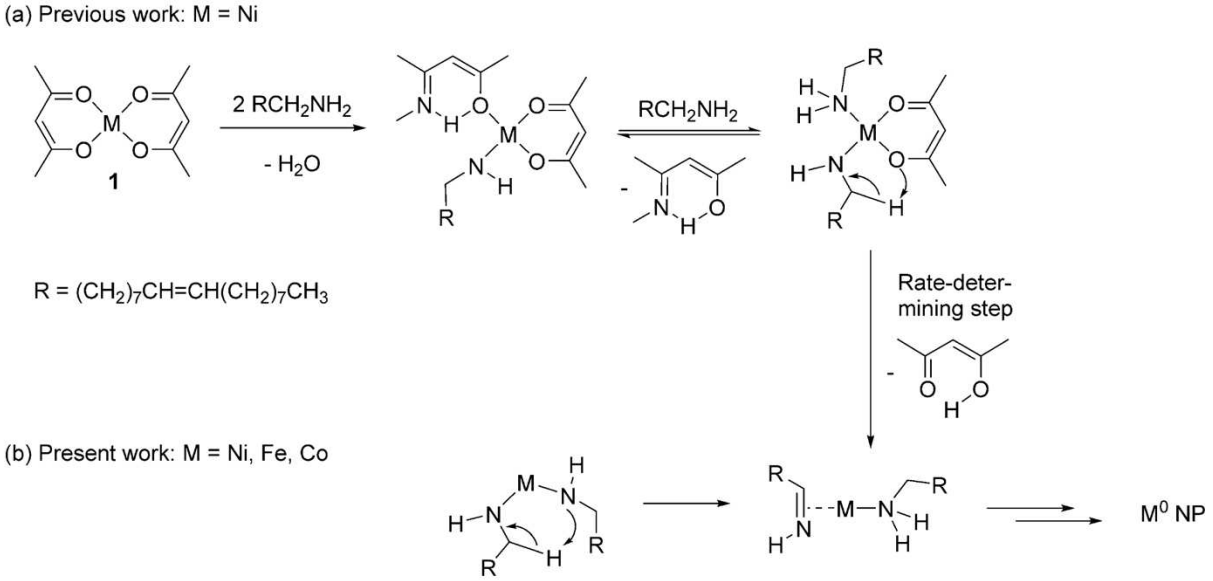

Fig. 1.13. a, Reaction scheme for the reduction of $M(acac)_2$ by OLA via β-H transfer. **b,** By adapting the metal precursor to a dioleylamide species, the authors speculated an analogous reaction mechanism could exist avoiding the evolution of water. Reproduced with permission from ref [48]. Copyright 2017 Wiley-VCH Verlag GmbH & Co.

The authors compared analogous reactions in which either the Ni dioleylamide precursor was prepared and isolated ex situ or generated in situ prior to Ni NP formation. Initial observations showed smaller NPs (~4 nm) formed from in situ-generated Ni dioleylamide compared to larger NPs (~11 nm) from the ex situ isolated precursor. However, the preparation of Ni dioleylamide involved stirring at room temperature overnight. The authors carried out the control reaction of preparing the Ni dioleylamide in situ followed by aging of the solution at room temperature overnight followed by heating for Ni NP formation. This produced larger NPs, consistent with the isolated Ni dioleylamide precursor. The authors speculated that the degree of oligomerization of the Ni dioleylamide precursor influenced the resultant Ni NP size with monomeric forms generating more nuclei and smaller NPs compared to the oligomeric form resulting in fewer nuclei and larger particles. To experimentally examine the Ni dioleylamide precursor, the authors determined hydrodynamic radii via ^1H 2D diffusion-ordered (DOSY) NMR spectroscopy.

They found that Ni dioleylamide tended to oligomerize over time (in days) at room temperature. To target monomeric species, the solvent OLA was added. This limited the hydrodynamic radius and therefore degree of oligomerization despite aging of the solution over three days.

However, one control was somewhat puzzling in consideration of the suggested link between degree of oligomerization and NP size. A solution of oligomeric Ni dioleylamide was heated to the NP growth temperature but held for a shorter amount of time (5 min) which the authors reported involved initiation of the reduction process but only a small collection of NPs. This solution was analyzed via NMR, and monomeric Ni dioleylamide species were detected. Thus, the Ni dioleylamide species appears to depolymerize upon reaching the NP growth conditions, but the NP sizes are still dependent on the state of precursor aggregation from the onset of the reaction. This characterization of the degree of oligomerization present for metal amide species is unprecedented in amide-assisted NP syntheses and would be useful for exploration of other material systems. The authors displayed preliminary results adapting the reaction to form both Fe and Co NPs exhibiting the utility of this synthetic strategy for other unary, metal NPs. It would be interesting to explore how these chemical reactions and oligomerization processes could be altered by the presence of an anion species for binary NP syntheses.

2.3.3 InN NP Reaction Mechanism: in Situ Generation of $[NH_2]^-$ from Alkylamides

In NP synthesis, alkylamides have been used to form nitride materials, but an understanding of a reaction mechanism for nitrogen delivery has evaded the field. Previous studies found InN to form catalytically from metallic In core particles by the SLS mechanism,[52–54] but the chemical mechanisms allowing cleavage of the stable C–N bond have posed a significant question for the field. In 2018, Chen et al. published a suggested reaction scheme for their synthesis of InN which involved injection of a Li alkylamide into an In halide/alkylamine solution.[49] The authors studied the byproducts of the reaction mixture. Via ^{1}H NMR, secondary aldimines ($R_1HC{=}NR_2$) were detected which was supported by MS data identifying a *m*/*z* value corresponding to *N*-oleyl-oleylimine. This is the expected product of the condensation of two oleylamide molecules and it encouraged the authors to suggest the following reaction mechanism. Beginning with an oleylamide species (known to form from the combination of *n*-BuLi and

OLA[46]), further oxidation of this species would give the primary oleylimine. Due to the instability of these moieties, it was suggested to carry out condensation with another oleylamide forming the more stable secondary aldimine, the detected byproduct. The complete suggested reaction scheme is shown in Fig. 1.14, with the secondary aldimine formation depicted in steps 1a-b.

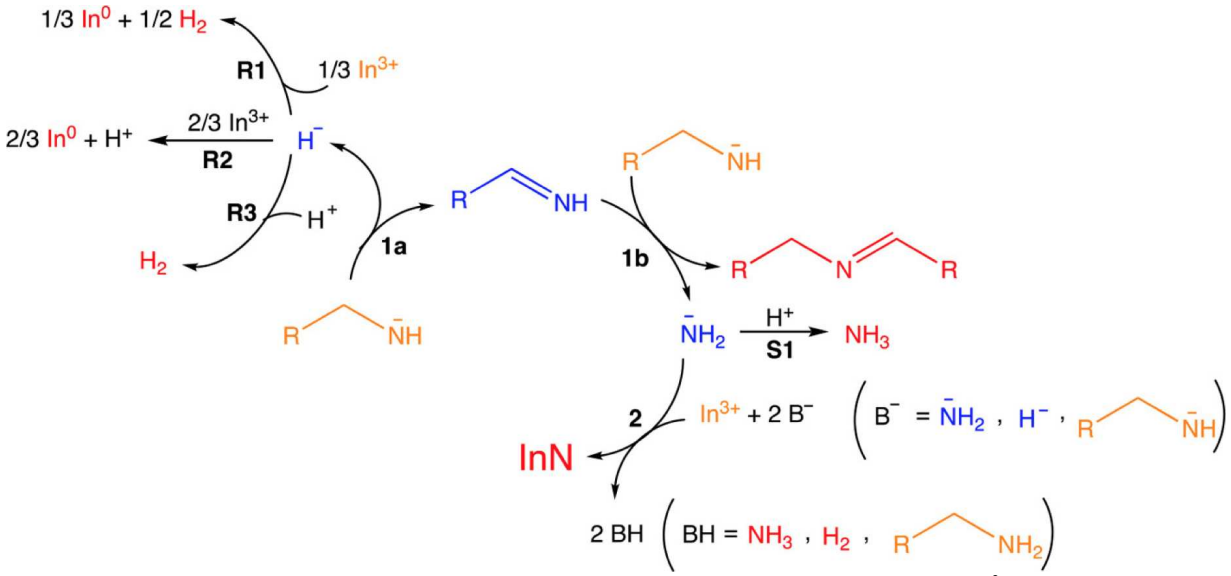

Fig. 1.14. Overall reaction scheme proposed for the transformation of alkylamide and In^{3+} precursors forming reduced In^0 species and the desired product, InN. The in situ production of the proposed $[NH_2]^-$ intermediate and active species for InN is outlined. Reproduced with permission from ref [49]. Copyright 2018 American Chemical Society.

Two key points were raised related to the proposed mechanism for the aldimine formation: energy compensation of the C–N bond division and the formation of the amido group, $[NH_2]^-$. The breaking of one C–N bond was suggested to be compensated by the formation of one during condensation of the aldimine (step 1b). The amido group, $[NH_2]^-$, was then hypothesized to be the active species for InN formation. Step 2 illustrates nitride formation from In^{3+}, $[NH_2]^-$, and two electron donors ($[NH_2]^-$, H^-, or $[RNH]^-$ species). The observed side product In^0 was described as likely stemming from reduction of In^{3+} by the hydride species, shown in steps R1 and R2. Supporting but not conclusive evidence resided in the detection of H_2 during the reaction. The detrimental side reaction generating NH_3 (S1) was also supported by its detection via gas chromatography. Additionally, the observation of higher In^0:InN ratios than would be expected if all $[NH_2]^-$ moieties were converted to InN suggested some of the active amido

species were lost in the production of ammonia. The highest yield of InN relative to In^0 was achieved with the use of a 3:1 alkylamide to In^{3+} ratio, as predicted by the scheme. All other precursor ratios resulted in lower yields of InN relative to In^0. We point out this study as a detailed example in which byproducts of NP reactions were examined in order to backtrack a possible reaction mechanism with special consideration of many different reaction routes of the various interacting species.

The authors noted the similarity in chemistry of this reaction mechanism with that of inorganic amides ($NaNH_2$) reacting with In salts, with the largest difference being an in situ formation of the $[NH_2]^-$ species. Based on the findings of Kravchyk et al. on the in situ formation of oleylamide from n-BuLi and OLA[45], the important discovery of the generated $[NH_2]^-$ in this reaction mechanism may inform future synthetic developments. Similar reaction conditions may allow synthesis of other nitride NPs. Additionally, the similarity in components and temperatures might spark questions regarding the ease of possibly forming metal nitride impurities in other metal NP syntheses. In exploring this possibility, it would be useful to check the reaction products for metal nitrides and to employ the analytical techniques used in this study to identify the aldimine byproduct. If it were detected, the formation of $[NH_2]^-$ would be likely. However, the amide species has the possibility to completely convert to ammonia rather than form metal nitrides. This study points out the utility of adapting synthetic strategies to other material systems but emphasizes the need for continued critical examination and exploration of new reaction mechanisms without assuming the occurrence of exactly the same processes.

2.4 Use of HMDS in NP Syntheses

The following discussion encompasses the use of hexamethyldisilazane (HMDS), the conjugate acid of $LiN(SiMe_3)_2$, in solution-based NP syntheses. In most cases, HMDS is added without an understanding of its chemical role. Its use has provided access to similar NP products as compared to $LiN(SiMe_3)_2$-based reactions; thus, we strive to compare the two fields in this section. A table of general properties for the two compounds is given in Table 1.1.

2.4.1 HMDS: a Necessary but Puzzling Additive

Although a direct comparison has yet to be made, a parallel field of solution-based NP syntheses employs the conjugate acid of $LiN(SiMe_3)_2$, HMDS, as an additive. Its presence generally allows access to certain aspects of nanostructured products: crystalline versus amorphous products[55–58] or no products[59–63], metastable instead of more thermodynamic polymorphs[64–67], or smaller, more monodisperse versus larger particles[67]. A detailed understanding of its role has yet to be determined; however, speculations often involve either its function in capping NP surfaces for limiting growth and stabilizing certain products or coordination to precursor elements affecting monomer reactivity.

Table 1.1. Properties of $HN(SiMe_3)_2$ and $LiN(SiMe_3)_2$

Property	$HN(SiMe_3)_2$	$LiN(SiMe_3)_2$
Molar Mass (g/mol)	161.39	167.11
Physical state	colorless liquid	white or light yellow crystalline powder
Density (g/mL)	0.774	0.891
Melting Point (˚C)	–78	94
Boiling Point (˚C)	125	410

The first reports using HMDS in solution-based NP syntheses employed the compound as a nitriding reagent in solvothermal reactions spanning temperatures of ~180-300 ˚C. Combined with metal salts, HMDS allowed access to the following materials: GaN[68], AlN[69], In-doped GaN[70], herzenbergite SnS[71], Co-doped GaN[72], and Tb-doped GaN[73]. In 2010, the first non-pressurized NP syntheses that included HMDS came from the Schaak group for Ge[55], GeS, and GeSe nanostructures[56]. Vaughn II et al. suggested the presence of HMDS could allow the reaction to proceed through a Ge(II)-HMDS complex, $Ge[N(SiMe_3)_2]_2$[55], referencing work by Gerung et al. in which the Ge silylamide was used as a precursor to form Ge NPs[74]. The use of $Sn[N(SiMe_3)_2]_2$ for Sn chalcogenide NPs[33–35] reported prior to these HMDS-based syntheses may have also inspired the use of HMDS. The Schaak group identified the necessity for HMDS because its absence resulted in amorphous products that were highly susceptible to oxidation formed.[55,56] Following HMDS-based NP reactions reports identified similar results upon the exclusion of HMDS[57,59–63]. Kumar et al. reported a series of NP syntheses for In_2S_3[59], CuS[75], Ag_2S[60], and Ag/Ag_2S[76] NPs for which HMDS was the only solvent. The authors suggest the reactions proceed through an

oligomeric S–N intermediate and produce trimethylsilyl chloride as a byproduct. For the Ag_2S NP synthesis, S_4N_4 was isolated and suggested as the active S intermediate[60].

Solution-based NP syntheses for which HMDS in an additive in common solvents (long alkyl-chain amines, phosphines, and carboxylic acids, etc.) instead of the sole solvent presents a more complex system for understanding the intermediates and reaction mechanisms. The inclusion of HMDS was not discussed in the following synthetic reports: SnSe nanosheets[77], SnS NPs and nanosheets[64], Fe_3Ge_2 NPs and FeGe nanowires[65], and $GaPt_3$ NPs[78]. Biacchi et al. mentioned that their SnS syntheses[64] were adapted from Hickey et al.[34] Interestingly, the authors were able to substitute $Sn[N(SiMe_3)_2]_2$ for $SnCl_4$ alongside an addition of HMDS, but the authors did not speculate or investigate on the Sn speciation in reaction. This report did provide important crystallographic characterization of the SnS products identifying that the commonly reported metastable cubic SnS phase had likely been misidentified in the literature and was more accurately described as a pseudotetragonal distortion of the orthorhombic SnS phase. Despite potential incorrect indexing, some previous SnS synthetic reports identified that amorphous products formed in the absence of HMDS[57,58]. Huang et al. published a subsequent SnS NP report identifying small, metastable, zinc blende SnS NPs upon the inclusion of HMDS and large, orthorhombic α-SnS nanosheets in its absence[67]. Even if the products did not form two different polymorphs, the presence of HMDS made an obvious difference in the morphology and size of the nanostructure products. In one Sn and Sn chalcogenide NP study, Zhao et al. reported that no products resulted from the exclusion of HMDS and speculated on the formation of a Sn(II)-HMDS intermediate[62].

Other reports have identified the formation of different phases when comparing synthesis with and without HMDS. In 2012, Buckley et al. provided syntheses for the $Sn_xGe_{1-x}Se$ solid solution series, and observed that HMDS was required for Ge incorporation into the ternary phases[79]. However, HMDS omission was required to form the GeSe end-member. With HMDS, an unknown GeSe phase of 1:1 molar Ge:Se composition was detected. Following, our group reported the first Fe_2GeS_4 NP synthesis[80] and used HMDS taking inspiration from the Buckley et al. report in order to attain Ge incorporation. In its absence, the impurities GeS and FeS were detected alongside the ternary. This is discussed in greater

detail in Chapter 2. In 2014, Mahler et al. reported nanosheet syntheses of the metastable 2H-WS_2 phase upon inclusion of HMDS and the more thermodynamically stable 1T-WS_2 phase without it[66]. The authors speculated on potentially dual roles of HMDS. It could react with oleate ligands coordinated to W resulting in activation of WS_2 formation. Also, its potential to act as a nanosheet surface ligand was suggested to stabilize the formation of the metastable 2H-WS_2 phase. Finally, a synthetic report for SnS nanosheets from Kobylinski et al. in 2018 provided a proposed reaction mechanism that involved all solvent components as well as HMDS[63]. We will discuss this below in Section 3.1.

2.4.2. Evolution of HMDS from Metal Silylamide Precursors & Effect on NP Morphology

Interestingly, one of the best examples of understanding the role of HMDS in solution-based NP syntheses occurred in a report for which HMDS was not an added precursor. In 2012, Liakakos et al. reported on the curious variation in Co NP morphology dependent on the rate of precursor addition rate during stock solution preparation[81]. As $Co[N(SiMe_3)_2]_2$ was added to the hexadecylamine and lauric acid ligand mixture, HMDS evolved, and the authors detected its impact on Co speciation and NP formation. This study is exemplary in its approach to understanding the broad impacts often overlooked synthetic parameters may have on NP products. Immediately, the authors acknowledge the difficulty in controlling nanostructures at will. "NC synthesis is still largely empirical, and while several aspects can be explained a posteriori, it is nearly impossible to predict the results of a reaction that involves new reactants. Specific unexpected aspects inherent to each reaction can turn out to be dominant over general principles." Specifically, this study focused on understanding the reaction dynamics of one system due to observed irreproducible results. Nanostructures of Co were formed from a solution of $[Co\{N(SiMe_3)_2\}_2(thf)]$, lauric acid (LA), and HDA in the molar ratios of 1 to 2.04 to 0.36. The stock solution was held at 150 °C under 3 bar H_2, resulting in reduction of the Co species. Surprisingly, the addition rate of the Co precursor solution to the HDA/LA mixture was discovered to be instrumental in the varying Co morphology attained, as shown in Fig. 1.15.

Structural characterizations indicated the slow addition rate solution resulted in metallic Co material at an early stage of crystallization, lacking long-range order. The intermediate and fast addition

rates gave rise to crystalline, metallic Co material with a majority phase of face-centered cubic (*fcc)* and hexagonal close-packed (*hcp*) phases, respectively. The fast addition product core phase was unidentifiable by HRTEM due to its large thickness, but the arms were identified as *hcp* Co. Admirably, the authors clearly stated these structural and morphological characterizations allowed them to identify differences and speculate indications for their formation, but do not give direct understanding of the precursor addition rate's effect. The slow addition rate was speculated to give rise to a higher amount of nucleation and therefore small particles, and oppositely, the fast addition was supposed to cause limited nucleation and form larger particles.

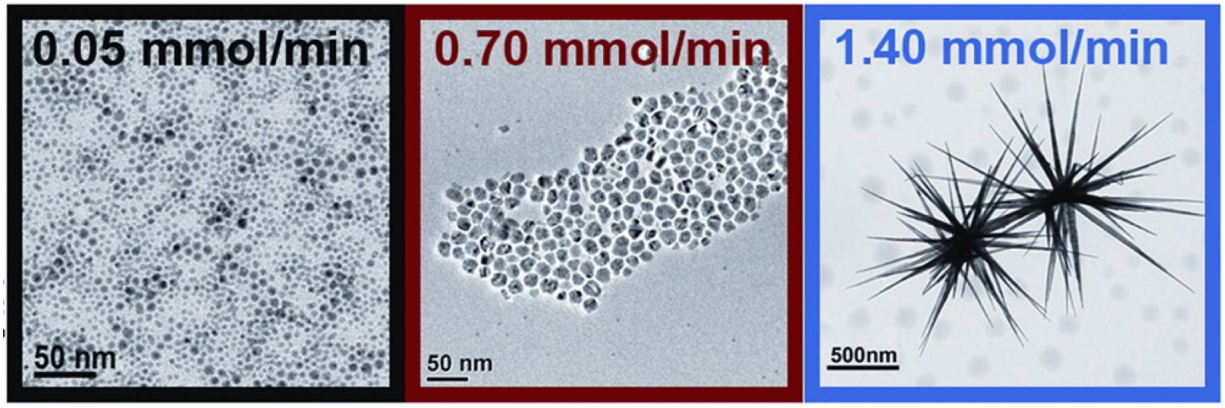

Fig. 1.15. TEM images of Co nanostructures formed from stock solutions of the same concentrations of [Co{N(SiMe$_3$)$_2$}$_2$(thf)], hexadecylamine, and lauric acid but prepared by different Co precursor addition rates. Note the differently-sized scale bars for the three images. Reproduced with permission from ref [81]. Copyright 2012 American Chemical Society.

These results inspired the authors to examine the reaction solution prior to reduction by H_2. Initial observations from UV-Vis spectroscopy included the lack of a peak characteristic of the [Co{N(SiMe$_3$)$_2$}$_2$(thf)] precursor, indicating its rapid transformation in all cases. Three major peaks were observed in the UV-Vis spectra but in varying ratios of intensity for the different addition rate solutions, and these were observed to evolve over time. A key observation was the presence of a dominant peak in the slow addition solution that was almost absent from the fast addition spectra, which, when aged, closely resembled that of independently synthesized Co[LA]$_2$. The authors hypothesized the slow addition rate gave rise to an extended nucleation period, and this solution's dominant UV-Vis peak was suggested

to correspond to an easily reduced Co species, forming non-crystalline, small Co particles. Correspondingly, fast addition products indicated to the authors a brief nucleation period; thus, $Co[LA]_2$ was suggested to constitute part of the "growth reservoir," favoring slow growth of Co multipod structures. However, despite the observed UV-Vis spectra changes in both the fast and slow addition solutions over the course of time, aged solutions reacted under H_2 gave Co morphologies consistent with their respective fresh solutions. The authors admitted this questioned the legitimacy of correlation between the UV-Vis solution spectra and the observed Co morphology.

Attempting to replicate the hypothesized composition of the fast addition rate solution, $Co[LA]_2$ was put under H_2 at 150 °C but did not reduce to Co^0. Upon the inclusion of HDA, Co multipods formed. Thus, the interaction of HDA and Co was investigated computationally and experimentally. Various HDA-containing Co complexes were calculated to be stable enough to exist in solution, and attempts to isolate possible Co compounds from combinations of $[Co\{N(SiMe_3)_2\}_2(thf)]$, lauric acid (LA), and HDA were carried out. One Co complex for which a crystal structure could be determined was $[Co[LA]_2(NH_3)_2]$. The existence of ammonia indicated the possibility of the following side reaction. Following deprotonation and coordination of the carboxylic acid moiety of LA with the Co precursor, $HN(SiMe_3)_2$ (HMDS) evolved. Subsequently, two equivalents of excess LA and HMDS would produce NH_3 and two silyl ester molecules. NMR (^1H) spectra of the fast and slow addition solutions demonstrated the presence of HMDS and the silyl ester. Interestingly, the slow addition solution revealed a much higher concentration of the silyl ester than the fast addition solution.

Altogether, the authors then correlated the importance of this side reaction to the Co reduction reactions. When the Co precursor is slowly added and reacts with LA, the generated HMDS provides a competing reaction with LA, forming the silyl esters. A lesser amount of LA is left to coordinate Co, and a smaller $Co[LA]_2$ growth reservoir exists relative to the fast addition solution. In that scenario, the majority of Co is complexed by LA, constituting a large "growth reservoir" and a smaller "nucleation reservoir." Further, the formation of the interesting multipod morphologies from this fast addition reaction solution is explained in the following way, depicted in Fig. 1.16. A brief nucleation period results

in a smaller amount of Co primary nuclei, which may coalesce into polycrystalline cores. As this continues and the growth reservoir, $Co[LA]_2$, is consumed, liberation of LA is suggested to influence a change in the growth mechanism. The competitive reaction of LA with HMDS occurs, but as the LA concentration becomes significantly high, it begins to selectively coordinate to the growing Co particles. The (002) *hcp* and (111) *fcc* facets are suggested to be free, causing growth of the *hcp* multipod arms, as the LA coordinates along the *c* axis of the growing arms. In all, the fast and slow additions of $[Co\{N(SiMe_3)_2\}_2(thf)]$ into LA/HDA mixtures of identical initial compositions resulted in significantly different proportions of the nucleation and growth reservoirs, heavily influencing NP formation.

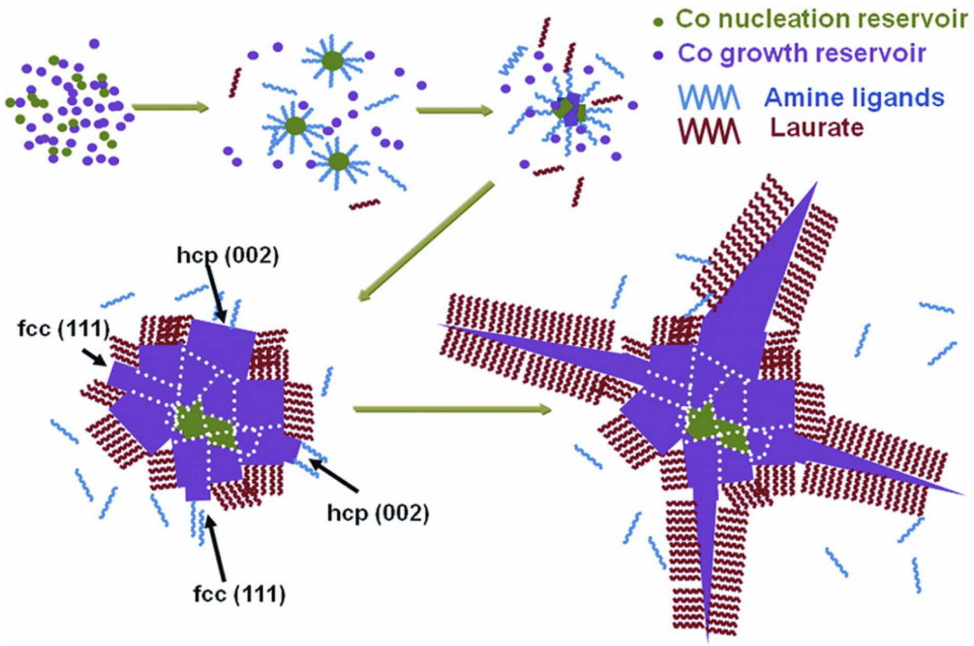

Fig. 1.16. Proposed reaction pathway for the formation of Co multipods from the fast addition stock solution under reduction by H_2. Reproduced with permission from ref [81]. Copyright 2012 American Chemical Society.

This study stands out as an eye-opening account of the possibility for apparently negligible details to heavily impact a NP reaction system. The authors point out the need for scrutiny and consideration of many possible transformations of all components of NP reaction solutions including those different from this silylamide/carboxylic acid/amine mixture. It is always a possibility for unforeseen and changing side reactions to occur during NP synthesis and for their effects to impact the eventual products. The strengths in this study lie beyond the careful characterization of both solid-state and solution-based products but

also in the authors' direct and mindful discussion of which ideas could be taken away from their observations and data collected without speculating beyond their means. The role of HMDS is multifold; its reaction with LA affects both the speciation and reactivity of Co as well as the solvent system concentrations. The Co speciation impacts the degree of nucleation versus growth while the solvent system concentrations affect the growth of various Co NP morphologies. Thus, HMDS may play similar roles in other NP synthetic systems, and this work highlights the necessity to examine NP material systems individually because specific conditions can prove to be difficult to translate. As this level of investigation becomes more common, then more general trends in NP syntheses may be discovered.

3. Future Directions for Amide-Assisted NP Syntheses

In this section, we highlight some amide-assisted studies that would be interesting to revisit given the broad scope of literature considered in this chapter. We identify some alternative hypotheses that could be viable considerations for understanding these reaction systems. This area of NP synthesis is considerably large and diverse, but some similar themes have been identified whether HMDS, $LiN(SiMe_3)_2$, other Brønsted bases, or metal silylamide precursors were employed. Direct comparison of most systems is hindered due to the vital interplay of the solvent system. However, significant progress has been made within individual NP synthetic systems. We believe further systematic studies would be of use to advance the development of NP synthesis beyond the slow process of trial and error.

One of the most promising next steps in uncovering the actions of HMDS and $LiN(SiMe_3)_2$ in NP syntheses could be to thoroughly characterize the reaction intermediates and byproducts of Sn chalcogenide NPs syntheses. The Kovalenko group reported on Sn speciation in the presence of alkylamides and Brønsted bases via ^{119}Sn NMR[45], and advancing this work from the realm of unary Sn^0 to binary Sn chalcogenide NPs would be a promising next step. In order to minimize complexity, a set of comparable syntheses for SnS in oleylamine with the separate use of each $Sn[N(SiMe_3)_2]_2$, $LiN(SiMe_3)_2$, and HMDS could be developed and characterized. A number of Sn chalcogenide NP syntheses involving either $Sn[N(SiMe_3)_2]_2$ or HMDS have been reported, and although their synthetic differences exclude the possibility of directly comparing them, they stand as useful resources for developing comparable

reactions for these explorations. [34,37,57,58,63,64,67,71,79] Following characterization of alkylamine-based syntheses, it would be interesting to explore the role of other common NP solvents, such as carboxylic acids (lauric or oleic acid), alkenes (1-octadecene), and phosphines (trioctylphosphine).

3.1 Proposed Reaction Mechanism for HMDS-Based SnS Nanosheet Synthesis

To this aim, a SnS nanosheet synthesis reported by Kobylinski et al. in 2018[63] would be useful. The solvent system is oleylamine (OLA) and oleic acid (OA) with $SnCl_2$ as the Sn precursor and HMDS as an additive. The authors provided a speculated reaction mechanism shown in Fig. 1.17. Upon combination of $SnCl_2$ with OLA and OA, the Sn oleate and oleylammonium chloride species were suggested to form. HMDS was added and suggested to react with Sn oleate ligands and additional OLA, abstracting a proton each from the amine headgroup of two OLA molecules and donating its trimethylsilyl groups to the oleate ligands resulting in two oleic silylesters, NH_3, and Sn dioleylamide. This Sn complex then reacted upon injection of a S in OLA solution to form SnS. Based on work by Thomson et al.[82], the authors suggested the active S species were H_2S and thioamide (a thiocarbonyl carbon bonded to NH_2). Finally, HMDS was suggested to carry out a secondary role of quenching any HCl that might have evolved to form trimethylsilyl chloride and NH_3. These proposed reactions are reasonable, and the authors detected both gaseous NH_3 and a gaseous S species (claimed to be H_2S). To do so, the reaction headspace was bubbled through distilled water. Following, a pH of 10 was measured, and upon combination with a concentrated hydrochloric acid solution resulted in the white fog of ammonium chloride. To indirectly detect H_2S, the authors introduced a lead acetate-soaked filter paper to the reaction headspace and observed a black precipitate. This is a common control employed to support the claim of both H_2S formation but also that H_2S is the active S species in NP formation. While logistically difficult, further characterization of reaction intermediates by ex or in situ techniques would be advantageous for evaluating the proposed reaction mechanisms.

As observed by Liakakos et al. in the formation of Co NPs, NH_3 is a possible byproduct of HMDS and carboxylic acids.[81] Therefore, the detection of NH_3 in the SnS nanosheet synthesis from Kobylinski et al. is not sufficient evidence to suggest the full reaction mechanism. The reagents HMDS

and OA could have produced NH_3 without involving the Sn ions. Further, the authors reported that very similar NP products, hexagonal nanosheets of SnS albeit with less defined edges, formed upon the omission of oleic acid. The increased definition of the hexagonal morphology with inclusion of OA was explained by preferential attachment of OA to specific crystallographic facets of SnS. However, the authors did not address how the proposed reaction scheme might have been altered in the absence of oleic acid. It would have been interesting to test for NH_3 production in the absence of OA. Also, because SnS did not form in the absence of HMDS, the reaction mechanism may be somewhat more complex than initially proposed. Characterizing the speciation and reaction progress of these Sn chalcogenide NP syntheses would be of interest not only for fundamental understanding but also because Sn chalcogenides may form in a number of different phases, sizes, and morphologies which can have impacts on material properties.

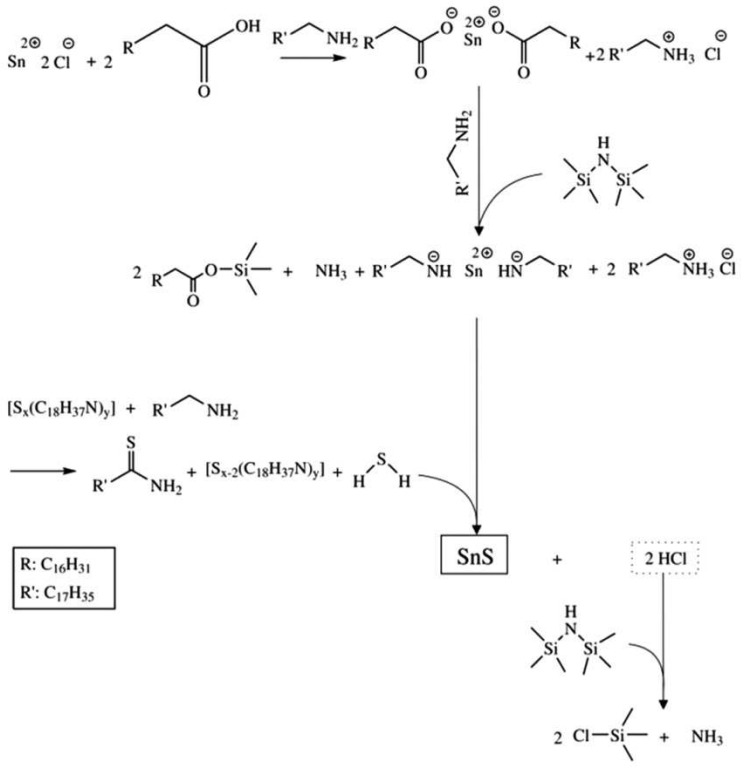

Fig. 1.17. Proposed reaction scheme for the formation of SnS nanosheets. Tin oleate intermediates are formed prior to reaction with HMDS and OLA, forming silylesters and Sn dioleylamide. This is proposed to be the active Sn species in the formation of SnS. HMDS is also suggested to quench any HCl generated in the reaction. Reproduced with permission from ref [63]. Copyright 2018 American Chemical Society.

3.2 Computational Modeling for Understanding Cation Speciation

Progress for other amide-assisted NP syntheses would benefit from characterization of the cation speciation but may be limited by containing elements with low isotope abundance and/or activity for NMR spectroscopy. In these cases, other techniques such as electron paramagnetic resonance (EPR) and Mössbauer spectroscopy could be worth developing for characterizing NP monomer speciation. Additionally, modeling reaction intermediates could lend a parallel path to understanding the vital chemical reactions of NP formation for a variety of systems. However, the role of the solvent system cannot be ignored in these cases.

For example, the Snee group developed syntheses for InAs, Cd_3As_2, and Cu_3AsS_4 NPs via an arsenic silylamide precursor, $[(Me_3Si)_2N]_2AsCl$[83]. For the formation of InAs NPs, the authors discussed a proposed reaction mechanism beginning with the interaction of As silylamide, $[(Me_3Si)_2N]_2AsCl$, and superhydride, suggesting the silylamide was reduced to $[(Me_3Si)_2N]_2AsH$. This first step was investigated with ^1H NMR, and the following steps were investigated by computational modeling. In the NMR experimentation, As silylamide and superhydride were combined in toluene-d_8; however, this simplifies the reaction system by ignoring any possible role of the solvents, ODE and OLA, or any possible impurities therein. This should be especially important because the As silylamide is dissolved in ODE and OLA prior to introduction of any other reaction components, including the reducing agent, $LiEt_3BH$ (superhydride). Considering the brevity of literature in which solvent components were considered innocent but in truth played large roles, these experiments seem a missed opportunity for elucidating a more complete reaction mechanism. While computational explorations are hindered by taking bulky solvent molecules into account, shortened versions of the solvent molecules have been included in other speciation models.[48,51] Potentially 1-butene could substitute for ODE, and 1-butylamine could substitute for OLA. It also would have been advantageous to include the solvents in the ^1H NMR experiments.

This report also stands as one example of a number of NP syntheses that could be enhanced by possible adaptation to designing syntheses in which the corresponding metal amides are formed in situ. Instead of requiring extensive and air-free synthesis and isolation of metal silylamides for use as

precursors in NP syntheses, it would be interesting to explore NP reactions that employ the corresponding metal salts and alkali Brønsted bases as precursors. If the initial preparation of these pnictide silylamide precursors is necessary, then it would be compelling to characterize reaction solutions at all points throughout the procedure in order to gain better understanding about the formation of the end products. Identifying the active pnictide intermediates in these reaction systems might enable the choice of more direct synthetic routes to the same end. This would also provide insight advantageous for continuing the important work done in these studies: development of new, ternary material systems plagued by the lack of straightforward pnictide precursors.

3.3 Brønsted Base Effects on Anion Speciation

Although much emphasis has been placed on the interaction of Brønsted bases and cation precursors, the presence of the base may also impact the chalcogen reactivity. For example, cyclo-S_8 rings may be opened via nucleophilic attack by amines and amides[84], but to our knowledge, no study has specifically examined the interaction of Brønsted bases and chalcogens in NP synthetic conditions. A study focused on the degree of ring-opening carried out by equivalent amines versus deprotonated amides would be of interest. Our work on the Fe_2GeS_4 NP synthesis has preliminarily considered these factors (Ch. 2), but there exists much room for advancement in this area. As we suggested earlier, we believe that understanding Sn chalcogenide NP syntheses would be a promising model system for advancing amide-assisted reactions, and this future direction would provide the opportunity to explore both cation and anion speciation with respect to the presence of a Brønsted base.

4. Conclusions

This narrative has sought to highlight the similar trends observed in NP syntheses that employ either metal silylamides, Brønsted bases, or HMDS. In the ongoing effort to translate synthetic strategies to new material systems, amide-assisted reactions present a promising area for advancement. The acid-base chemistry possible for $LiN(SiMe_3)_2$ and HMDS in conjunction with typical NP solvents (i.e. alkylamines, carboxylix acids) and NP precursors under dynamic conditions (i.e. temperature ramps, solution injections) is complex. In general, the roles of HMDS and $LiN(SiMe_3)_2$ in NP syntheses have not

been linked to one another in the literature, and we believe a thorough study on the effects of each the conjugate acid and base on the same NP reaction would be impactful. Careful characterization and control procedures have advanced understanding of amide-assisted NP syntheses. Because of the versatility shown for some of these synthetic schemes, it is important to consider how these processes might have an unintended effect in the development of new NP systems employing similar precursors and solvents. As knowledge of the reaction mechanisms possible for amide-assisted syntheses increases so does synthetic control over a multitude of NP compositions, phases, and morphologies.

REFERENCES

(1) De Yoreo, J.; Mandrus, D.; Soderholm, L. *Basic Research Needs for Synthesis Science*; 2016.

(2) Yin, Y.; Alivisatos, A. P. Colloidal Nanocrystal Synthesis and the Organic–Inorganic Interface. *Nature* **2005**, *437* (7059), 664–670.

(3) Reiss, P.; Carrière, M.; Lincheneau, C.; Vaure, L.; Tamang, S. Synthesis of Semiconductor Nanocrystals, Focusing on Nontoxic and Earth-Abundant Materials. *Chem. Rev.* **2016**, *116* (18), 10731–10819.

(4) Lee, J. M.; Miller, R. C.; Moloney, L. J.; Prieto, A. L. The Development of Strategies for Nanoparticle Synthesis: Considerations for Deepening Understanding of Inherently Complex Systems. *J. Solid State Chem.* **2019**, *273*, 243–286.

(5) Pietryga, J. M.; Park, Y.-S.; Lim, J.; Fidler, A. F.; Bae, W. K.; Brovelli, S.; Klimov, V. I. Spectroscopic and Device Aspects of Nanocrystal Quantum Dots. *Chem. Rev.* **2016**, *116* (18), 10513–10622.

(6) Kovalenko, M. V.; Manna, L.; Cabot, A.; Hens, Z.; Talapin, D. V.; Kagan, C. R.; Klimov, V. I.; Rogach, A. L.; Reiss, P.; Milliron, D. J.; Guyot-Sionnest, P.; Konstantatos, G.; Parak, W. J.; Hyeon, T.; Korgel, B. A.; Murray, C. B.; Heiss, W. Prospects of Nanoscience with Nanocrystals. *ACS Nano* **2015**, *9* (2), 1012–1057.

(7) Abécassis, B.; Bouet, C.; Garnero, C.; Constantin, D.; Lequeux, N.; Ithurria, S.; Dubertret, B.; Pauw, B. R.; Pontoni, D. Real-Time in Situ Probing of High-Temperature Quantum Dots Solution Synthesis. *Nano Lett.* **2015**, *15* (4), 2620–2626.

(8) Andersen, H. L.; Bøjesen, E. D.; Birgisson, S.; Christensen, M.; Iversen, B. B. Pitfalls and Reproducibility of in Situ Synchrotron Powder X-Ray Diffraction Studies of Solvothermal Nanoparticle Formation. *J. Appl. Crystallogr.* **2018**, *51* (2), 526–540.

(9) Li, J.; Wang, H.; Lin, L.; Fang, Q.; Peng, X. Quantitative Identification of Basic Growth Channels for Formation of Monodisperse Nanocrystals. *J. Am. Chem. Soc.* **2018**, *140* (16), 5474–5484.

(10) Murray, C. B.; Norris, D. J.; Bawendi, M. G. Synthesis and Characterization of Nearly Monodisperse CdE (E = S, Se, Te) Semiconductor Nanocrystallites. *J. Am. Chem. Soc.* **1993**, *115* (19), 8706–8715.

(11) Peng, Z. A.; Peng, X. Formation of High-Quality CdTe, CdSe, and CdS Nanocrystals Using CdO as Precursor. *J. Am. Chem. Soc.* **2001**, *123* (1), 183–184.

(12) Milliron, D.; Hughes, S. M.; Cui, Y.; Manna, L.; Li, J.; Wang, L. W.; Alivisatos, A. P. Colloidal Nanocrystal Heterostructures with Linear and Branched Topology. *Nature* **2004**, *430* (6996), 190–195.

(13) Miller, R. C.; Neilson, J. R.; Prieto, A. L. Amide-Assisted Synthesis of Iron Germanium Sulfide (Fe_2GeS_4) Nanostars: The Effect of $LiN(SiMe_3)_2$ on Precursor Reactivity for Favoring Nanoparticle Nucleation or Growth. *J. Am. Chem. Soc.* **2020**, https://doi.org/10.1021/jacs.0c00260.

(14) Pearson, R. G. Hard and Soft Acids and Bases. *J. Am. Chem. Soc.* **1963**, *85* (22), 3533–3539.

(15) Parr, R. G.; Pearson, R. G. Absolute Hardness: Companion Parameter to Absolute Electronegativity. *J. Am. Chem. Soc.* **1983**, *105* (26), 7512–7516.

(16) Pearson, R. G. *Chemical Hardness*; Wiley-VCH Verlag GmbH: Weinheim, Germany, 1997.

(17) Yarema, M.; Caputo, R.; Kovalenko, M. V. Precision Synthesis of Colloidal Inorganic Nanocrystals Using Metal and Metalloid Amides. *Nanoscale* **2013**, *5* (18), 8398–8410.

(18) Nayral, C.; Ould-Ely, T.; Maisonnat, A.; Chaudret, B.; Fau, P.; Lescouzères, L.; Peyre-Lavigne, A.

A Novel Mechanism for the Synthesis of Tin/Tin Oxide Nanoparticles of Low Size Dispersion and of Nanostructured SnO_2 for the Sensitive Layers of Gas Sensors. *Adv. Mater.* **1999**, *4* (1), 61–63.

(19) Cordente, N.; Respaud, M.; Senocq, F.; Casanove, M.-J.; Amiens, C.; Chaudret, B. Synthesis and Magnetic Properties of Nickel Nanorods. *Nano Lett.* **2001**, *1* (10), 565–568.

(20) Pan, C.; Pelzer, K.; Philippot, K.; Chaudret, B.; Dassenoy, F.; Lecante, P.; Casanove, M. J. Ligand-Stabilized Ruthenium Nanoparticles: Synthesis, Organization, and Dynamics. *J. Am. Chem. Soc.* **2001**, *123* (31), 7584–7593.

(21) Meffre, A.; Lachaize, S.; Gatel, C.; Respaud, M.; Chaudret, B. Use of Long Chain Amine as a Reducing Agent for the Synthesis of High Quality Monodisperse Iron(0) Nanoparticles. *J. Mater. Chem.* **2011**, *21* (35), 13464.

(22) Desvaux, C.; Amiens, C.; Fejes, P.; Renaud, P.; Respaud, M.; Lecante, P.; Snoeck, E.; Chaudret, B. Multimillimetre-Large Superlattices of Air-Stable Iron–Cobalt Nanoparticles. *Nat. Mater.* **2005**, *4* (10), 750–753.

(23) Dumestre, F.; Chaudret, B.; Amiens, C.; Fromen, M. C.; Casanove, M. J.; Renaud, P.; Zurcher, P. Shape Control of Thermodynamically Stable Cobalt Nanorods through Organometallic Chemistry. *Angew. Chemie - Int. Ed.* **2002**, *41* (22), 4286–4289.

(24) Monge, M.; Kahn, M. L.; Maisonnat, A.; Chaudret, B. Room-Temperature Organometallic Synthesis of Soluble and Crystalline ZnO Nanoparticles of Controlled Size and Shape. *Angew. Chemie - Int. Ed.* **2003**, *42* (43), 5321–5324.

(25) Glaria, A.; Kahn, M. L.; Cardinal, T.; Senocq, F.; Jubera, V.; Chaudret, B. Lithium Ion as Growth-Controlling Agent of ZnO Nanoparticles Prepared by Organometallic Synthesis. *New J. Chem.* **2008**, *32* (4), 662–669.

(26) Kahn, M. L.; Glaria, A.; Pages, C.; Monge, M.; Saint MacAry, L.; Maisonnat, A.; Chaudret, B. Organometallic Chemistry: An Alternative Approach towards Metal Oxide Nanoparticles. *J. Mater. Chem.* **2009**, *19* (24), 4044–4060.

(27) Kahn, M. L.; Monge, M.; Collière, V.; Senocq, F.; Maisonnat, A.; Chaudret, B. Size- and Shape-Control of Crystalline Zinc Oxide Nanoparticles: A New Organometallic Synthetic Method. *Adv. Funct. Mater.* **2005**, *15* (3), 458–468.

(28) Amiens, C.; Chaudret, B.; Ciuculescu-Pradines, D.; Collière, V.; Fajerwerg, K.; Fau, P.; Kahn, M.; Maisonnat, A.; Soulantica, K.; Philippot, K. Organometallic Approach for the Synthesis of Nanostructures. *New J. Chem.* **2013**, *37* (11), 3374–3401.

(29) Yu, H.; Li, J.; Loomis, R. A.; Gibbons, P. C.; Wang, L. W.; Buhro, W. E. Cadmium Selenide Quantum Wires and the Transition from 3D to 2D Confinement. *J. Am. Chem. Soc.* **2003**, *125* (52), 16168–16169.

(30) Yu, H.; Gibbons, P. C.; Buhro, W. E. Bismuth, Tellurium, and Bismuth Telluride Nanowires. *J. Mater. Chem.* **2004**, 595–602.

(31) Wang, F.; Tang, R.; Yu, H.; Gibbons, P. C.; Buhro, W. E. Size- and Shape-Controlled Synthesis of Bismuth Nanoparticles. *Chem. Mater.* **2008**, *20* (11), 3656–3662.

(32) Wang, F.; Buhro, W. E. An Easy Shortcut Synthesis of Size-Controlled Bismuth Nanoparticles and Their Use in the SLS Growth of High-Quality Colloidal Cadmium Selenide Quantum Wires. *Small* **2010**, *6* (4), 573–581.

(33) Kovalenko, M. V.; Heiss, W.; Shevchenko, E. V.; Lee, J.-S.; Schwinghammer, H.; Alivisatos, A. P.; Talapin, D. V. SnTe Nanocrystals: A New Example of Narrow-Gap Semiconductor Quantum Dots. *J. Am. Chem. Soc.* **2007**, *129*, 11354–11355.

(34) Hickey, S. G.; Waurisch, C.; Rellinghaus, B.; Eychmüller, A. Size and Shape Control of Colloidally Synthesized IV−VI Nanoparticulate Tin(II) Sulfide. *J. Am. Chem. Soc.* **2008**, *130* (45), 14978–14980.

(35) Baumgardner, W. J.; Choi, J. J.; Lim, Y.-F.; Hanrath, T. SnSe Nanocrystals: Synthesis, Structure, Optical Properties, and Surface Chemistry. *J. Am. Chem. Soc.* **2010**, *132* (28), 9519–9521.

(36) Polking, M. J.; Zheng, H.; Ramesh, R.; Alivisatos, A. P. Controlled Synthesis and Size-Dependent Polarization Domain Structure of Colloidal Germanium Telluride Nanocrystals. *J. Am. Chem. Soc.* **2011**, *133* (7), 2044–2047.

(37) Antunez, P. D.; Buckley, J. J.; Brutchey, R. L. Tin and Germanium Monochalcogenide IV–VI Semiconductor Nanocrystals for Use in Solar Cells. *Nanoscale* **2011**, *3* (6), 2399–2411.

(38) Kovalenko, M. V.; Talapin, D. V.; Loi, M. A.; Cordella, F.; Hesser, G.; Bodnarchuk, M. I.; Heiss, W. Quasi-Seeded Growth of Ligand-Tailored PbSe Nanocrystals through Cation-Exchange-Mediated Nucleation. *Angew. Chemie - Int. Ed.* **2008**, *47* (16), 3029–3033.

(39) Yarema, M.; Pichler, S.; Sytnyk, M.; Seyrkammer, R.; Lechner, R. T.; Fritz-Popovski, G.; Jarzab, D.; Szendrei, K.; Resel, R.; Korovyanko, O.; Loi, M. A.; Paris, O.; Hesser, G.; Heiss, W. Infrared Emitting and Photoconducting Colloidal Silver Chalcogenide Nanocrystal Quantum Dots from a Silylamide Promoted Synthesis. *ACS Nano* **2011**, *4040* (5), 3758–3765.

(40) Yarema, O.; Bozyigit, D.; Rousseau, I.; Nowack, L.; Yarema, M.; Heiss, W.; Wood, V. Highly Luminescent, Size- and Shape-Tunable Copper Indium Selenide Based Colloidal Nanocrystals. *Chem. Mater.* **2013**, *25* (18), 3753–3757.

(41) Zhong, H.; Wang, Z.; Bovero, E.; Lu, Z.; Van Veggel, F. C. J. M.; Scholes, G. D. Colloidal $CuInSe_2$ Nanocrystals in the Quantum Confinement Regime: Synthesis, Optical Properties, and Electroluminescence. *J. Phys. Chem. C* **2011**, *115* (25), 12396–12402.

(42) Yarema, O.; Yarema, M.; Bozyigit, D.; Lin, W. M. M.; Wood, V. Independent Composition and Size Control for Highly Luminescent Indium-Rich Silver Indium Selenide Nanocrystals. *ACS Nano* **2015**, *9* (11), 11134–11142.

(43) Yarema, O.; Yarema, M.; Lin, W. M. M.; Wood, V. Cu–In–Te and Ag–In–Te Colloidal Nanocrystals with Tunable Composition and Size. *Chem. Commun.* **2016**, *52* (72), 10878–10881.

(44) Yarema, O.; Yarema, M.; Wood, V. Tuning the Composition of Multicomponent Semiconductor Nanocrystals: The Case of I–III–VI Materials. *Chem. Mater.* **2018**, *30* (5), 1446–1461.

(45) Kravchyk, K.; Protesescu, L.; Bodnarchuk, M. I.; Krumeich, F.; Yarema, M.; Walter, M.; Guntlin, C.; Kovalenko, M. V. Monodisperse and Inorganically Capped Sn and Sn/SnO_2 Nanocrystals for High-Performance Li-Ion Battery Anodes. *J. Am. Chem. Soc.* **2013**, *135* (11), 4199–4202.

(46) He, M.; Protesescu, L.; Caputo, R.; Krumeich, F.; Kovalenko, M. V. A General Synthesis Strategy for Monodisperse Metallic and Metalloid Nanoparticles (In, Ga, Bi, Sb, Zn, Cu, Sn, and Their Alloys) via in Situ Formed Metal Long-Chain Amides. *Chem. Mater.* **2015**, *27* (2), 635–647.

(47) Srivastava, V.; Dunietz, E.; Kamysbayev, V.; Anderson, J. S.; Talapin, D. V. Monodisperse InAs Quantum Dots from Aminoarsine Precursors: Understanding the Role of Reducing Agent. *Chem. Mater.* **2018**, *30* (11), 3623–3627.

(48) Bhattacharyya, K. X.; Pradel, C.; Lecante, P.; Mézailles, N. Mechanistic Investigations of the Synthesis of Size-Tunable Ni Nanoparticles by Reduction of Simple Ni^{II} Diamide Precursors. *Chem. - A Eur. J.* **2017**, *23* (39), 9352–9361.

(49) Chen, Y.; Landes, N. T.; Little, D. J.; Beaulac, R. Conversion Mechanism of Soluble Alkylamide Precursors for the Synthesis of Colloidal Nitride Nanomaterials. *J. Am. Chem. Soc.* **2018**, *140* (33), 10421–10424.

(50) Lamer, V. K.; Dinegar, R. H. Theory, Production and Mechanism of Formation of Monodispersed Hydrosols. *J. Am. Chem. Soc.* **1950**, *72* (11), 4847–4854.

(51) Carenco, S.; Labouille, S.; Bouchonnet, S.; Boissière, C.; Le Goff, X. F.; Sanchez, C.; Mézailles, N. Revisiting the Molecular Roots of a Ubiquitously Successful Synthesis: Nickel(0) Nanoparticles by Reduction of [Ni(acetylacetonate)$_2$]. *Chem. - A Eur. J.* **2012**, *18* (44), 14165–

14173.

(52) Dingman, S. D.; Rath, N. P.; Markowitz, P. D.; Gibbons, P. C.; Buhro, W. E. Low-Temperature, Catalyzed Growth of Indium Nitride Fibers from Azido-Indium Precursors. *Angew. Chemie - Int. Ed.* **2000**, *39* (8), 1470–1472.

(53) Karan, N. S.; Chen, Y.; Liu, Z.; Beaulac, R. R. R. Solution-Liquid-Solid Approach to Colloidal Indium Nitride Nanoparticles from Simple Alkylamide Precursors. *Chem. Mater.* **2016**, *28* (16), 5601–5605.

(54) Wang, F.; Dong, A.; Buhro, W. E. Solution-Liquid-Solid Synthesis, Properties, and Applications of One-Dimensional Colloidal Semiconductor Nanorods and Nanowires. *Chem. Rev.* **2016**, *116* (18), 10888–10933.

(55) Vaughn, D. D., I.; Bondi, J. F.; Schaak, R. E. Colloidal Synthesis of Air-Stable Crystalline Germanium Nanoparticles with Tunable Sizes and Shapes. *Chem. Mater.* **2010**, *22* (22), 6103–6108.

(56) Vaughn, D. D. I.; Patel, R. J.; Hickner, M. A.; Schaak, R. E. Single-Crystal Colloidal Nanosheets of GeS and GeSe. *J. Am. Chem. Soc.* **2010**, *132* (43), 15170–15172.

(57) Deng, Z.; Han, D.; Liu, Y. Colloidal Synthesis of Metastable Zinc-Blende IV–VI SnS Nanocrystals with Tunable Sizes. *Nanoscale* **2011**, *3* (10), 4346.

(58) Deng, Z.; Cao, D.; He, J.; Lin, S.; Lindsay, S. M.; Liu, Y. Solution Synthesis of Ultrathin Single-Crystalline SnS Nanoribbons for Photodetectors via Phase Transition and Surface Processing. *ACS Nano* **2012**, *6* (7), 6197–6207.

(59) Kumar, B. G.; Muralidharan, K. Hexamethyldisilazane-Assisted Synthesis of Indium Sulfide Nanoparticles. *J. Mater. Chem.* **2011**, *21* (30), 11271–11275.

(60) Kumar, B. G.; Muralidharan, K. S_4N_4 as an Intermediate in Ag_2S Nanoparticle Synthesis. *RSC Adv.* **2014**, *4* (54), 28219–28224.

(61) Srinivas, B.; Kumar, B. G.; Muralidharan, K. Stabilizer Free Copper Sulphide Nanostructures for Rapid Photocatalytic Decomposition of Rhodamine B. *J. Mol. Catal. A Chem.* **2015**, *410*, 8–18.

(62) Zhao, X.; Di, Q.; Wu, X.; Liu, Y.; Yu, Y.; Wei, G.; Zhang, J.; Quan, Z. Mild Synthesis of Monodisperse Tin Nanocrystals and Tin Chalcogenide Hollow Nanostructures. *Chem. Commun.* **2017**, *53* (80), 11001–11004.

(63) Kobylinski, M. M.; Ruhmlieb, C.; Kornowski, A.; Mews, A. Hexagonally Shaped Two-Dimensional Tin(II)sulfide Nanosheets: Growth Model and Controlled Structure Formation. *J. Phys. Chem. C* **2018**, *122* (10), 5784–5795.

(64) Biacchi, A. J.; Vaughn, D. D., I.; Schaak, R. E. Synthesis and Crystallographic Analysis of Shape-Controlled SnS Nanocrystal Photocatalysts: Evidence for a Pseudotetragonal Structural Modification. *J. Am. Chem. Soc.* **2013**, *135* (31), 11634–11644.

(65) Vaughn, D. D., I.; Sun, D.; Moyer, J. A.; Biacchi, A. J.; Misra, R.; Schiffer, P.; Schaak, R. E. Solution-Phase Synthesis and Magnetic Properties of Single-Crystal Iron Germanide Nanostructures. *Chem. Mater.* **2013**, *25* (21), 4396–4401.

(66) Mahler, B.; Hoepfner, V.; Liao, K.; Ozin, G. A. Colloidal Synthesis of 1T-WS_2 and 2H-WS_2 Nanosheets: Applications for Photocatalytic Hydrogen Evolution. *J. Am. Chem. Soc.* **2014**, *136* (40), 14121–14127.

(67) Huang, P. C.; Huang, J. L.; Wang, S. C.; Shaikh, M. O.; Lin, C. Y. Photoelectrochemical Properties of Orthorhombic and Metastable Phase SnS Nanocrystals Synthesized by a Facile Colloidal Method. *Thin Solid Films* **2015**, *596*, 135–139.

(68) Sardar, K.; Rao, C. N. R. New Solvothermal Routes for GaN Nanocrystals. *Adv. Mater.* **2004**, *16* (5), 425–429.

(69) Sardar, K.; Rao, C. N. R. AlN Nanocrystals by New Chemical Routes. *Solid State Sci.* **2005**, *7* (2), 217–220.

(70) Bhat, S. V.; Biswas, K.; Rao, C. N. R. Synthesis and Optical Properties of In-Doped GaN Nanocrystals. *Solid State Commun.* **2007**, *141* (6), 325–328.

(71) Chauhan, H.; Singh, M. K.; Hashmi, S. A.; Deka, S. Synthesis of Surfactant-Free SnS Nanorods by a Solvothermal Route with Better Electrochemical Properties towards Supercapacitor Applications. *RSC Adv.* **2015**, *5* (22), 17228–17235.

(72) Kumar, D.; Singh, K.; Kaur, G.; Verma, V.; Bhatti, H. S. Synthesis and Optical Characterization of Pure and Cobalt Doped Gallium Nitride Nanocrystals. *J. Mater. Sci. Mater. Electron.* **2015**, *26* (8), 6068–6074.

(73) Kumar, D.; Singh, K.; Kaur, G.; Verma, V.; Bhatti, H. S. Synthesis and Characterization of Terbium Doped Gallium Nitride Nanocrystals. *J. Mater. Sci. Mater. Electron.* **2015**, *26* (8), 6068–6074.

(74) Gerung, H.; Bunge, S. D.; Boyle, T. J.; Brinker, C. J.; Han, S. M. Anhydrous Solution Synthesis of Germanium Nanocrystals from the Germanium(II) Precursor $Ge[N(SiMe_3)_2]_2$. *Chem. Commun.* **2005**, No. 14, 1914–1916.

(75) Kumar, B. G.; Muralidharan, K. Organic-Free Self-Assembled Copper Sulfide Microflowers. *Eur. J. Inorg. Chem.* **2013**, *2013* (12), 2102–2108.

(76) Kumar, B. G.; Srinivas, B.; Prasad, M. D.; Muralidharan, K. Ag/Ag_2S Heterodimers: Tailoring the Metal–Semiconductor Interface in a Single Nanoparticle. *J. Nanoparticle Res.* **2015**, *17* (7), 1–11.

(77) Vaughn, D. D., I.; In, S.-I.; Schaak, R. E. A Precursor-Limited Nanoparticle Coalescence Pathway for Tuning the Thickness of Laterally-Uniform Colloidal Nanosheets: The Case of SnSe. *ACS Nano* **2011**, *5* (11), 8852–8860.

(78) Lim, S. C.; Chan, C. Y.; Chen, K. T.; Tuan, H. Y. Synthesis of Popcorn-Shaped Gallium-Platinum ($GaPt_3$) Nanoparticles as Highly Efficient and Stable Electrocatalysts for Hydrogen Evolution Reaction. *Electrochim. Acta* **2019**, *297*, 288–296.

(79) Buckley, J. J.; Rabuffetti, F. A.; Hinton, H. L.; Brutchey, R. L. Synthesis and Characterization of Ternary $Sn_xGe_{1-x}Se$ Nanocrystals. *Chem. Mater.* **2012**, *24* (18), 3514–3516.

(80) Fredrick, S. J.; Prieto, A. L. Solution Synthesis and Reactivity of Colloidal Fe_2GeS_4: A Potential Candidate for Earth Abundant, Nanostructured Photovoltaics. *J. Am. Chem. Soc.* **2013**, *135* (49), 18256–18259.

(81) Liakakos, N.; Cormary, B.; Li, X.; Lecante, P.; Respaud, M.; Maron, L.; Falqui, A.; Genovese, A.; Vendier, L.; Koïnis, S.; Chaudret, B.; Soulantica, K. The Big Impact of a Small Detail: Cobalt Nanocrystal Polymorphism as a Result of Precursor Addition Rate during Stock Solution Preparation. *J. Am. Chem. Soc.* **2012**, *134* (43), 17922–17931.

(82) Thomson, J. W.; Nagashima, K.; Macdonald, P. M.; Ozin, G. A. From Sulfur−Amine Solutions to Metal Sulfide Nanocrystals: Peering into the Oleylamine−Sulfur Black Box. *J. Am. Chem. Soc.* **2011**, *133* (13), 5036–5041.

(83) Das, A.; Shamirian, A.; Snee, P. T. Arsenic Silylamide: An Effective Precursor for Arsenide Semiconductor Nanocrystal Synthesis. *Chem. Mater.* **2016**, *28* (11), 4058–4064.

(84) Oae, S. *Organic Chemistry of Sulfur*; Springer US: Boston, MA, 1977.

CHAPTER 2

AMIDE-ASSISTED SYNTHESIS OF IRON GERMANIUM SULFIDE (Fe_2GeS_4) NANOSTARS: THE EFFECT OF $LiN(SiMe_3)_2$ ON PRECURSOR REACTIVITY FOR FAVORING NANOPARTICLE NUCLEATION OR GROWTH[‡]

1. Overview

Olivine Fe_2GeS_4 has been identified as a promising photovoltaic absorber material introduced as an alternate candidate to iron pyrite, FeS_2. The compounds share similar benefits in terms of elemental abundance and relative non-toxicity, but Fe_2GeS_4 was predicted to have higher stability with respect to decomposition to alternate phases and, therefore, more optimal device performance. Our initial report of the nanoparticle (NP) synthesis for Fe_2GeS_4 was not well understood and required an inefficient 24 h growth to dissolve an iron sulfide impurity. Here, we report an amide-assisted Fe_2GeS_4 NP synthesis that directly forms the phase-pure product in minutes. This significant advance was achieved by the replacement of the poorly-understood hexamethyldisilazane (HMDS) additive and TMS_2S by the conjugate base, lithium bis(trimethylsilyl)amide ($LiN(SiMe_3)_2$), and elemental S, respectively. We hypothesized that fragments of both TMS_2S and HMDS had carried out the roles that Brønsted bases play in amide-assisted NP syntheses and were necessary for Ge incorporation. Convolution of this role with the supply of S in TMS_2S caused the iron sulfide impurities. Separating these effects in the use of $LiN(SiMe_3)_2$ and elemental S resulted in synthetic control over the ternary phase. Herein we explore the Fe-Ge-S reaction landscape and the role of the base. Its concentration was found to increase the reactivities of the Fe, Ge, and S precursors, and we discuss possible metal-amide intermediates. This affords tunability in two areas: favorability of NP nucleation versus growth and phase formation. The

[‡] This article is published in The Journal of the American Chemical Society with Rebecca C. Miller, James R. Neilson, and Amy L. Prieto as authors (*J. Am. Chem. Soc.* **2020**, *142* (15), 7023–7035.). Rebecca C. Miller carried out all of the experimental procedures, characterization, and prepared the manuscript. Prof. Neilson carried out the Rietveld analysis and provided editing advice, and Amy L. Prieto guided the research aims with ideas, discussion, and editing advice.

phase-purity of Fe_2GeS_4 depends on the molar ratios of the cations, base, and amine as well as the Fe:Ge:S molar ratios. The resultant Fe_2GeS_4 NPs exhibit an interesting star anise-like morphology with stacks of nanoplates that intersect along a 6-fold rotation axis. The optical properties of the Fe_2GeS_4 NPs are consistent with previously published measurements showing a measured band gap of 1.48 eV.

2. Introduction

The current technological age requires significant advances in energy conversion and storage. It is of economic and environmental interest to develop renewable energy technologies that minimize the production of greenhouse gases. Despite the amount of solar energy striking the earth's surface over two hours being greater than the total worldwide energy consumption from the year 2015, solar energy accounted for only 0.012% of the world net electricity generation in 2016[1]. Increasing the role of solar cells in the energy market would benefit from increased cell efficiency and decreased cost of the solar module[2].

The development of photovoltaic absorber materials in the form of nanoparticles (NPs) is motivated by the possibility for accessing size-dependent properties as well as the ability to produce thin films. Photovoltaic absorber layers with high absorption coefficients require less material (i.e. thin films). This could lower module cost and increase cell efficiency through efficient charge separation[3,4]. Solution-phase NP synthesis offer a range of tunable parameters opening possibilities for the formation of stable and metastable phases as well as unique morphologies in the solid-state. However, these reactions exhibit significant complexity that originates from the necessity to consider principles from a wide collection of chemical disciplines (solid-state, organometallic, organic, etc.). Thus, understanding the roles of important NP synthetic components is required in order to apply synthetic strategies across a range of material systems and develop new strategies with control[5–8].

Here, we examine the solution-phase NP reaction for iron germanium sulfide (Fe_2GeS_4). In the pursuit of photovoltaic materials consisting of highly-abundant and relatively non-toxic constituent elements[3,4,9–11], Yu et al. introduced the olivine Fe_2MS_4 (M = Si, Ge) compounds as compositionally-similar substitutes with appropriate absorption properties for the heavily studied iron pyrite (FeS_2)[3].

Photovoltaic cells employing FeS_2 have exhibited low photovoltages and efficiencies[12,13], and a number of explanations have been suggested including the presence of a surface inversion layer and the ionization of high density deep donor states[14–17]. Synthetically, sulfur-deficient Fe-S impurities are difficult to avoid. In comparison, Yu et al. used computational methods to posit that the Fe_2MS_4 compounds have an improved stability with respect to decomposition to alternate phases.

Previous studies on bulk Fe_2GeS_4 focused on structural and magnetic characterization[18–23]. Since 2013, seven synthetic[24–30] and one computational report[31] on Fe_2GeS_4 have been published. Further, the Radu group presented the first Fe_2GeS_4 photovoltaic device[28]. Liu et al. reported a low solar cell efficiency of 0.03% and attributed this to the short-circuit current density of 0.19 mA/cm^2 although a promising open circuit voltage of 361 mV was attained. The Fe_2GeS_4 thin film was formed via a two-step process: solution-based synthesis of an Fe-Ge-S precursor powder followed by its deposition onto a substrate and annealing under S and Ar. This report[28] and other synthetic studies[25,29,30] issued since 2013 provide routes to the material but typically use higher temperatures and longer reaction times. Further, these methods do not result in regularly-shaped particles (i.e. traditional bulk solid state synthesis and/or ball-milling) impeding the use of solution-based thin film processing. The shape control afforded by solution-phase solid state synthesis allows exploration into understanding the formation and properties of unique morphologies.

In 2013, we reported the first solution-phase NP synthesis of Fe_2GeS_4[24] which was followed by Lim et al. demonstrating a solution-based synthesis for 800 nm long nanosheets[26]. Developing syntheses of multinary nanoparticles is often hindered by the competitive formation of possible unary and binary impurity phases. Some of these Fe_2GeS_4 syntheses suggest the possibility[25] or presence[30] of small concentrations of impurity phases. Moreover, our previous Fe_2GeS_4 NP synthesis involved the concurrent formation and eventual dissolution of an Fe-S impurity phase[24]. High quality syntheses of promising compounds are critical in order to assess the materials' properties and performance.

In this report, we outline a solution-phase Fe_2GeS_4 NP synthesis that directly produces the crystalline, phase-pure product in 10 min growth rather than 24 h. We propose that this results from the

role of both TMS_2S and HMDS fragments acting as Brønsted bases in amide-assisted NP syntheses[32,33] which was necessary for Ge incorporation. Convolution of these species with the supply of S in TMS_2S caused the iron sulfide impurities. Separating these effects by the use of $LiN(SiMe_3)_2$ and elemental S resulted in our synthetic control over the ternary phase. We mapped out the Fe-Ge-S reaction landscape and examined the role of the base, finding its presence to affect the reactivities of the NP precursors. This afforded tunability in two areas: favorability of nucleation versus growth and phase formation. The reaction optimization was carried out considering the balance of three interrelated components: the Fe, Ge, and S precursors; the base; and the alkylamine solvent. We speculate that the base acts to deprotonate the alkylamine solvent, oleylamine, allowing the formation of metal-oleylamide intermediates. These may exhibit higher reactivity compared to analogous metal-amido species and attain balanced reactivity between the cations of differing valency (Fe^{2+}, Ge^{4+}) required to produce the phase-pure ternary. The findings of this Fe-Ge-S NP reaction system may aid in the exploration and understanding of other material systems using the amide-assisted approach.

3. Experimental Section

3.1 Materials

Unless stated, all chemicals were used as received. Oleylamine was sparged with N_2 under heating at 70 ˚C prior to use, and dissolved gases were minimized in washing solvents (toluene, chloroform, hexanes) used in the glove box by the freeze-pump-thaw degassing process. Iron(II) chloride (anhydrous, beads, –10 mesh, 99.99% trace metals basis), germanium(IV) iodide (99.99% trace metals basis), sulfur (reagent grade, purified by sublimation, –100 mesh particle size, powder), and oleylamine (technical grade, 70%) were purchased from Sigma-Aldrich; lithium bis(trimethylsilyl)amide (>98.0%) was purchased from Alfa Aesar. Technical grade toluene, hexanes (mixture of isomers), ethanol, and chloroform were obtained from Fisher Scientific.

3.2 Exploratory Fe_2GeS_4 NP syntheses

In a N_2 glove box, $FeCl_2$, GeI_4, and 6 mL of OLA were loaded in a 50 mL three-neck round-bottom flask equipped with a magnetic stir bar, thermocouple, and condenser and sealed with rubber septa. A scintillation vial was loaded with S powder, $LiN(SiMe_3)_2$, and 2 mL of OLA prior to being capped with a rubber septum. The $FeCl_2$, GeI_4, S, and $LiN(SiMe_3)_2$ amounts were calculated in order to fulfill various cationic charge to base to amine ratios. The Fe:Ge:S molar ratio of 2:1.25:4 was used (25% excess Ge). Outside of the glove box, the Fe/Ge/OLA flask was attached to a Schlenk line under Ar and heated to 120 ˚C under vacuum with stirring. It was held under these degassing conditions for 1 h. The S/$LiN(SiMe_3)_2$/OLA vial was sonicated during the degassing hour for dissolution of the powders. The Fe/Ge/OLA solution was heated to 320 ˚C under Ar at 500 ˚C/h. At temperature, the S/$LiN(SiMe_3)_2$/OLA solution was rapidly injected into the flask using a gas-tight syringe followed by a 10 min growth. To quench the reaction, the solution was removed from the reaction flask with a gas-tight syringe and injected into toluene. Workup followed immediately.

3.3 Optimized 0.16 mmol scale Fe_2GeS_4 NP synthesis

In a N_2 glove box, 41 mg (0.32 mmol) $FeCl_2$, 141 mg (0.243 mmol) GeI_4, and 6.0 mL (18.2 mmol) OLA were loaded in a 50 mL three-neck round-bottom flask equipped with a magnetic stir bar, thermocouple, and condenser and sealed with rubber septa. A scintillation vial was loaded with 19 mg (0.59 mmol) S, 81 mg (0.49 mmol) $LiN(SiMe_3)_2$, and 2.0 mL (6.1 mmol) OLA prior to being capped by a rubber septum. The subsequent reaction procedure was carried out identically to the exploratory syntheses.

3.4 Optimized 0.5 mmol scale Fe_2GeS_4 NP synthesis

In a N_2 glove box, 128 mg (1.01 mmol) $FeCl_2$, 440 mg (0.759 mmol) GeI_4, and 18.75 mL (57.0 mmol) OLA were loaded in a 100 mL three-neck round bottom flask equipped with a magnetic stir bar, thermocouple, and condenser and sealed with rubber septa. A scintillation vial was loaded with 59 mg (1.8 mmol) S, 254 mg (1.52 mmol) $LiN(SiMe_3)_2$, and 6.25 mL (19.0 mmol) OLA prior to being capped by

a rubber septum. The subsequent reaction procedure was carried out identically to the exploratory syntheses.

3.5 NP product workup and purification

The reaction solution/toluene mixture (~1:1 vol) was divided among centrifuge tubes, and ethanol was added to achieve a 1:1:2 volume ratio of reaction solution to toluene to ethanol. The solutions were shaken to mix and centrifuged at 3500 rpm for 2 min to precipitate the solid products. The clear, red-brown supernatant was discarded. A small amount of chloroform was added to each centrifuge tube (just enough to disperse the NP pellet) and the mixture was shaken to disperse the NPs followed by addition of an excess of ethanol. The tubes were shaken once more and then centrifuged at 3500 rpm for 2 min. The supernatant was discarded prior to the addition of an excess of hexanes to each tube. The pellets were shaken to disperse followed by centrifugation at 3500 rpm for 2 min. Finally, the pellets were either dried under vacuum or dispersed in a solvent for characterization. The bench-top version of purification was carried out in air with ACS grade solvents that were used as received. The glovebox version of purification was carried out in a N_2 glovebox and with solvents that either were purchased anhydrous (ethanol) or had dissolved gases minimized through the freeze-pump-thaw degassing process (toluene, chloroform, hexanes).

3.6 Characterization of NP products

Powder X-ray diffraction (PXRD) was performed on a Bruker D8 Discover X-ray diffractometer using a Cu Kα radiation source (λ = 1.54 Å) and a Lynxeye XE-T positron-sensitive detector. Samples were dropcast from chloroform onto zero-background Si wafers which were held in PMMA pucks in the diffractometer. We think the PMMA puck surrounding the sample and/or an amorphous SiO_2 layer on the Si wafer provided background signal in broad peaks at 27-31˚ and 37-44˚ 2θ (Fig. S2.1). Rietveld refinements were performed using TOPAS v4.2 (Bruker AXS) with Ectors and coworkers' method to model anisotropic peak broadening due to crystallite morphology[34]. Transmission electron microscopy (TEM) was carried out on a JEOL JEM2100F at a working voltage of 200 keV. Images were collected and

analyzed in Digital Micrograph of the Gatan Microscopy Suite software. Scanning transmission electron microscopy (STEM) energy dispersive X-ray spectroscopy (EDS) was carried out with an Oxford X-Max 80 mm^2 detector and analyzed using AZtecTEM software. TEM samples were prepared by dip casting carbon-coated Cu grids (200 mesh, Electron Microscopy Sciences) into dilute particle dispersions in chloroform and hexanes. Scanning electron microscopy (SEM) analysis was performed on a JEOL JSM-6500F field emission electron microscope at a working voltage of 20.0 kV and with an Oxford X-Max 80 mm^2 EDS detector. ^1H Nuclear magnetic resonance (NMR) spectra were recorded on an Agilent Varian 400 MHz instrument. NMR samples were prepared in a N_2 glovebox with the deuterated solvent C_6D_6. Diffuse reflectance and UV-Vis absorption spectra were collected in the range of 200-1100 nm and 300-1100 nm, respectively, on a Nicolet Evolution 300 spectrometer equipped with a Harrick Praying Mantis diffuse reflection accessory. Photoluminescence spectra (15 averaged scans) were collected on a HORIBA Scientific Flurolog®–3 spectrofluorometer with a 600 nm excitation and a 775-875 nm emission range. UV-Vis absorption and photoluminescence spectra were collected on dilute suspensions of Fe_2GeS_4 NPs in chloroform.

4. Results and Discussion

4.1 HMDS-Based Fe_2GeS_4 NP Synthesis

With the future aim to optimize the thin film production and assess the photovoltaic performance of Fe_2GeS_4 NPs, we were motivated to understand and improve our original solution-based synthesis developed by Fredrick et al[24]. The procedure involved the evolution of both Fe_2GeS_4 and $Fe_{1-x}S$ upon reaching the growth temperature of 320 ˚C and required 24 h for the elimination of $Fe_{1-x}S$ from the solid products. The Fe_2GeS_4 NPs were 76 ± 31 nm in diameter and ~7 nm thick. The procedure involved injection of a TMS_2S, HMDS, and 1-octadecene solution into a flask containing $FeCl_2$, GeI_4, 1-octadecene, and hexadecylamine under Ar at 120 ˚C prior to ramping to 320 ˚C for a 24 h growth time. The Fe:Ge:S ratio required 1.5 times the stoichiometric amount of GeI_4. Additionally, the reactions were unintentionally carried out with ~2.1 times the stoichiometric amount of S. Our initial work aimed to

adapt the conditions in order to produce phase-pure Fe_2GeS_4 NPs from the onset such that the growth time could be significantly shortened and NP size and morphology tuning might be afforded.

We initially hypothesized that the $Fe_{1-x}S$ impurity during the growth of Fe_2GeS_4 could be avoided if the TMS_2S precursor was lowered a stoichiometric amount. However, both Fe_2GeS_4 and $Fe_{1-x}S$ were still observed to have formed when the reaction solution initially reached 320 ˚C (Fig. S2.2). Following the 24 h growth, additional phases, FeGe and $FeGe_2$, were identified in the products. Because Ge-containing impurities formed after 24 h upon decreasing the S precursor amount, we explored the reaction at stoichiometric amounts for all constituent elements and lowered the GeI_4 amount (Fig. S2.3). Identical results were observed with the formation of Fe_2GeS_4 and $Fe_{1-x}S$ upon initially reaching 320 ˚C and the additional formation of FeGe and $FeGe_2$ after 24 h. Therefore, the role of TMS_2S appeared to be complex in the original synthesis of Fe_2GeS_4 NPs.

Because simply changing the reagents to stoichiometric amounts did not access nucleation of phase-pure Fe_2GeS_4, we hypothesized we might be able to favor the growth of Fe_2GeS_4 over other phases if we could find a surfactant with preferential attachment. Thus, common NP synthetic solvents (oleylamine, octadecylamine, 1-dodecanethiol, oleic acid, and trioctylphosphine) were individually included in the reaction system, but either precipitation was inhibited or impurity phases formed. Attempts to alter the reaction conditions for the direct formation of Fe_2GeS_4 were hindered by a lack of understanding on the roles held by each reagent and the reaction pathway of the original synthesis. This is a common challenge in NP syntheses: attempts to control the reaction via trial and error exploration of precursor identities, concentrations, and other reaction conditions is time consuming and inefficient.

In particular, the necessity of HMDS for the formation of Fe_2GeS_4 in the original synthesis was unclear. Its use was inspired by its inclusion in a solution-phase synthesis of $Sn_xGe_{1-x}Se$ nanocrystals (NCs) from Buckley et al[35]. In that report, HMDS was critical for Ge inclusion and ternary formation; without it, SnSe formed. The authors speculated on its role in the reduction of Ge(IV) to Ge(II), especially considering the more negative reduction potential of Ge(IV) compared to Sn(IV). Curiously, obtaining the

orthorhombic GeSe end member required the omission of HMDS. For Fredrick et al., omission of HMDS resulted in the formation of Fe_2GeS_4 alongside GeS and FeS[24]. This contradicts the hypothesis of HMDS aiding in the reduction of Ge(IV) because Ge holds a 4+ oxidation state in Fe_2GeS_4, and GeS (Ge(II)) formed upon omission of HMDS.

A wide variety of NP syntheses have demonstrated the critical presence of HMDS for specific phase formation and particle morphology. Generally, inclusion of HMDS has aided in favoring certain aspects of nanostructured products: crystalline instead of amorphous products[36–39] or no solid products[40], metastable instead of more thermodynamically stable polymorphs[38,41,42], and certain morphologies and sizes[42,43]. It is common to report the products of the control reaction in which HMDS is omitted, and any speculation on its role is typically related to NP capping[38,40–42] and precursor reactivity[35,36,38,40,41]. In some cases, the inclusion of HMDS is not discussed and no control reactions are explored[44–47]. Biacchi et al. formed SnS NCs[46] with a synthesis adapted from Hickey et al.[48] in which the use of $Sn[N(SiMe_3)_2]_2$ was replaced with $SnCl_2$ by adding a step for HMDS addition to the Sn solution prior to S injection. The authors did not discuss possible Sn speciation in solution or the adaptation to a more benign Sn precursor.

4.2 Amide-Assisted NP Syntheses

However, a broader understanding exists for the conjugate base of HMDS, $LiN(SiMe_3)_2$, in solution-based NP syntheses. Its inclusion in NP syntheses has resulted in similar outcomes, allowing access to smaller, more monodisperse particles and certain phases[8,32,33,49–57]. Metal silylamides have been widely used in solvothermal syntheses in which their reduction under hydrogen or via thermal decomposition produces metal nanostructures; this was highly developed by Chaudret et al[58–62]. and Buhro et al[63–65]. Thus, the use of alkali silylamides in NP syntheses was originally motivated by the proposed metathesis reaction with metal precursor salts to form metal silylamide complexes in situ. These have been suggested to exist as the active species undergoing reduction to form NPs (unary or multinary). This understanding has aided in the development of I-III-VI NCs by the Wood group in which the authors use $LiN(SiMe_3)_2$ to balance the reactivities of cation precursors of varied valency[50,54,57,66]. Notably, these

reactions utilized trioctylphosphine as the solvent, which would be unlikely to interact with $LiN(SiMe_3)_2$ unless the alkyl chains could be deprotonated.

In 2013, Kravchyk et al. uncovered an alternative reaction mechanism for the interaction of metals salts and Brønsted bases involving the vital interplay of the alkylamine solvent system[32]. Using ^{119}Sn NMR to study the formation of Sn/SnO_2 NCs, the authors identified the in situ production of a Sn-oleylamide species due to the deprotonation of the alkylamine solvent by the base. Reduction of Sn-oleylamide then afforded small, monodisperse NCs in comparison to the large Sn particles formed in the absence of $LiN(SiMe_3)_2$. The high reactivity of metal amides is generally attributed to the polarity of the M–N bond[33,55]. This general strategy was broadened and He et al. reported syntheses for a wide variety of metal and metalloid unary and alloy NCs[33]. Thus, in other NP syntheses involving metal salts, Brønsted bases, and alkylamines, these interactions may play a role in the reaction mechanism.

4.3 In Situ Amides in HMDS-Based Fe_2GeS_4 NP Synthesis

While our original HMDS-based Fe_2GeS_4 NP synthesis did not include a Brønsted base precursor, fragments of both TMS_2S and HMDS could carry out this functionality. Because the reaction growth temperature (320 ˚C) greatly exceeds the boiling points of TMS_2S (163 ˚C)[67], and HMDS (125 ˚C)[67], the $[SiMe_3]^-$ and $[N(SiMe_3)_2]^-$ moieties likely evolve. The $[SiMe_3]^-$ species are especially possible early in the reaction because $Fe_{1-x}S$ is produced, and TMS_2S is the only S source. We believe these then act as very strong Brønsted bases to deprotonate the hexadecylamine solvent. Considering calculated and measured pK_a values of the conjugate acids as a gauge of relative base strengths, $[SiMe_3]^-$ should be a stronger base than $[N(SiMe_3)_2]^-$. The calculated pK_a of $HSiMe_3$ in DMSO is 44.9[68], and the pK_a of $HN(SiMe_3)_2$ in THF is ~26-30[33,69].

The resultant hexadecylamides could coordinate the cations forming intermediates of higher reactivity. We think this may be especially important for Ge because all reactions utilizing elemental S instead of TMS_2S produced iron sulfides[24]. While HMDS was motivated by its possible role in incorporating Ge into the end products, without it, Fe_2GeS_4, GeS, and $Fe_{1-x}S$ formed[24]. Thus, HMDS was

not solely responsible for increasing the Ge reactivity in this reaction, and we believe the $[–SiMe_3]^–$ moieties from TMS_2S likely played a dominant role. The necessity of HMDS for the phase-pure formation of Fe_2GeS_4 was probably related to the acid-base chemistry possible for it and its fragments, shifting equilibria and affecting the reactivities of the Fe, Ge, and S intermediates.

One control reaction we performed was to carry out the HMDS-based Fe_2GeS_4 NP reaction with the addition of 2 mL of oleic acid to the Fe and Ge-containing reaction flask. No crystalline products were observed, and we hypothesize this was due to quenching of the Brønsted base species by the proton-donating carboxylic acid. Liakakos et al. detected the reaction of HMDS with oleic acid to form NH_3 and silylesters[70], so we think this reaction as well as the reaction of oleic acid with $[SiMe_3]^–$ to form oleate anions and $HSiMe_3$ occurred in our system. This would have diverted the reaction system's ability to form metal-hexadecylamides, limiting the reactivity of the cation precursors.

Thus, we believe metal-hexadecylamides were intermediates for the HMDS-based Fe_2GeS_4 NP reaction and that the synthetic control over this system was limited by the dual role of TMS_2S. It supplied both strong Brønsted base species, $[SiMe_3]^–$, as well as S monomers. The base's likely deprotonation of hexadecylamine would have increased the cation precursors' reactivities and allowed the incorporation of Ge into the final products; however, this effect was convoluted with the reactive S supply. This is problematic for Fe_2GeS_4 for which iron sulfide impurities are difficult to avoid.

Truly understanding the speciation and chemical reactions taking place would require development of in situ characterization that would be specific to the constituent elements and could be carried out in the harsh reaction conditions (320˚C, in HDA, ODE). The field of NP synthesis is progressing toward this area of investigation[6,71–74] but is still severely limited, especially for multinary materials. The aim of this research article has been to redesign the Fe_2GeS_4 NP synthesis by separating the dual roles TMS_2S played in the HMDS-based synthesis. By replacing HMDS with $LiN(SiMe_3)_2$ and TMS_2S with S, we were able to tune the cation monomer reactivities and control the S stoichiometry separately. This allowed the direct formation of Fe_2GeS_4 NPs, free from impurity phases and in minutes

instead of 24 h. The replacement of TMS_2S with elemental S avoided the use of a volatile, highly reactive precursor, and employing OLA as the solvent instead of the combination of hexadecylamine and 1-octadecene simplified the number of reaction components.

4.4 Design of Amide-Assisted Fe_2GeS_4 NP Synthesis

As mentioned, binary impurity phases are difficult to avoid in the synthesis of multinary NP material systems. This amide-assisted Fe_2GeS_4 NP synthesis required careful design of several synthetic parameters to achieve phase-purity. Based on the literature precedence of amide-assisted NP syntheses discussed previously, we anticipated the molar ratios of the three following reaction components would be critical for synthetic control: the amine, the base, and the cations. These ratios were varied in our initial exploratory Fe_2GeS_4 syntheses. The base ($LiN(SiMe_3)_2$) may act to deprotonate the amine (OLA), and the resultant oleylamide may coordinate cation species in solution. In the simplest system, we might imagine each equivalence of base deprotonating an equal amount of the amine. If the cations form homoleptic complexes with oleylamide ligands, the stoichiometries between the base, amine, and cations can be relatively simple.

However, the system may deviate from this for a number of reasons. First, $LiN(SiMe_3)_2$ has been reported to form a deprotonation equilibrium with OLA[33]. However, the presence of a metal salt can influence the amine-base equilibrium due to preferential metal-oleylamide coordination[33], which has been reported for Sn^{2+}. It is unknown whether this occurs with Fe^{2+} or Ge^{4+}. The resultant mixture of oleylamine, oleylamide, silylamide, and HMDS provides a number of possibilities for metal cation speciation. Second, metal silylamides may form dimers, tetramers, and more complex clusters[55,75]. Third, amides have been known to take on oligomeric forms often with amines incorporated for solvation[33]. Therefore, the use of this mixture of reagents presents difficulty in predicting promising starting ratios. Because there are three interrelated components, simply varying amounts of one component changes two important ratios. Thus, we have defined reactions in terms of the molar ratios of base to amine (B:A) and cationic charge to base (C:B) (Fig. 2.1). Base and amine indicate the molar amounts of $LiN(SiMe_3)_2$ and

OLA, respectively. Cationic charge indicates the molar amount of cationic charge of the $FeCl_2$ and GeI_4 precursors (2·mol $FeCl_2$ + 4·mol GeI_4). With a constant amount of amine (8 mL total OLA), and a constant Fe:Ge:S precursor molar ratio (2:1.25:4, 25% excess Ge), we calculated the required masses of $FeCl_2$, GeI_4, S, and $LiN(SiMe_3)_2$ to fulfill the chosen ratios. The eight points on the plot in Fig. 2.1 describe the ratios tested, and the specific amounts are given in Table S1.

These reactions were carried out as described in the Exploratory Fe_2GeS_4 NP Syntheses part of the Experimental Section. PXRD patterns and TEM images of each of the products are provided in Fig. 2.2. Within the range of conditions tested, we observed a variety of phases and NP sizes among the products. The targeted Fe_2GeS_4 phase was observed in six of eight reaction products; however, only the reaction at (3,0.02) showed phase-purity by PXRD. Generally, we observed increasing NP sizes with increasing C:B ratios. Elemental mapping via STEM EDS (Fig. S2.4) aided in matching the compositions and the morphologies of the NPs. Further, it allowed identification of the small Fe-S particles in reaction (2,0.03) that were too small to diffract with sufficient intensity by PXRD (Fig. S2.4).

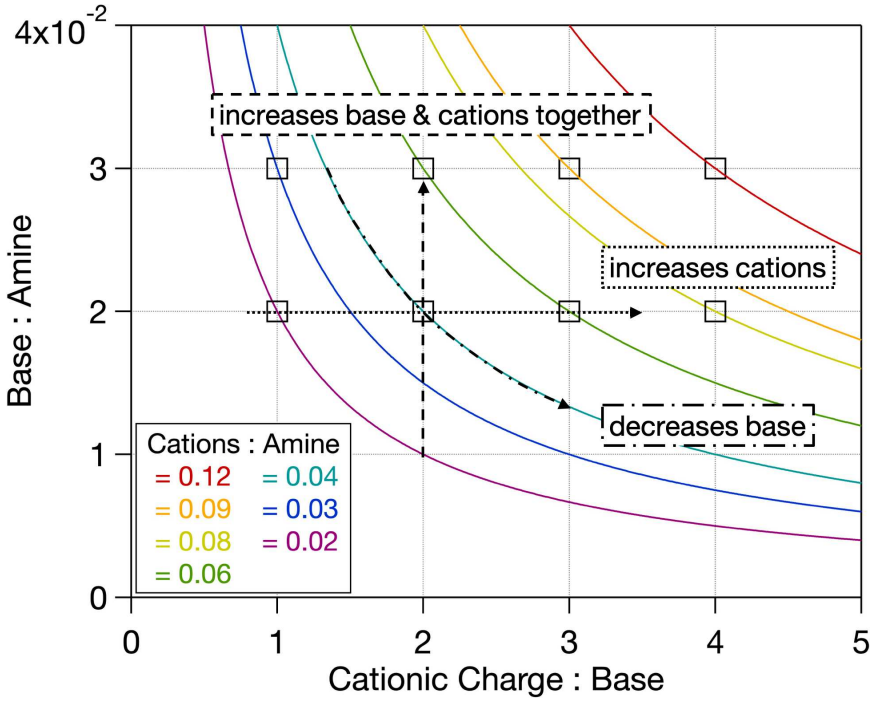

Fig. 2.1. The base to amine (B:A) and cationic charge to base (C:B) molar ratios tested for coarse optimization of the Fe_2GeS_4 NP reaction system. Each spot on the plot describes one set of reaction amounts. The synthetic parameters changing in various directions along the plot are labeled.

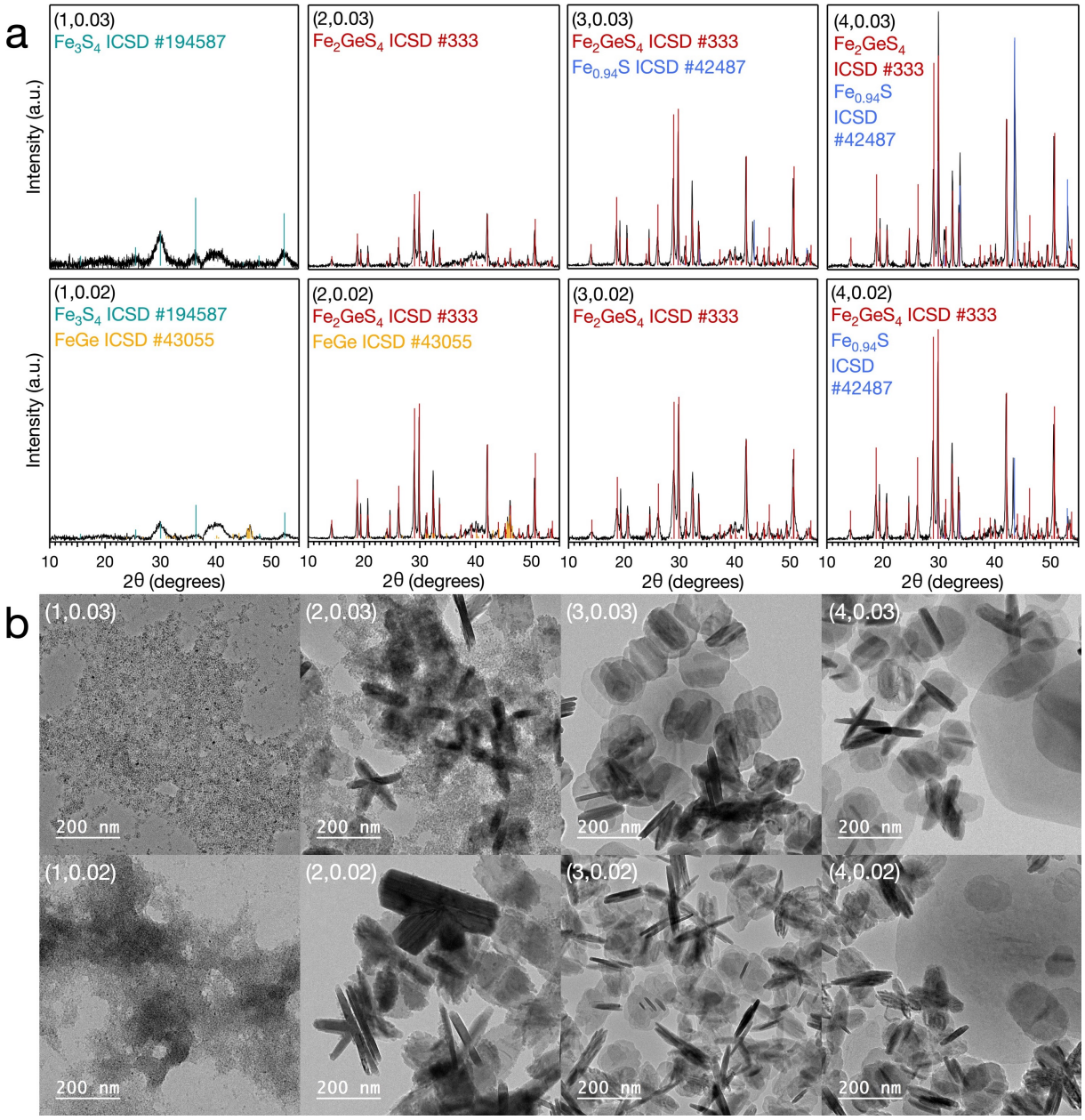

Fig. 2.2. a, PXRD patterns and, **b**, TEM images of NP products from 10 min growths at various base to amine and cationic charge to amine molar ratios corresponding to the spots on the plot in Fig. 2.1. The targeted Fe_2GeS_4 was detected in six of eight reactions, and was pure by PXRD in the (3,0.02) reaction. Impurity phases such as $Fe_{1-x}S$, FeGe, and Fe_3S_4 were detected in all other conditions. In general, larger NPs formed at higher

4.5 Control over NP Nucleation versus Growth

To understand the trends, we first describe the changes occurring in the system along different directions within the reaction ratios plot (Fig. 2.1). Comparing reaction plot points going up parallel to the y-axis, the concentrations of $LiN(SiMe_3)_2$ and the constituent elements (Fe, Ge, and S) increase while

remaining at a constant ratio to one another. The NP reaction essentially increases in concentration in this direction, and the $LiN(SiMe_3)_2$ plus OLA equilibrium may be pushed to the products. Empirically, we observe higher amounts of precipitated product, but the phases formed also vary along these trend lines. This indicates the difficulty of scaling these reactions to higher concentrations and the importance of considering the solvent's role in the reaction. Along one of the lines for which the C:A ratio is constant, the amount of $LiN(SiMe_3)_2$ decreases going to the right. At higher amounts of base, smaller particles form; larger particles form at lower amounts of base. Comparing plot points along lines parallel to the x-axis and going to higher C:B values, the Fe, Ge, and S amounts increase while the amounts of $LiN(SiMe_3)_2$ and OLA are constant. Similar to the observations along a constant C:A ratio, smaller particles were observed to form at low C:B ratios (relatively high amounts of base), and larger particles formed at high C:B ratios (relatively low amounts of base).

The variation in NP sizes throughout these reactions suggest differences in the favorability of NP nucleation versus growth. Smaller particles originate when a high degree of nucleation has occurred, consuming the majority of the Fe, Ge, and S monomers, with minimal remaining precursor for NP growth. The larger particles likely occur due to a lower degree of nucleation with a larger growth reservoir of Fe, Ge, and S monomers. Because the smaller particles and higher degree of nucleation occur at relatively high amounts of base, we speculate that the base increases the reactivity of the Fe, Ge, and S species. This would be consistent with the proposed formation of metal-oleylamide intermediates with higher reactivity due to the inclusion of the Brønsted base, $LiN(SiMe_3)_2$. In a control reaction carrying out the injection without $LiN(SiMe_3)_2$, no precipitation occurred. Further, injection of OLA alone (removing both S and $LiN(SiMe_3)_2$ from the reaction system) resulted in no reaction. This control was carried out because alkylamines have been reported to reduce metal species[61]. Thus, the reactivity of Fe, Ge, and S appeared to be too low for reaction in all cases without the presence of the base.

At the high C:B ratio of 4 (a small amount of base relative to cations), the constituent elements were sufficiently reactive to form NPs. Because the particles were large in size, we speculate that a large

amount of monomer remained in solution following nucleation and provided a large growth reservoir. This indicated a relatively low reactivity level of the constituent elements. Additionally, because both Fe_2GeS_4 and $Fe_{1-x}S$ formed, an imbalance in the reactivity of the cation monomers, Fe at greater reactivity than Ge, may exist at relatively low amounts of base. However, it is difficult to interpret the formation of specific phases as a function of the concentration of base because there are a number of other factors that likely play a significant role, including selective adhesion of ligands and enthalpies of formation, for example. At the C:B ratio of 3, the reactivities of Fe and Ge existed at a more balanced level and formed the ternary phase alone when B:A = 0.02. Beyond this, at C:B ratios of 2, the reactivity of the constituent elements increased sufficiently such that the nucleation of NPs began to be favored over growth. The desired Fe_2GeS_4 phase formed although it was accompanied by FeGe and small Fe_3S_4 NP impurities. This trend followed at C:B = 1 for which the large majority of products were small Fe_3S_4 NPs, and nucleation dominated, leaving a small growth reservoir of monomers for NP growth.

Of note, interpreting reactions along the B:A = 0.02 row in terms of the B:C ratio ignores the potential role of the changing Fe, Ge, and S concentrations (changing C:A ratio). Comparing the reactions (3,0.02) and (1,0.02), the base and amine amounts are constant with lower Fe, Ge, and S amounts in the (1,0.02) reaction. This maintains the $LiN(SiMe_3)_2$:OLA equilibrium based on the $LiN(SiMe_3)_2$ concentration alone but ignores how lower Fe, Ge, and S concentrations might limit monomer diffusion and affect the occurrence of nucleation versus growth. An alternative hypothesis could be that the smaller particles formed at (1,0.02) because of the lower concentrations of Fe, Ge, and S. Larger NP growth following nucleation would be disallowed due to diffusion limitations rather than higher monomer reactivity. In order to test this, we carried out the reaction at (1,0.06) which has the same concentrations of Fe, Ge, and S as the (3,0.02) reaction (C:A = 0.06) but a higher base amount in order to achieve the C:B ratio equal to 1 (Table S1). We observed similar products as found for the reactions (1,0.02) and (1, 0.03), a large collection of small Fe_3S_4 NPs (Fig. S2.5). Therefore, the higher amount of the base relative to the

constituent elements (Fe, Ge, and S) resulted in the monomers' higher reactivities and the favoring of nucleation over growth.

In order to test the breadth of this hypothesis, we carried out a collection of the reactions (those for which B:A = 0.02) with the variation of removing S from the reaction system. Various Fe-Ge nanostructures formed, and the trend of smaller NPs at low C:B ratios and larger NPs at high C:B ratios was observed (Fig. 2.3). Iron germanide phases can be difficult to discern from one another[45]. PXRD, TEM lattice spacings, and STEM EDS compositional data of the reaction products are given in Figs. S2.6-S2.10. For C:B = 1, small $Fe_{1.5}Ge$ NPs were the only crystalline product observed. Their presence was detected for all of the other reactions alongside small Ge NPs for C:B = 3 and 4. At higher C:B ratios, FeGe nanowires were observed and at qualitatively larger sizes as the C:B ratio increased. This trend is consistent with our hypothesis of a higher base concentration increasing precursor reactivity and favoring nucleation over growth.

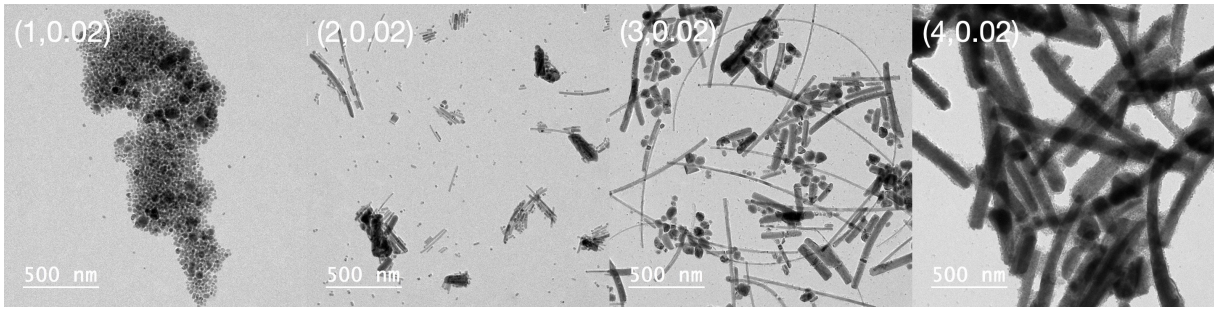

Fig. 2.3. TEM images of the products for B:A = 0.02 reactions upon excluding S from the reaction system.

4.6 Fe_2GeS_4 NP Phase-Purity

Upon determination of the reaction at (C:B, B:A) = (3,0.02) as the conditions suitable for forming Fe_2GeS_4 NPs, more rigorous characterization was pursued. Despite having identified reaction conditions for which the major product was Fe_2GeS_4, we observed occasional instances of low concentrations of $Fe_{1-x}S$ NPs. Various reaction conditions near that of (3,0.02) were carried out for fine optimization of the cationic charge to base to amine ratios (Fig. S2.11, Table S2.1). The PXRD patterns of the additional

reactions all indicated phase-pure Fe_2GeS_4 (Fig. S2.12); however, small concentrations of binary impurity phases were observed by STEM EDS (Fig. S2.13).

We hypothesized the system's tendency to form low concentrations of impurity NPs might depend more on the Fe:Ge:S ratios rather than the cationic charge to base to amine ratios. When a ~10% excess of S was used (23 mg instead of 21 mg), a high concentration of $Fe_{1-x}S$ formed alongside Fe_2GeS_4 (Fig. S2.14). Using a ~10% deficiency of S (19 mg instead of 21 mg), phase-pure Fe_2GeS_4 NPs formed (Fig. S2.14-S2.15). Thus, small fluctuations in the Fe:Ge:S ratios from one reaction to the next or heterogeneous local Fe:Ge:S concentrations within one reaction may account for occasional small concentrations of impurity phases. Regarding the Ge stoichiometry, our exploratory syntheses had all used a 25% excess. Lowering the GeI_4 amount to a stoichiometric value resulted in Fe_2GeS_4 and $Fe_{1-x}S$ NPs (Fig. S2.16). Therefore, we speculated that a Ge excess greater than 25% might result in a more robust reaction in terms of avoiding $Fe_{1-x}S$ impurities. Indeed, adjusting the (3,0.02) reaction conditions to use a 50% excess of Ge has reliably formed Fe_2GeS_4 NPs free from small concentrations of impurity phases. Taking into account the additional cations, this optimized reaction would lie at the point (3.33, 0.02) on Fig. 2.1.

This optimized Fe_2GeS_4 NP synthesis could be scaled up (0.16 mmol to 0.5 mmol) but required the use of 10% deficient S relative to the stoichiometric amount. The directly scaled up reaction, employing a stoichiometric amount of S, occasionally produced low concentrations of $Fe_{1-x}S$ impurities. We think that the increased probability of impurity formation in the scaled up reaction was related to the slower reheating rate of the reaction solution post-injection. Following the temperature drop due to injection, the large-scale (0.5 mmol) reaction typically required roughly twice as long to reheat relative to the small-scale (0.16 mmol) reaction (Fig. S2.17). This could not be remedied by simply stirring the large-scale reaction faster. In a control reaction (at low scale) carried out with an injection temperature of 300 ˚C, amorphous solids with low concentrations of crystalline S_8 and $Fe_{1-x}S$ were formed (Fig. S2.18). Thus, because the 0.5 mmol scale reaction reheated at a slower rate than the low scale reaction, the

probability for forming impurity phases increased. Decreasing the S amount by 10% in the 0.5 mmol scale reaction produced phase-pure Fe_2GeS_4 despite the longer reheating period inherent to the large scale reaction. Thus, we identified conditions to reproducibly form phase-pure Fe_2GeS_4 NPs at both the 0.16 and 0.5 mmol scales. This resulted from identifying the importance of each of the following synthetic parameters: base to amine to cation molar ratios, Fe:Ge:S molar ratios, and reaction temperature.

4.7 Characterization of the Injection Solution

Having identified conditions sufficient for forming Fe_2GeS_4 NPs free from impurities and given the complex chemistry possible between the components of the injection solution, we sought to characterize and understand the interactions of S, $LiN(SiMe_3)_2$, and OLA. Solutions were prepared in the glove box and sonicated as the 0.16 mmol scale Fe_2GeS_4 NP procedure entailed, and ^1H NMR spectroscopy was carried out. Fig. 2.4 compares the spectra of OLA alone with the Fe_2GeS_4 injection solution as well as solutions of S and $LiN(SiMe_3)_2$ individually dissolved in OLA.

In general, the spectra showed the same resonances as that for OLA, but the $–NH_2$ resonance was shifted downfield for all three sets of solutions (Fig. 2.4c, S2.19-S2.21). The downfield shift occurred with increasing concentrations of each S and $LiN(SiMe_3)_2$, from 0.52 ppm for OLA to 0.74 ppm for the 0.17:1 S:OLA molar ratio solution (Fig. S2.19) and to 0.57 ppm for the 0.13:1 $LiN(SiMe_3)_2$:OLA molar ratio solution (Fig. S2.20). For the S solutions, this is consistent with the results from Thomson et al. in their study of S in octylamine in which they observed downfield shifting of the $–NH_2$ resonance as a function of an increasing S concentration[76]. Cyclo-S_8 may be opened into polysulfide chains via nucleophilic attack by Lewis bases such as amines[77]. These may decompose further, and polysulfide radicals are suggested to occur in sulfur-amine solutions[78].

Both the $LiN(SiMe_3)_2$ in OLA and the injection solutions showed broadening of the $–NH_2$ ($\delta \approx$ 0.6 ppm) and the $–C\underline{H_2}–NH_2$ ($\delta \approx 2.5$ ppm) resonances (Fig. 2.4, S2.20-S2.22). We think this may be due to the formation of oleylamide from deprotonation of OLA by $LiN(SiMe_3)_2$. Further, amides are known to form oligomers which could contribute to the peak broadening, too. These resonances did not show

broadening for any concentration of S in OLA (Fig. S2.19), and the presence of S in the injection solutions did not hinder this effect when all three components were combined (Fig. 2.4,S2.21,S2.22).

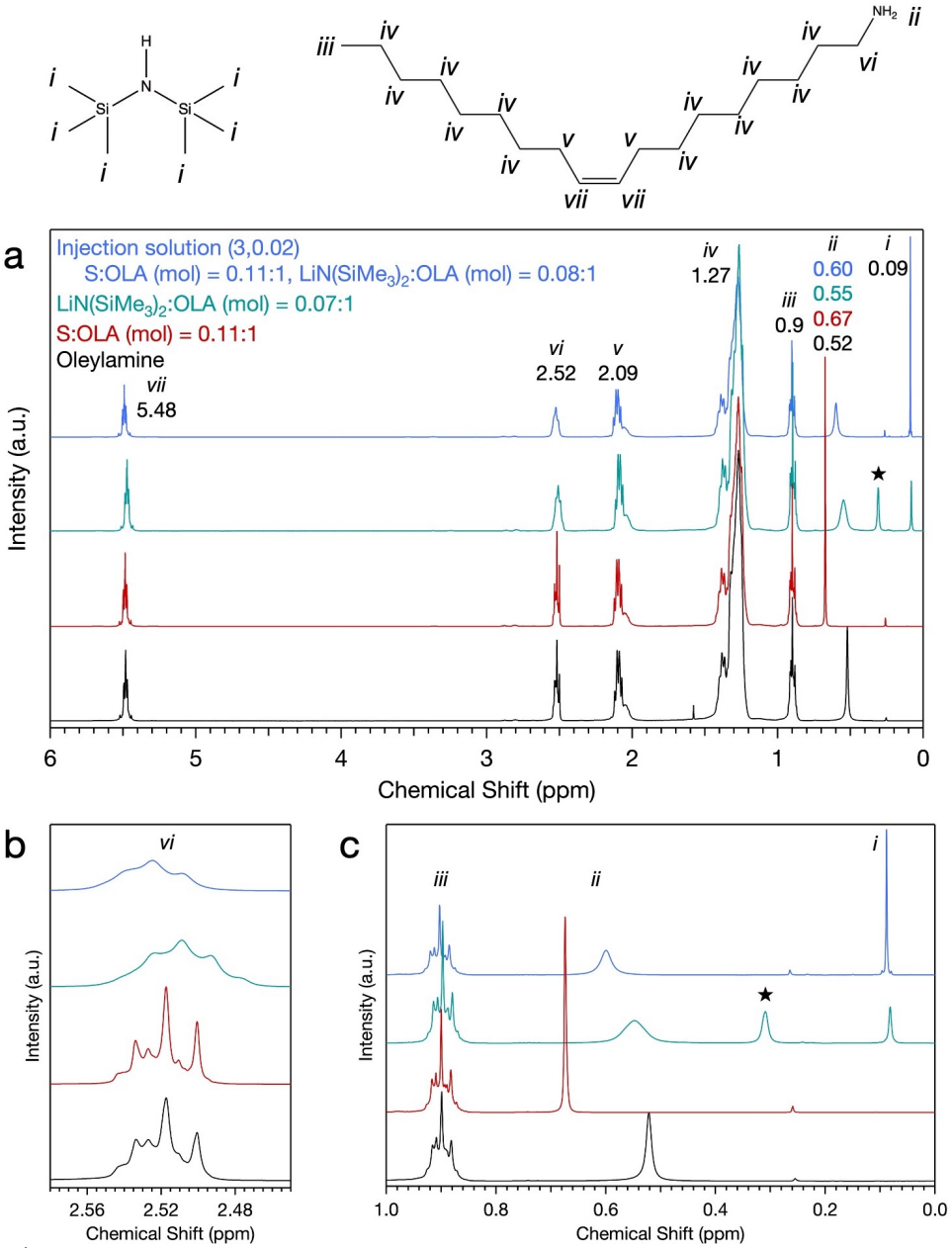

Fig. 2.4. a, ^{1}H NMR spectra of the following solutions: the injection solution from the optimal reaction conditions for Fe_2GeS_4 NPs (containing both S and $LiN(SiMe_3)_2$), S in OLA, $LiN(SiMe_3)_2$ in OLA, and neat OLA. The peak assignments are labeled on the spectra and on the corresponding proton locations in the molecular structures of $HN(SiMe_3)_2$ and OLA. **b,** The range δ = 2.6-2.4 ppm is plotted to show the peak broadness of the $–C\underline{H}_2–NH_2$ resonance when $LiN(SiMe_3)_2$ is present. **c,** The range δ = 1.0-0.0 ppm is plotted to show the downfield shifting of the $–NH_2$ resonance in all solutions compared to OLA and the peak broadness when $LiN(SiMe_3)_2$ is present. The peak at ~0.3 ppm labeled with a star corresponds to the proposed $LiN(SiMe_3)_2$OLA solvate. The peaks at 0.09 ppm originate from $HN(SiMe_3)_2$.

The compound $HN(SiMe_3)_2$ was detected (δ = 0.09 ppm) in all solutions for which $LiN(SiMe_3)_2$ was included and indicated protonation of the base. The $LiN(SiMe_3)_2$ in OLA solution showed an additional peak at ~0.3 ppm corresponding to a $LiN(SiMe_3)_2$OLA solvate, as suggested by He et al[33]. The $LiN(SiMe_3)_2$ methyl protons occur at 0.13 ppm in C_6D_6 alone[33]. This is consistent with the chemical equilibrium of OLA and $LiN(SiMe_3)_2$ to form oleylamide and HMDS. Solutions of increasing concentration of $LiN(SiMe_3)_2$ in OLA showed increased intensity of the peak at 0.3 ppm (Fig. S2.20). However, none of the injection solutions had the $LiN(SiMe_3)_2$OLA solvate peak at ~0.3 ppm (Fig. S2.21). The presence of sulfur may push the equilibrium reaction of $LiN(SiMe_3)_2$ and OLA to the products. Because this would increase the production of oleylamide, this could increase the cation monomer reactivity via increased concentration of metal-oleyamides. Conversely, the elimination of the $LiN(SiMe_3)_2$OLA solvate peak may be due to competitive reaction of $LiN(SiMe_3)_2$ with S. As mentioned earlier, cyclo-S_8 rings open by nucleophilic attack[77] to form polysulfides, and this could be carried out by the amide species. Thus, the presence of $LiN(SiMe_3)_2$ may also increase the reactivity of the S monomers.

4.8 Proposed Reaction Intermediates

Overall, we speculate the injection solution contains polysulfide chains due to interaction of S with both OLA and $LiN(SiMe_2)_2$. We observe protonation of the base, $LiN(SiMe_2)_2$, which is consistent with its reaction with OLA to form an equilibrium and produce oleylamide species. We speculate that S affects this chemical equilibrium and that its reactivity may be increased by the base; however, we found that the interaction of all three components prior to injection into the Fe and Ge reaction flask was not essential. This was shown via a control NP reaction in which S and $LiN(SiMe_2)_2$ were separately but simultaneously injected, and phase-pure Fe_2GeS_4 was detected by PXRD (Fig. S2.23). The S and $LiN(SiMe_3)_2$ amounts were prepared in separate 1 mL solutions of OLA instead of the typical combined 2 mL solution. Therefore, the trends observed in mapping out the Fe-Ge-S NP reaction landscape (Figs. 1-2) likely depend on balancing the concentrations and reactivities of all components in the reaction flask

upon injection at 320 ˚C rather than the formation of a specific S-$LiN(SiMe_3)_2$-OLA complex or oligomer following sonication.

It would be difficult to directly observe the intermediates of the cation precursors post-injection, but we speculate that metal-oleylamide species are most likely to occur. While $Fe[N(SiMe_3)_2]_2$[79] and the analogous Ge(II)-silylamide[80] have been reported, the Ge(IV) tetrasilylamide would be sterically hindered. The trisamide $BrGe[N(SiMe_3)_2]_3$[81] and $LiGe[N(SiMe_3)_2]_3$[82] complexes have been reported. To indirectly probe the potential formation of metal-silylamides, we substituted LiH for $LiN(SiMe_3)_2$ in the Fe_2GeS_4 NP reaction. We aimed to test whether the reaction could form the ternary phase if metal-silylamides were unavailable as intermediates. Indeed, we were able to form Fe_2GeS_4 using LiH as the Brønsted base albeit at twice the molar amount compared to $LiN(SiMe_3)_2$ and with $Fe_{1-x}S$ as an impurity phase (Fig. S2.24). We think these variations originate from a number of factors affecting the acid-base chemistry of these two bases and their conjugate acids (H_2 vs $HN(SiMe_3)_2$), including pK_a values, solubility, volatility. This does not disprove the formation of metal-silylamides in the $LiN(SiMe_3)_2$-based reaction, but it points to the possibility of metal-oleylamide intermediates in the formation of Fe_2GeS_4. A general reaction scheme is given in Figure 2.5.

4.9 Fe_2GeS_4 NP Characterization

The Fe_2GeS_4 NPs from the scaled up reaction were characterized in the following manner. Elemental analysis by SEM EDS gave 29.8 ± 0.1 at. % Fe, 14.0 ± 0.1 at. % Ge, and 56.3 ± 0.2 at. % S which is consistent with the stoichiometric ratio for the compound ($Fe_{0.29}Ge_{0.14}S_{0.57}$) (Fig. S2.25). The PXRD pattern of the NPs matches reference Fe_2GeS_4 diffraction patterns of the *Pnma* space group, and by Rietveld refinement, we determined the lattice parameters to be a = 12.4888(6) Å, b = 7.2212(3) Å, and c = 5.9130(2) Å. The data, fit, background, and difference are plotted in Fig. 2.6; Miller indices of intensity greater than 1.5% the maximum intensity from the Fe_2GeS_4 reference (ICSD Coll. Code 333)[20] are labeled on the pattern. The anisotropy of the particles is evident from the varied peak broadness of different reflections and was modeled with Ectors and coworkers' approach for anisotropic peak

broadening due to crystallite morphology[34]. The domains were modelled as triaxial ellipsoids with semi-axis dimensions of 32(5), 22(1), and 7.9(1) nm in the [002], [020], and [200] crystallographic directions. To refine the crystallite geometric model considering all possible orientations, rotation matrices were applied and gave rotation angles of 0.000˚ and 0.025˚ away from the [200] and [002] crystallographic directions, respectively, and 4.85˚ rotation around the [200] axis. The statistical metrics and a plot of the refined triaxial ellipsoid shape are given in Table S2.2 and Fig. S2.26, respectively.

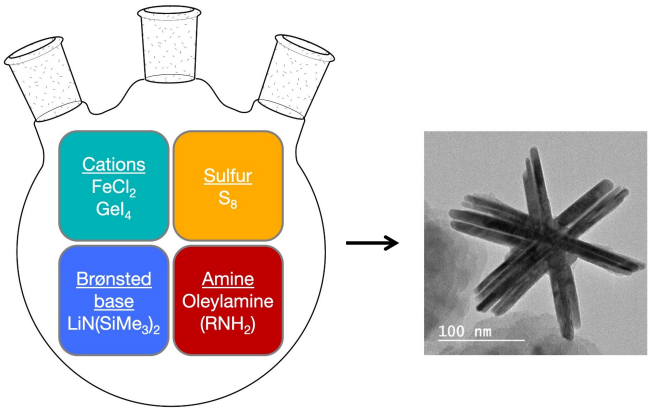

Brønsted Base Deprotonates Amine

$RNH_2 + Li^+[N(SiMe_3)_2]^- \rightleftharpoons Li^+[RNH]^- + HN(SiMe_3)_2$

forms equilibrium which can be affected by presence of M^{n+} species

Oleylamides Coordinate Cations (monomers, dimers, oligomers, etc.)

$6Li^+[RNH]^- + FeCl_2 + GeI_4 \rightarrow \{Fe^{2+}[RNH]_2\}_n + \{Ge^{4+}[RNH]_4\}_n + 2LiCl + 4LiI$

monomers, dimers, clusters, oligomers possible

increases and balances reactivity of both Fe^{2+} and Ge^{4+}

Sulfur in OLA Forms Polysulfides, Radicals by Nucleophilic Attack

$S_8 + RNH_2 \rightarrow H–S–S_n–S–NRH$

$H–S–S_n–S–NRH \rightarrow H–S–S_n\cdot + \cdot S–NRH$

Metal-Oleylamides React with S to form Fe_2GeS_4

$2\{Fe^{2+}[RNH]_2\}_n + \{Ge^{4+}[RNH]_4\}_n$ + polysulfides/OLA $\rightarrow Fe_2GeS_4$ + OLA + byproducts

requires Fe to Ge to S = 2 to 1.5 to 3.6 (mol)

requires cationic charge to base to amine = 0.06 to 0.02 to 1 (mol)

direct formation of phase-pure Fe_2GeS_4

Figure 2.5. Scheme of the proposed intermediates and chemical reactions in the amide-assisted synthesis of Fe_2GeS_4 NPs. The Brønsted base deprotonates the alkylamine solvent, OLA. These alkylamides then coordinate the cation species, forming species of higher reactivity relative to the cations coordinated to the neutral, L-type ligand, OLA. Cyclo-S_8 breaks open into polysulfide chains via nucleophilic attack by amines and amides. When the cationic charge to base to amine molar ratios are 0.06:0.02:1, and the Fe:Ge:S molar ratios are 2:1.5:3.6, phase-pure Fe_2GeS_4 NPs form.

The particles' morphology generally consists of three stacks of nanoplates that intersect at their center and along the width to form nanostars with a 6-fold rotational axis (Fig. 2.7). Nanoplates within the NPs are 304 ± 26 nm long, 209 ± 16 nm wide, and 12.8 ± 3.2 nm thick (Fig. S2.27). This is consistent

with the aspect ratios of the crystallite dimensions determined by the Rietveld refinement. The shortest crystallite dimension was determined to exist along the [200] crystallographic direction which suggests that this direction occurs perpendicular to the faces of the nanoplates. A microscopy study on the growth directions and morphology of the NPs is currently in preparation. As seen from the size distribution analysis data, the length and width histograms are somewhat skewed to smaller particles. While care was taken to measure particles for which a top-down view was representative of the dimension of interest, the skewed data may be due to a portion of the measured particles residing at some angle not exactly parallel to the grid because of the NPs' morphology. Similarly, the thickness size distribution is skewed to larger sizes and may be due to some nanoplates not existing exactly perpendicular to the grid. Alternatively, the skewed size distribution histograms may result from a collection of particles beginning growth at later times than others. Via SEM, a larger collection of NPs can be observed, and the described morphology is consistent for the ensemble of the products (Fig. S2.28).

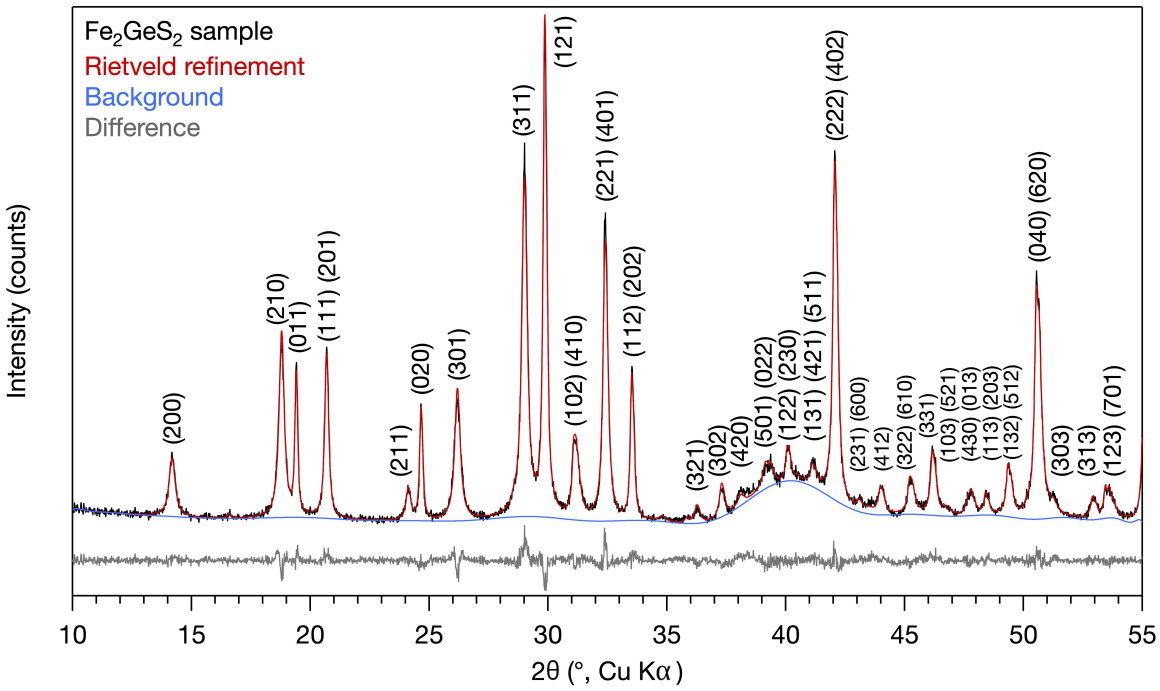

Fig. 2.6. PXRD pattern, Rietveld refinement, background, and difference data for the Fe_2GeS_4 NPs. Miller indices with intensities greater than 1.5% of the maximum intensity from the reference pattern (ICSD #333) are labeled. The Rwp was 7.133.

Diffuse reflectance spectroscopy measurements provided an estimate of the optical band gap for the Fe_2GeS_4 NPs. The Kubelka-Munk transformation, which is proportional to the extinction coefficient α[83], was plotted as a function of energy (Fig. 2.8a). The linear portion of the data was fit to extrapolate to the abscissa for the band gap estimation which gave a value of 1.48 eV. Our data are consistent with that reported for Fe_2GeS_4 from Yu et al. in their original paper suggesting the material as a photovoltaic absorber candidate[3]. The authors displayed diffuse reflectance data collected on both bulk pellet and thin film samples. In both cases, the linear portions of the data appeared to extrapolate to ~1.5 eV. However, in the text of the paper from Yu et al., a value of 1.36 eV was reported as the direct band gap of the material. While this value seemed to correspond with the energy at which the absorbance started to increase, it might be more indicative of a slightly lower energy gap rather than the dominant band gap transition. We observe a gradual onset in our data as well. Thus, we report a band gap of 1.48 eV for Fe_2GeS_4 and that it showed agreement with reported bulk Fe_2GeS_4 measurements.

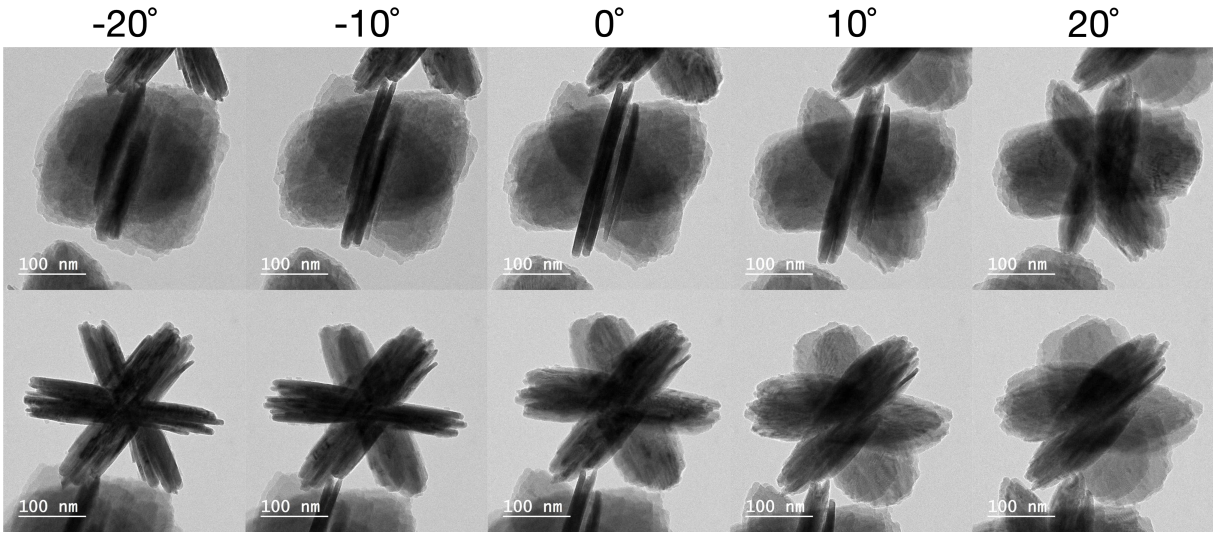

Fig. 2.7. TEM images of two particles at different tilt angles, showing the star-like morphology of the particles. They exhibit intersecting stacks of nanoplates on a six fold rotation axis.

The Fe_2GeS_4 NPs are larger than typical NCs and quantum dots, and considering that they achieve sizes of ~300 nm in length within a 10 min growth, the capping ligands may be dynamically bound to the NP surfaces. It is difficult to say whether this is inherent to the Fe_2GeS_4 surface or because

the reaction is carried out at the relatively high temperature of 320 ˚C. Once washed and isolated, the NPs form turbid suspensions of the washed NPs in common solvents, including chloroform, hexanes, and toluene. Both the NPs' large sizes and possible poor-capping may contribute to this. The particles appeared to disperse best in chloroform (Fig. S2.29). Concentrated solutions exhibit precipitation when centrifuged at 3500 rpm for 2 min, but stable, dilute suspensions can be formed via sonication. Thus, for UV-Vis absorption and photoluminescence spectroscopy, a low concentration solution of NPs in chloroform was used. The corresponding data (Fig. 2.8b) showed a slow onset of absorption around 900 nm and emission at 816 nm (1.52 eV). This is consistent with the diffuse reflectance data observed.

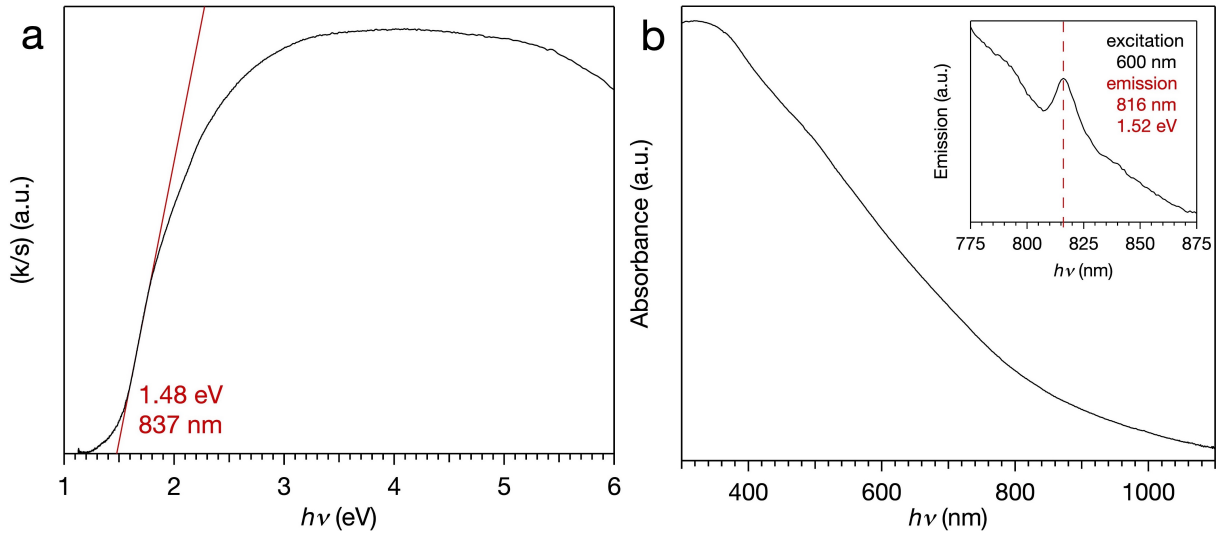

Fig. 2.8. a, Kubelka-Munk transformation of the diffuse reflectance spectrum for Fe_2GeS_4 NPs The linear portion of the data is extrapolated to the abscissa for the band gap estimation of 1.48 eV. **b,** Absorption and photoluminescence (inset) spectra of Fe_2GeS_4 NPs suspended in chloroform showing a gradual absorption onset and an emission peak at 816 nm.

5. Conclusions

We have reported an improved solution-based Fe_2GeS_4 NP synthesis, exhibiting the ability to directly form phase-pure product free from intermediate impurity phases in 10 min instead of 24 h. In our previous HMDS-based synthesis, we speculate that TMS_2S played a dual role in supplying strong Brønsted base species which increased the cation monomer reactivity alongside providing S. So, we redesigned the reaction system to separate these two roles. We used $LiN(SiMe_3)_2$ for the role of the Brønsted base, replacing its conjugate acid (HMDS), the poorly-understood additive, and were able to use

elemental S instead of the highly reactive TMS_2S. After mapping out the Fe-Ge-S reaction landscape, we explored the role of the base in this ternary NP synthesis. Generally, we found the base to increase the reactivity of the Fe, Ge, and S precursors, affording tunability of the system with respect to favorability for nucleation vs growth and for phase-pure ternary formation. This NP synthetic route provides a promising basis for future solution-based Fe_2GeS_4 NP thin film production, PV-related property measurements, and future device engineering.

While information on NP synthetic systems can be difficult to translate between different material systems, this work may be beneficial for other TMS_2S-, HMDS-, and $LiN(SiMe_3)_2$-containing NP syntheses. Other systems utilizing TMS_2S may want to consider possible convolution of its dual effect, providing both reactive Brønsted base species and sulfur. Those NP syntheses utilizing HMDS at conditions in which it could fragment may benefit from achieving better control by directly using a Brønsted base. To our knowledge, no study has directly compared HMDS and $LiN(SiMe_3)_2$ in NP synthetic systems. Characterizing intermediates and determining the chemical reactions occurring would be of interest for the community as a whole. Understanding the interrelated chemical roles of NP reaction components is vital for the efficient development of NP syntheses and enhances access to unique NP phases and morphologies.

REFERENCES

(1) *International Energy Outlook 2017*; U.S. Department of Energy, U.S. Energy Information Administration: Washington, DC, 2017.

(2) Sargent, E. H. Colloidal Quantum Dot Solar Cells. *Nat. Photonics* **2012**, *6* (3), 133–135.

(3) Yu, L.; Lany, S.; Kykyneshi, R.; Jieratum, V.; Ravichandran, R.; Pelatt, B.; Altschul, E.; Platt, H. A. S.; Wager, J. F.; Keszler, D. A.; Zunger, A. Iron Chalcogenide Photovoltaic Absorbers. *Adv. Energy Mater.* **2011**, *1* (5), 748–753.

(4) Yu, L.; Kokenyesi, R. S.; Keszler, D. A.; Zunger, A. Inverse Design of High Absorption Thin-Film Photovoltaic Materials. *Adv. Energy Mater.* **2013**, *3* (1), 43–48.

(5) Yin, Y.; Alivisatos, A. P. Colloidal Nanocrystal Synthesis and the Organic–Inorganic Interface. *Nature* **2005**, *437* (7059), 664–670.

(6) Kovalenko, M. V.; Manna, L.; Cabot, A.; Hens, Z.; Talapin, D. V.; Kagan, C. R.; Klimov, V. I.; Rogach, A. L.; Reiss, P.; Milliron, D. J.; Guyot-Sionnest, P.; Konstantatos, G.; Parak, W. J.; Hyeon, T.; Korgel, B. A.; Murray, C. B.; Heiss, W. Prospects of Nanoscience with Nanocrystals. *ACS Nano* **2015**, *9* (2), 1012–1057.

(7) Reiss, P.; Carrière, M.; Lincheneau, C.; Vaure, L.; Tamang, S. Synthesis of Semiconductor Nanocrystals, Focusing on Nontoxic and Earth-Abundant Materials. *Chem. Rev.* **2016**, *116* (18), 10731–10819.

(8) Lee, J. M.; Miller, R. C.; Moloney, L. J.; Prieto, A. L. The Development of Strategies for Nanoparticle Synthesis: Considerations for Deepening Understanding of Inherently Complex Systems. *J. Solid State Chem.* **2019**, *273*, 243–286.

(9) Wadia, C.; Alivisatos, P. A.; Kammen, D. M. Materials Availability Expands the Opportunity for Large-Scale Photovoltaics Deployment. *Environ. Sci. Technol.* **2009**, *43* (6), 2072–2077.

(10) Zhang, Y.; Wang, Y.; Zhang, J.; Xi, L.; Zhang, P.; Zhang, W. Pinning down High-Performance Cu-Chalcogenides as Thin-Film Solar Cell Absorbers: A Successive Screening Approach. *J. Chem. Phys.* **2016**, *144* (19), 194706.

(11) Kuhar, K.; Pandey, M.; Thygesen, K. S.; Jacobsen, K. W. High-Throughput Computational Assessment of Previously Synthesized Semiconductors for Photovoltaic and Photoelectrochemical Devices. *ACS Energy Lett.* **2018**, *3* (2), 436–446.

(12) Ennaoui, A.; Tributsch, H. Iron Sulphide Solar Cells. *Sol. Cells* **1984**, *13* (2), 197–200.

(13) Steinhagen, C.; Harvey, T. B.; Stolle, C. J.; Harris, J.; Korgel, B. A. Pyrite Nanocrystal Solar Cells: Promising, or Fool's Gold? *J. Phys. Chem. Lett.* **2012**, *3* (17), 2352–2356.

(14) Bronold, M.; Pettenkofer, C.; Jaegermann, W. Surface Photovoltage Measurements on Pyrite (100) Cleavage Planes: Evidence for Electronic Bulk Defects. *J. Appl. Phys.* **1994**, *76* (10), 5800–5808.

(15) Cabán-Acevedo, M.; Kaiser, N. S.; English, C. R.; Liang, D.; Thompson, B. J.; Chen, H. E.; Czech, K. J.; Wright, J. C.; Hamers, R. J.; Jin, S. Ionization of High-Density Deep Donor Defect States Explains the Low Photovoltage of Iron Pyrite Single Crystals. *J. Am. Chem. Soc.* **2014**, *136* (49), 17163–17179.

(16) Limpinsel, M.; Farhi, N.; Berry, N.; Lindemuth, J.; Perkins, C. L.; Lin, Q.; Law, M. An Inversion Layer at the Surface of N-Type Iron Pyrite. *Energy Environ. Sci.* **2014**, *7* (6), 1974–1989.

(17) Shukla, S.; Xing, G.; Ge, H.; Prabhakar, R. R.; Mathew, S.; Su, Z.; Nalla, V.; Venkatesan, T.; Mathews, N.; Sritharan, T.; Sum, T. C.; Xiong, Q. Origin of Photocarrier Losses in Iron Pyrite

(FeS_2) Nanocubes. *ACS Nano* **2016**, *10* (4), 4431–4440.

(18) Vincent, H.; Bertaut, E. F. Etude Cristallographique Et Magnetique De Fe_2GeS_4 Structures Magnetiques A 85 Et 4,2°K. *J. Phys. Chem. Solids* **1973**, *34* (2), 151–158.

(19) Meyer, C.; Gros, Y.; Vincent, H. Etude Par Effet Mossbauer Des Proprieties Cristallographiques et Magnetiques de Fe_2GeS_4. *Solid State Commun.* **1975**, *16*, 625–629.

(20) Vincent, H.; Bertaut, E. F.; Baur, W. H.; Shannon, R. D. Polyhedral Deformations in Olivine-Type Compounds and the Crystal Structure of Fe_2SiS_4 and Fe_2GeS_4. *Acta Crystallogr. Sect. B Struct. Crystallogr. Cryst. Chem.* **1976**, *32* (6), 1749–1755.

(21) Junod, A.; Wang, K. Q.; Triscone, G.; Lamarche, G. Specific Heat, Magnetic Properties and Critical Behaviour of Mn_2SiS_4 and Fe_2GeS_4. *J. Magn. Magn. Mater.* **1995**, *146* (1–2), 21–29.

(22) Ohgushi, K.; Ueda, Y. Anomalous Magnetic Properties of Fe_2GeS_4 and Mn_2SiS_4. *AIP Conf. Proc.* **2006**, *850* (May 2015), 1277–1278.

(23) Lin, X.; Bud'ko, S. L.; Canfield, P. C. Development of Viable Solutions for the Synthesis of Sulfur Bearing Single Crystals. *Philos. Mag.* **2012**, *92* (19–21), 2436–2447.

(24) Fredrick, S. J.; Prieto, A. L. Solution Synthesis and Reactivity of Colloidal Fe_2GeS_4: A Potential Candidate for Earth Abundant, Nanostructured Photovoltaics. *J. Am. Chem. Soc.* **2013**, *135* (49), 18256–18259.

(25) Park, B.-I.; Yu, S.; Hwang, Y.; Cho, S.-H.; Lee, J.-S.; Park, C.; Lee, D.-K.; Lee, S. Y. Highly Crystalline Fe_2GeS_4 Nanocrystals: Green Synthesis and Their Structural and Optical Characterization. *J. Mater. Chem. A* **2015**, *3* (5), 2265–2270.

(26) Lim, D. H.; Ramasamy, P.; Lee, J. S. Solution Synthesis of Single-Crystalline Fe_2GeS_4 Nanosheets. *Mater. Lett.* **2016**, *183*, 65–68.

(27) Nagai, H.; Hayashi, K.; Miyazaki, Y. Thermoelectric Properties of Olivine-Type Sulfides Tm_2XS_4 (Tm = Mn, Fe, X = Si, Ge). *Trans. Mat. Res. Soc. Japan* **2018**, *43* (1), 13–17.

(28) Liu, M.; Berg, D. M.; Hwang, P. Y.; Lai, C. Y.; Stone, K. H.; Babbe, F.; Dobson, K. D.; Radu, D. R. The Promise of Solution-Processed Fe_2GeS_4 Thin Films in Iron Chalcogenide Photovoltaics. *J. Mater. Sci.* **2018**, *53* (10), 7725–7734.

(29) Hwang, P. Y.; Berg, D. M.; Liu, M.; Lai, C. Y.; Radu, D. R. A Rapid Molecular Precursor Solid-State Route to Crystalline Fe_2GeS_4 Nanoparticles. *Mater. Lett.* **2018**, *223*, 128–132.

(30) Shi, X.; Tian, A.; You, J.; Yang, H.; Wang, Y.; Xue, X. Degradation of Organic Dyes by a New Heterogeneous Fenton Reagent - Fe_2GeS_4 Nanoparticle. *J. Hazard. Mater.* **2018**, *353*, 182–189.

(31) Gudelli, V. K.; Kanchana, V.; Vaitheeswaran, G. Predicted Thermoelectric Properties of Olivine-Type Fe_2GeCh_4 (Ch = S, Se and Te). *J. Phys. Condens. Matter* **2016**, *28* (2), 025502.

(32) Kravchyk, K.; Protesescu, L.; Bodnarchuk, M. I.; Krumeich, F.; Yarema, M.; Walter, M.; Guntlin, C.; Kovalenko, M. V. Monodisperse and Inorganically Capped Sn and Sn/SnO_2 Nanocrystals for High-Performance Li-Ion Battery Anodes. *J. Am. Chem. Soc.* **2013**, *135* (11), 4199–4202.

(33) He, M.; Protesescu, L.; Caputo, R.; Krumeich, F.; Kovalenko, M. V. A General Synthesis Strategy for Monodisperse Metallic and Metalloid Nanoparticles (In, Ga, Bi, Sb, Zn, Cu, Sn, and Their Alloys) via in Situ Formed Metal Long-Chain Amides. *Chem. Mater.* **2015**, *27* (2), 635–647.

(34) Ectors, D.; Goetz-Neunhoeffer, F.; Neubauer, J. A Generalized Geometric Approach to Anisotropic Peak Broadening Due to Domain Morphology. *J. Appl. Crystallogr.* **2015**, *48* (1), 189–194.

(35) Buckley, J. J.; Rabuffetti, F. A.; Hinton, H. L.; Brutchey, R. L. Synthesis and Characterization of Ternary $Sn_xGe_{1-x}Se$ Nanocrystals. *Chem. Mater.* **2012**, *24* (18), 3514–3516.

(36) Vaughn, D. D., I.; Bondi, J. F.; Schaak, R. E. Colloidal Synthesis of Air-Stable Crystalline Germanium Nanoparticles with Tunable Sizes and Shapes. *Chem. Mater.* **2010**, *22* (22), 6103–

6108.

(37) Vaughn, D. D. I.; Patel, R. J.; Hickner, M. A.; Schaak, R. E. Single-Crystal Colloidal Nanosheets of GeS and GeSe. *J. Am. Chem. Soc.* **2010**, *132* (43), 15170–15172.

(38) Deng, Z.; Han, D.; Liu, Y. Colloidal Synthesis of Metastable Zinc-Blende IV–VI SnS Nanocrystals with Tunable Sizes. *Nanoscale* **2011**, *3* (10), 4346.

(39) Deng, Z.; Cao, D.; He, J.; Lin, S.; Lindsay, S. M.; Liu, Y. Solution Synthesis of Ultrathin Single-Crystalline SnS Nanoribbons for Photodetectors via Phase Transition and Surface Processing. *ACS Nano* **2012**, *6* (7), 6197–6207.

(40) Zhao, X.; Di, Q.; Wu, X.; Liu, Y.; Yu, Y.; Wei, G.; Zhang, J.; Quan, Z. Mild Synthesis of Monodisperse Tin Nanocrystals and Tin Chalcogenide Hollow Nanostructures. *Chem. Commun.* **2017**, *53* (80), 11001–11004.

(41) Mahler, B.; Hoepfner, V.; Liao, K.; Ozin, G. A. Colloidal Synthesis of 1T-WS_2 and 2H-WS_2 Nanosheets: Applications for Photocatalytic Hydrogen Evolution. *J. Am. Chem. Soc.* **2014**, *136* (40), 14121–14127.

(42) Huang, P. C.; Huang, J. L.; Wang, S. C.; Shaikh, M. O.; Lin, C. Y. Photoelectrochemical Properties of Orthorhombic and Metastable Phase SnS Nanocrystals Synthesized by a Facile Colloidal Method. *Thin Solid Films* **2015**, *596*, 135–139.

(43) Chauhan, H.; Singh, M. K.; Hashmi, S. A.; Deka, S. Synthesis of Surfactant-Free SnS Nanorods by a Solvothermal Route with Better Electrochemical Properties towards Supercapacitor Applications. *RSC Adv.* **2015**, *5* (22), 17228–17235.

(44) Vaughn, D. D., I.; In, S.-I.; Schaak, R. E. A Precursor-Limited Nanoparticle Coalescence Pathway for Tuning the Thickness of Laterally-Uniform Colloidal Nanosheets: The Case of SnSe. *ACS Nano* **2011**, *5* (11), 8852–8860.

(45) Vaughn, D. D., I.; Sun, D.; Moyer, J. A.; Biacchi, A. J.; Misra, R.; Schiffer, P.; Schaak, R. E. Solution-Phase Synthesis and Magnetic Properties of Single-Crystal Iron Germanide Nanostructures. *Chem. Mater.* **2013**, *25* (21), 4396–4401.

(46) Biacchi, A. J.; Vaughn, D. D., I.; Schaak, R. E. Synthesis and Crystallographic Analysis of Shape-Controlled SnS Nanocrystal Photocatalysts: Evidence for a Pseudotetragonal Structural Modification. *J. Am. Chem. Soc.* **2013**, *135* (31), 11634–11644.

(47) Lim, S. C.; Chan, C. Y.; Chen, K. T.; Tuan, H. Y. Synthesis of Popcorn-Shaped Gallium-Platinum ($GaPt_3$) Nanoparticles as Highly Efficient and Stable Electrocatalysts for Hydrogen Evolution Reaction. *Electrochim. Acta* **2019**, *297*, 288–296.

(48) Hickey, S. G.; Waurisch, C.; Rellinghaus, B.; Eychmüller, A. Size and Shape Control of Colloidally Synthesized IV−VI Nanoparticulate Tin(II) Sulfide. *J. Am. Chem. Soc.* **2008**, *130* (45), 14978–14980.

(49) Tamang, S.; Kim, K.; Choi, H.; Kim, Y.; Jeong, S. Synthesis of Colloidal InSb Nanocrystals via in Situ Activation of $InCl_3$. *Dalt. Trans.* **2015**, *44* (38), 16923–16928.

(50) Yarema, O.; Yarema, M.; Lin, W. M. M.; Wood, V. Cu–In–Te and Ag–In–Te Colloidal Nanocrystals with Tunable Composition and Size. *Chem. Commun.* **2016**, *52* (72), 10878–10881.

(51) Glaria, A.; Kahn, M. L.; Cardinal, T.; Senocq, F.; Jubera, V.; Chaudret, B. Lithium Ion as Growth-Controlling Agent of ZnO Nanoparticles Prepared by Organometallic Synthesis. *New J. Chem.* **2008**, *32* (4), 662–669.

(52) Zolotavin, P.; Guyot-Sionnest, P. Meissner Effect in Colloidal Pb Nanoparticles. *ACS Nano* **2010**, *4* (10), 5599–5608.

(53) Yarema, M.; Pichler, S.; Sytnyk, M.; Seyrkammer, R.; Lechner, R. T.; Fritz-Popovski, G.; Jarzab, D.; Szendrei, K.; Resel, R.; Korovyanko, O.; Loi, M. A.; Paris, O.; Hesser, G.; Heiss, W. Infrared Emitting and Photoconducting Colloidal Silver Chalcogenide Nanocrystal Quantum Dots from a

Silylamide Promoted Synthesis. *ACS Nano* **2011**, *4040* (5), 3758–3765.

(54) Yarema, O.; Bozyigit, D.; Rousseau, I.; Nowack, L.; Yarema, M.; Heiss, W.; Wood, V. Highly Luminescent, Size- and Shape-Tunable Copper Indium Selenide Based Colloidal Nanocrystals. *Chem. Mater.* **2013**, *25* (18), 3753–3757.

(55) Yarema, M.; Caputo, R.; Kovalenko, M. V. Precision Synthesis of Colloidal Inorganic Nanocrystals Using Metal and Metalloid Amides. *Nanoscale* **2013**, *5* (18), 8398–8410.

(56) Li, W.; Zamani, R.; Gil, P. R.; Pelaz, B.; Ibáñez, M.; Cadavid, D.; Shavel, A.; Alvarez-Puebla, R. A.; Parak, W. J.; Arbiol, J.; Cabot, A. CuTe Nanocrystals: Shape and Size Control, Plasmonic Properties, and Use as SERS Probes and Photothermal Agents CuTe Nanocrystals: Shape and Size Control, Plasmonic Properties, and Use as SERS Probes and Photothermal Agents. *J. Am. Chem. Soc.* **2013**, *135* (19), 1–4.

(57) Yarema, O.; Yarema, M.; Bozyigit, D.; Lin, W. M. M.; Wood, V. Independent Composition and Size Control for Highly Luminescent Indium-Rich Silver Indium Selenide Nanocrystals. *ACS Nano* **2015**, *9* (11), 11134–11142.

(58) Nayral, C.; Ould-Ely, T.; Maisonnat, A.; Chaudret, B.; Fau, P.; Lescouzères, L.; Peyre-Lavigne, A. A Novel Mechanism for the Synthesis of Tin/Tin Oxide Nanoparticles of Low Size Dispersion and of Nanostructured SnO_2 for the Sensitive Layers of Gas Sensors. *Adv. Mater.* **1999**, *4* (1), 61–63.

(59) Dumestre, F.; Chaudret, B.; Amiens, C.; Renaud, P.; Fejes, P. Superlattices of Iron Nanocubes Synthesized from $Fe[N(SiMe_3)_2]_2$. *Science* **2004**, *303* (5659), 821–823.

(60) Desvaux, C.; Amiens, C.; Fejes, P.; Renaud, P.; Respaud, M.; Lecante, P.; Snoeck, E.; Chaudret, B. Multimillimetre-Large Superlattices of Air-Stable Iron–Cobalt Nanoparticles. *Nat. Mater.* **2005**, *4* (10), 750–753.

(61) Meffre, A.; Lachaize, S.; Gatel, C.; Respaud, M.; Chaudret, B. Use of Long Chain Amine as a Reducing Agent for the Synthesis of High Quality Monodisperse Iron(0) Nanoparticles. *J. Mater. Chem.* **2011**, *21* (35), 13464.

(62) Amiens, C.; Chaudret, B.; Ciuculescu-Pradines, D.; Collière, V.; Fajerwerg, K.; Fau, P.; Kahn, M.; Maisonnat, A.; Soulantica, K.; Philippot, K. Organometallic Approach for the Synthesis of Nanostructures. *New J. Chem.* **2013**, *37* (11), 3374–3401.

(63) Yu, H.; Gibbons, P. C.; Buhro, W. E. Bismuth, Tellurium, and Bismuth Telluride Nanowires. *J. Mater. Chem.* **2004**, 595–602.

(64) Wang, F.; Tang, R.; Yu, H.; Gibbons, P. C.; Buhro, W. E. Size- and Shape-Controlled Synthesis of Bismuth Nanoparticles. *Chem. Mater.* **2008**, *20* (11), 3656–3662.

(65) Wang, F.; Buhro, W. E. An Easy Shortcut Synthesis of Size-Controlled Bismuth Nanoparticles and Their Use in the SLS Growth of High-Quality Colloidal Cadmium Selenide Quantum Wires. *Small* **2010**, *6* (4), 573–581.

(66) Yarema, O.; Yarema, M.; Wood, V. Tuning the Composition of Multicomponent Semiconductor Nanocrystals: The Case of I–III–VI Materials. *Chem. Mater.* **2018**, *30* (5), 1446–1461.

(67) *CRC Handbook of Chemistry and Physics*, 100th ed.; Rumble, J., Ed.; CRC Press, 2019.

(68) Fu, Y.; Liu, L.; Li, R. Q.; Liu, R.; Guo, Q. X. First-Principle Predictions of Absolute pK_a's of Organic Acids in Dimethyl Sulfoxide Solution. *J. Am. Chem. Soc.* **2004**, *126* (3), 814–822.

(69) Fraser, R. R.; Mansour, T. S. Acidity Measurements with Lithiated Amines: Steric Reduction and Electronic Enhancement of Acidity. *J. Org. Chem.* **1984**, *49* (18), 3442–3443.

(70) Liakakos, N.; Cormary, B.; Li, X.; Lecante, P.; Respaud, M.; Maron, L.; Falqui, A.; Genovese, A.; Vendier, L.; Koïnis, S.; Chaudret, B.; Soulantica, K. The Big Impact of a Small Detail: Cobalt Nanocrystal Polymorphism as a Result of Precursor Addition Rate during Stock Solution Preparation. *J. Am. Chem. Soc.* **2012**, *134* (43), 17922–17931.

(71) Tao, F. F.; Salmeron, M. In Situ Studies of Chemistry and Structure of Materials in Reactive Environments. *Science* **2011**, *331* (6014), 171–174.

(72) Abécassis, B.; Bouet, C.; Garnero, C.; Constantin, D.; Lequeux, N.; Ithurria, S.; Dubertret, B.; Pauw, B. R.; Pontoni, D. Real-Time in Situ Probing of High-Temperature Quantum Dots Solution Synthesis. *Nano Lett.* **2015**, *15* (4), 2620–2626.

(73) Li, J.; Wang, H.; Lin, L.; Fang, Q.; Peng, X. Quantitative Identification of Basic Growth Channels for Formation of Monodisperse Nanocrystals. *J. Am. Chem. Soc.* **2018**, *140* (16), 5474–5484.

(74) Andersen, H. L.; Bøjesen, E. D.; Birgisson, S.; Christensen, M.; Iversen, B. B. Pitfalls and Reproducibility of in Situ Synchrotron Powder X-Ray Diffraction Studies of Solvothermal Nanoparticle Formation. *J. Appl. Crystallogr.* **2018**, *51* (2), 526–540.

(75) Schnepf, A.; Köppe, R. $[Ge_8\{N(SiMe_3)_2\}_6]$: A Ligand-Stabilized Ge Cluster Compound with Formally Zero-Valent Ge Atoms. *Angew. Chem. Int. Ed.* **2003**, *42* (8), 911–913.

(76) Thomson, J. W.; Nagashima, K.; Macdonald, P. M.; Ozin, G. A. From Sulfur−Amine Solutions to Metal Sulfide Nanocrystals: Peering into the Oleylamine−Sulfur Black Box. *J. Am. Chem. Soc.* **2011**, *133* (13), 5036–5041.

(77) Oae, S. *Organic Chemistry of Sulfur*; Springer US: Boston, MA, 1977.

(78) Hodgson, W. G.; Buckler, S. A.; Peters, G. Free Radicals in Amine Solutions of Elemental Sulfur. *J. Am. Chem. Soc.* **1963**, *85* (5), 543–546.

(79) Andersen, R. A.; Faegri, K.; Haaland, A.; Rypdal, K.; Green, J. C.; Lappert, M. F.; Leung, W. P. Synthesis of Bis[Bis(Trimethylsilyl)Amido]Iron(II). Structure and Bonding in $M[N(SiMe_3)_2]_2$ (M = Mn, Fe, Co): Two-Coordinate Transition-Metal Amides. *Inorg. Chem.* **1988**, *27* (10), 1782–1786.

(80) Harris, D. H.; Lappert, M. F. Monomeric, Volatile Bivalent Amides of Group IV B Elements, $M(NR^1R^2)_2$ and $M(NR^1R^2)_2$ (M=Ge, Sn, or Pb; R^1=Me_3Si, R^2=Me_3C). *J. Chem. Soc., Chem. Commun.* **1974**, No. 21, 895–896.

(81) Lappert, M. F.; Misra, M. C.; Onyszchuk, M.; Rowe, R. S.; Power, P. P.; Slade, M. J. Subvalent Group 14 Metal Compounds XI. Oxidative Addition Reactions of Organic Halides or Acid Anhydrides (Including $CH_{4-n}Cl_n$, PhBr, $BrN(SiMe_3)_2$, Bu^tCOCl, or $(CF_3CO)_2O$) to Some Bivalent Group 14 Metal Amides or Alkyls. *J. Organomet. Chem.* **1987**, *330* (1–2), 31–46.

(82) Walding, J. L.; Fanwick, P. E.; Weinert, C. S. Synthesis and Reactivity of the Bulky Germanium(IV) Trisamide Complexes $BrGe[N(SiMe_3)_2]_3$ and $LiGe[N(SiMe_3)_2]_3$: X-Ray Crystal Structures of $BrGe[N(SiMe_3)_2]_3$ and $[(Me_3Si)_2N]_3Ge(CH_2CH_2CH_2CH_3)$. *Inorganica Chim. Acta* **2005**, *358* (4), 1186–1192.

(83) López, R.; Gómez, R. Band-Gap Energy Estimation from Diffuse Reflectance Measurements on Sol-Gel and Commercial TiO_2: A Comparative Study. *J. Sol-Gel Sci. Technol.* **2012**, *61* (1), 1–7.

CHAPTER 3

OLIVINE CRYSTAL STRUCTURE-DIRECTED TWINNING IN IRON GERMANIUM SULFIDE (Fe_2GeS_4) NANOPARTICLES[‡]

1. Introduction

The field of bottom-up nanoparticle synthesis is advancing toward the reproducible formation of homogenous NPs for increasingly complex compositions and crystal structures. With this, the field can advance beyond understanding the fundamentals of crystal nucleation and growth using unary nanoparticles of high symmetry to more complex structural phenomena of solid-state chemistry. Nanoparticle systems have the advantage of forming on the order of moles of individual crystals in one batch, which is useful for statistical analysis. In the case of crystal twinning, most studies are limited by the scarcity of macroscopic twinned crystal samples and may be further limited by small but potentially significant differences in elemental composition. Thus, a synthetic route to phase-pure, homogeneous twinned NPs presents a valuable system for examining the probability and variations of twinning that may occur as a function of both underlying structural characteristics and environmental conditions.

As understanding of the energetics and structural features required for crystal twinning advances, this general knowledge can have widespread implications. Determining twin boundaries and defects is important for understanding a material's properties and performance for numerous applications. The distorted coordination of atoms at twin boundaries can alter transport within materials, including electron, ion, and phonon transport. Off-stoichiometry and strain at a twin boundary can affect the band structure of the material[1,2] and twin superlattices have been predicted to induce a direct band gap for indirect gap materials[3–5]. Ion conducting materials are affected by twin boundaries due to variations in ion diffusion

[‡] This chapter is a manuscript prepared for submission by Rebecca C. Miller, Roy H. Geiss, and Amy L. Prieto. Rebecca C. Miller carried out the experimental procedures, collected the majority of the data, carried out the analysis, produced the olivine compound calculations, and wrote the manuscript. Roy H. Geiss taught electron microscopy techniques, and collected one of the SAED data sets of Fig. 3.3. Amy L. Prieto provided guidance and editing advice.

along or across a twin boundary compared to diffusion through single crystalline domains[2]. This would be influential for applications such as batteries, especially anisotropic ion conductors. In thermoelectric materials, twin boundaries are explored for synergistic benefits of minimal increases in electronic conductivity[6,7] and significant phonon scattering[8–12]. Further, other material properties such as hardness and ductility[13–17] as well as magnetic susceptibility[18,19] have been shown to be affected by twin boundaries. Thus, understanding whether a material is likely to form twinned domains would be useful for both the design of new compounds and examination of known materials for these applications. Twinning may present an advantageous alteration to a material's properties, or it could explain a material's limitation or mechanism of failure.

Here, we characterized the twinning of Fe_2GeS_4 NPs identifying the existence of triplets of twinned domains or trillings.[20,21] This is the first example of twinned NPs for the olivine crystal structure. The NPs form as three sets of stacked nanoplates that intersect at roughly 60˚ angles. The orthorhombic olivine structure may exhibit hexagonal pseudosymmetry if the unit cell dimensions are sufficiently close to the ratio $a_{Pnma} \approx \sqrt{3}\, b_{Pnma}$. Pseudomerohedral twinning may result, which occurs when the lattice parameters and/or angles of a crystal structure are close to values that would encompass a higher symmetry than described by the structure's space group. While Fe_2GeS_4 exists as one of the closest known olivine compounds to hexagonal pseudosymmetry and therefore should have low energetic barriers to forming twin boundaries, synthetic conditions also affect twin formation. Here we demonstrate a dependence of the number of twinned NPs on the concentration of the precursors. We are able to form twinned NPs with fewer grain boundaries by inducing coalescence of the stacked nanoplates existing within the NPs. This synthetic control is advantageous because twinning and grain boundaries are known to affect material properties. The twinned NPs with stacked nanoplates might be beneficial for use in thermoelectric applications whereas the more crystalline NPs (with fewer grain boundaries) might exhibit better charge transport and photovoltaic performance.

More broadly, because the olivine crystal structure features compounds in areas of interest ranging from geology and mineralogy to energy conversion and storage applications, we have ranked all of the

olivine compounds from the Inorganic Crystal Structure Database (ICSD) according to their degree of hexagonal pseudosymmetry. Not only does this stand as a resource for identifying compounds to examine the fundamentals of crystal twinning based on both structural characteristics and synthetic parameters, it is of use for considering material functionality. It may point to scarcely examined compounds that could be targeted for their probability (or improbability) to form twins. However, more importantly, it identifies compounds already present in a number of applications for which it would be useful to consider the likelihood of twinning in terms of their formation and function. Olivine compounds of note include the traditional olivine mineral, $(Mg,Fe)SiO_4$, which is the most abundant compound in the earth's shallow upper mantle[22]. Its grain boundaries contribute to the mechanical and therefore seismic characteristics of the earth's mantle[23]. In lithium-ion batteries, $LiFePO_4$ is a common cathode material and exhibits anisotropic lithium-ion diffusion; thus, twinning may play an important role in its performance. Our synthesis for Fe_2GeS_4 NPs with control over twinning is a reliable model system useful for both fundamental and application-based science.

2. Growth and Characterization of Twinned Fe_2GeS_4 NPs

Solution-based synthesis of colloidal nanoparticles is a rapidly advancing field that has benefited from the ability to controllably form homogenous, reproducible NPs due to increased understanding of precursor roles and reaction mechanisms. However, adjusting NP syntheses to target various alterations (i.e. composition, size, morphology, and scale, etc.) still remains a challenge, especially for multinary compounds and complex crystal structures. Our group was the first to publish a solution-phase synthesis of Fe_2GeS_4 NPs[24], and recently we reported a thorough redesign of the synthesis accessing the direct formation of phase-pure Fe_2GeS_4 NPs[25] by replacing the poorly understood additive, hexamethyldisilazane, with its conjugate base, lithium bis(trimethylsilyl)amide and substituting elemental sulfur for the highly reactive hexamethyldisilathiane (TMS_2S). Amide-assisted syntheses exist for a number of compounds, and the presence of the amide has been found to increase the reactivity of metal cations allowing control over the formation of multinary NPs in which cation precursors of differing reactivity must be balanced. This high

precursor reactivity provided the opportunity for Fe_2GeS_4 to form in the unusual morphology of twinned NPs.

The NPs have three sets of stacked nanoplates that intersect at ~60˚ angles to form a triplet of twins, or a trilling. The individual nanoplates are oblong with the width of each nanoplate shared along the axis of the twinned NP. Transmission and scanning electron microscopy (TEM, SEM) images of the NPs are given in Fig 1. An individual NP with one set of nanoplates oriented parallel to the page is shown in Fig. 3.1a, and the two sets of 60˚ angled nanoplates can be seen in their darker contrast on the flat nanoplates. The 60˚ angles between the stacked nanoplates can be viewed in a NP oriented with its axis perpendicular to the page (Fig. 3.1b). The TEM and SEM images in Fig. 3.1c,d show that the large majority of NPs form trillings. By counting individual NPs, only 2% of NPs in the products do not exhibit twinning (n = 427 NPs counted).

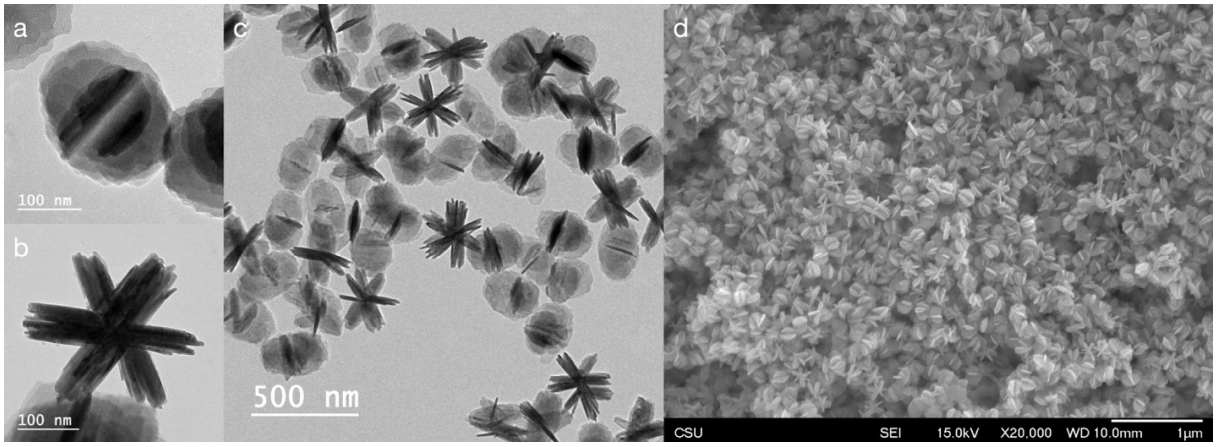

Fig. 3.1. Electron microscopy images of Fe_2GeS_4 NPs. **a,** TEM image in which the face of one stack of nanoplates is parallel to the page with the other two stacks of nanoplates seen in the darker contrast. The core axis of the NP is seen in the lighter contrast across the width of the NP. **b,** TEM image in which the core axis of the NP is perpendicular to the page showing the 60˚ angles of the intersecting stacks of nanoplates within a NP. **c,d,** TEM image and SEM image, respectively, of a collection of Fe_2GeS_4 NPs showing the high frequency of twinned NPs.

Examining the morphology of the NPs, we first identified the crystallographic growth directions within the nanoplates. High resolution (HR) TEM allowed measurement of the (200) lattice spacings at 6.3 Å existing in parallel with the faces of the nanoplates (Fig. 3.2a). In Fig. 3.2b, the (301) and (121) lattice spacings and the 61˚ angle between the two sets of planes were measured. Because each of the nanoplates showed the same crystallographic orientation, the 60˚ angles between sets of nanoplates could not be

explained by the orthorhombic crystal structure (*Pnma*, Fig. S3.1) without some kind of grain boundary at their intersection. Selected area electron diffraction (SAED) patterns of individual NPs displayed important differences between non-twinned nanoplates and twinned NPs. Fig. 3.3a,b shows a TEM image of a non-twinned nanoplate oriented parallel to the page and the corresponding SAED pattern. It matches the simulated SAED pattern (Fig. 3.3c) of the [200] zone axis with the [020] and [002] directions oriented along its length and width, respectively. This particle originated from a Fe_2GeS_4 NP synthesis carried out at lower precursor concentrations, which was done to probe the effect of supersaturation on twinning and is discussed later. For a twinned NP oriented such that one set of nanoplates is parallel to the page, the SAED pattern produces the summation of the [200] and [130] zone axes diffraction patterns (Fig 3d-f). The [200] zone axis pattern originates from the nanoplate oriented parallel to the carbon substrate of the TEM grid, consistent with the nanoplate without twinning (Fig 3a-c). The two nanoplates oriented at ~60˚ angles produce the [130] zone axis diffraction pattern. Because Fe_2GeS_4 is a non-cubic structure and the zone axis is the vector normal to the diffracted vectors in reciprocal space, the *UVW* values of the zone axis do not always correspond to the *hkl* lattice planes normal to the incident beam in real space. The [200] and [130] zone axis diffraction patterns correspond to the (200) and (220) lattice planes existing normal to the incident beam, respectively (Fig. S3.2). The spots originating from the {002} family of planes directly overlap for the two patterns and indicate that this direction is oriented along the core axis of the NP for all of the twinned domains. This is direct evidence of twinning in one NP; if the particle were single crystalline but formed the anisotropic star shape due to other factors, we would expect to see a single zone axis in the diffraction pattern.

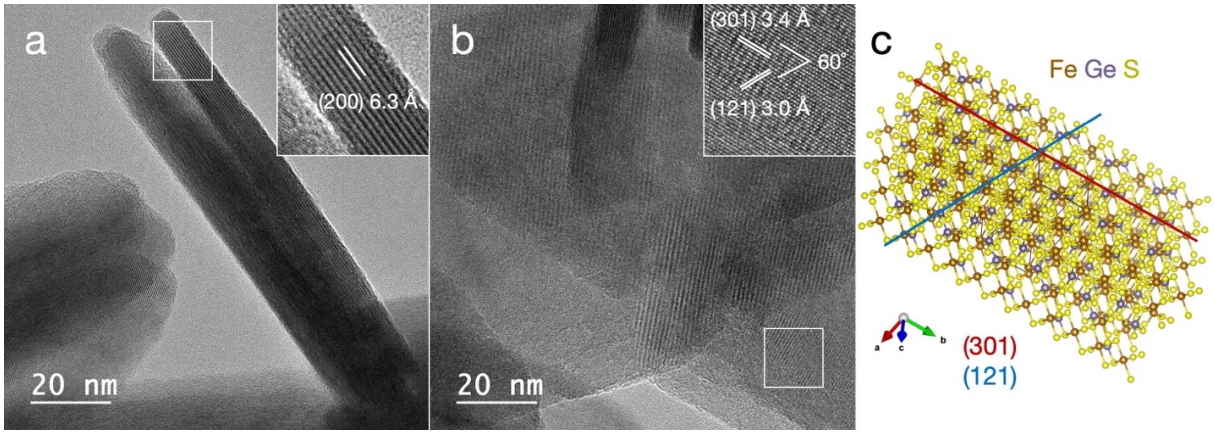

Fig. 3.2. Fe_2GeS_4 growth directions by lattice spacing measurements. **a,** HRTEM image viewed down the width of a nanoplate within a NP exhibiting the (200) lattice spacings measured at 6.3 Å. **b,** HRTEM image of the core of a NP and the measurements of the (301) and (121) lattice spacings of 3.4 Å and 3.0 Å, respectively. **c,** The measured angle of 61˚ between these sets of lattice planes is also consistent with the lattice plane assignments as depicted in the crystal structure.

A NP with one stack of nanoplates oriented perpendicular to the carbon substrate of the TEM grid produces a combined pattern of the [020] zone axis from the perpendicular nanoplates plus the [220] zone axis pattern from the nanoplates oriented at 30˚ to the carbon substrate of the TEM grid (Fig. S3.2). The reciprocal space [220] zone axis corresponds to the real space (310) lattice planes existing normal to the incident beam. Indeed, we observe this in the fast Fourier transform (FFT) of a HRTEM image in Fig. 3.4a,b. The [020] and [220] zone axis spots are labeled in green and pink, respectively, and match the simulated electron diffraction patterns (Fig. S3.3). The colored TEM image (Fig. 3.4c) identifies the locations of the lattice spacings that produce the FFT spots. This image was formed by applying two sets of masks (green and pink circles in Fig. 3.4b) individually to the FFT pattern. Generating inverse fast Fourier transform (IFFT) patterns from the masked FFT spots spatially identified the responsible lattice spacings with respect to the original TEM image (Fig. S3.4). These IFFT patterns were colored green and pink and combined with a blue-colored version of the original TEM image to highlight that the (200) lattice spacings (green) exist in the perpendicular nanoplate and the $(2\bar{2}0)$ lattice spacings (pink) are visible in the tilted nanoplates, as would be expected for twinned NPs. A depiction of the lattice spacings in the crystal structure is given in Fig. 3.4d.

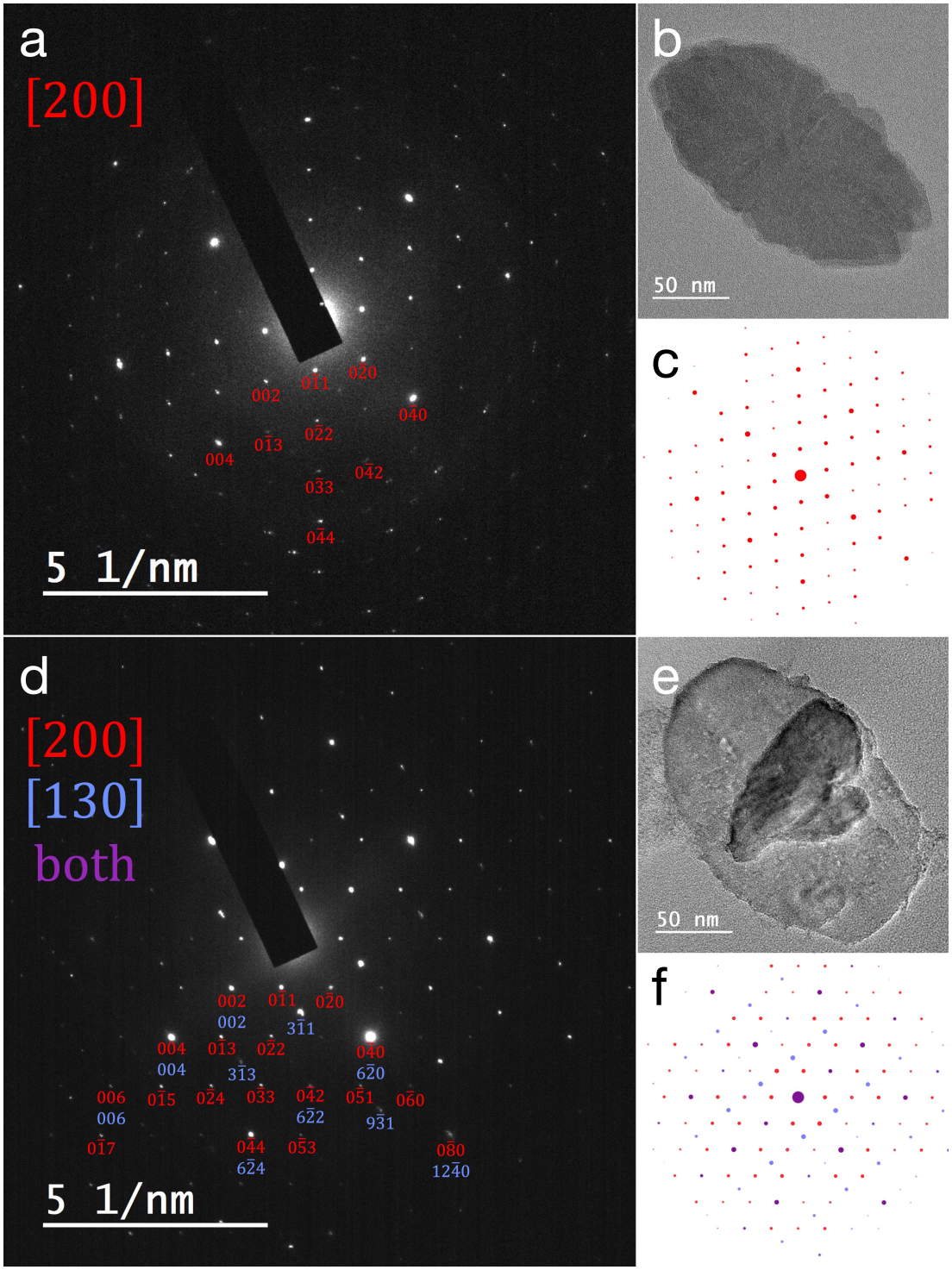

Fig. 3.3. SAED of Fe_2GeS_4 NPs with nanoplates parallel to the page. **a,** SAED pattern and, **b,** the TEM image of an Fe_2GeS_4 nanoplate without intersecting twinned nanoplates. This NP was produced in the reaction that was carried out at one quarter of the precursor concentrations and produced a collection of twinned and non-twinned Fe_2GeS_4 NPs. **c,** Simulated electron diffraction pattern for the [200] zone axis. **d,** SAED pattern and, **e,** and the TEM image of an Fe_2GeS_4 NP with intersecting twinned nanoplates. **f,** Simulated electron diffraction patterns for the [200] and [130] zone axes overlaid with the [200] spots in red, the [130] spots in blue, and the overlapping spots in purple.

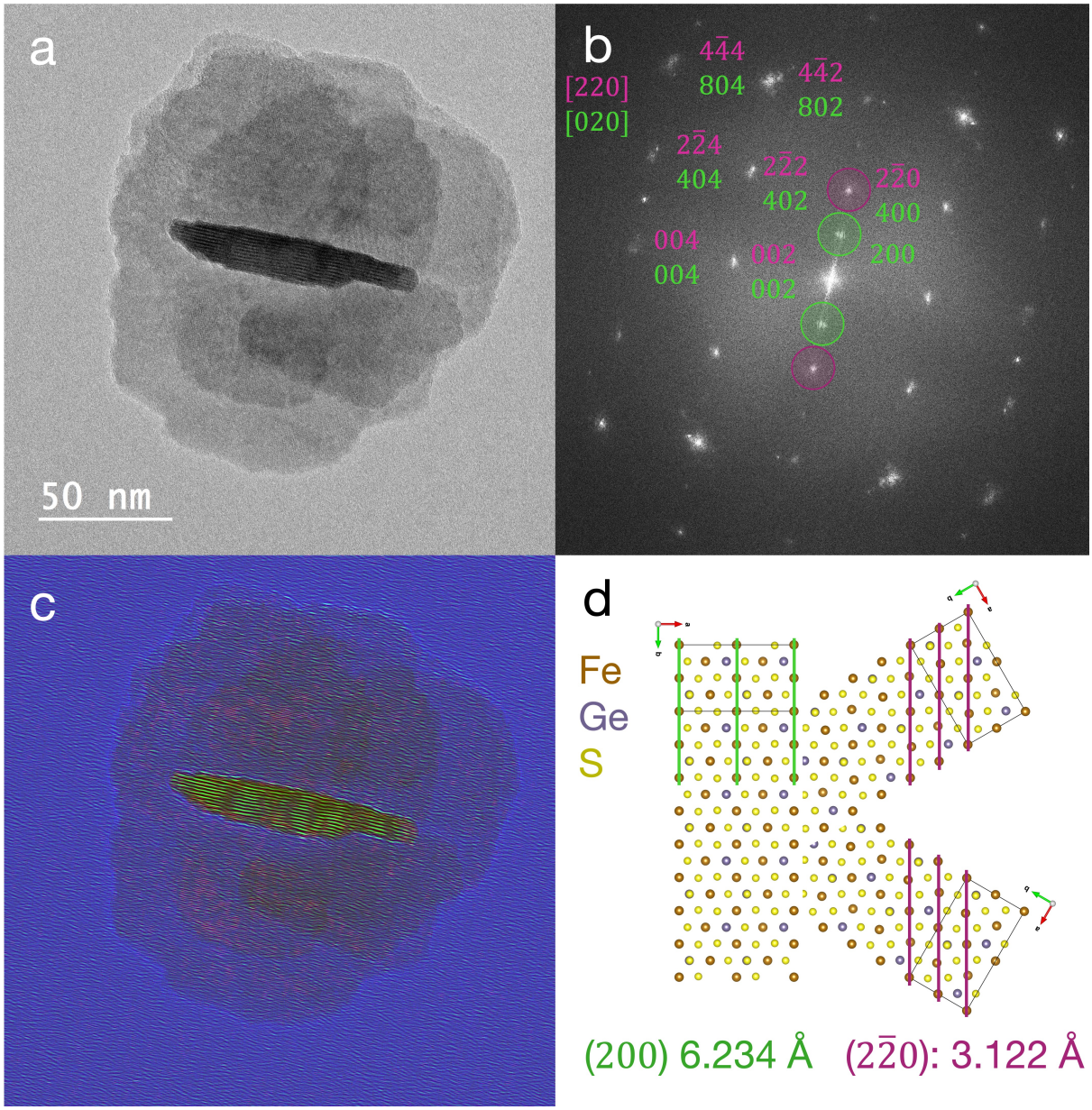

Fig. 3.4. Inverse FFT TEM images. **a,** TEM image of a Fe_2GeS_4 NP. **b,** FFT of the TEM image with spots labeled according to both the [020] and [220] zone axes in green and pink, respectively. **c,** Overlaid and colored inverse FFT images produced from masked FFT images that isolated the spots circled in green and pink in the FFT image. **d,** Fe_2GeS_4 crystal structure modeled to depict the orientation of the (200) and $(2\bar{2}0)$ lattice planes and their respective d-spacings in a twinned NP.

For a NP oriented with the core axis perpendicular to the page, all of the twinned domains exhibit the (002) zone axis. Fig. 3.5a-c shows the SAED pattern, TEM image, and simulated pattern for one set of nanoplates in the NP. Diffraction spots are labeled and indicate that the [020] and [200] directions occur along the length and perpendicular to the face of the nanoplate, respectively. Thus, an SAED pattern of the

entire NP results in an overlay of three (002) zone axis patterns at 60˚ angles relative to one another (Fig. 3.5d). Colored arrows on the TEM image (Fig. 3.5e) indicate the nanoplates that correspond to the three simulated diffraction patterns in Fig. 3.5f. Diffraction spots in the SAED pattern are circled to show the diffraction spots that are unique to each of the three individual patterns; these are labeled in Fig. S3.5. The six strong spots that form a hexagonal shape are shared by all three diffraction patterns and correspond to either the {620} or {040} families of planes. These spots are fairly well overlaid and show a small degree of smearing because some of the nanoplates are not exactly parallel to one another. The relation between these families of planes stems from the underlying hexagonal pseudosymmetry of the orthorhombic olivine crystal structure, which is the structural cause of the twinning.

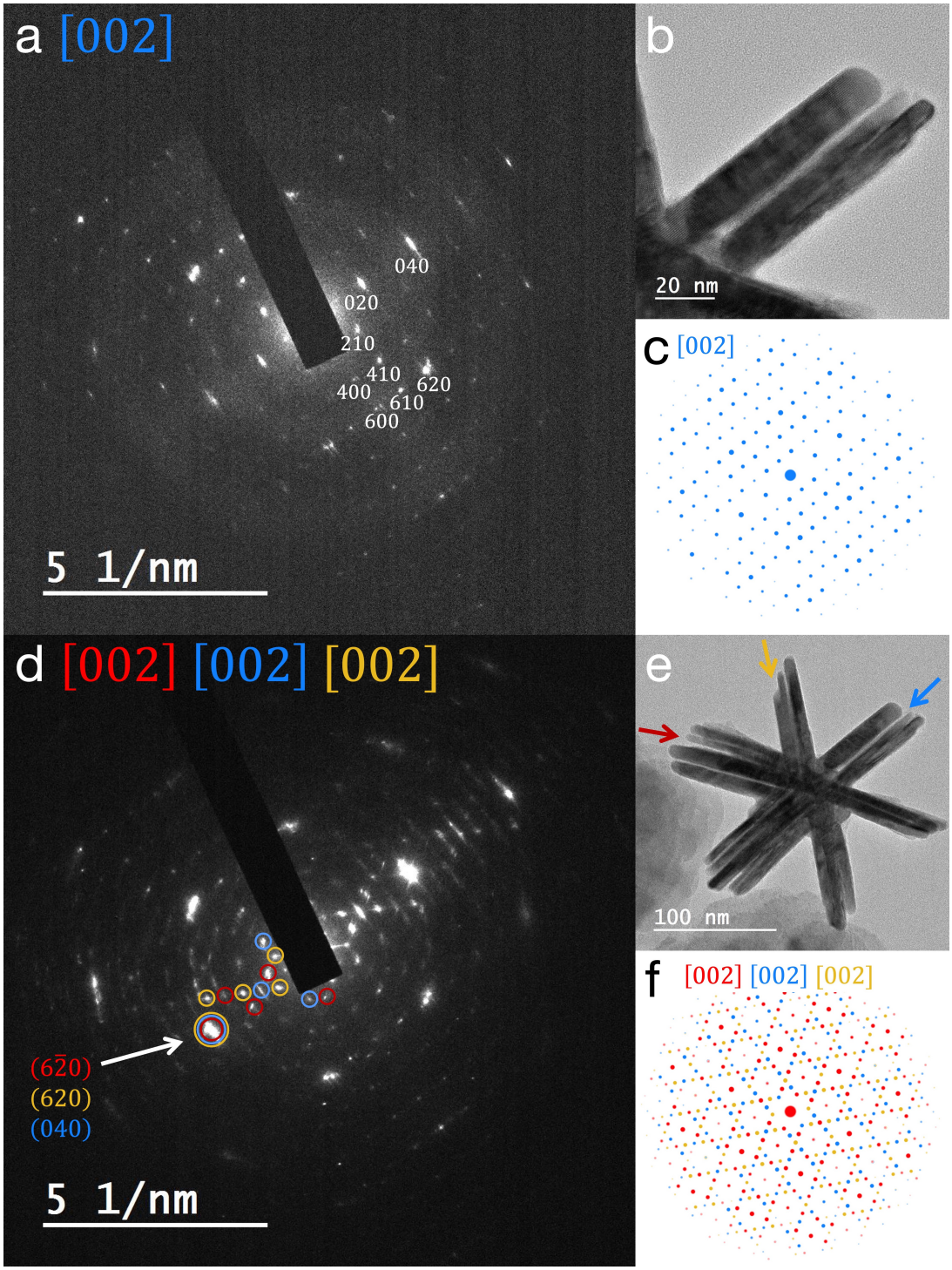

Fig. 3.5. SAED of a Fe_2GeS_4 NP with the core axis perpendicular to the page. **a,** SAED pattern and, **b,** the TEM image of one set of nanoplates in a Fe_2GeS_4 NP. The pattern matches, **c,** the simulated [002] zone axis pattern. **d,** SAED pattern and, **e,** the TEM image of the full NP. The nanoplates are all oriented viewing along the [002] zone axis but exist at 60˚ angles to one another. The SAED pattern matches, **f,** the simulated pattern of three [002] zone axis patterns overlaid at 60˚ angles. The three patterns are shown in red, yellow, and blue and correspond to the sets of nanoplates as indicated by the arrows in the TEM image (**e**). Spots on the SAED pattern (**d**) are circled to indicate the presence of diffraction from the unique twin domains.

3. Hexagonal Pseudosymmetry of Fe_2GeS_4

This type of twinning, a trilling, has been observed for olivine minerals but is reported to be relatively scarce[26]. In fact, it can occur for any orthorhombic crystal structure for which the ratio of two of the unit cell dimensions is sufficiently close to $\sqrt{3}:1$. A wide assortment of non-olivine compounds fall into this pseudosymmetry, including $BaAl_2Si_2O_8$,[27] the open framework germanate ASU-21,[28] muscovite,[29] as well as ScPtGa and ScAuGa.[30] However, we will focus on this sort of twinning for compounds of the olivine structure type. In Fe_2GeS_4, $a \approx \sqrt{3}\, b$ and the S anions exist in a slightly distorted *hcp* sublattice providing the hexagonal pseudosymmetry. With this ratio, the face diagonal of the unit cell *ab* face is $\approx 2b$ and a ~60˚ angle forms between twinned domains (Fig. S3.6). The degree of distortion from these ideal hexagonal ratios is quite small for Fe_2GeS_4 (0.2%) and results in a high likelihood of trilling formation.

Generally, the twinning can be visualized as growth of the [020] direction of two twin domains off the (310) and $(3\bar{1}0)$ lattice planes of the third twin domain (Fig. 3.6). Accordingly, the angles between these three sets of planes are either 59.9 or 60.1˚. Our determination of the [200] and [002] directions oriented perpendicular to the faces of the nanoplates and along the core of the NP, respectively, is consistent with this crystal twinning. Depending on atomic placement, the twinning could be described by reflection twins across either {110} or {310} or rotation twins about <110> or <310> (Fig. 3.7, S3.7) because these two sets of planes are perpendicular to one another. The composition surface is the set of atoms shared by both twin domains, so the twin plane of reflection twins is also its composition surface. Similarly, the twin axis for rotation twins is the axis of atoms that is shared by both rotation twin domains. Figure S3.7 outlines these four possible twin operations and shows that they are unique relative to one another with respect to atom placement.

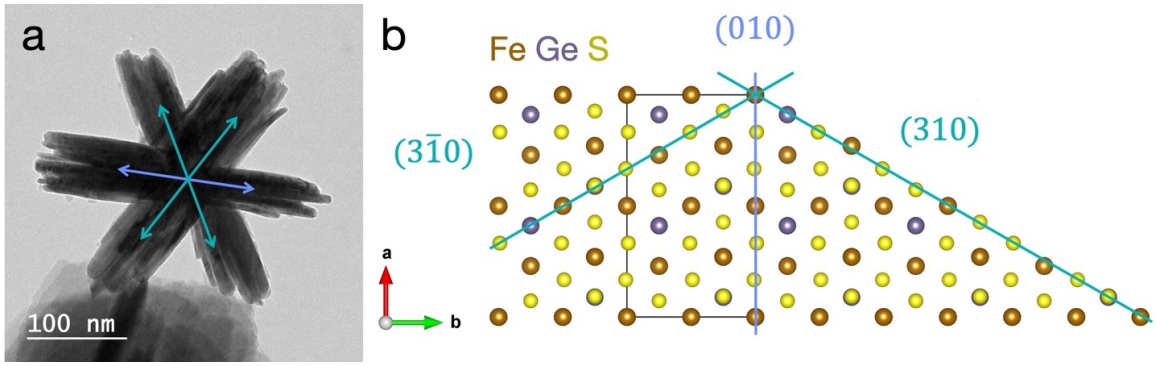

Fig. 3.6. a, TEM image of a Fe_2GeS_4 NP with teal and blue arrows overlaid to indicate the 60˚ angles between the [020] growth directions of each set of stacked nanoplates. The [020] directions of the diagonal nanoplates (teal arrows overlaid) could grow off the [310] and [3$\bar{1}$0] directions of the horizontal nanoplates (blue arrow overlaid). **b,** The crystal structure of Fe_2GeS_4, viewed along the [002] zone axis which corresponds to the crystallographic direction oriented along the core axis of the NP where the three sets of nanoplates intersect. The ~60˚ angles between the (310), (3$\bar{1}$0), and (010) lattice planes is depicted.

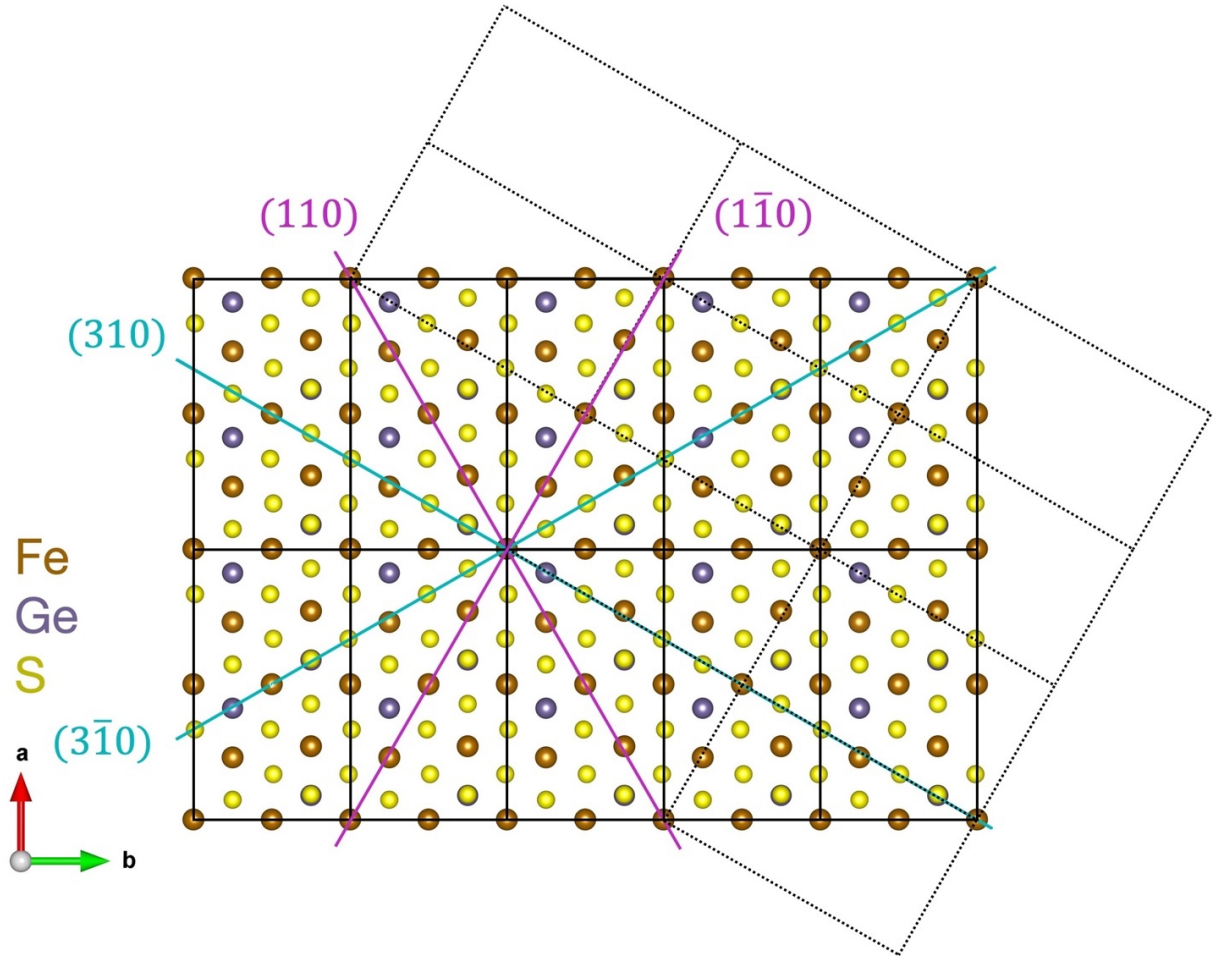

Fig. 3.7. Crystal structure of Fe_2GeS_4 with a twinned domain's unit cell framework overlaid in dotted lines. The teal and pink lines show the {310} and {110} lattice planes, both of which may be twin planes for reflection twinning in olivine compounds. For rotation twins, the rotation axis may be either <110> or <310>. Because the two sets of planes are perpendicular to one another, the [110] axis lies within the (3$\bar{1}$0) plane and the [310] axis lies within the (1$\bar{1}$0) plane.

Comparing the linked polyhedra of the (040) and (310) lattice planes, shared motifs can be identified along the [002] crystallographic direction (Fig. 3.8). Vertex-sharing between iron octahedra and germanium tetrahedra exist as a row of germanium tetrahedra surround by two rows of iron octahedra. The octahedra and tetrahedra are not linked to their same kind in the [002] direction. For individual (310) planes, this motif occurs at longer intervals in the [110] direction than for the individual (040) planes in the [200] (Fig. S3.8,S3.9). However, if one considered growth in the [310] direction off a nanoplate with a (100) face, the motif is present at shorter intervals in the [110] direction and occurs in a stepped fashion (Fig 9). The precise distances of the motif spacing in the stepped (310) planes is equal to the (110) d-spacing (6.243 Å), and the motif spacing in the (040) planes corresponds to the (200) d-spacing (6.234 Å). The near identical nature of these two d-spacing values originates from the hexagonal pseudosymmetry of the Fe_2GeS_4 crystal structure.

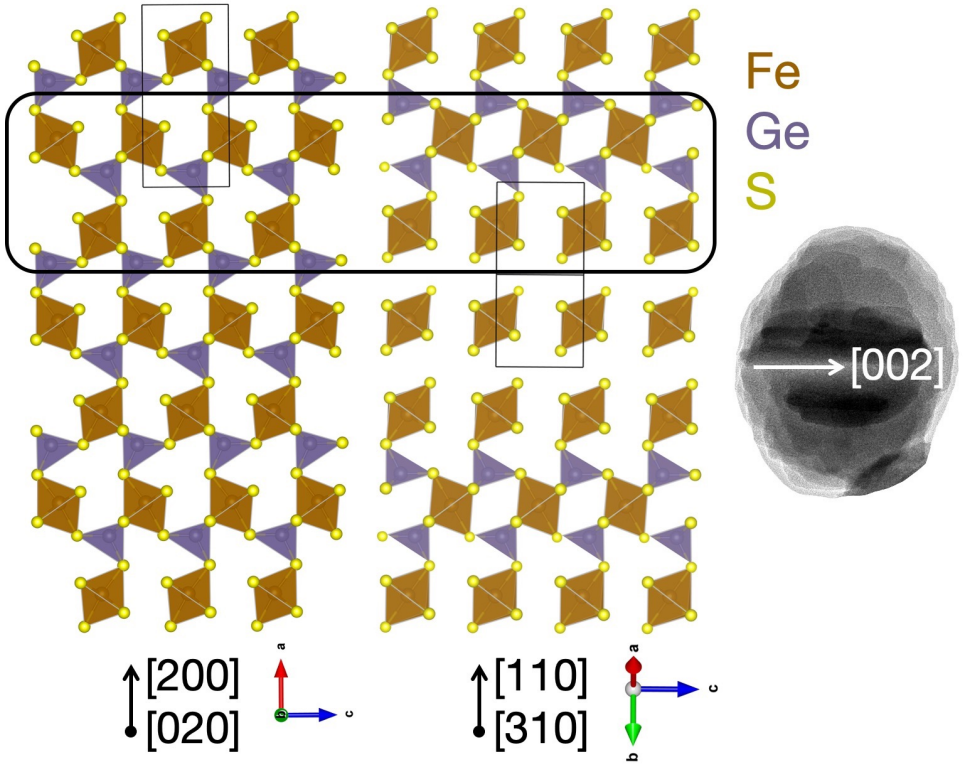

Fig. 3.8. Comparison of individual (040) and (310) lattice planes. The motif of vertex-sharing between germanium tetrahedra and iron octahedra with one row of germanium tetrahedra surrounded by two rows of iron octahedra occurs in both the (040) and (310) lattice planes. The rows extend along the [001] direction. Also, the motifs occur at shorter intervals for the (040) slices (in the [200] direction) than for the (310) slices (in the [110] direction).

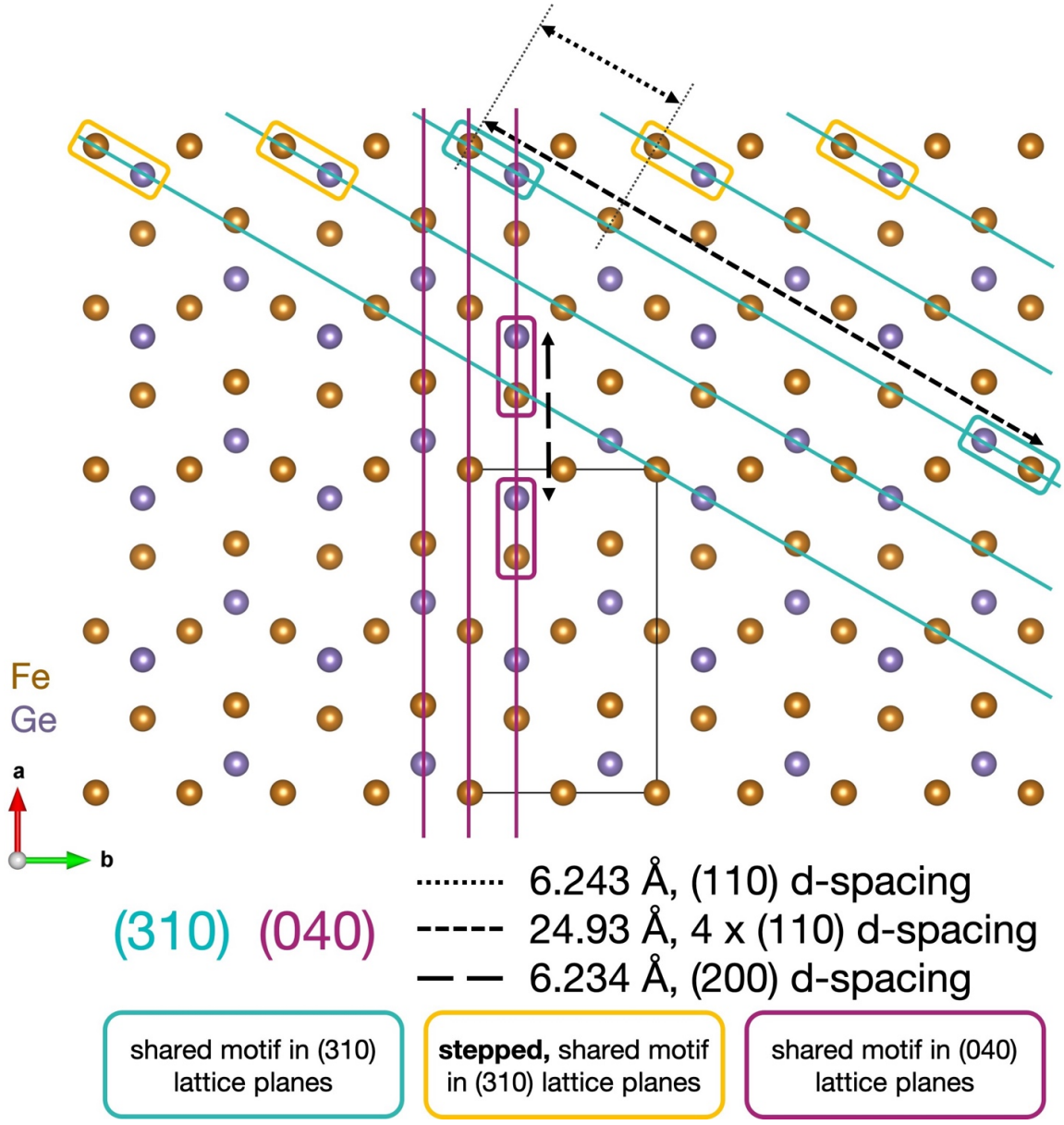

Fig. 3.9. Depiction of the distances between the shared motifs of the (040) and (310) lattice planes. The S atoms of the Fe_2GeS_4 crystal structure have been removed for clarity. The shared motifs are outlined in rectangles within the different lattice planes. They occur at intervals of 6.234 Å in the (040) lattice planes, which is equal to the (200) d-spacing. In an individual (310) lattice plane, they occur at intervals of 24.93 Å, which is four times the (110) d-spacing. However, if one considers the shared motifs in the collection of layered (310) lattice planes, the distance between the steps of the shared motifs is 6.243 Å, which corresponds to the (110) d-spacing. The almost equal values of the (110) and (200) d-spacings originate from the hexagonal pseudosymmetry of the crystal structure.

4. Synthetic Control of Twinned Fe_2GeS_4 NPs

The geometrical aspects of the crystal structure underlie the tendency of this compound to form trillings, but environmental (synthetic) conditions provide control over the occurrence of twinning. A

supersaturation of monomers increases the likelihood of twin and trilling formation because atoms deposited initiating twin defects are less likely to detach before additional monomers adhere[31]. With high monomer concentrations and rapid crystal growth, the twinned domain may continue growth despite the relative instability of the twin boundary. Our solution-based system involves injection of the S precursor into the Fe and Ge precursors at 320 ˚C. Especially with the use of a Brønsted base, lithium bis(trimethylsilyl)amide, these conditions rapidly provide high concentrations of monomers. We speculate the NPs nucleate with a high formation probability of twinned interfaces followed by a swift decrease of monomer concentrations resulting in growth of the individual nanoplates. As a control, we carried out the reaction at one quarter of the molar precursor concentrations in the same volume of solvent and observed that phase-pure Fe_2GeS_4 formed but fewer NPs exhibited twinning (Fig. S3.10). The lower concentration reaction produced 38% non-twinned NPs (n = 554 NPs counted), and the original reaction produced 2% non-twinned NPs (n = 427 NPs counted). This supports the understanding that a higher concentration of monomers increases the tendency for twinning.

Design of the original synthesis required a thorough investigation of the precursors' roles and the effects of the reaction parameters, which has resulted in the ability to probe this synthesis synthetically to understand crystal twinning while avoiding impurity formation. In order to control the number of non-twinned grain boundaries in the NPs, we were able to induce coalescence of the stacked nanoplates and overall increased crystallinity by carrying out a second injection (Fig. 3.10). Without isolating and washing the NPs formed via the standard procedure, both a $FeCl_2$, GeI_4, and OLA solution as well as a S, $LiN(SiMe_3)_2$, and OLA solution were simultaneously injected into the reaction flask and an additional 10 min of growth was carried out. The additional precursors grew on the existent NPs instead of inducing a secondary nucleation of new, smaller NPs or of impurity phases. The PXRD pattern showed Fe_2GeS_4 alone (Fig. S3.11). We believe this induced coalescence of the stacked nanoplates for two reasons. The nanoplate thickness increased from 13 ± 3 nm in the original NPs to 21 ± 4 nm in this product, and the number of nanoplates per stack decreased from 2.7 ± 1.4 nanoplates in the original NPs to 1.9 ± 1.0 in the coalesced ones. The change in the distribution of nanoplates per stack for the two reactions can be observed in Fig.

3.10c. Lastly, the edges of the individual nanoplates are smoother and more faceted which indicates increased crystallinity. These NPs exhibit a decreased number of grain boundaries in the stacks of nanoplates but retain the crystal twinning which may be advantageous for understanding the effect of crystal twinning on properties relative to non-twinned Fe_2GeS_4. The original NPs with higher amounts of grain boundaries could be useful for thermoelectric application via increased phonon scattering. Property measurements of these Fe_2GeS_4 NP variants are a focus of future work.

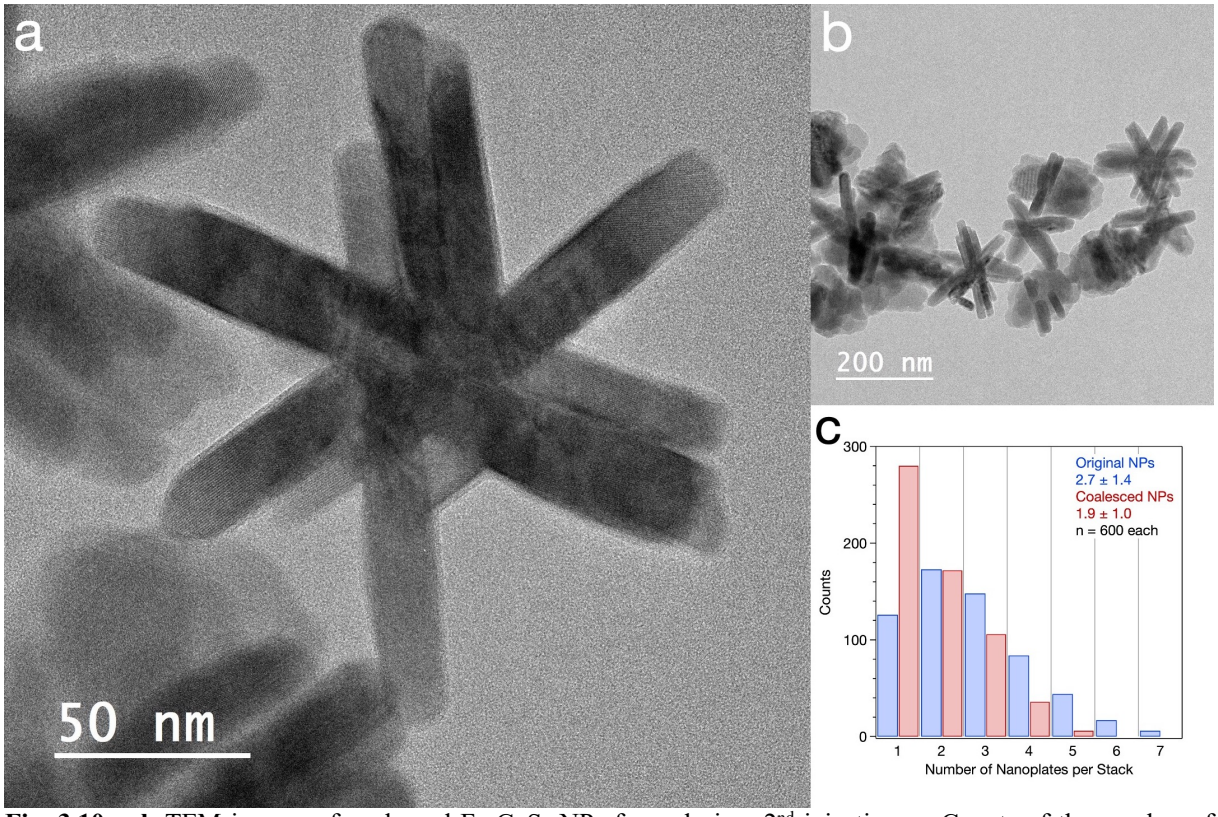

Fig. 3.10. a,b TEM images of coalesced Fe_2GeS_4 NPs formed via a 2nd injection. **c,** Counts of the number of nanoplates per stack in NPs for both the coalesced and the original NPs. **c** The coalesced NPs show fewer coalesced nanoplates per stack with 1.9 ± 1.0 nanoplates versus the original NPs with 2.7 ± 1.4 nanoplates.

5. Pseudohexagonal Twins and Trillings in Olivines

In order to understand the twinning of the Fe_2GeS_4 NPs, we first look to reported instances of twins and trillings in other olivine compounds. This includes forsterite-fayalite mixtures ($Mg_{2-x}Fe_xSiO_4$)[32–36], monticellite ($CaMgSiO_4$)[20,32,36], and chrysoberyl (Al_2BeO_4)[36,37]. These minerals are typically assigned the non-standard setting of space group #62, *Pbnm*, instead of the standard setting, *Pnma*, used for Fe_2GeS_4 and throughout this paper. The difference between the settings involves a permutation of the *a*, *b*, and *c*

lattice directions. Both the $(310)_{Pnma}$ and $(110)_{Pnma}$ planes have been reported as twin planes for olivines with Arzruni et al. citing the presence of both in the same trilling[32]. Schmetzer has made the distinction that $(310)_{Pnma}$ twinning occurs in alexandrite (Cr-containing Al_2BeO_4) trillings as opposed to twinning on $(110)_{Pnma}$[37]. The difficulty to distinguish between the two twin planes in olivines based simply on crystal habit and reentrant angles was addressed as early as 1935 by Burri et al[20]. Computationally, Azevedo and Nespolo examined variations in the atomic restoration of Mg_2SiO_4 across various twin planes in order to predict which mode of twinning should be most probable[26]. The authors reported a higher citation frequency of $(110)_{Pnma}$ twinning but identified $(310)_{Pnma}$ as the more probable twin plane and called for a reinvestigation of twinning in olivines. While twinning in macroscopic olivine crystals are relatively scarce, twinned NP syntheses present a valuable system for carrying out a statistical evaluation of the distribution of twin planes. Because the distorted coordination of atoms at twin boundaries can influence material properties[1], it would be of interest to understand the distinction between these possible twin operations in olivines.

However, this would rely on the ability to characterize the atomic structure of the twin boundaries unambiguously in the NPs. High resolution electron microscopy techniques can provide powerful methods to understand the arrangement of atoms at defect sites, but very thin samples lend themselves best to these methods, including two-dimensional materials (i.e. MoS_2)[1] and smaller NPs[38]. Because the width of the Fe_2GeS_4 NPs can be up to ~200 nm, it is difficult to detect the exact atomic composition of the twin boundaries. Shorter growth times were explored, but sufficiently small particles could not be attained, and at very early stages of growth, the majority of the product was amorphous. The NPs tend to grow to large sizes quickly but require ~10 min of growth to increase their crystallinity (Fig. S3.12). Thus, we believe the twinning in these NPs is best described as a possible combination of different twinning operations (reflection and rotation) about both the (110) and (310) twin planes and axes. A 2D scheme of exclusively {310} twin boundaries compared to a mixture of {310} and {110} twin boundaries is given in Fig. S3.13. Often, twin boundaries are imagined to be highly regular interfaces between two domains; however, it is common for twins to exhibit irregular, defective boundaries[39,40]. Therefore, if the twin boundaries could be

characterized, the massive collection of twinned NPs produced would provide an adequate collection for carrying out statistical analysis.

6. Prediction of Twinning Tendency in Olivine Compounds

Because this twinning should be probable for other olivines for which $a_{Pnma} \approx \sqrt{3}\, b_{Pnma}$, we searched the Inorganic Crystal Structure Database (ICSD) for compounds of the olivine structure type (Mg_2SiO_4). For each compound, we calculated the ratio of the largest lattice parameter (a_{Pnma}) to the median lattice parameter (b_{Pnma}) and ranked the structures according to the percent difference of this ratio from $a_{Pnma}/b_{Pnma} = \sqrt{3} \approx 1.732$ (Appendix A). As the lattice parameter ratio approaches this value, the distortion of the anion sublattice from an *hcp* lattice decreases. Additionally, because the *hcp* stacking of the anion sublattice in olivines occurs in the direction of the smallest lattice parameter (c_{Pnma}), the ratio of c_{Pnma} to either a_{Pnma} or b_{Pnma} exists as a means to measure the extent of the distortion from the ideal *hcp* anion sublattice in terms of the distance between the close-packed *ABAB* layers. The percentage differences of these two lattice parameter ratios from their ideal values, $c_{Pnma}/a_{Pnma} = \sqrt{2/9}$ and $c_{Pnma}/b_{Pnma} = \sqrt{2/3}$, were also calculated for the olivine compounds (Appendix A). The derivations of the ideal *hcp* ratios for the anion sublattice of the olivine crystal structure are outlined in Fig. S3.14.

Of these three lattice parameter comparisons, the $a_{Pnma}/b_{Pnma} \approx \sqrt{3}$ ratio appears to be the most influential for the tendency of an olivine compound to form twins and trillings in this manner. For example, Burri et al. noted that forsterite (Mg_2SiO_4) was more likely to form twins upon the presence of Ca and connected the observation to the change in the lattice parameters[20]. The compound $CaMgSiO_4$ lies extremely close to the $a_{Pnma}/b_{Pnma} \approx \sqrt{3}$ ratio at 0.01% off, while Mg_2SiO_4 is 1.3% off according to our calculations from the respective ICSD listings. Considering deviation of the compounds from the ideal *hcp* ratio with respect to the distance between the close-packed *ABAB* layers, $CaMgSiO_4$ is ~8% off while Mg_2SiO_4 is only ~2% off. Thus, it appears as though the distortion of an olivine compound from the ideal *hcp* distance between the *ABAB* layers does not dominate the probability for a compound to form twins and trillings. This seems reasonable because the twin or trilling domains all share the $[001]_{Pnma}$ axis along the

core of the NP. Even if the *hcp ABAB* stacked layers are spaced out at intervals smaller or greater than the ideal *hcp* ratio, the compound exhibits the pseudo-hexagonal symmetry required for [020] growth off the (310) and $(3\bar{1}0)$ faces. Thus, closeness of an olivine compound to the $a_{Pnma}/b_{Pnma} \approx \sqrt{3}$ ratio should indicate increased probability of the material to form twins. However, to our knowledge, this comparison to the influence of the c_{Pnma}/a_{Pnma} and c_{Pnma}/b_{Pnma} ratios has not been specifically studied for olivine compounds and might be of interest to examine less anecdotally.

Our search of the ICSD enabled us to assemble a list of olivine compounds which points to predictable compounds for twin formation that range in composition over the entire periodic table. In the A_2BX_4 form, A may be alkali, alkaline earth, or transition metals; B may be a wide variety of main group elements (Al, Ga, In, Si, Ge, Sn, P, or As); and X may be any of the chalcogen or halogen elements. Of note, this list comprises only those compounds reported in the ICSD; thus, undiscovered olivine compositions may show hexagonal pseudosymmetry as well. This list can be useful for designing research targeted at understanding fundamental aspects of crystal nucleation and growth. It would be interesting to explore the tolerance of twinning in compounds despite existing relatively far from the ideal $a_{Pnma} \approx \sqrt{3}\, b_{Pnma}$ lattice parameter ratio. This work could parallel research seeking to understand whether other chemical and structural aspects exhibit a dominant influence on twin formation over the degree of hexagonal pseudosymmetry. The ranked olivine compounds could be used to identify sets of compounds for which the $a_{Pnma} \approx \sqrt{3}\, b_{Pnma}$ ratio is similar while having divergent properties in another area that might play a role in the tendency of a compound to form twins (i.e. atomic size, enthalpy of formation, HSAB compatibility between constituent elements, crystal structure polarity, etc.). Additionally, because twinning has been studied in relation to material properties ranging from transport properties (electronic[1,2], ionic[2], and of phonons[8–12]) to material hardness[13–17] and magnetism[18,19], it is of interest to have a measure of how likely twins might form in various materials. Our exploration has only included olivines; however, a search for hexagonal pseudosymmetry could be extended to all orthorhombic compounds. Further, other

examples of pseudomerohedral symmetry could be targeted and ranked (i.e. monoclinic compounds for which $a \approx b$, $\beta \approx 120^{\circ}$).

7. Conclusions

The synthetic control of amide-assisted synthesis has allowed us to manipulate the degree of twinning and morphology of the NPs. Here, we characterized the microstructure of twinned Fe_2GeS_4 NPs through a combination of TEM imaging, diffraction, and crystallographic analysis. Due to the hexagonal pseudosymmetry of the olivine crystal structure when the lattice parameters $a_{Pnma}/b_{Pnma} \approx \sqrt{3}$, Fe_2GeS_4 is highly probable to form twins or triplets of twins, called trillings. Despite the relative scarcity of twinned crystals in the vast majority of bulk samples, our synthesis formed 98% twinned NPs (n = 427 NPs counted). By lowering the concentration of precursors, we were able to produce a lower percentage of twinned Fe_2GeS_4 NPs at 62% (n = 554 NPs counted). Through a second injection of precursors, we observed the coalescence of the stacked nanoplates that exist in the original Fe_2GeS_4 NPs. This produced more crystalline, but still twinned, NPs that may be useful for applications for which a higher number of grain boundaries would be detrimental, such as photovoltaic absorption. Conversely, the twinned NPs with stacked nanoplates could be advantageous for thermoelectric applications. Comparing relevant properties of these NP variants is the focus of future work. More broadly, because this pseudomerohedral twinning should occur for any olivine compound that is near the pseudohexagonal $a_{Pnma}/b_{Pnma} \approx \sqrt{3}$ ratio, we ranked all of the olivine compounds listed in the ICSD and discussed future research possibilities. The work in this study presents an area ripe for future exploration with respect to multiple aspects: olivine-type compounds hold interesting properties for a wide variety of applications, nanoparticle systems can show unique properties based on size-dependent effects, and material properties and functionality have been shown to be affected by the presence of twin boundaries. We believe the control advancing in the NP synthetic community holds promise to understand crystal nucleation and growth fundamentals in further depth as well as improve the performance of materials in a number of applications.

REFERENCES

(1) van der Zande, A. M.; Huang, P. Y.; Chenet, D. A.; Berkelbach, T. C.; You, Y.; Lee, G. H.; Heinz, T. F.; Reichman, D. R.; Muller, D. A.; Hone, J. C. Grains and Grain Boundaries in Highly Crystalline Monolayer Molybdenum Disulphide. *Nat. Mater.* **2013**, *12* (6), 554–561.

(2) Moriwake, H.; Kuwabara, A.; Fisher, C. A. J.; Huang, R.; Hitosugi, T.; Ikuhara, Y. H.; Oki, H.; Ikuhara, Y. First-Principles Calculations of Lithium-Ion Migration at a Coherent Grain Boundary in a Cathode Material, $LiCoO_2$. *Adv. Mater.* **2013**, *25* (4), 618–622.

(3) Ikonić, Z.; Srivastava, G. P.; Inkson, J. C. Electronic Properties of Twin Boundaries and Twinning Superlattices in Diamond-Type and Zinc-Blende-Type Semiconductors. *Phys. Rev. B* **1993**, *48* (23), 17181–17193.

(4) Ikonic, Z.; Srivastava, G. P.; Inkson, J. C. Optical Properties of Twinning Superlattices in Diamond-Type and Zinc-Blende-Type Semiconductors. *Phys. Rev. B* **1995**, *52* (19), 14078–14085.

(5) Algra, R. E.; Verheijen, M. A.; Borgström, M. T.; Feiner, L. F.; Immink, G.; Van Enckevort, W. J. P.; Vlieg, E.; Bakkers, E. P. A. M. Twinning Superlattices in Indium Phosphide Nanowires. *Nature* **2008**, *456* (7220), 369–372.

(6) Billig, E.; Ridout, M. S. Transmission of Electrons and Holes Across a Twin Boundary in Germanium. *Nature* **1954**, *173* (4402), 496–497.

(7) Tsurekawa, S.; Kido, K.; Watanabe, T. Measurements of Potential Barrier Height of Grain Boundaries in Polycrystalline Silicon by Kelvin Probe Force Microscopy. *Philos. Mag. Lett.* **2005**, *85* (1), 41–49.

(8) Ibáñez, M.; Zamani, R.; Li, W.; Cadavid, D.; Gorsse, S.; Katcho, N. A.; Shavel, A.; López, A. M.; Morante, J. R.; Arbiol, J.; et al. Crystallographic Control at the Nanoscale to Enhance Functionality: Polytypic Cu_2GeSe_3 Nanoparticles as Thermoelectric Materials. *Chem. Mater.* **2012**, *24* (23), 4615–4622.

(9) Shin, H. S.; Jeon, S. G.; Yu, J.; Kim, Y. S.; Park, H. M.; Song, J. Y. Twin-Driven Thermoelectric Figure-of-Merit Enhancement of Bi_2Te_3 Nanowires. *Nanoscale* **2014**, *6* (11), 6158–6165.

(10) Jang, J. I.; Lee, J. E.; Kim, B. S.; Park, S. D.; Lee, H. S. Twinning and Its Formation Mechanism in a Binary Mg_2Si Thermoelectric Material with an Anti-Fluorite Structure. *RSC Adv.* **2017**, *7* (35), 21671–21677.

(11) Yu, Y.; He, D.-S.; Zhang, S.; Cojocaru-Mirédin, O.; Schwarz, T.; Stoffers, A.; Wang, X.-Y.; Zheng, S.; Zhu, B.; Scheu, C.; et al. Simultaneous Optimization of Electrical and Thermal Transport Properties of $Bi_{0.5}Sb_{1.5}Te_3$ Thermoelectric Alloy by Twin Boundary Engineering. *Nano Energy* **2017**, *37* (May), 203–213.

(12) Zhang, A.; Zhang, B.; Lu, W.; Xie, D.; Ou, H.; Han, X.; Dai, J.; Lu, X.; Han, G.; Wang, G.; et al. Twin Engineering in Solution-Synthesized Nonstoichiometric Cu_5FeS_4 Icosahedral Nanoparticles for Enhanced Thermoelectric Performance. *Adv. Funct. Mater.* **2018**, *28* (10), 1705117.

(13) Lu, K.; Lu, L.; Suresh, S. Strengthening Materials by Engineering Coherent Internal Boundaries at the Nanoscale. *Science* **2009**, *324* (5925), 349–352.

(14) Huang, Q.; Yu, D.; Xu, B.; Hu, W.; Ma, Y.; Wang, Y.; Zhao, Z.; Wen, B.; He, J.; Liu, Z.; et al. Nanotwinned Diamond with Unprecedented Hardness and Stability. *Nature* **2014**, *510* (7504), 250–253.

(15) Chen, G.; Peng, Y.; Zheng, G.; Qi, Z.; Wang, M.; Yu, H.; Dong, C.; Liu, C. T. Polysynthetic Twinned TiAl Single Crystals for High-Temperature Applications. *Nat. Mater.* **2016**, *15* (8), 876–881.

(16) Wang, Y. M.; Voisin, T.; McKeown, J. T.; Ye, J.; Calta, N. P.; Li, Z.; Zeng, Z.; Zhang, Y.; Chen, W.; Roehling, T. T.; et al. Additively Manufactured Hierarchical Stainless Steels with High Strength and Ductility. *Nat. Mater.* **2018**, *17* (1), 63–70.

(17) Ke, X.; Ye, J.; Pan, Z.; Geng, J.; Besser, M. F.; Qu, D.; Caro, A.; Marian, J.; Ott, R. T.; Wang, Y. M.; et al. Ideal Maximum Strengths and Defect-Induced Softening in Nanocrystalline-Nanotwinned Metals. *Nat. Mater.* **2019**, *18* (11), 1207–1214.

(18) Alexandre, S. S.; Anglada, E.; Soler, J. M.; Yndurain, F. Magnetism of Two-Dimensional Defects in Pd: Stacking Faults, Twin Boundaries, and Surfaces. *Phys. Rev. B - Condens. Matter Mater. Phys.* **2006**, *74* (5), 1–7.

(19) Abakumov, A. M.; Tsirlin, A. A.; Bakaimi, I.; Van Tendeloo, G.; Lappas, A. Multiple Twinning as a Structure Directing Mechanism in Layered Rock-Salt-Type Oxides: $NaMnO_2$ Polymorphism, Redox Potentials, and Magnetism. *Chem. Mater.* **2014**, *26* (10), 3306–3315.

(20) Burri, C. Notiz Über Zwillinge Und Drillinge Gesteinsbildender Olivine. *Schweizerische Mineral. und Petrogr. Mitteilungen* **1935**, *15*, 160–167.

(21) Schmetzer, K.; Bernhardt, H.-J.; Hainschwang, T. Measurement and Interpretation of Growth Patterns in Chrysoberyl, Including Alexandrite. *J. Gemmol.* **2011**, *32* (5), 129–144.

(22) Pearson, D. G.; Brenker, F. E.; Nestola, F.; McNeill, J.; Nasdala, L.; Hutchison, M. T.; Matveev, S.; Mather, K.; Silversmit, G.; Schmitz, S.; et al. Hydrous Mantle Transition Zone Indicated by Ringwoodite Included within Diamond. *Nature* **2014**, *507* (7491), 221–224.

(23) Cline, C. J.; Faul, U. H.; David, E. C.; Berry, A. J.; Jackson, I. Redox-Influenced Seismic Properties of Uppermantle Olivine. *Nature* **2018**, *555* (7696), 355–358.

(24) Fredrick, S. J.; Prieto, A. L. Solution Synthesis and Reactivity of Colloidal Fe_2GeS_4: A Potential Candidate for Earth Abundant, Nanostructured Photovoltaics. *J. Am. Chem. Soc.* **2013**, *135* (49), 18256–18259.

(25) Miller, R. C.; Neilson, J. R.; Prieto, A. L. Amide-Assisted Synthesis of Iron Germanium Sulfide (Fe_2GeS_4) Nanostars: The Effect of $LiN(SiMe_3)_2$ on Precursor Reactivity for Favoring Nanoparticle Nucleation or Growth. *J. Am. Chem. Soc.* **2020**, *142* (15), 7023–7035.

(26) Azevedo, S.; Nespolo, M. Twinning in Olivine Group Revisited. *Eur. J. Mineral.* **2017**, *29* (2), 213–226.

(27) Takéuchi, Y. A Detailed Investigation of the Structure of Hexagonal $BaAl_2Si_2O_8$ with Reference to Its Alpha-Beta Inversion. *Mineral. J.* **1958**, *2* (5), 311–332.

(28) Bonneau, C.; Sun, J.; Sanchez-Smith, R.; Guo, B.; Zhang, D.; Inge, A. K.; Edén, M.; Zou, X. Open-Framework Germanate Built from the Hexagonal Packing of Rigid Cylinders. *Inorg. Chem.* **2009**, *48* (21), 9962–9964.

(29) Zhao, S. R.; Xu, C.; Li, C. Identification of Twins in Muscovite: An Electron Backscattered Diffraction Study. *Zeitschrift fur Krist. - Cryst. Mater.* **2019**, *234* (5), 329–340.

(30) Heletta, L.; Block, T.; Klenner, S.; Pöttgen, R. Ternary Transition Metal Gallides with TiNiSi, ZrBeSi and $MgZn_2$-Type Structure. *Zeitschrift fur Naturforsch. - Sect. B J. Chem. Sci.* **2019**, *74* (3), 297–306.

(31) Buerger, M. J. The Genesis of Twin Crystals. *J. Mineral. Soc. Am.* **1945**, *30*, 469–482.

(32) Arzruni, A. Forsterit Vom Monte Somma. *Zeitschrift für Krist. - Cryst. Mater.* **1900**, *25*, 471–476.

(33) Piazza, M. Forsterite Dei Proietti Dei Sabatini. *Period. di Mineral.* **1932**, *3*, 167–180.

(34) Brothers, R. N. A Penetration-Twin in Olivine. *Am. Mineral.* **1959**, *44* (100), 1086–1089.

(35) Mu, Z.; Liu, R.; Cao, Z.; Meng, G. Injected Twin Chrysolites Hosted in Late-Cenozoic Alkaline-Basalts in China. *Dizhi Kexue* **1994**, *29* (4), 399–403.

(36) Gaines, R. V. *Dana's New Mineralogy: The System of Mineralogy of James Dwight Dana and*

Edward Salisbury Dana; 8th Edition; Skinner, H. C. W., Foord, E. E., Mason, B., Rosenzweig, A., King, V. T., Eds.; John Wiley & Sons: New York, NY, United States, 1997.

(37) Schmetzer, K. *Russian Alexandrites*; Schweizerbart Science Publishers: Stuttgart, Germany, 2010.

(38) Hu, W.; Liu, S.; Zhang, Y.; Xiang, J.; Wen, F.; Xu, B.; He, J.; Yu, D.; Tian, Y.; Liu, Z. Annealing-Induced {011}-Specific Cyclic Twins in Tetragonal Zirconia Nanoparticles. *J. Phys. Chem. C* **2012**, *116* (39), 21052–21058.

(39) Morris Wang, Y.; Sansoz, F.; Lagrange, T.; Ott, R. T.; Marian, J.; Barbee, T. W.; Hamza, A. V. Defective Twin Boundaries in Nanotwinned Metals. *Nat. Mater.* **2013**, *12* (8), 697–702.

(40) Chen, C. C.; Zhu, C.; White, E. R.; Chiu, C. Y.; Scott, M. C.; Regan, B. C.; Marks, L. D.; Huang, Y.; Miao, J. Three-Dimensional Imaging of Dislocations in a Nanoparticle at Atomic Resolution. *Nature* **2013**, *496* (7443), 74–77.

(41) Momma, K.; Izumi, F. VESTA 3 for Three-Dimensional Visualization of Crystal, Volumetric and Morphology Data. *J. Appl. Crystallogr.* **2011**, *44* (6), 1272–1276.

CHAPTER 4

SUMMARY OF THIS WORK AND OUTLOOK FOR FUTURE RESEARCH[‡]

1. Summary

In the current technological age, the need for renewable energy sources continues to grow. Capturing, storing, and harnessing solar energy presents a promising route to this aim, and the work described here was inspired by the potential for iron germanium sulfide (Fe_2GeS_4) to act as a photovoltaic absorber layer in solar cells[1]. Assessing the performance of the material is a focus of future work and has been made possible by the careful formulation and understanding of this reliable, direct synthesis of phase-pure Fe_2GeS_4 NPs. In Chapter 1, we outlined the literature of amide-assisted NP syntheses that employ either metal silylamide precursors or metal salts and alkali amide Brønsted bases. The amide additive generally increases the reactivity of precursor monomers providing control over NP nucleation versus growth. This has been demonstrated for a variety of materials with tunability of the following aspects: smaller, more monodisperse NPs instead of large particles, metastable instead of more thermodynamically-stable phases, and phase-pure ternary compounds without binary impurities. The role of the base has been especially important for balancing the reactivity of multiple metal species of varied valency. In a parallel but more puzzling area of NP synthesis, HMDS has been used as an additive to achieve similar end products without a clear understanding of its role. We have connected the HMDS-based and the amide-assisted NP synthetic literature in Chapter 1, and in this chapter we will outline next steps to further these advances.

Chapter 2 detailed our redesign of an HMDS-based Fe_2GeS_4 NP synthesis in which we exchanged HMDS for its conjugate base, $LiN(SiMe_3)_2$ and the highly reactive hexamethyldisilathiane (TMS_2S) for elemental S powder.[2] We hypothesized the formation of the ternary was possible due to the in situ evolution of Brønsted base species; thus, we aimed to add $LiN(SiMe_3)_2$ directly. This eliminated the convoluted roles

[‡] Rebecca C. Miller carried out the synthetic work, characterization, analysis, and wrote the chapter. The data and discussion regarding the $Fe_2GeS_{4-x}Se_x$ solid solution are being prepared in a manuscript for submission to Chemical Communications. Amy L. Prieto provided guidance and editing advice.

of TMS_2S; it had provided both $[SiMe_3]^-$ species and the S monomers. This development avoided the $Fe_{1-x}S$ impurity of the HMDS-based reaction and reduced the growth time from 24 h to 10 min. Finally, we characterized the S and base injection solution and speculated on intermediates and chemical reactions taking place. This synthesis is a viable a starting point for carrying out thin film production, electron transport property measurements, and photovoltaic device engineering.

In Chapter 3, we examined the interesting star morphology of the NPs and determined that the NP products exhibited crystal twinning. We identified the underlying geometric basis for twinning of olivine compounds with hexagonal pseudosymmetry and predicted other reported olivine compounds that should have high tendencies for crystal twinning. This NP synthesis presents an interesting system for both understanding the fundamentals of crystal twinning and for understanding the effect of twinning on the properties of Fe_2GeS_4. The amide-assisted approach allows control to explore the effects of synthetic parameters on the twinning and morphology of the particles. Because this synthesis provides a massive population of twinned NPs, it exists as a valuable resource for statistical analysis on crystal twinning. Here, we discuss future possibilities for designing analogous non-twinned Fe_2GeS_4 NPs, which would be of use to directly compare properties. Further, we present preliminary results from synthetic exploration to adapt the Fe_2GeS_4 reaction to other M_2GeQ_4 (M = transition metal, Q = chalcogen) compounds.

2. Understanding Amide-Assisted Metal Chalcogenide NP Syntheses

As mentioned in Chapter 1, we propose the development and thorough characterization of SnS NPs as a model system to compare the roles of $Sn[N(SiMe_3)_2]_2$, $LiN(SiMe_3)_2$, and HMDS. The Kovalenko group has thoroughly examined Sn speciation and the reaction mechanisms for unary Sn^0 NPs from both metal and alkali amide precursors. However, no direct characterization has been done to understand the interaction of Sn monomers and HMDS. Kobylinski et al. provided a proposed reaction mechanism.[3] A number of Sn chalcogenide nanostructure syntheses have been reported, but their synthetic differences preclude their direct comparison due to the vital roles each of the different solvent species play. However, these would stand as valuable resources to design equivalent syntheses for SnS from Sn silylamide, alkali silylamide, and HMDS.

The second research aim would be to characterize the Sn speciation via ^{119}Sn NMR and understand how the presence of the chalcogen species might alter the acid-base equilibria. Work by the Kovalenko group identified the ability for Brønsted bases to deprotonate the alkylamine solvent which then coordinated Sn, forming reactive monomers that could be reduced to Sn^0. Understanding of the chalcogen role might benefit from development of equivalent SnSe NP syntheses for the use of ^{77}Se NMR spectroscopy. In order to probe the possibility for monomeric versus oligomeric amide species, ^{1}H DOSY NMR could be used to extract diffusion coefficients and calculate hydrodynamic radii. If the reaction systems can be adapted to capillaries, NMR spectra collected while heating the samples for in situ detection of intermediates could be achieved via an active collaboration that exists between the Prieto Group and the Yu Group (Florida State University). Complementary techniques would be used to probe for the existence of hypothesized intermediates including gas chromatography-mass spectrometry (GC-MS), which has been used to identify byproducts that gave insight into the necessary reaction mechanisms for their formation. Other complementary methods may include infrared, UV-Vis, and Raman spectroscopy, ^{1}H and ^{13}C NMR, and modeling to predict reasonable intermediate complexes. Further, simple control reactions making concentrated precursor solutions and attempting to isolate single crystals of intermediate complexes could be carried out. The overall aim would be to be to piece together dominant reaction mechanisms to improve synthetic control of NP products.

3. Amide-Assisted Synthesis of Non-Twinned Fe_2GeS_4 NPs

In earlier chapters, we focused on the production of phase-pure Fe_2GeS_4 NPs (Ch 2) and the ability to form coalesced and more crystalline twinned NPs (Ch 3). In order to understand the effect of twinning on material properties, it would be necessary to develop an analogous reaction for non-twinned Fe_2GeS_4 NPs. The challenge would be to alter the reaction conditions for this aim without forming impurity phases or altering the reaction system too significantly. Non-twinned NPs of relatively comparable size and surface chemistry would be an ideal product because NPs can show size- and surface-dependent properties. Some systematic exploration of the effects that various parameters have on the NP products would be useful

simply due to the novel nature of this amide-assisted approach for Fe_2GeS_4. Here, we outline ideas for this end regarding the strength of the Brønsted base and the role of the solvent system.

Preliminary comparisons between twinned and non-twinned Fe_2GeS_4 NPs could be made using the original HMDS-based Fe_2GeS_4 synthesis for non-twinned particles. However, these particles were formed in a different solvent system and required a 24 h growth to dissolve the $Fe_{1-x}S$ impurity phase. If small concentrations of the impurity phase were not all eliminated, their presence could affect sensitive property measurements. The presence of crystal twinning tends to increase with higher concentrations of monomers.[4] As reported in Chapter 3, carrying out the $LiN(SiMe_3)_2$-based reaction at lower precursor concentrations resulted in a decreased portion of twinned NPs, but they were still the majority product (62% twinned and 38% non-twinned NPs). At concentrations much lower than 25%, the yield is highly compromised, and the risk of forming impurity phases increases.

Simply using a lower concentration of $LiN(SiMe_3)_2$ relative to all other reaction components resulted in both Fe_2GeS_4 and $Fe_{1-x}S$, as discussed in Chapter 2. A lithium amide base of weaker strength than $LiN(SiMe_3)_2$ might provide lower reactivity of the resultant monomers; however, $LiN(SiMe_3)_2$ is one of the weakest common amide bases. One can compare the pK_a values of the conjugate acids, and a higher pK_a value indicates a stronger base. The pK_a values for amines generally span ~26-38, and the value for HMDS is ~26 in THF.[5] Other common Brønsted bases for amide-assisted NP syntheses are lithium diisopropylamide (LDA, pK_a ~ 36-37) and *n*-BuLi (butane pK_a ~ 50).[5] Weaker nitrogen-containing bases tend to be amines or amidines instead of amides. Garrido et al. reported the pK_a values for the conjugate acids of an array of amines, anilines, pyridines, pyrrolidines, and iminophosphoranes in THF which spanned values from 7-22.[6] These compounds may not be sufficiently basic to deprotonate OLA (the pK_a of OLA is unknown). However, the broad idea of amide-assisted NP syntheses is to produce M-N bonded intermediates with higher reactivities than monomers produced from solvating the metal salts in the solvent system alone. Thus, some of these N-containing compounds may be of interest as NP synthetic additives with the potential to form viable M-N intermediates.

In Chapter 2, we preliminarily adapted the Fe_2GeS_4 NP synthesis to use LiH instead of $LiN(SiMe_3)_2$. This was carried out to indirectly test the alternative hypothesis that the reaction intermediates were metal silylamides instead of metal oleylamides. The use of LiH would disallow the formation of metal-silylamide intermediates, and we thought metal hydride intermediates would be unlikely due to the volatility of H_2. When the same molar amount of LiH as $LiN(SiMe_3)_2$ was used, only $Fe_{1-x}S$ formed (Fig. S2.24). In the $LiN(SiMe_3)_2$-based system, just lower than optimal concentrations of base gave $Fe_{1-x}S$ and Fe_2GeS_4 while just higher concentrations of base produced FeGe impurities. Thus, we hypothesized that we might observe the ternary phase if we increased LiH concentration. Indeed, upon doubling the LiH amount, both Fe_2GeS_4 and $Fe_{1-x}S$ NPs formed (Fig. S2.24). Fig. 4.1 shows the resultant NPs, which have the same twinned, star morphology as the Fe_2GeS_4 NPs. Although LiH did not provide access to non-twinned NPs, this adaptation shows that our Fe_2GeS_4 NP synthesis stands as a good launching point for exploring the use other Brønsted bases in ternary NP syntheses.

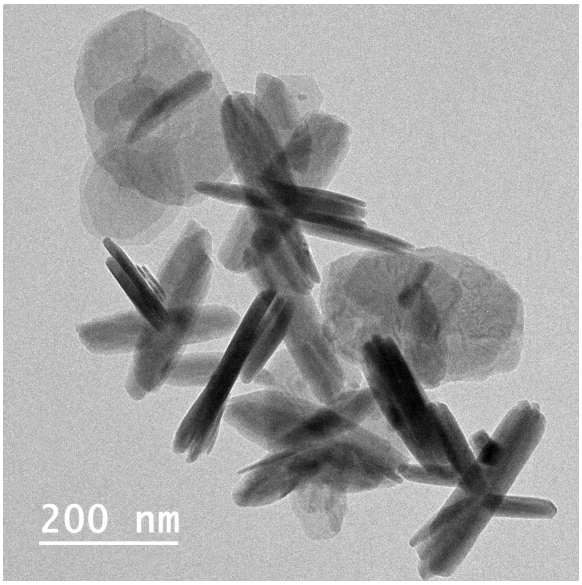

Fig. 4.1. TEM image of Fe_2GeS_4 NPs formed by substituting LiH for $LiN(SiMe_3)_2$ as the Brønsted base. The twinned, star morphology was still observed.

An alternate idea for hindering twinning in Fe_2GeS_4 NPs might be achieved by decreasing the concentration of active monomers via diluting the alkylamine in the solvent system. If metal oleylamides are the primary reactive species for NP formation, then substituting a long alkyl chain compound for OLA

as the primary solvent and optimizing for a sufficient amount of alkylamine might provide the adequate monomer species with a different solvation sphere and potentially lower reactivity. Further, if alkylamines act to stabilize twinned NP nuclei, substituting in a less coordinating solvent might decrease the number of twinned NP nuclei that remain and grow into full NPs.

Instead of solely focusing on the reactivity of the cations, the reactivity of the anions might be decreased by introducing a trialkylphosphine such as trioctylphosphine (TOP) to the solvent system. These phosphine compounds are known to react with chalcogens (Q) to form compounds with P=Q bonds. Of the following chalcogens, S, Se, and Te, phosphorus forms the strongest bond with S because it is small and has the highest electronegativity.[7] Empirically, we have observed a decreased S reactivity with the presence of TOP. In the HMDS-based Fe_2GeS_4 reaction, when TOP=S was substituted for TMS_2S as the S precursor and the reaction was otherwise carried out identically, we did not observe any solid products. Therefore, the P=S bond inhibited even the formation of iron sulfide NPs which were observed upon the use of S powder. In the $LiN(SiMe_3)_2$-based Fe_2GeS_4 reaction, substitution of OLA with TOP in both the metals and S solutions resulted in the formation of Fe_3Ge_2. While TOP=S may have too strong of a bond for S reactivity in this system, Ruberu et al. reported that the P=S bond could be weakened via using phosphorus compounds with more electron-withdrawing R groups.[8] Tribuylphosphine, Diphenylpropylphosphine, and triphenylphosphite would all be viable options for P=S precursors of higher reactivity relative to TOP=S. If these precursors show lower reactivity relative to S powder, they might access non-twinned Fe_2GeS_4 NPs. These experiments also provide a chance to broaden the understanding of amide-assisted Fe_2GeS_4 reactions beyond the scope of $LiN(SiMe_3)_2$ as the base and OLA as the solvent.

4. Property Measurements on Fe_2GeS_4 NPs

When adequate non-twinned Fe_2GeS_4 NPs can be formed, it would be interesting to investigate the role twinning may play on the material properties. The distorted coordination of atoms at the twin boundary can alter the properties that arise due to the extended structure of solids. The band structure of compounds can transform due to variations in stoichiometry or strain at the boundaries,[9,10] and regular spacing between twin planes in nanowire twin superlattices have been predicted to induce direct band gaps in nominally

indirect gap semiconductors.[11–13] Xu et al. compared photoluminescence in ZnSe nanowires with either transverse or longitudinal twinning.[14] The observed blue shift in photoluminescence emission for the sample with transverse twinning was suggested to arise due to quantum confinement because the period between twin planes was on the order of the Bohr exciton radius for the compound. Thus, even if the dimensions of individual NPs are greater than the Bohr exciton radius of a material, twin boundaries within it could induce the quantum confinement effect. Iron germanium sulfide has been proposed to be useful for both photovoltaic and thermoelectric conversion applications, but the material's Bohr exciton radius is not known.[1,15] Both time- and spatially-resolved spectroscopy techniques could be useful for understanding the effect this type of twinning has on light absorption and carrier transport. Further, twinning has been proposed as a viable strategy to enhance phonon scattering;[16–20] thus, thermal conductivity measurements of the Fe_2GeS_4 NPs would also be informative.

Because passivation of NP surfaces can influence the measured properties of NP suspensions and thin films, some of these characterization techniques and application evaluations would require the development of ligand exchange and thin film production processes. Many reports have identified the effectiveness of various ligand molecules,[21] and our group's work on this optimization for Cu_2ZnSnS_4 NPs provides a basis for processing Fe_2GeS_4 NPs.[22,23] Even further along, carrying out device engineering for testing small thin film solar cells with Fe_2GeS_4 as the absorber layer could be targeted but would require optimal band alignment with an appropriate n-type material.

5. Development of Other M_2GeQ_4 Olivine Compounds

The Fe_2GeS_4 NP synthesis also provides a good starting point for developing syntheses of other Ge-containing olivine compounds. Solid solutions of photovoltaic absorber compounds, such as $Cu_2ZnSnS_{4-x}Se_x$,[24,25] have been targeted for band gap tuning, and $Fe_2GeS_{4-x}Se_x$ could provide altered optoelectronic properties. To our knowledge, the transport properties of Fe_2GeSe_4 have yet to be reported. Gudelli et al. published a computational study and predicted that Fe_2GeSe_4 has a smaller band gap than Fe_2GeS_4 but that their band structures are similar.[15] Additionally, both compounds were suggested to be promising for thermoelectric applications. The lattice parameters of Fe_2GeSe_4 also show high hexagonal

pseudosymmetry at 0.2% off from the $a_{Pnma}/b_{Pnma} = \sqrt{3}$ ratio, which is the same percentage as for Fe_2GeS_4. We aimed to test whether twinned NPs would form for an olivine of altered composition relative to Fe_2GeS_4, and this end member and solid solution compounds were a promising initial target.

We carried out preliminary exploration in the formation of Fe_2GeSe_4 and $Fe_2GeS_{3.2}Se_{0.8}$ (20 mol% Se) by replacing S powder with Se powder. The main hindrance to adaptation of the NP reaction to the selenide arises in the lower solubility of Se in OLA compared to S. Upon carrying out an analogous version of the 0.16 mmol scale Fe_2GeS_4 NP synthesis reported in Chapter 2,[2] Fe_2GeSe_4 NPs formed alongside FeSe, GeSe, and unreacted Se. Interestingly, when the GeI_4 excess was lowered from 1.5 to 1.25 times the stoichiometric amount, a greater portion of Fe_2GeSe_4 formed relative to the impurity phases. The PXRD pattern for this reaction is given in Fig. 4.2. Unreacted Se particles were detected by STEM EDS elemental maps (Fig. 4.3).

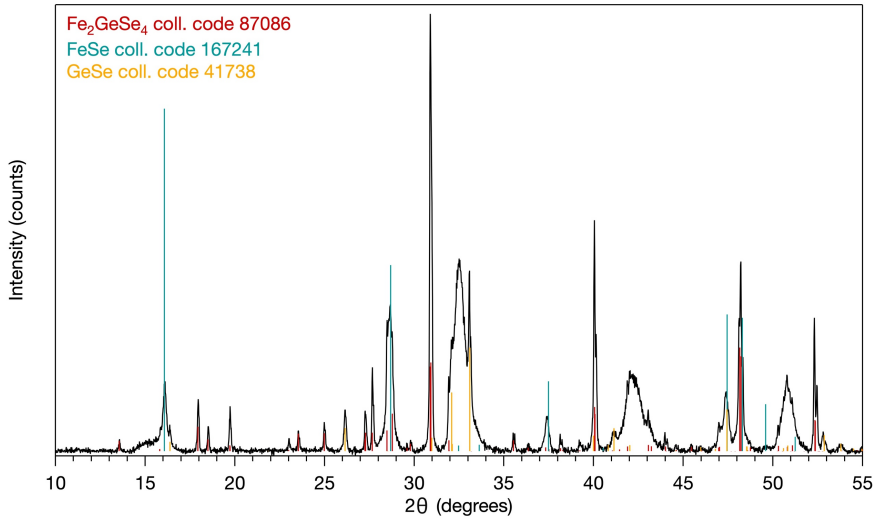

Fig. 4.2. PXRD pattern of the products from the reaction for which Se was substituted for S and a lower excess of Ge was used (1.25 times the stoichiometric amount). The phases Fe_2GeSe_4, FeSe, and GeSe were detected.

We hypothesized that sonication was not sufficient for dissolution of Se; however, a reaction carried out with controlled heating of the Se, $LiN(SiMe_3)_2$, and OLA solution at 120 ˚C did not provide phase-pure Fe_2GeSe_4. Because the ternary NPs show a hexagonal morphology, it is possible that they may be twinned; however, the NP thickness was too great to detect lattice spacings and hindered the possibility to detect twinning. Future synthetic development to increase Se solubility and find the right balance between the

constituent elements may benefit from two strategies. If an increased amount of base were used, the solubility of Se in OLA may be increased. Alternatively, it would be worthwhile to explore other solvent systems. Trialkylphosphines would be useful for targeting phosphine-selenide intermediates, and 1-octadecene has been more thoroughly studied as a solvent for incorporating Se in NP syntheses.[26]

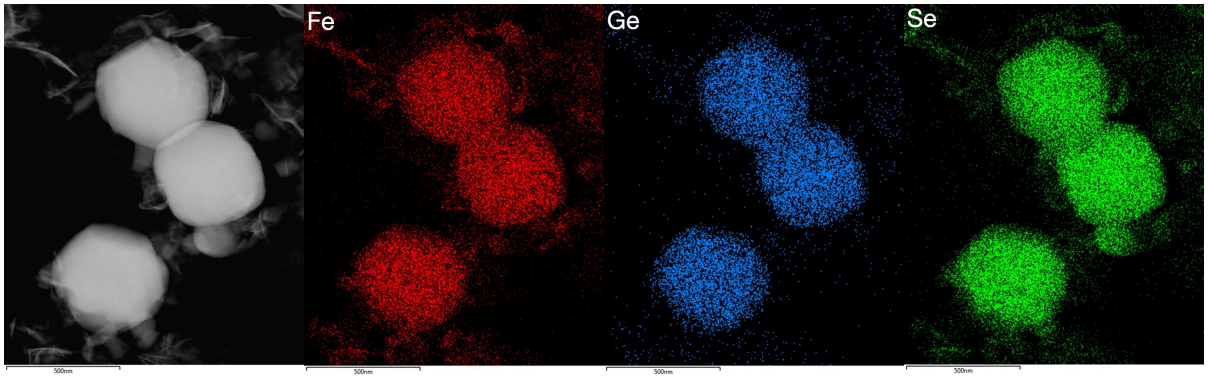

Fig. 4.3. STEM image and elemental maps of the NP products. The Fe_2GeSe_4 NPs form large particles. FeSe and Se particles are detected in the background.

We hypothesized a lower concentration of Se might dissolve to a greater extent in OLA, so we targeted the solid solution $Fe_2GeS_{4-x}Se_x$ (x = 0.8, 20 mol% Se). To our knowledge, a solid solution compound for Fe_2GeS_4 with any other element has never been reported, either as NPs or in the bulk. Indeed, we observed the formation of phase-pure $Fe_2GeS_{4-x}Se_x$ (x = 0.96, 24 mol% Se) according to PXRD (Fig. 4.4). The chalcogen occupancies from the Rietveld refinement match the composition measured for the NPs via SEM EDS (Fig. 4.5), and the refined lattice parameters follow Vegard's Law (Fig. 4.4b). Electron microscopy showed that the products contained some amorphous material that had not been sufficiently washed away during work up. Due to this, the elemental composition from SEM EDS did not reflect the exact Fe:Ge:Se ratios determined from PXRD and was rich in both Fe and Ge. The amorphous material could be examined via STEM EDS free from $Fe_2GeS_{4-x}Se_x$ NPs (Fig. 4.6). It was mostly composed of organic matter, and the chalcogen amounts were near negligible. Iron was detected, and Ge might have been present, but importantly, this meant we could compare the S:Se molar ratio from the SEM EDS analysis to complement the Rietveld refinement. Indeed, EDS gave a molar ratio of 0.76:0.24 for S:Se which agreed with the site occupancies.

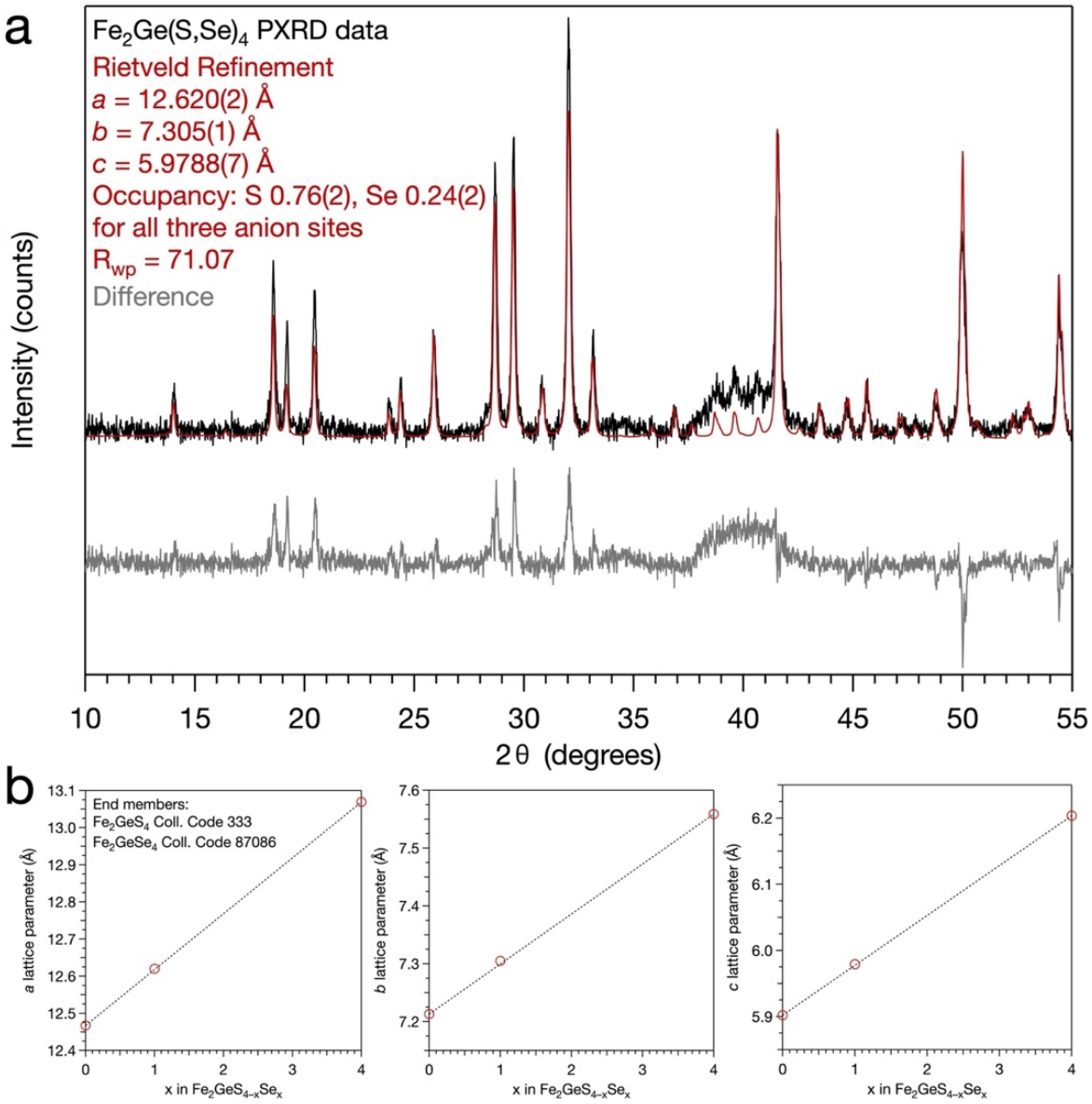

Fig. 4.4. a, PXRD pattern and Rietveld refinement of $Fe_2GeS_{4-x}Se_x$. The refined S and Se occupancies for all three anion sites were 0.76(2) and 0.24(2), respectively, which corresponds to a composition of $Fe_2GeS_{3.04}Se_{0.96}$. **b,** The refined lattice parameters are plotted as a function of Se content in $Fe_2GeS_{4-x}Se_x$, and the values follow Vegard's law.

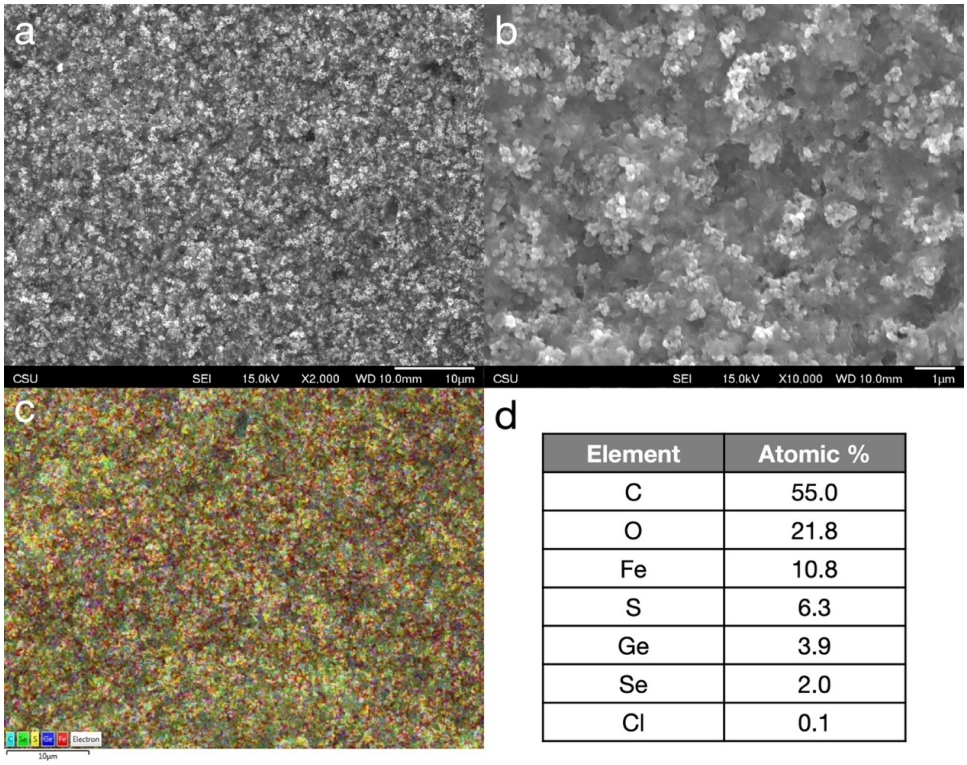

Element	Atomic %
C	55.0
O	21.8
Fe	10.8
S	6.3
Ge	3.9
Se	2.0
Cl	0.1

Fig. 4.5. a,b, SEM images of the products from the $Fe_2GeS_{4-x}Se_x$ NP reaction. **c,** SEM EDS elemental map of the products and the corresponding atomic percentages of the detected elements. **d,** The S:Se atomic ratio is 0.76:0.24, which corresponds with the site occupancy determined from the Rietveld Refinement in Fig. 4.4.

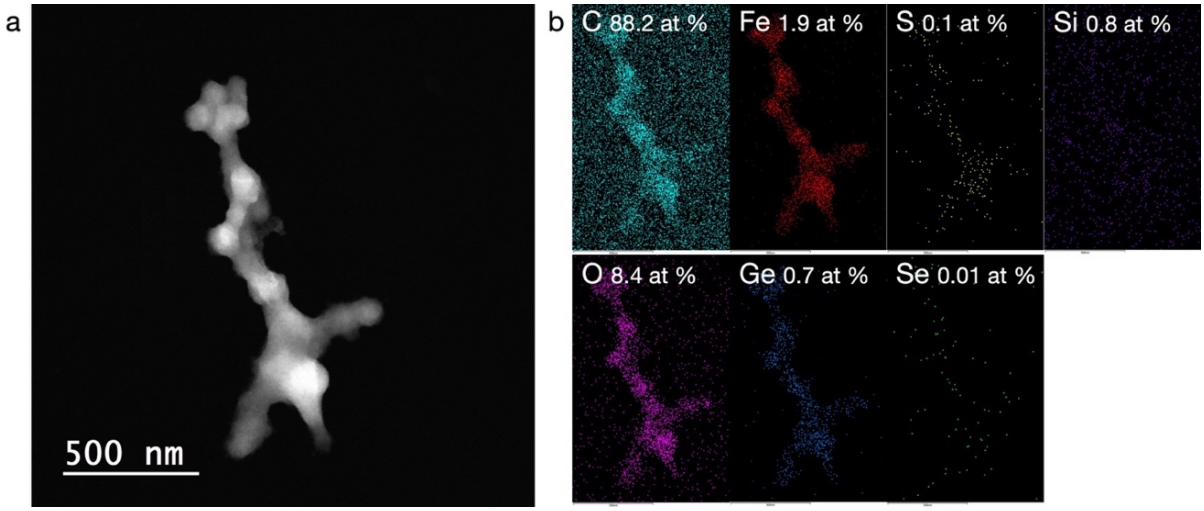

Fig. 4.6. a, STEM image of amorphous material from the $Fe_2GeS_{4-x}Se_x$ NP reaction. **b,** STEM EDS elemental maps of all of the detected elements. Because of the amorphous nature, the high carbon content, and the iron content, we speculate this solid originates from unreacted precursor and solvent molecules. The detection of silicon may be from the lithium amide base. Most importantly, the anion concentrations are extremely low. This allows us to consider the S:Se atomic ratios from the SEM EDS elemental mapping (Fig. 4.5) despite the inflated Fe and Ge concentrations relative to stoichiometric $Fe_2GeS_{4-x}Se_x$ atomic ratios.

STEM EDS maps of the NPs showed an even distribution of all four elements (Fig. 4.7), and TEM images showed the same twinning morphology as the Fe_2GeS_4 NPs (Fig. 4.8). The presence of twinning in these NPs is further supported by the SAED pattern of a particle in Fig. 4.9. It shows the summation of electron diffraction patterns predicted for both a twin domain oriented parallel to the page as well as nanoplates oriented at 60˚ angles. Reproductions of this synthesis were carried out, and low concentrations of FeGe NPs were detected. As detailed in Chapter 2, optimizing the Fe:Ge:S molar ratios aided in avoiding low concentrations of $Fe_{1-x}S$ and FeGe impurities; therefore, it would be worth attempting these reactions with a lower GeI_4 excess. These syntheses were carried out with 1.5 times the stoichiometric amount of Ge, so lowering this to ~1.25 times would be a promising initial alteration. Once a reliable synthesis is developed, possibly in conjunction with the synthetic exploration of other Brønsted bases and solvent systems as mentioned earlier, it would be interesting to characterize the optoelectronic properties of the particles. To our knowledge, the transport properties of Fe_2GeSe_4 have yet to be measured. Therefore, it would be useful to produce the bulk compound and measure the relevant properties for baseline comparison. If non-twinned solid solution NPs could also be developed, they would be of interest for examining the role of twinning as outlined earlier in the discussion on the S-end member NPs.

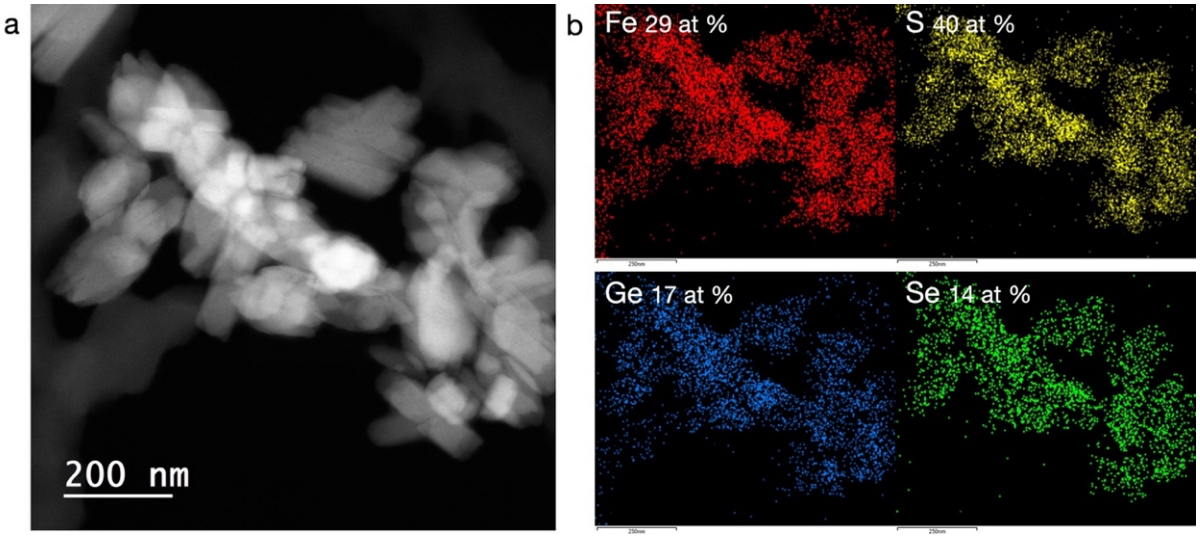

Fig. 4.7. a, STEM image of $Fe_2GeS_{4-x}Se_x$ NPs with some amorphous material in the background. **b**, STEM EDS elemental maps depict the even distribution of all four elements in the NPs. This supports the understanding that a solid solution of $Fe_2Ge(S,Se)_4$ has formed rather than separate Fe_2GeS_4 and Fe_2GeSe_4 NPs.

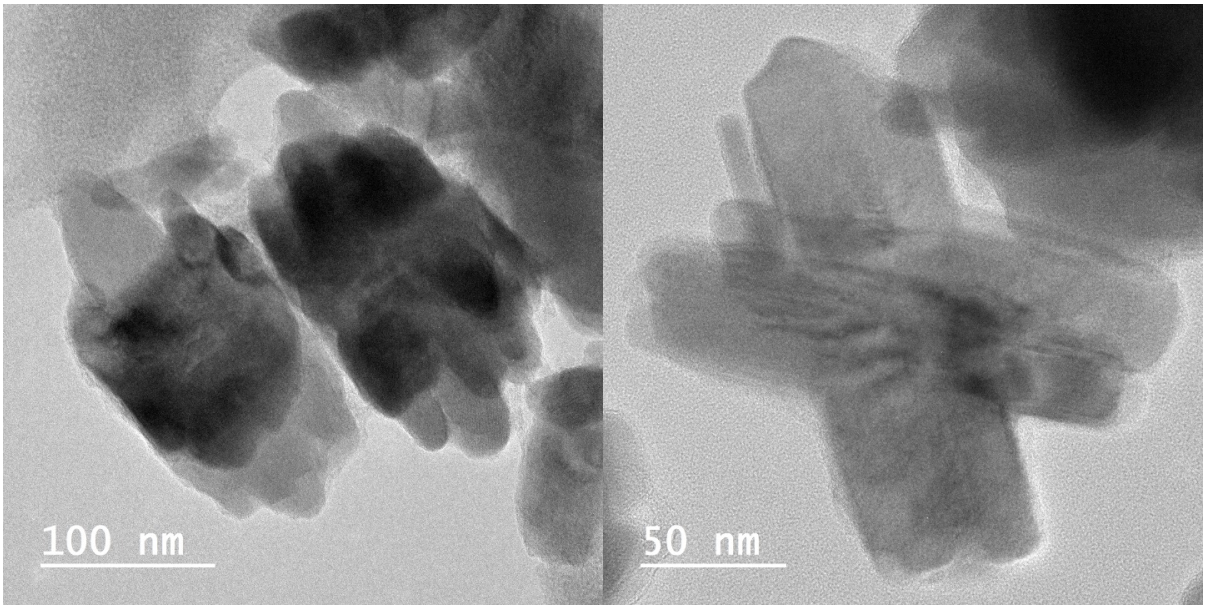

Fig. 4.8. TEM images of the $Fe_2GeS_{4-x}Se_x$ NPs depicting a similar morphology as the twinned Fe_2GeS_4 NPs from Chapter 3.

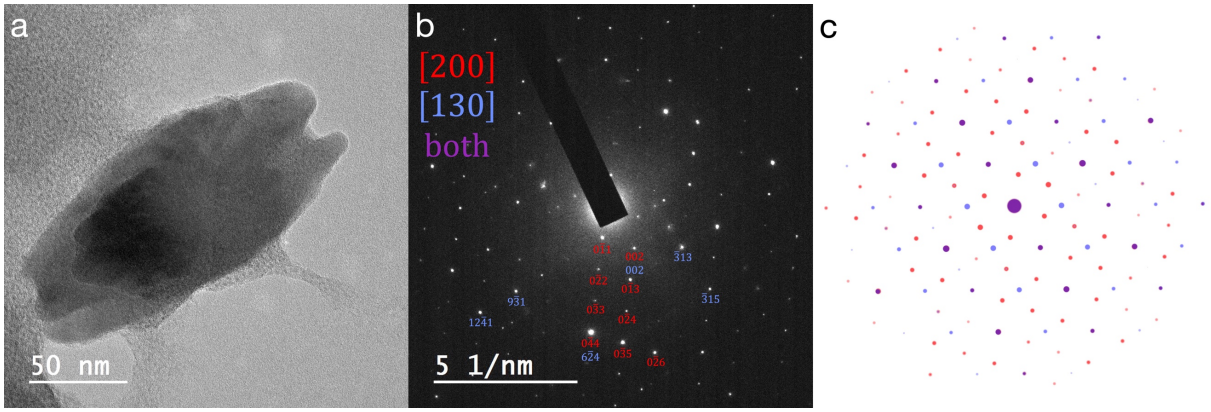

Fig. 4.9. a, TEM image of a $Fe_2GeS_{4-x}Se_x$ NP, and **b**, the corresponding SAED pattern with labeled diffraction spots from both the [200] zone axis of the nanoplates oriented parallel to the TEM grid and the [130] zone axis of the nanoplates oriented at 60˚ angles to the TEM grid. **c**, Simulated SAED patterns of the [200] and [130] zone axes in red and blue, respectively, that correspond to the measured SAED pattern.

Lastly, we targeted a solid solution of the cations, $Fe_{2-x}Mn_xGeS_4$ (x = 1.2). Hauesler et al. published a structural report on this compound and other transition metal thiogermanates.[27] Of the M_2GeS_4 olivine compounds reported in the ICSD, its lattice parameters have the next lowest percentage difference from the hexagonal ratio between a_{Pnma} and b_{Pnma} at 0.3% relative to 0.2% for Fe_2GeS_4. No other Mn-Fe-Ge-S compounds are listed in the ICSD. We adapted the 0.16 mmol scale Fe_2GeS_4 synthesis reported in Chapter 2 to use a mixture of $FeCl_2$ and Mn(II) acetate instead of only $FeCl_2$ at the molar ratio of 0.8:1.2 for Fe:Mn,

and the PXRD pattern showed a phase-pure $Fe_{2-x}Mn_xGeS_4$ solid solution (Fig. 4.10). By TEM, the NPs showed a polycrystalline nature without readily apparent crystal twinning (Fig. 4.11a). Elemental mapping by STEM EDS confirmed the even distribution of all four elements in the NPs although the atomic ratios indicated higher values for the Fe and Ge amounts than expected (Fig. 4.11b) . STEM EDS does not provide the best handle for overall composition due to the inherently small sample size, so it would be useful to pursue elemental analysis by SEM EDS. Overall, these amide-assisted reactions stand as a versatile synthetic space for exploring a variety of olivine compounds.

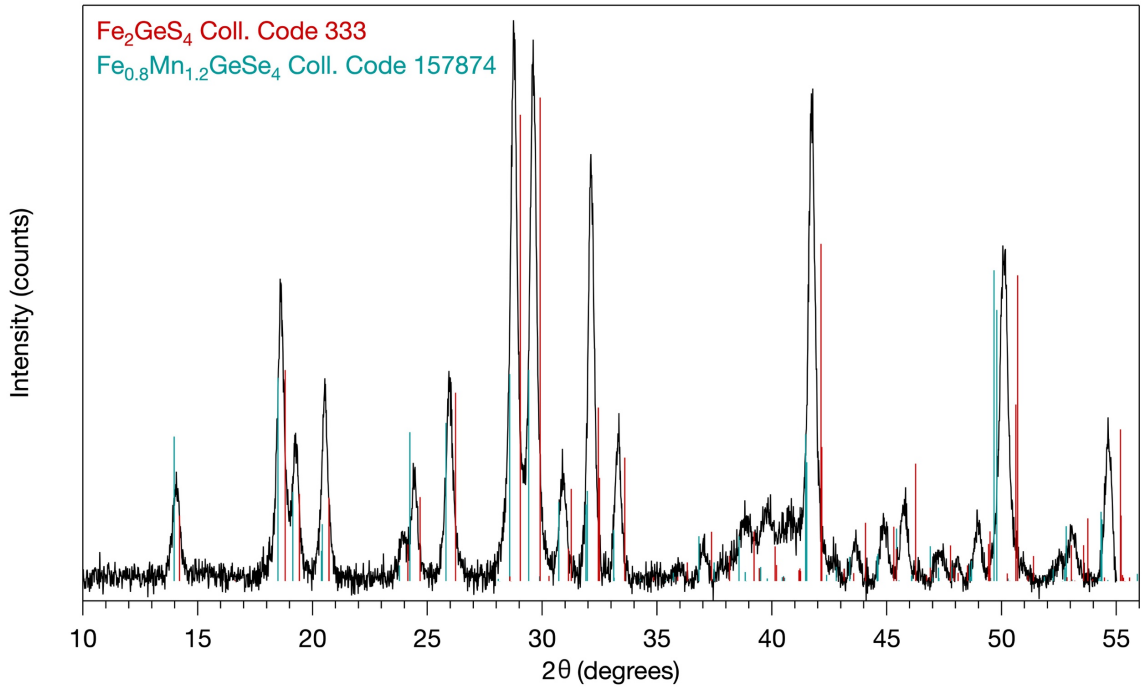

Fig. 4.10. The PXRD pattern of the products from the $Fe_{2-x}Mn_xGeS_4$ NP reaction. The reference patterns for $Fe_{0.8}Mn_{1.2}GeS_4$ and Fe_2GeS_4 were overlaid, and all of the diffraction peaks fall between the corresponding peaks. Therefore, the NPs are likely more Fe-rich than the $Fe_{0.8}Mn_{1.2}GeS_4$ composition. No other peaks for impurity phases were detected.

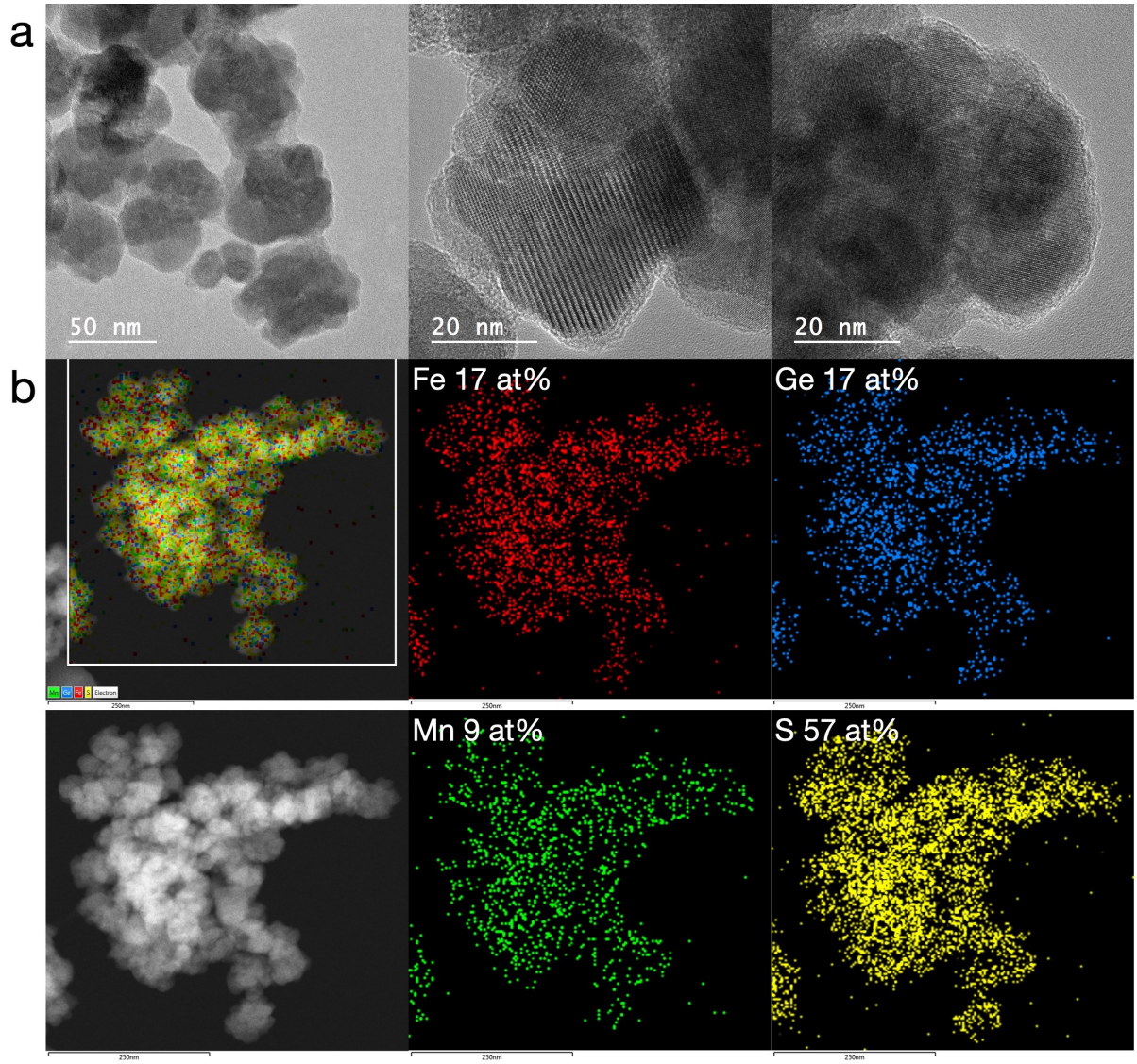

Fig. 4.11. a, TEM images of $Fe_{2-x}Mn_xGeS_4$ NPs display their polycrystalline nature. **b,** STEM EDS elemental mapping of the NPs. The elements are evenly distributed among the particles, and impurity phases were not detected.

6. Consideration of Twinning in Battery Cathode Olivine $LiFePO_4$

One significant material with a high degree of hexagonal pseudosymmetry for which twinning may be interesting is lithium iron phosphate, a highly studied battery cathode material.[28,29] Many studies on lithium iron phosphates focus on the material's low electronic conductivity[30,31] and its anisotropic ionic conductivity with favorable Li^+ diffusion along the $[010]_{Pnma}$ channels (Fig. 4.12).[31–35] There exists much exploration on the possible reaction mechanism for lithium (de)intercalation,[32,35,36] the identification of a possible solid solution or superstructure of partially (de)lithiated iron phosphate,[33,34,37–40] and studies linking

particle morphology with battery cycling performance.[34,39–42] Thus, the material's potential to form twin boundaries may be crucial for understanding and improving its performance as a battery cathode. If twin boundaries form upon synthesis or battery cycling, it would be interesting to understand how these defects affect the electronic and ionic conductivity of the material. Twin boundaries might exist as barriers for Li^+ ion diffusion, hindering cycling performance. However, the tendency of a material to form twin defects could potentially aid in the mechanical aspects of battery cycling. Due to the volume expansion and contraction involved, battery electrodes often face degradation by pulverization with a loss of electronic contact to active material. If stress on a crystalline battery electrode might induce the formation of twinned domains rather than pulverization, longer battery lifetimes might be more accessible. All of the $Li_{1-x}Fe_xPO_4$ compounds from the ICSD are plotted in Fig. 4.13 according to the degree of hexagonal pseudosymmetry of the reported lattice parameters.

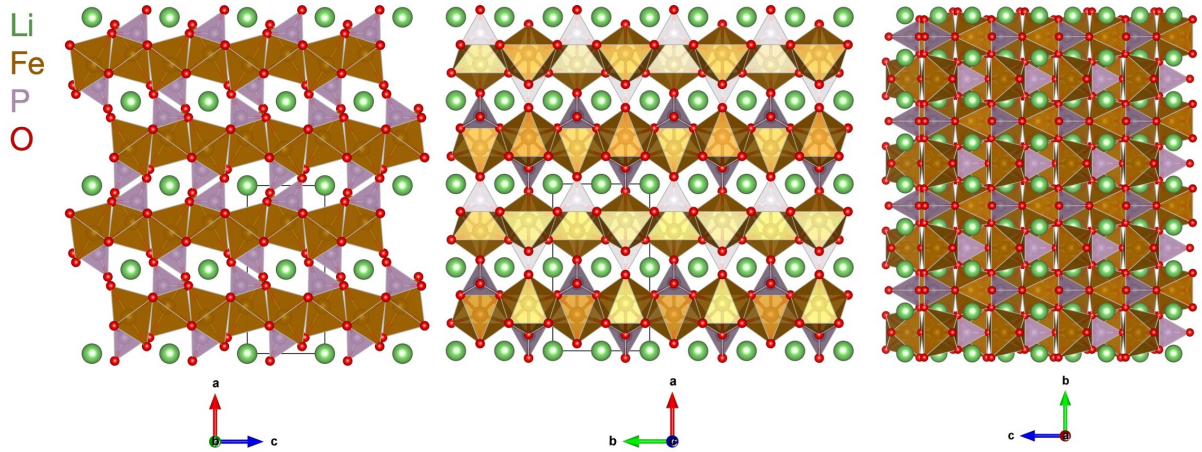

Fig. 4.12. Crystal structure of $LiFePO_4$ viewed along the [010], [001], and [100] crystallographic directions. The anisotropy of the crystal structures provides favorable Li^+ ion diffusion along these directions in the trend: [010] > [001] > [100].

In terms of lithium iron phosphate particle morphology, typically plates with large *ac* faces and short *b* dimensions are identified as favorable, granting many access points to [010] channels and requiring short diffusion lengths. If twinned lithium iron phosphate particles could be formed, they would exhibit an interesting morphology to study for Li^+ (de)intercalation. Because each of the twin domains grow in the [010] direction, the outer surface of the particles could present access to [010] channels on all sides except

for the direction along the core of the particle, which would have (001) faces. This may be one of many potential strategies for engineering the microstructure and morphology of olivine materials to enhance functionality.

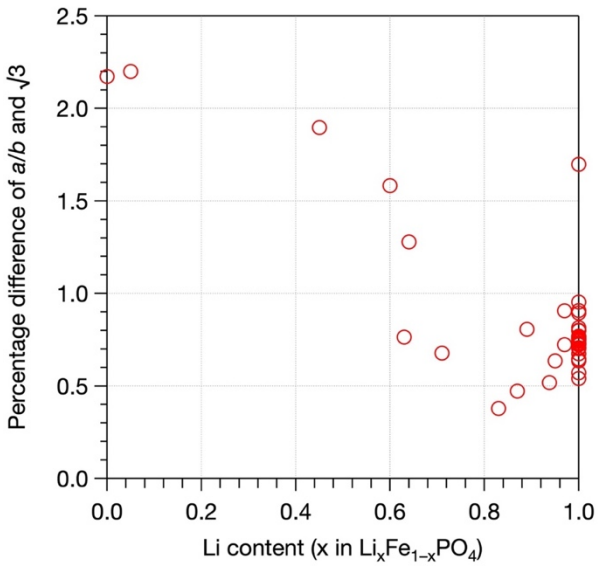

Fig. 4.13. The difference of the a_{Pnma}/b_{Pnma} ratio from $\sqrt{3}$ for compounds of the $Li_xFe_{1-x}PO_4$ crystal structure listed in the ICSD plotted as a function of the lithium concentration. The lithiated $LiFePO_4$ compound appears to have a higher hexagonal pseudosymmetry relative to the partially or fully delithiated $Li_xFe_{1-x}PO_4$. Few compounds exist at intermediate compositions; whether or not a solid solution between the two end compounds exists is speculated in the literature.

7. Conclusions

This work has aimed to understand the intricacies of NP synthesis and develop synthetic control over interesting NP compositions and morphologies. Based on an understanding of the possibly multifold roles that precursors may hold, a complex HMDS-based Fe_2GeS_4 NP synthesis was redesigned to directly form phase-pure particles via an amide-assisted approach. The unique star-shape morphology was identified as crystal twinning stemming from the hexagonal pseudosymmetry of the olivine crystal structure. This synthesis provides twinning in 98% of the particles and stands as an interesting system for understanding the fundamentals and synthetic control of crystal twinning as well as the effect twinning may have on the Fe_2GeS_4 material properties.

Because of the possibility for olivine compounds with high hexagonal pseudosymmetry to form twins, we ranked all of the olivine compounds listed in the ICSD. This highlighted the possibility to form

twins in the Se-analog, Fe_2GeSe_4, and we presented preliminary data on the formation of these particles. Further, we formed the solid solution, $Fe_2GeS_{4-x}Se_x$ (x = 0.96, 24 mol% Se), and characterized the same form of crystal twinning in these NPs. A solid solution of the cations, $Fe_{2-x}Mn_xGeS_4$, was formed although these particles appeared to be polycrystalline rather than twinned. Lastly, we discuss the possible ramifications of twinning for a commonly studied battery cathode olivine material, $LiFePO_4$.

This work stands as an interesting platform for continued advances in the synthesis and application of olivine compounds. Careful consideration of the potentially multifold roles of each precursor in NP syntheses can lead to considerable synthetic control over the products. Identifying intermediate species and reaction mechanisms accelerate scientists' abilities to adapt synthetic strategies to new compounds and nanostructured architectures. These routes have allowed the discovery of structure-, size-, morphology-, and microstructure-property relationships. Understanding the formation and effects of semiconductor defects (twinned or otherwise) is vital for their production and use. Therefore, the synthetic and microstructural understanding gained for this system stands as a vital step in advancing the fields of inorganic NP synthesis and energy conversion and storage.

REFERENCES

(1) Yu, L.; Lany, S.; Kykyneshi, R.; Jieratum, V.; Ravichandran, R.; Pelatt, B.; Altschul, E.; Platt, H. A. S.; Wager, J. F.; Keszler, D. A.; Zunger, A. Iron Chalcogenide Photovoltaic Absorbers. *Adv. Energy Mater.* **2011**, *1* (5), 748–753.

(2) Miller, R. C.; Neilson, J. R.; Prieto, A. L. Amide-Assisted Synthesis of Iron Germanium Sulfide (Fe2GeS4) Nanostars: The Effect of $LiN(SiMe_3)_2$ on Precursor Reactivity for Favoring Nanoparticle Nucleation or Growth. *J. Am. Chem. Soc.* **2020**, https://doi.org/10.1021/jacs.0c00260.

(3) Kobylinski, M. M.; Ruhmlieb, C.; Kornowski, A.; Mews, A. Hexagonally Shaped Two-Dimensional Tin(II)Sulfide Nanosheets: Growth Model and Controlled Structure Formation. *J. Phys. Chem. C* **2018**, *122* (10), 5784–5795.

(4) Buerger, M. J. The Genesis of Twin Crystals. *J. Mineral. Soc. Am.* **1945**, *30*, 469–482.

(5) He, M.; Protesescu, L.; Caputo, R.; Krumeich, F.; Kovalenko, M. V. A General Synthesis Strategy for Monodisperse Metallic and Metalloid Nanoparticles (In, Ga, Bi, Sb, Zn, Cu, Sn, and Their Alloys) via in Situ Formed Metal Long-Chain Amides. *Chem. Mater.* **2015**, *27* (2), 635–647.

(6) Garrido, G.; Koort, E.; Ràfols, C.; Bosch, E.; Rodima, T.; Leito, I.; Rosés, M. Acid-Base Equilibria in Nonpolar Media. Absolute pK_a Scale of Bases in Tetrahydrofuran. *J. Org. Chem.* **2006**, *71* (24), 9062–9067.

(7) Lee, J. M.; Miller, R. C.; Moloney, L. J.; Prieto, A. L. The Development of Strategies for Nanoparticle Synthesis: Considerations for Deepening Understanding of Inherently Complex Systems. *J. Solid State Chem.* **2019**, *273*, 243–286.

(8) Ruberu, T. P. A.; Albright, H. R.; Callis, B.; Ward, B.; Cisneros, J.; Fan, H. J.; Vela, J. Molecular Control of the Nanoscale : Effect of Phosphine-Chalcogenide Reactivity on CdS-CdSe Nanocrystal Composition and Morphology. *ACS Nano* **2012**, *6* (6), 5348–5359.

(9) van der Zande, A. M.; Huang, P. Y.; Chenet, D. A.; Berkelbach, T. C.; You, Y.; Lee, G. H.; Heinz, T. F.; Reichman, D. R.; Muller, D. A.; Hone, J. C. Grains and Grain Boundaries in Highly Crystalline Monolayer Molybdenum Disulphide. *Nat. Mater.* **2013**, *12* (6), 554–561.

(10) Moriwake, H.; Kuwabara, A.; Fisher, C. A. J.; Huang, R.; Hitosugi, T.; Ikuhara, Y. H.; Oki, H.; Ikuhara, Y. First-Principles Calculations of Lithium-Ion Migration at a Coherent Grain Boundary in a Cathode Material, $LiCoO_2$. *Adv. Mater.* **2013**, *25* (4), 618–622.

(11) Ikonić, Z.; Srivastava, G. P.; Inkson, J. C. Electronic Properties of Twin Boundaries and Twinning Superlattices in Diamond-Type and Zinc-Blende-Type Semiconductors. *Phys. Rev. B* **1993**, *48* (23), 17181–17193.

(12) Ikonic, Z.; Srivastava, G. P.; Inkson, J. C. Optical Properties of Twinning Superlattices in Diamond-Type and Zinc-Blende-Type Semiconductors. *Phys. Rev. B* **1995**, *52* (19), 14078–14085.

(13) Algra, R. E.; Verheijen, M. A.; Borgström, M. T.; Feiner, L. F.; Immink, G.; Van Enckevort, W. J. P.; Vlieg, E.; Bakkers, E. P. A. M. Twinning Superlattices in Indium Phosphide Nanowires. *Nature* **2008**, *456* (7220), 369–372.

(14) Xu, J.; Wang, C.; Wu, B.; Xu, X.; Chen, X.; Oh, H.; Baek, H.; Yi, G. C. Twinning Effect on Photoluminescence Spectra of ZnSe Nanowires. *J. Appl. Phys.* **2014**, *116* (17).

(15) Gudelli, V. K.; Kanchana, V.; Vaitheeswaran, G. Predicted Thermoelectric Properties of Olivine-Type Fe_2GeCh_4 (Ch = S, Se and Te). *J. Phys. Condens. Matter* **2016**, *28* (2), 025502.

(16) Ibáñez, M.; Zamani, R.; Li, W.; Cadavid, D.; Gorsse, S.; Katcho, N. A.; Shavel, A.; López, A. M.; Morante, J. R.; Arbiol, J.; Cabot, A. Crystallographic Control at the Nanoscale to Enhance

Functionality: Polytypic Cu_2GeSe_3 Nanoparticles as Thermoelectric Materials. *Chem. Mater.* **2012**, *24* (23), 4615–4622.

(17) Shin, H. S.; Jeon, S. G.; Yu, J.; Kim, Y. S.; Park, H. M.; Song, J. Y. Twin-Driven Thermoelectric Figure-of-Merit Enhancement of Bi_2Te_3 Nanowires. *Nanoscale* **2014**, *6* (11), 6158–6165.

(18) Jang, J. I.; Lee, J. E.; Kim, B. S.; Park, S. D.; Lee, H. S. Twinning and Its Formation Mechanism in a Binary Mg_2Si Thermoelectric Material with an Anti-Fluorite Structure. *RSC Adv.* **2017**, *7* (35), 21671–21677.

(19) Yu, Y.; He, D.-S.; Zhang, S.; Cojocaru-Mirédin, O.; Schwarz, T.; Stoffers, A.; Wang, X.-Y.; Zheng, S.; Zhu, B.; Scheu, C.; Wu, D.; He, J.-Q.; Wuttig, M.; Huang, Z.-Y.; Zu, F.-Q. Simultaneous Optimization of Electrical and Thermal Transport Properties of $Bi_{0.5}Sb_{1.5}Te_3$ Thermoelectric Alloy by Twin Boundary Engineering. *Nano Energy* **2017**, *37* (May), 203–213.

(20) Zhang, A.; Zhang, B.; Lu, W.; Xie, D.; Ou, H.; Han, X.; Dai, J.; Lu, X.; Han, G.; Wang, G.; Zhou, X. Twin Engineering in Solution-Synthesized Nonstoichiometric Cu_5FeS_4 Icosahedral Nanoparticles for Enhanced Thermoelectric Performance. *Adv. Funct. Mater.* **2018**, *28* (10), 1705117.

(21) Owen, J. The Coordination Chemistry of Nanocrystal Surfaces. *Science* **2015**, *347* (6222), 615–616.

(22) Riha, S. C.; Fredrick, S. J.; Sambur, J. B.; Liu, Y.; Prieto, A. L.; Bruce, A.; Parkinson, B. A. Photoelectrochemical Characterization of Nanocrystalline Thin-Film Cu_2ZnSnS_4 Photocathodes. *ACS Appl. Mater. Interfaces* **2011**, *3* (1), 58–66.

(23) Korala, L.; Braun, M. B.; Kephart, J. M.; Tregillus, Z.; Prieto, A. L. Ligand-Exchanged CZTS Nanocrystal Thin Films: Does Nanocrystal Surface Passivation Effectively Improve Photovoltaic Performance? *Chem. Mater.* **2017**, *29* (16), 6621–6629.

(24) Riha, S. C.; Parkinson, B. A.; Prieto, A. L. Compositionally Tunable $Cu_2ZnSn(S_{1-x}Se_x)_4$ Nanocrystals: Probing the Effect of Se-Inclusion in Mixed Chalcogenide Thin Films. *J. Am. Chem. Soc.* **2011**, *133* (39), 15272–15275.

(25) Braun, M. B.; Korala, L.; Kephart, J. M.; Prieto, A. L. Synthetic Control of Quinary Nanocrystals of a Photovoltaic Material: The Clear Role of Chalcogen Ratio on Light Absorption and Charge Transport for $Cu_{2-x}Zn_{1+x}Sn(S_{1-y}Se_y)4$. *ACS Appl. Energy Mater.* **2018**, *1* (3), 1053–1059.

(26) Bullen, C.; van Embden, J.; Jasieniak, J.; Cosgriff, J. E.; Mulder, R. J.; Rizzardo, E.; Gu, M.; Raston, C. L. High Activity Phosphine-Free Selenium Precursor Solution for Semiconductor Nanocrystal Growth. *Chem. Mater.* **2010**, *22* (14), 4135–4143.

(27) Haeuseler, H.; Wagener, M.; Zhang, J. Structural Investigations of the Olivine Type Thiogermanates $Mn_{2-x}T_xGeS_4$ (T = Fe, Co, Ni, Cd). *Neues Jahrb. für Mineral.* **2006**, *182* (3), 285–290.

(28) Padhi, A. K.; Nanjundaswamy, K. S.; Goodenough, J. B. Phospho-Olivines as Positive-Electrode Materials for Rechargeable Lithium Batteries. *J. Electrochem. Soc.* **1997**, *144* (4), 1188–1194.

(29) Yuan, L. X.; Wang, Z. H.; Zhang, W. X.; Hu, X. L.; Chen, J. T.; Huang, Y. H.; Goodenough, J. B. Development and Challenges of $LiFePO_4$ Cathode Material for Lithium-Ion Batteries. *Energy Environ. Sci.* **2011**, *4* (2), 269–284.

(30) Chung, S.-Y.; Bloking, J. T.; Chiang, Y.-M. Electronically Conductive Phospho-Olivines as Lithium Storage Electrodes. *Nat. Mater.* **2002**, *1* (2), 123–128.

(31) Morgan, D.; Van der Ven, A.; Ceder, G. Li Conductivity in Li_xMPO_4 (M = Mn, Fe, Co, Ni) Olivine Materials. *Electrochem. Solid-State Lett.* **2004**, *7* (2), 2003–2005.

(32) Islam, M. S.; Driscoll, D. J.; Fisher, C. A. J.; Slater, P. R. Atomic-Scale Investigation of Defects, Dopants, and Lithium Transport in the $LiFePO_4$ Olivine-Type Battery Material. *Chem. Mater.* **2005**, *17* (20), 5085–5092.

(33) Laffont, L.; Delacourt, C.; Gibot, P.; Wu, M. Y.; Kooyman, P.; Masquelier, C.; Tarascon, J. M. Study of the $LiFePO_4/FePO_4$ Two-Phase System by High-Resolution Electron Energy Loss Spectroscopy. *Chem. Mater.* **2006**, *18* (23), 5520–5529.

(34) Gibot, P.; Casas-Cabanas, M.; Laffont, L.; Levasseur, S.; Carlach, P.; Hamelet, S.; Tarascon, J. M.; Masquelier, C. Room-Temperature Single-Phase Li Insertion/Extraction in Nanoscale Li_xFePO_4. *Nat. Mater.* **2008**, *7* (9), 741–747.

(35) Nishimura, S. I.; Kobayashi, G.; Ohoyama, K.; Kanno, R.; Yashima, M.; Yamada, A. Experimental Visualization of Lithium Diffusion in Li_xFePO_4. *Nat. Mater.* **2008**, *7* (9), 707–711.

(36) Brunetti, G.; Robert, D.; Bayle-Guillemaud, P.; Rouvière, J. L.; Rauch, E. F.; Martin, J. F.; Colin, J. F.; Bertin, F.; Cayron, C. Confirmation of the Domino-Cascade Model by $LiFePO_4/FePO_4$ Precession Electron Diffraction. *Chem. Mater.* **2011**, *23* (20), 4515–4524.

(37) Delacourt, C.; Poizot, P.; Tarascon, J. M.; Masquelier, C. The Existence of a Temperature-Driven Solid Solution in Li_xFePO_4 for $0 \leq x \leq 1$. *Nat. Mater.* **2005**, *4* (3), 254–260.

(38) Boucher, F.; Gaubicher, J.; Cuisinier, M.; Guyomard, D.; Moreau, P. Elucidation of the $Na_{2/3}FePO_4$ and $Li_{2/3}FePO_4$ Intermediate Superstructure Revealing a Pseudouniform Ordering in 2D. *J. Am. Chem. Soc.* **2014**, *136* (25), 9144–9157.

(39) Li, Z.; Yang, J.; Li, C.; Wang, S.; Zhang, L.; Zhu, K.; Wang, X. Orientation-Dependent Lithium Miscibility Gap in $LiFePO_4$. *Chem. Mater.* **2018**, *30* (3), 874–878.

(40) Lim, J.; Li, Y.; Alsem, D. H.; So, H.; Lee, S. C.; Bai, P.; Cogswell, D. A.; Liu, X.; Jin, N.; Yu, Y.; Salmon, N. J.; Shapiro, D. A.; Bazant, M. Z.; Tyliszczak, T.; Chueh, W. C. Origin and Hysteresis of Lithium Compositional Spatiodynamics within Battery Primary Particles. *Science* **2016**, *353* (6299), 566–571.

(41) Lim, J.; Mathew, V.; Kim, K.; Moon, J.; Kim, J. One-Pot Synthesis of Multi-Morphous $LiFePO_4$ Nanoparticles in Polyol Medium. *J. Electrochem. Soc.* **2011**, *158* (6), 736–740.

(42) Strobridge, F. C.; Orvananos, B.; Croft, M.; Yu, H. C.; Robert, R.; Liu, H.; Zhong, Z.; Connolley, T.; Drakopoulos, M.; Thornton, K.; Grey, C. P. Mapping the Inhomogeneous Electrochemical Reaction Through Porous $LiFePO_4$-Electrodes in a Standard Coin Cell Battery. *Chem. Mater.* **2015**, *27* (7), 2374–2386.

APPENDIX A

SUPPORTING INFORMATION FOR CHAPTER 2: AMIDE-ASSISTED SYNTHESIS OF IRON GERMANIUM SULFIDE (Fe_2GeS_4) NANOSTARS: THE EFFECT OF $LiN(SiMe_3)_2$ ON PRECURSOR REACTIVITY FOR FAVORING NANOPARTICLE NUCLEATION OR GROWTH

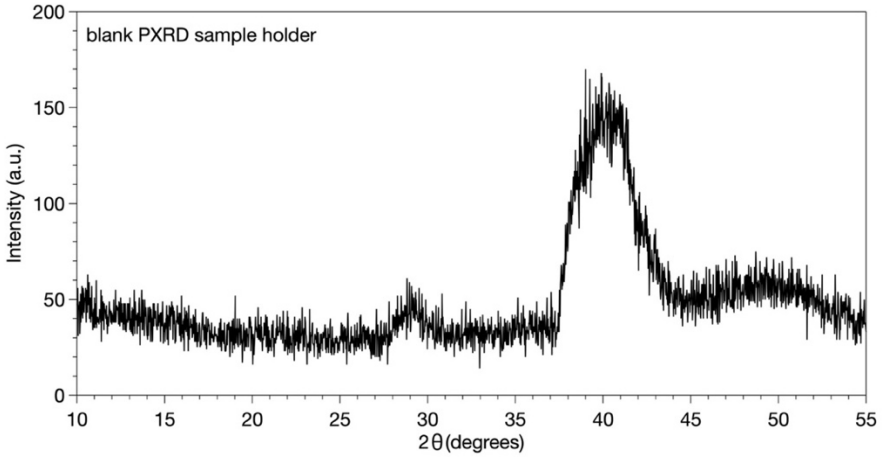

Fig. S2.1. PXRD pattern of a blank Si wafer sample holder and PMMA puck. We believe the intensity from 27-31˚ and 37-44˚ 2θ originates from the PMMA puck and/or an amorphous SiO_2 surface layer on the Si wafer.

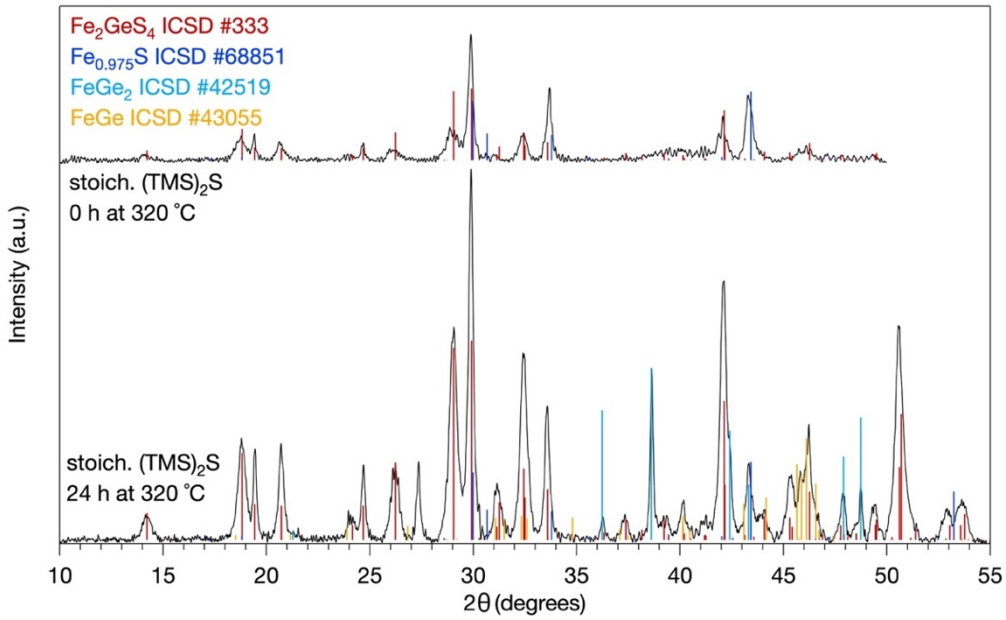

Fig. S2.2. PXRD patterns of the products from the Fredrick et al. Fe_2GeS_4 reaction adjusted to use a stoichiometric amount of $(TMS)_2S$ instead of ~2.1 times the stoichiometric amount. Two replicates of this reaction were run. One was quenched and worked up immediately after the reaction temperature reached 320 ˚C, and the second was quenched and worked up after 24 h at 320 ˚C.

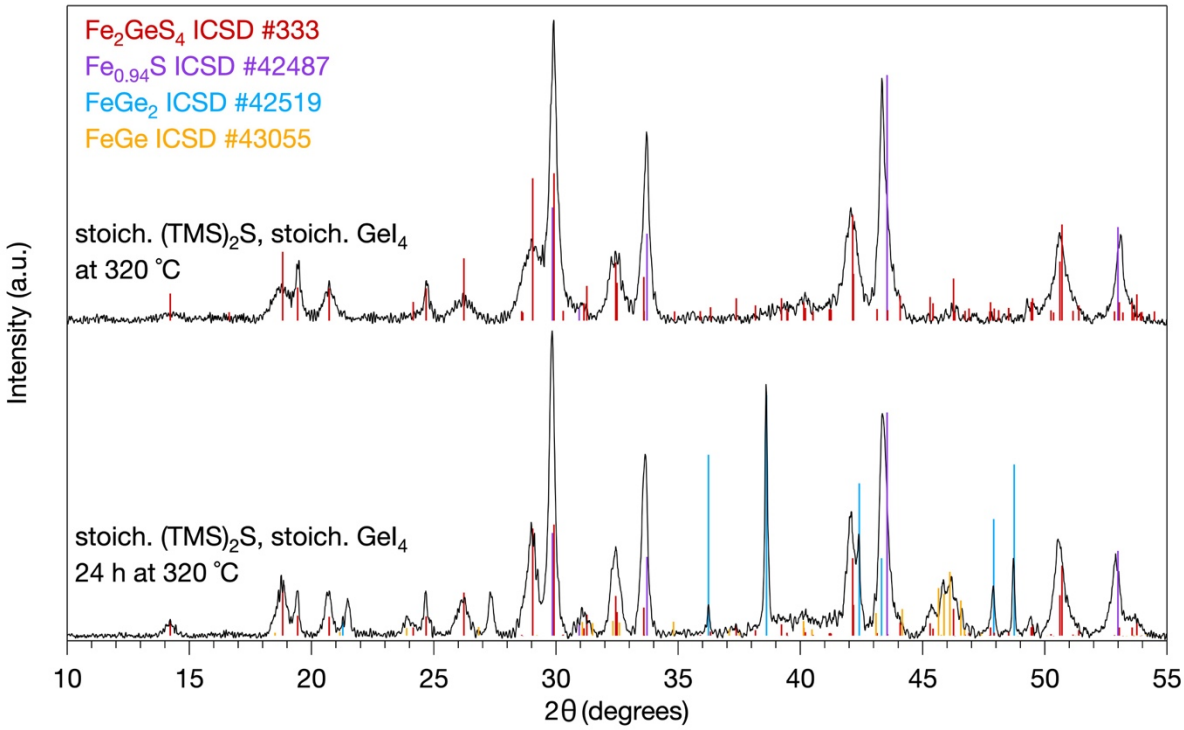

Fig. S2.3. PXRD patterns of the products from the Fredrick et al. Fe_2GeS_4 synthesis adjusted to use a stoichiometric amount of $(TMS)_2S$ and a stoichiometric amount of GeI_4. Two replicates of the reaction were run. One was quenched and worked up immediately after the reaction temperature reached 320 ˚C, and the second was quenched and worked up after 24 h at 320 ˚C.

Table S2.1. Precursor amounts for Fe_2GeS_4 reactions carried out in the optimization of amine, base, and cation molar ratios.

Reaction (C:B,B:A)	$FeCl_2$ (mg)	GeI_4 (mg)	OLA in flask (mL)	S (mg)	$LiN(SiMe_3)_2$ (mg)	OLA in scin vial (mL)	S:OLA (mol) in scin vial	$LiN(SiMe_3)_2$:OLA (mol) in scin vial
(1,0.02)	14	39	6	7	81	2	0.04	0.08
(2,0.02)	27	78	6	14	81	2	0.07	0.08
(3,0.02)	41	118	6	21	81	2	0.11	0.08
(4,0.02)	55	157	6	28	81	2	0.14	0.08
(1,0.03)	21	59	6	10	122	2	0.05	0.12
(2,0.03)	41	118	6	21	122	2	0.11	0.12
(3,0.03)	62	176	6	31	122	2	0.16	0.12
(4,0.03)	82	235	6	42	122	2	0.22	0.12
(1,0.06)	41	118	6	21	244	2	0.11	0.24
(3.5,0.017)	41	118	6	21	70	2	0.11	0.07
(3.5,0.02)	48	137	6	24	81	2	0.12	0.08
(4,0.015)	41	118	6	21	61	2	0.11	0.06

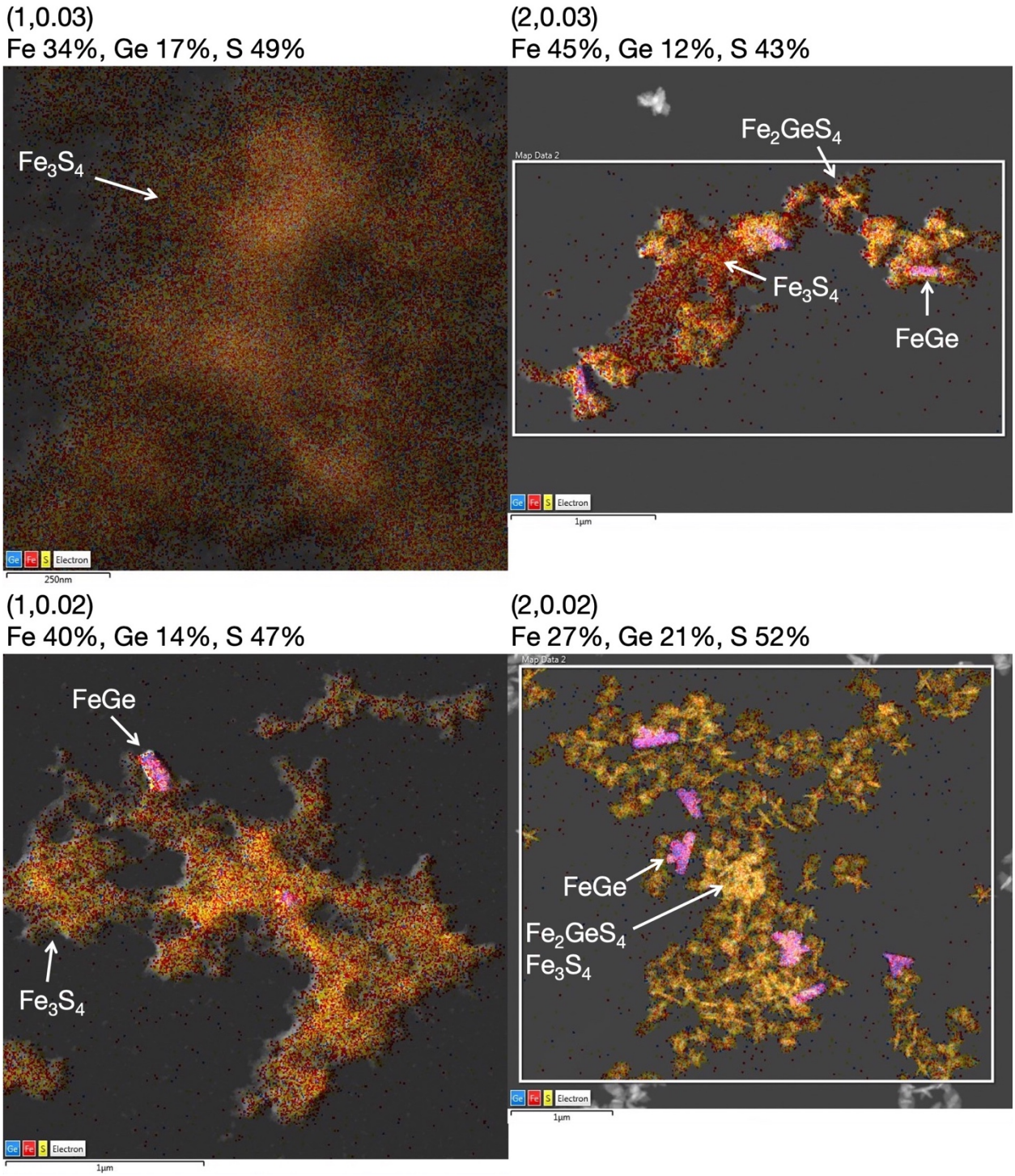

Fig. S2.4a. STEM EDS elemental mapping of products from four of the eight reactions outlined in Fig 1. The atomic percentages of Fe, Ge, and S, correspond to the overall composition of the maps. The (1,0.03) reaction had small Fe_3S_4 NPs as well as Ge content, likely due to the presence of unreacted precursor. The (1,0.02) reaction showed small Fe_3S_4 NPs and few FeGe NPs. The (2,0.03) reaction had Fe_2GeS_4, FeGe, and many small Fe_3S_4 NPs. The (2,0.02) reaction showed Fe_2GeS_4, FeGe, and fewer Fe_3S_4 NPs compared to the (2,0.03) reaction.

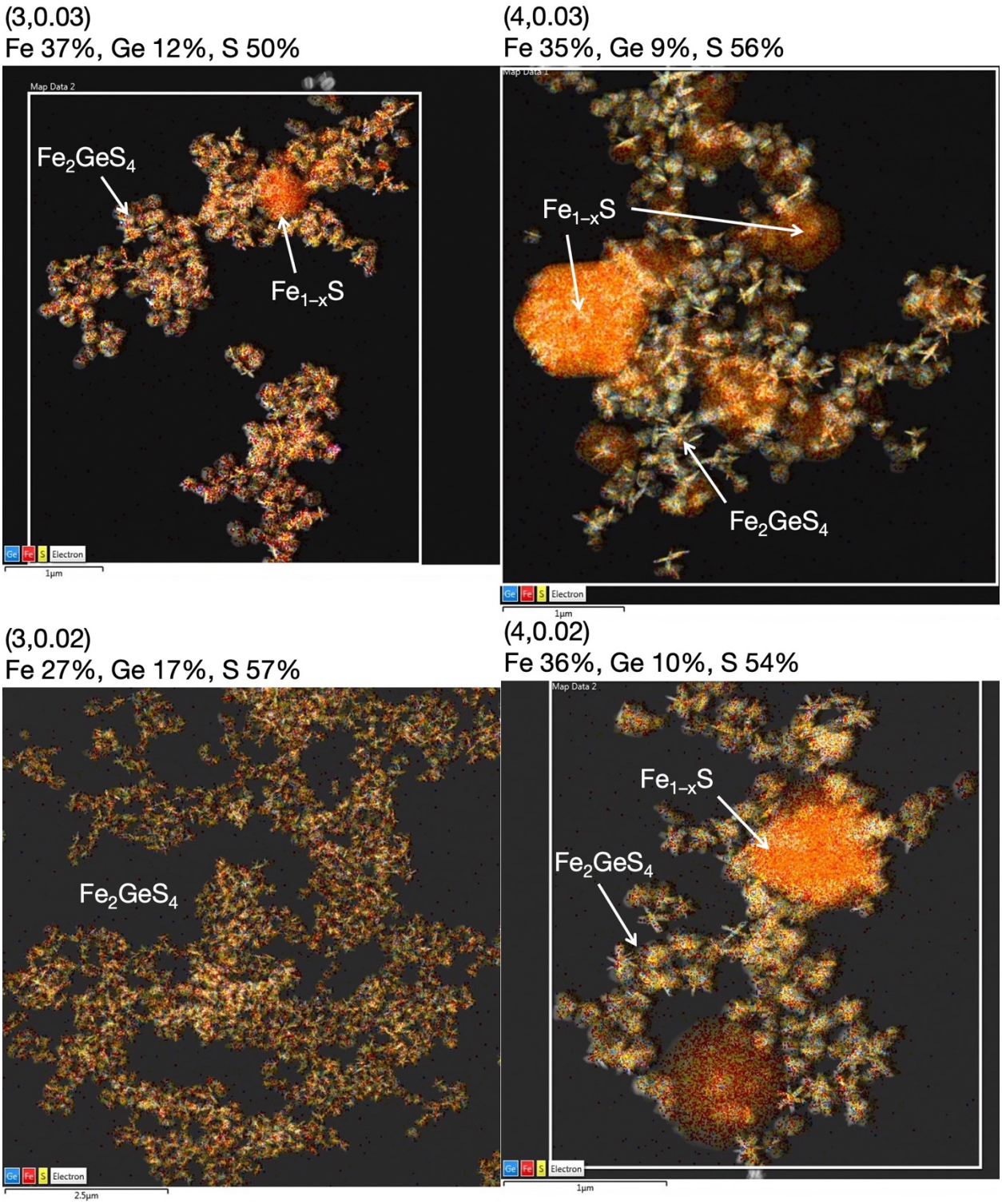

Fig. S2.4b. STEM EDS elemental mapping of products from four of the eight reactions outlined in Fig 1. The atomic percentages of Fe, Ge, and S, correspond to the overall composition of the maps. The (3,0.02) reaction showed Fe_2GeS_4 NPs. The (3,0.03), (4,0.03), and (4,0.02) reactions had Fe_2GeS_4 and $Fe_{1-x}S$ NPs.

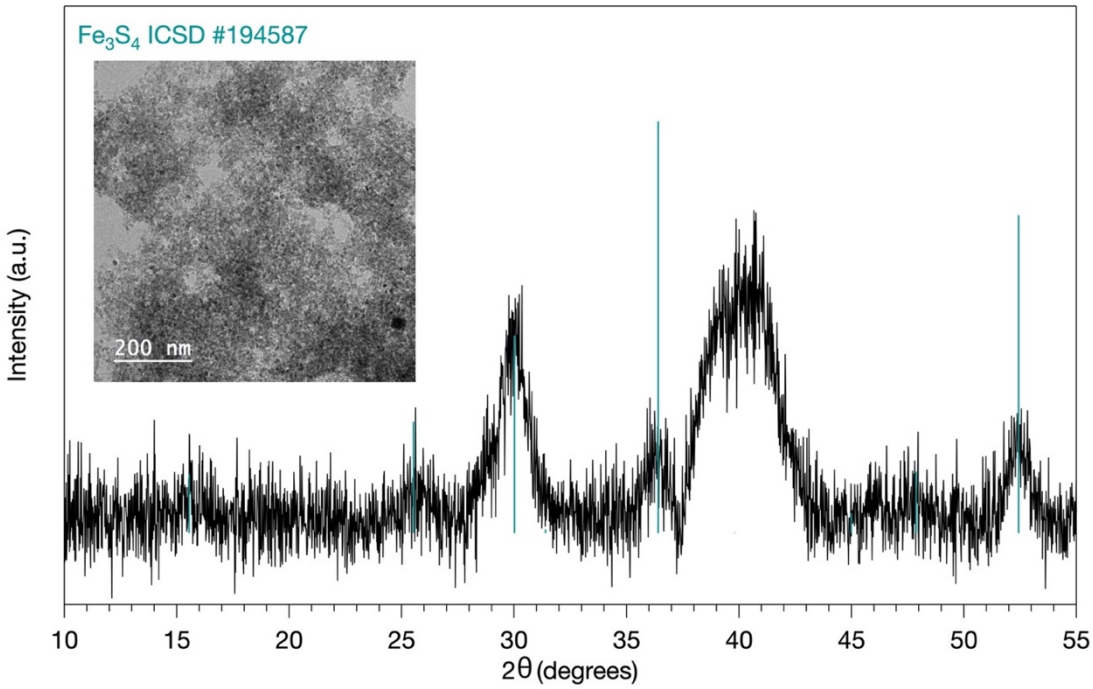

Fig. S2.5. PXRD pattern and TEM image of the products from the reaction (1,0.06). We observed small, crystalline Fe_3S_4 NPs.

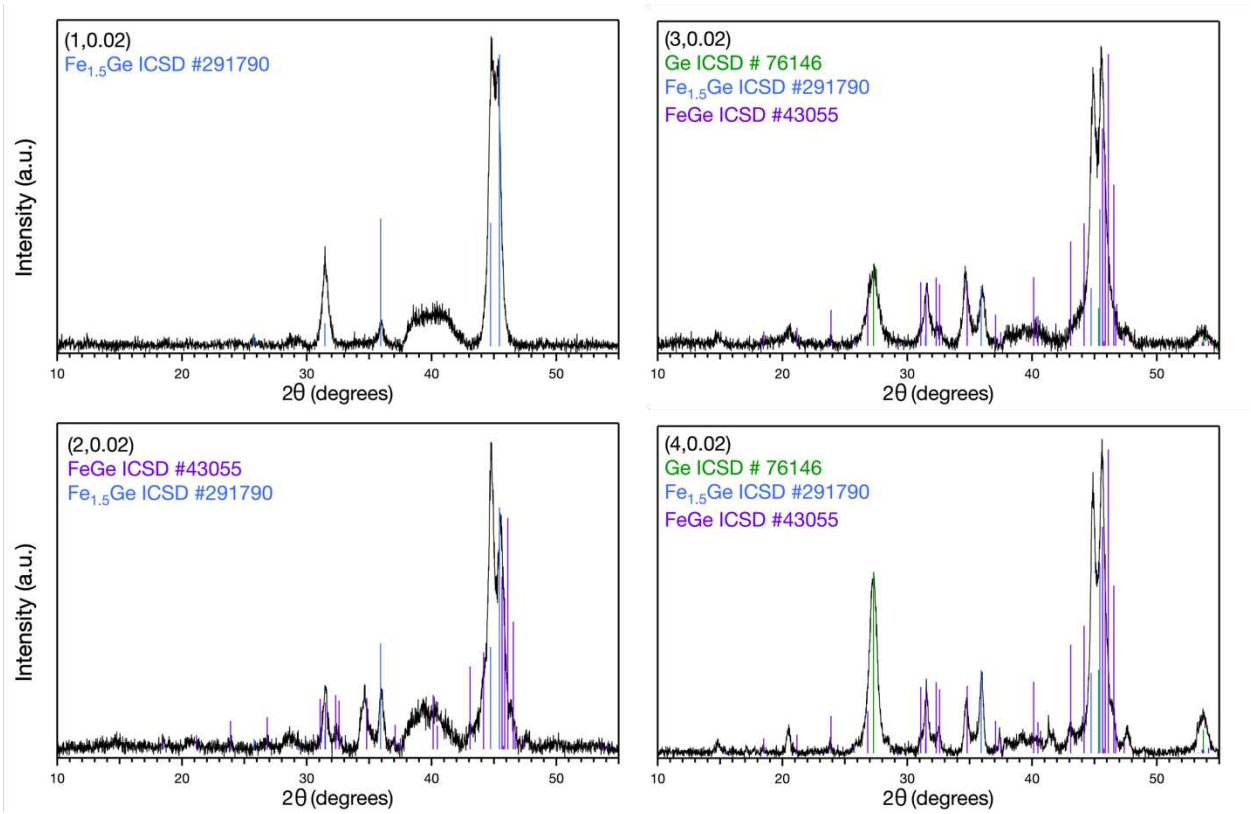

Fig. S2.6. PXRD patterns of products from the control reactions carried out without S. The corresponding (C:B,B:A) molar ratios are listed on each diffraction patterns, and the reference patterns are overlaid.

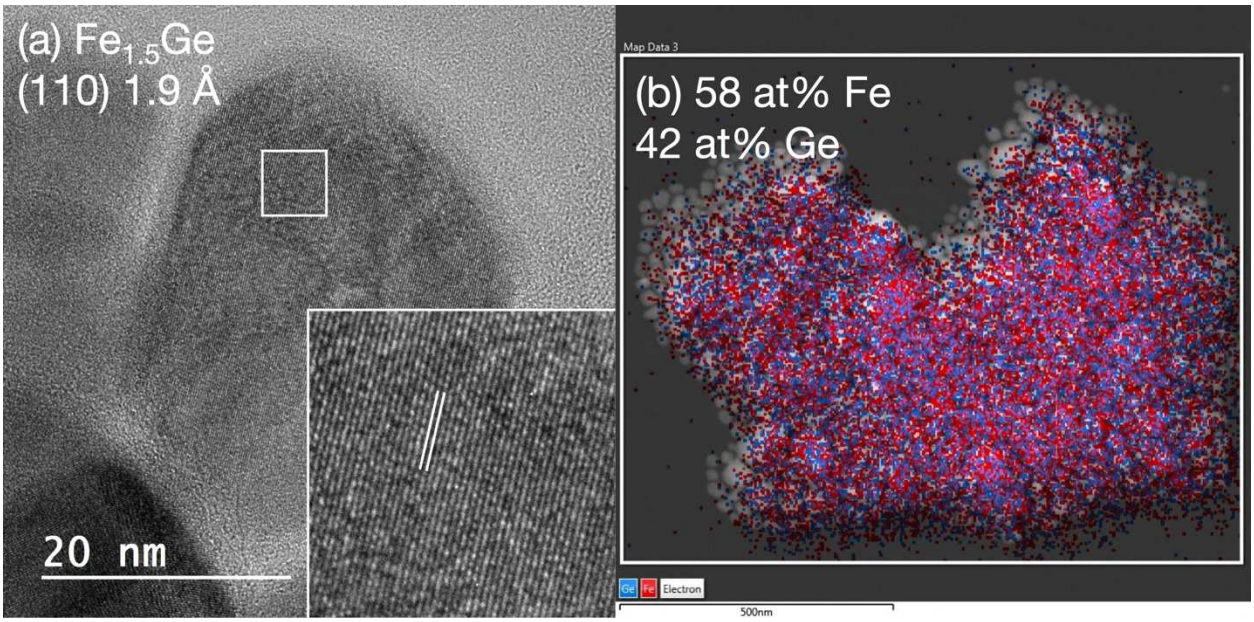

Fig. S2.7. Electron microscopy analysis of the products from reaction (1,0.02) carried out without S. The HRTEM image, **a,** showed a measured 1.9 Å lattice spacing corresponding to the (110) planes of $Fe_{1.5}Ge$ (ICSD #291790). The STEM EDS map, **b,** showed a Fe:Ge molar ratio of 1.38:1.

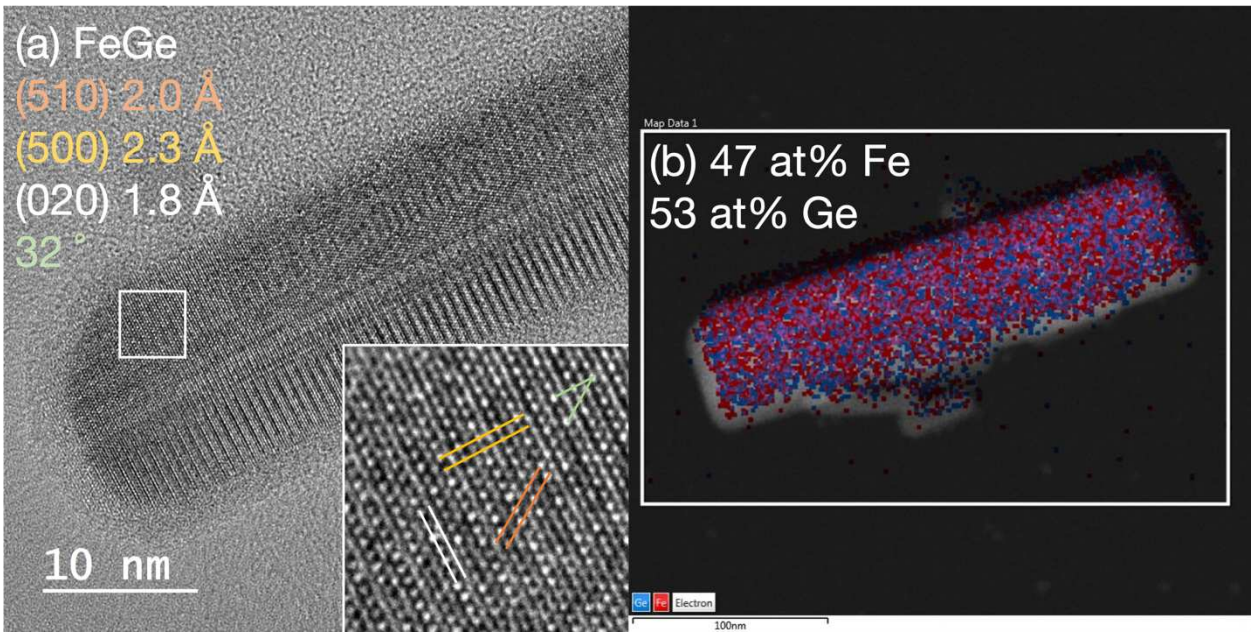

Fig. S2.8. Electron microscopy analysis of the products from reaction (2,0.02) carried out without S. The HRTEM image, **a,** showed lattice spacings and angles that correspond to the phase FeGe (ICSD #43055). The STEM EDS map, **b,** showed a Fe:Ge molar ratio of 0.89:1 in a rectangular particle.

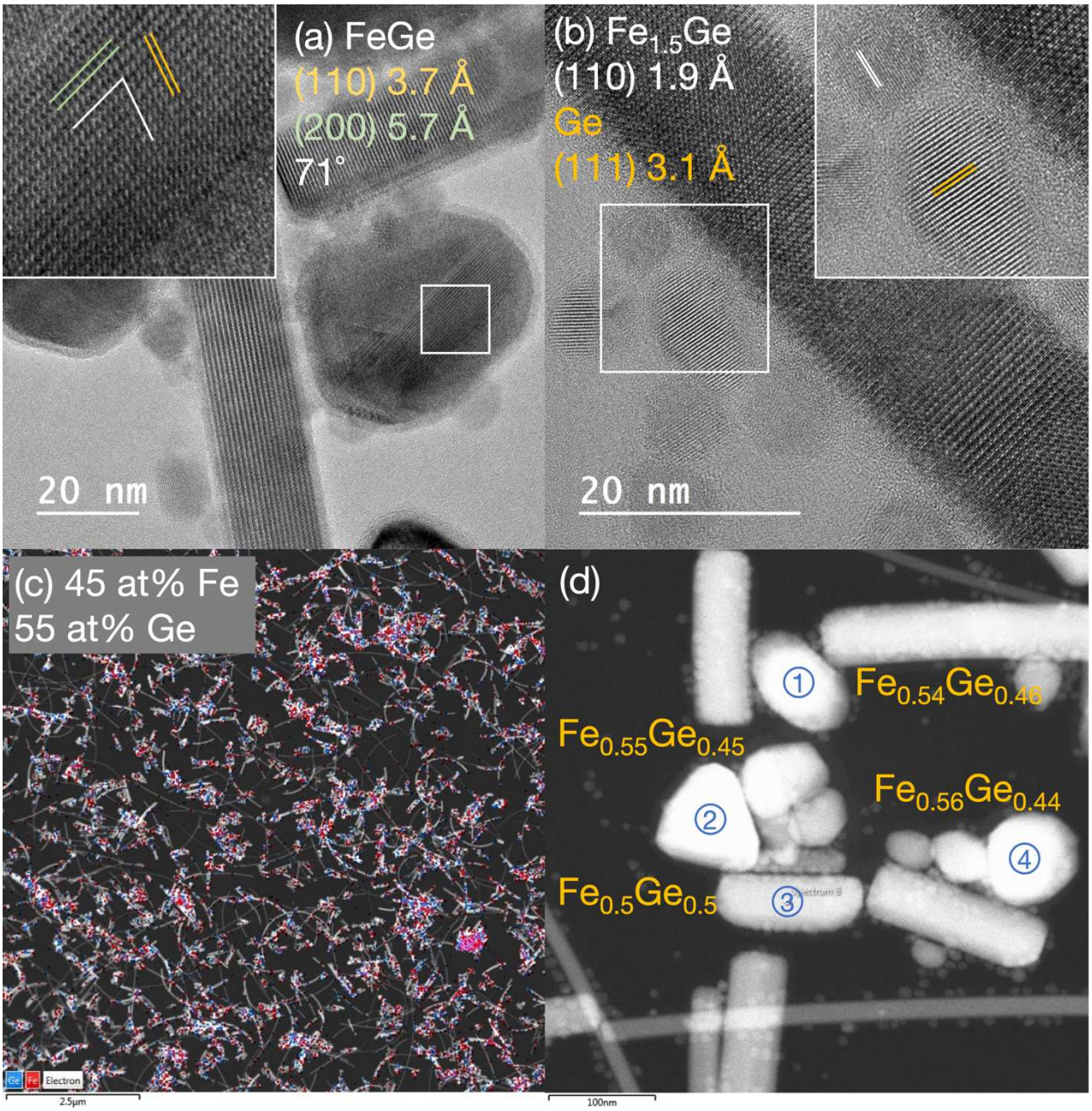

Fig. S2.9. Electron microscopy analysis of the products from reaction (3,0.02) carried out without S. The HRTEM image on the top left, **a,** depicts a FeGe NP in a different morphology than the long nanowires and rectangles typically seen. The HRTEM image on the top right, **b,** shows the presence of both small, round Ge and $Fe_{1.5}Ge$ NPs. The STEM EDS map on the bottom left, **c,** gave a Fe:Ge molar ratio of 0.82:1. The STEM EDS analysis on the right, **d,** shows the Fe and Ge compositions of the indicated particles. The rectangular particle (#3) seems to be FeGe; the oval and angular particles might be $Fe_{1.5}Ge$. The molar ratio in particles 1, 2, and 4 might be off from the 1.5:1 Fe:Ge molar ratio due to off-stoichiometry in the particles and/or from small Ge particles adhered to the larger $Fe_{1.5}Ge$ particles.

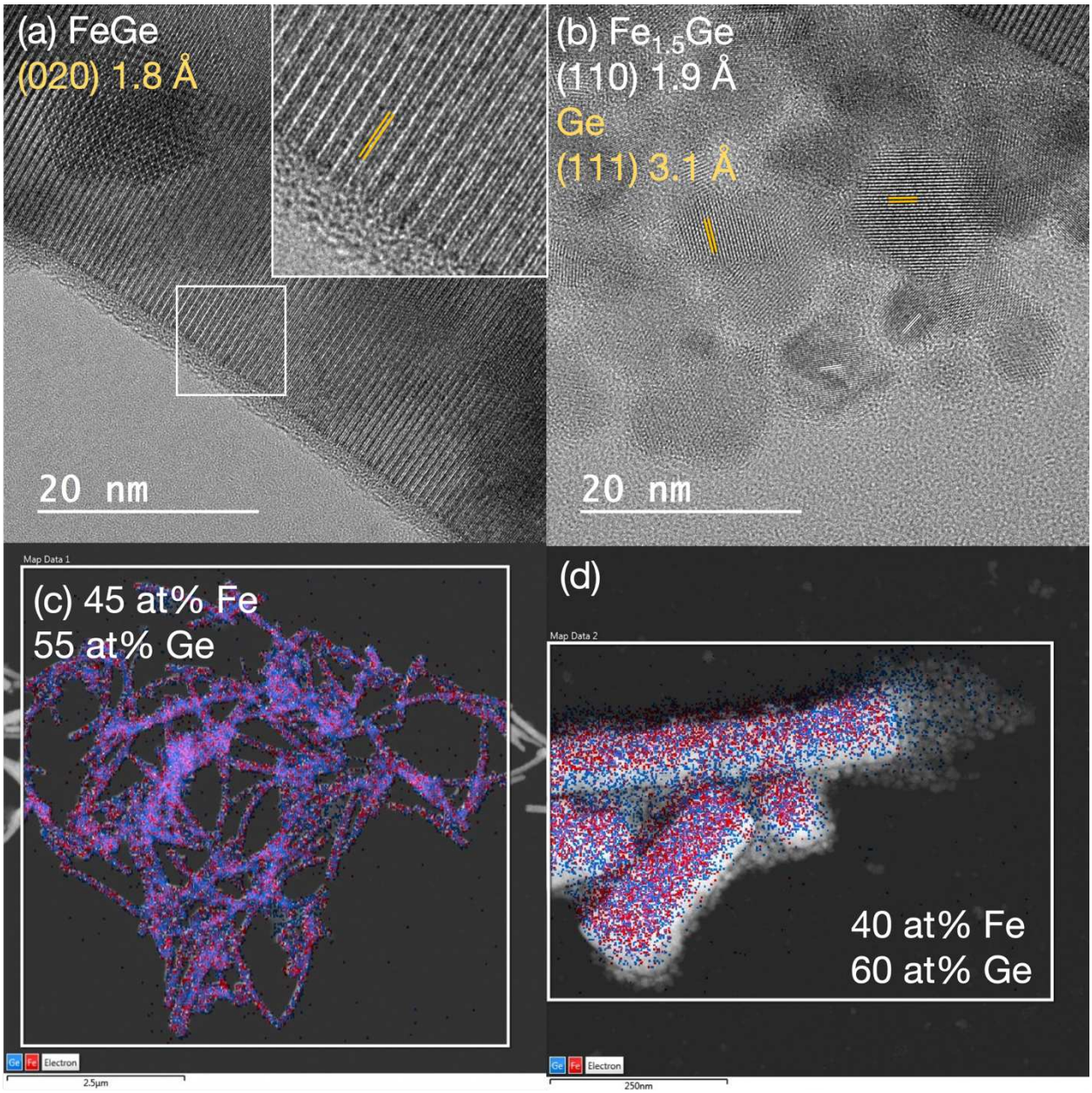

Fig. S2.10. Electron microscopy analysis of the products from reaction (4,0.02) carried out without S. The HRTEM image on the top left, **a,** depicts a FeGe nanowire, and the top right image, **b,** shows small, round Ge and $Fe_{1.5}Ge$ NPs. The STEM EDS map on the bottom left, **c,** gives a Fe:Ge molar ratio of 0.82:1, and the map on the bottom right, **d,** shows rectangular, larger particles that are likely FeGe and smaller particles with a dominant presence of Ge.

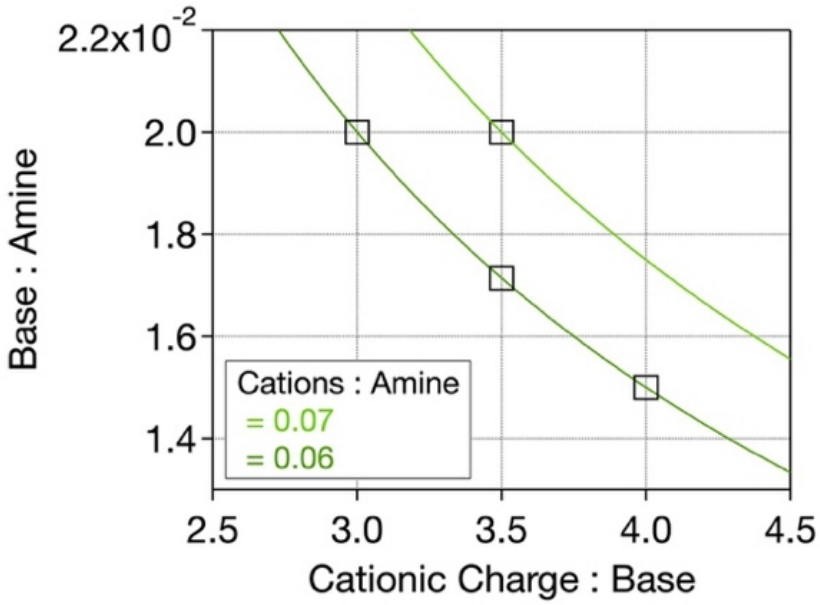

Fig. S2.11. The molar ratios tested in the attempt to carry out a a fine optimization of the cationic charge:base:amine ratios of the Fe_2GeS_4 NP reaction system.

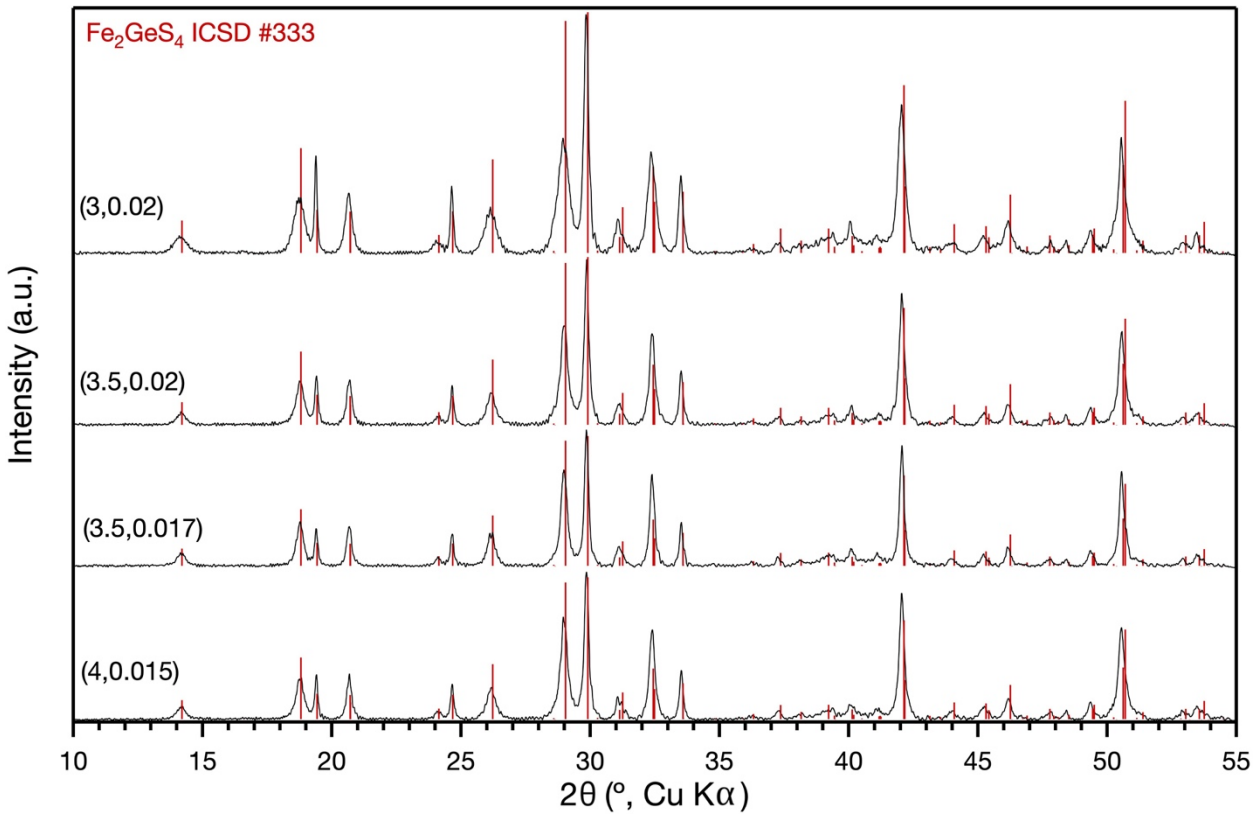

Fig. S2.12. PXRD patterns of the products from the reactions for the fine optimization of the Fe_2GeS_4 NP reaction system, as outlined in Fig. S2.10. Multiple diffraction patterns are shown for (3,0.02) and (3.5, 0.017) because these reactions were carried out twice. All of the patterns index to Fe_2GeS_4 and do not show identifiable signal from any other phases.

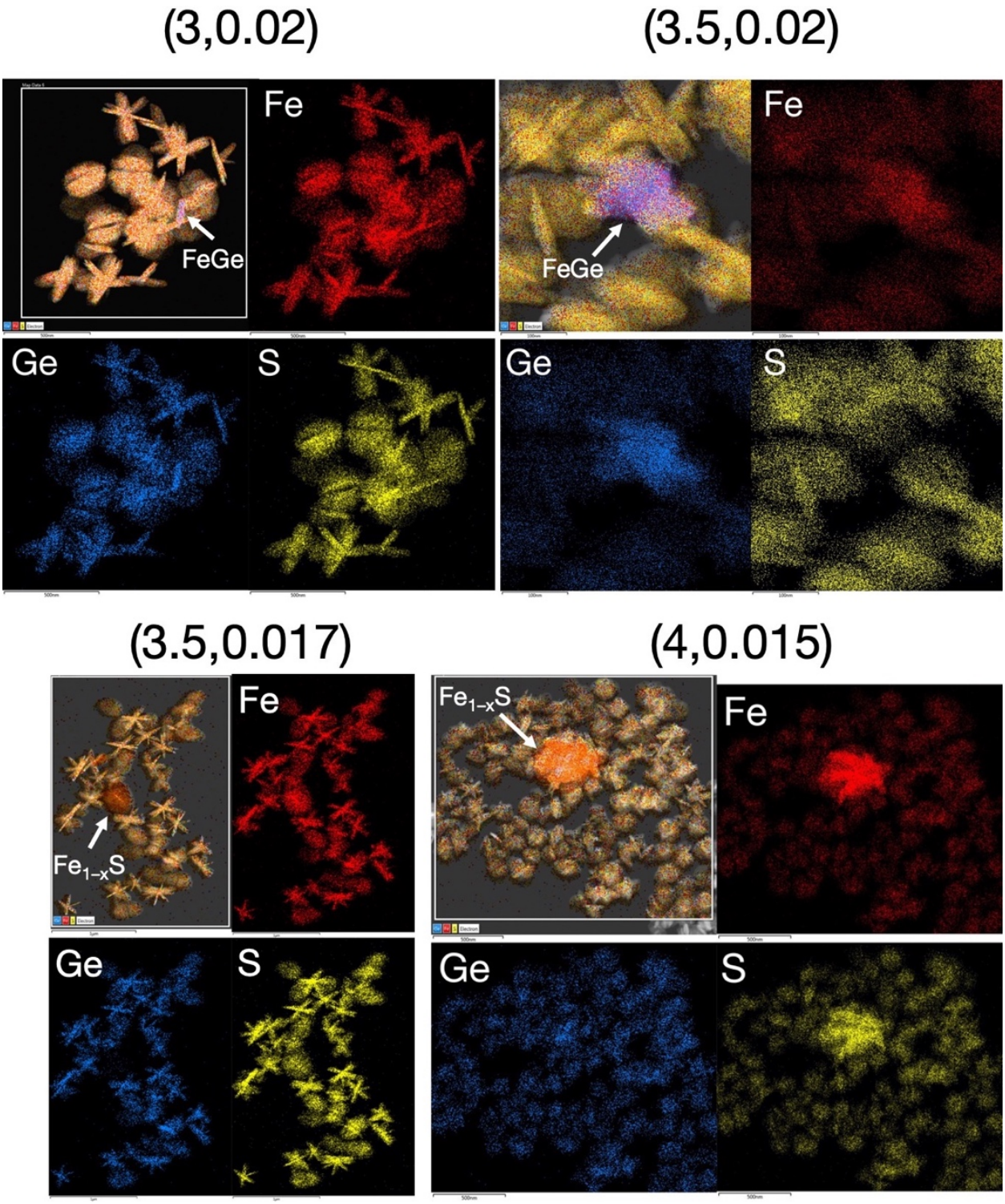

Fig. S2.13. STEM EDS elemental maps of products from the reactions described in Fig. S2.10. Small concentrations of impurity phases could be detected in all of the reactions. White arrows point to spots of impurity detection. Fe-Ge NPs were detected at low concentration in the reactions (3,0.02) and (3.5,0.02). Fe-S NPs were detected at low concentration in the reactions (3.5, 0.017) and (4,0.015).

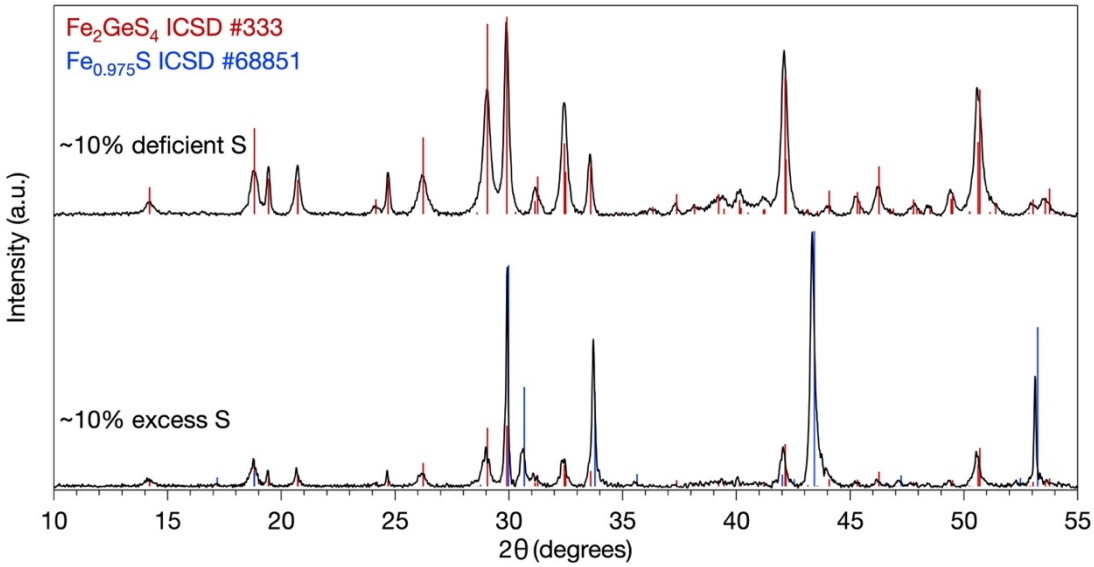

Fig. S2.14. PXRD patterns of the products from reactions carried out in which the S amount was altered relative to the optimal reaction conditions. The excess S reaction was carried out with +2 mg more than the standard amount (23 mg were used), and both Fe_2GeS_4 and $Fe_{1-x}S$ were detected. The deficient S reaction was carried out with –2 mg more than the standard amount (19 mg were used), and only Fe_2GeS_4 was detected by PXRD.

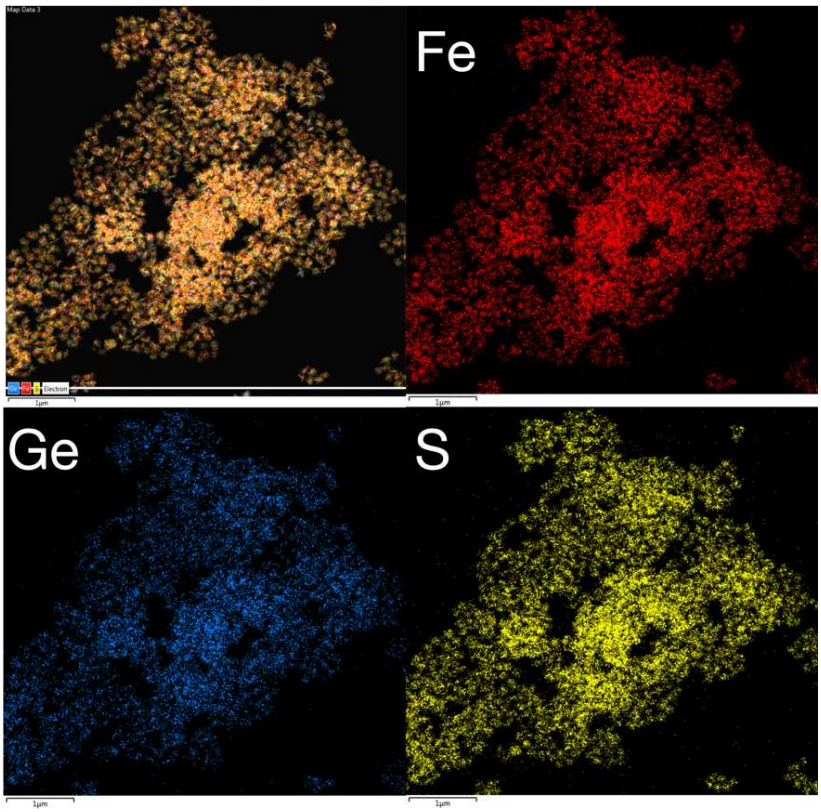

Fig. S2.15. STEM EDS mapping of the products from the reaction carried out in which the S amount was lowered compared to the stoichiometric amount by ~10% (using 19 mg instead of 21 mg). Fe_2GeS_4 was the only detected phase.

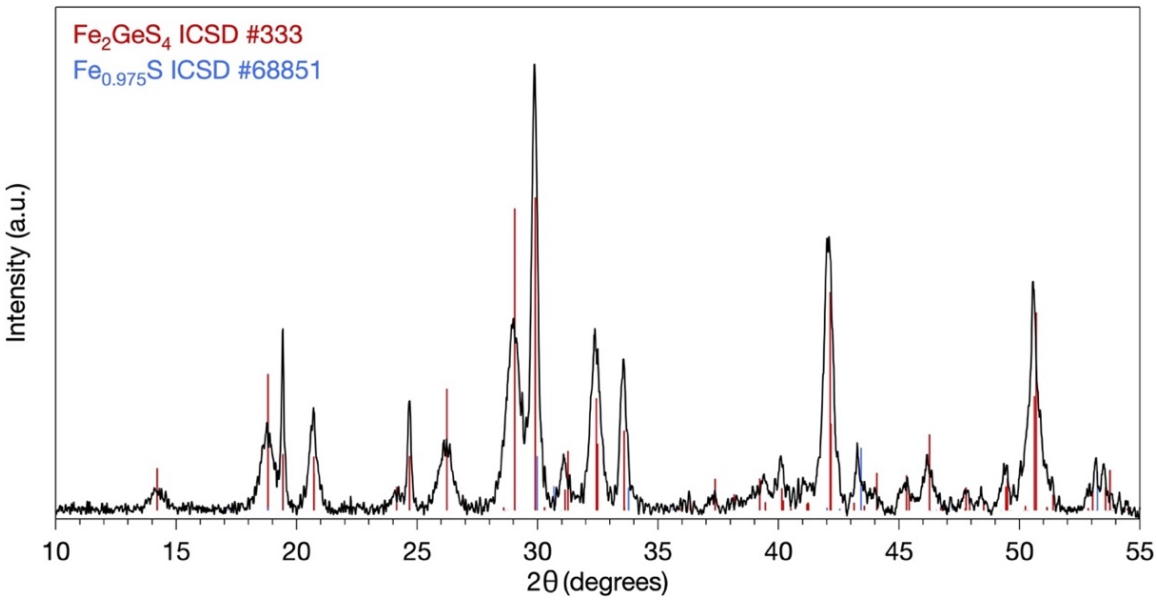

Fig. S2.16. PXRD pattern of the products from the lower scale Fe_2GeS_4 NP reaction when the optimal conditions were altered to use a stoichiometric amount of GeI_4, 0.162 mmol, instead of the standard 1.25·stoichiometric amount, 0.203 mmol).

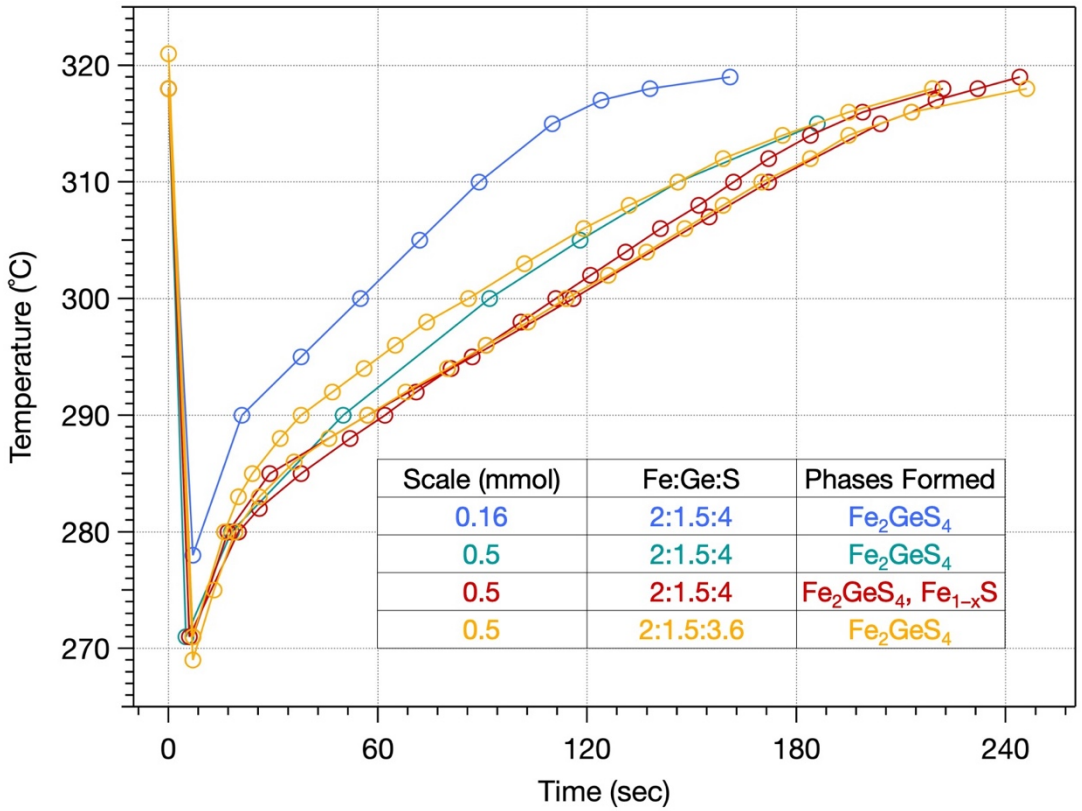

Fig. S2.17. Temperature profiles of Fe_2GeS_4 NP syntheses. Comparing the lower and higher scale Fe_2GeS_4 NP reactions, the higher scale reactions required roughly twice as long to reheat. Variability in phase formation was observed for the higher scale reactions when the Fe:Ge:S molar ratio was 2:1.5:4. Upon decreasing the S amount by 10%, phase-pure Fe_2GeS_4 NPs formed.

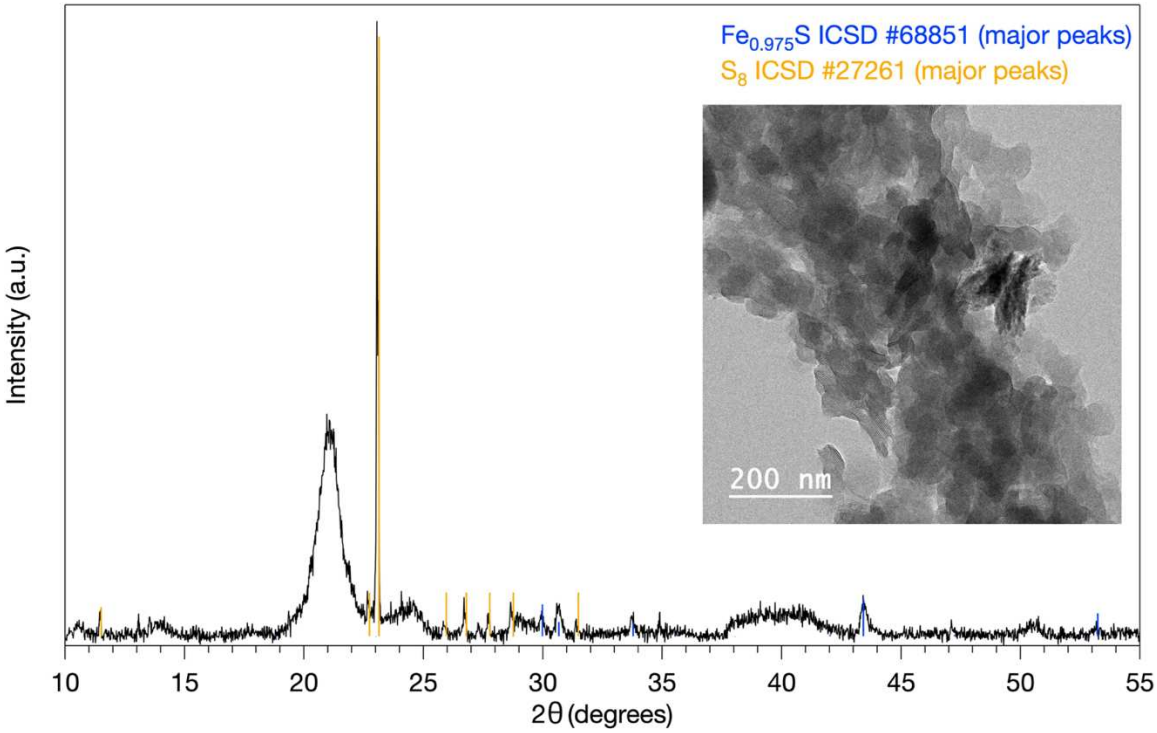

Fig. S2.18. PXRD pattern and TEM image of the product from the 0.16 mmol scale reaction with a Fe:Ge:S ratio of 2:1.25:4 carried out with a 300 ˚C injection and growth temperature. The reaction was allowed a 10 min growth but did not form highly crystalline products. Via PXRD, elemental S (S_8) and $Fe_{1-x}S$ could be detected at low concentrations. TEM images indicated the majority of the precipitate was amorphous matter.

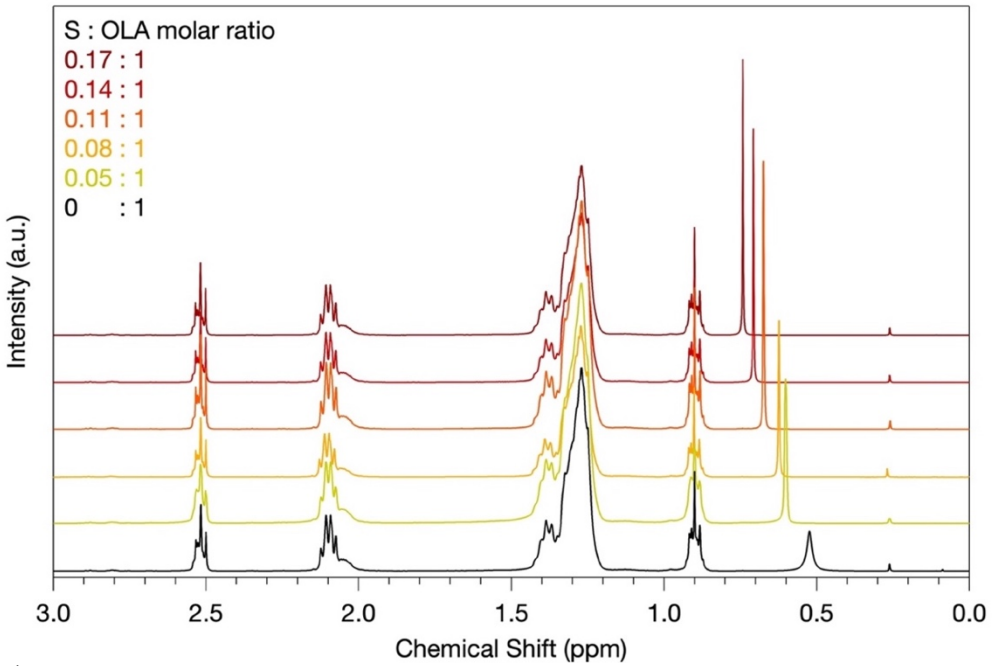

Fig. S2.19. ^{1}H NMR spectra of solutions of variable S concentration in OLA. The S_8/OLA solutions were prepared in a N_2 glovebox and sonicated to dissolve the powder. The NMR samples were prepared in the glove box with C_6D_6 as the deuterated solvent.

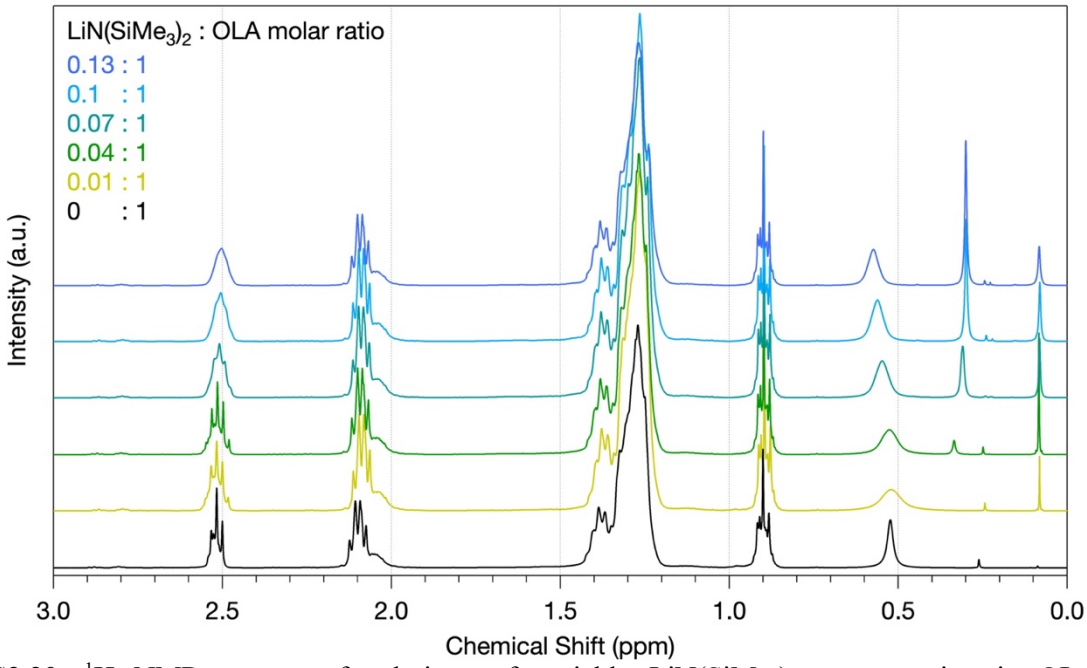

Fig. S2.20. ^{1}H NMR spectra of solutions of variable $LiN(SiMe_3)_2$ concentration in OLA. The $LiN(SiMe_3)_2$/OLA solutions were prepared in a N_2 glovebox and sonicated to dissolve the powder. The NMR samples were prepared in the glove box with C_6D_6 as the deuterated solvent.

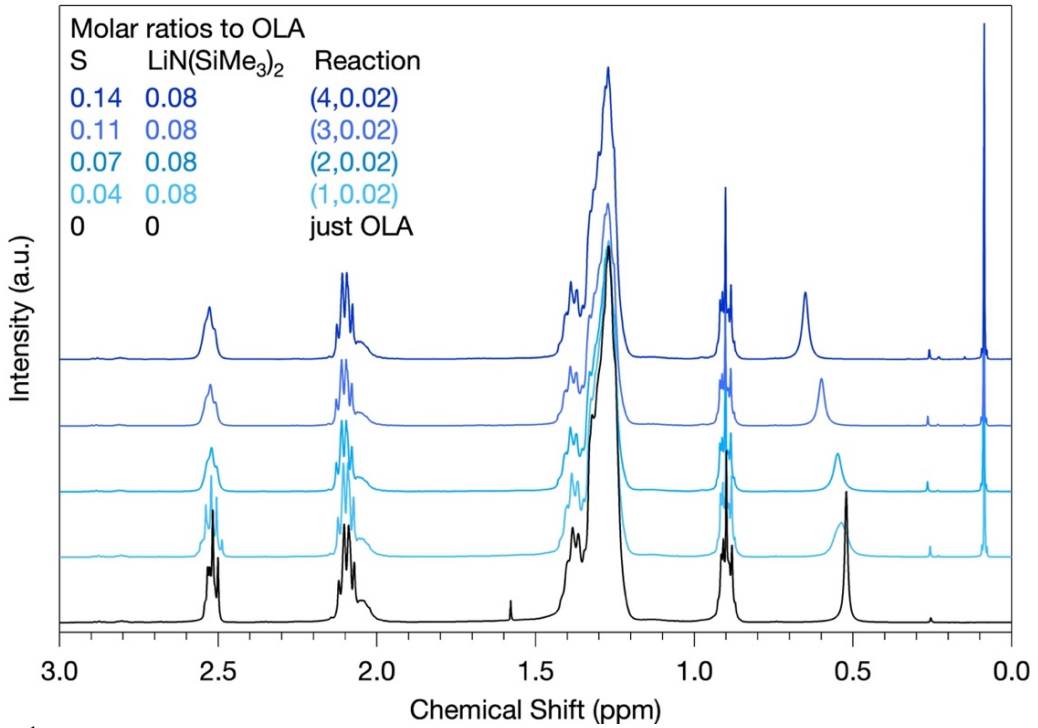

Fig S2.21. ^{1}H NMR spectra of the injection solutions from the Fe_2GeS_4 NP reactions for which the molar base:amine ratio = 0.02. The S_8/$LiN(SiMe_3)_2$/OLA solutions were prepared in a N_2 glovebox and sonicated to dissolve the powder. The NMR samples were prepared in a N_2 glovebox with C_6D_6 as the deuterated solvent.

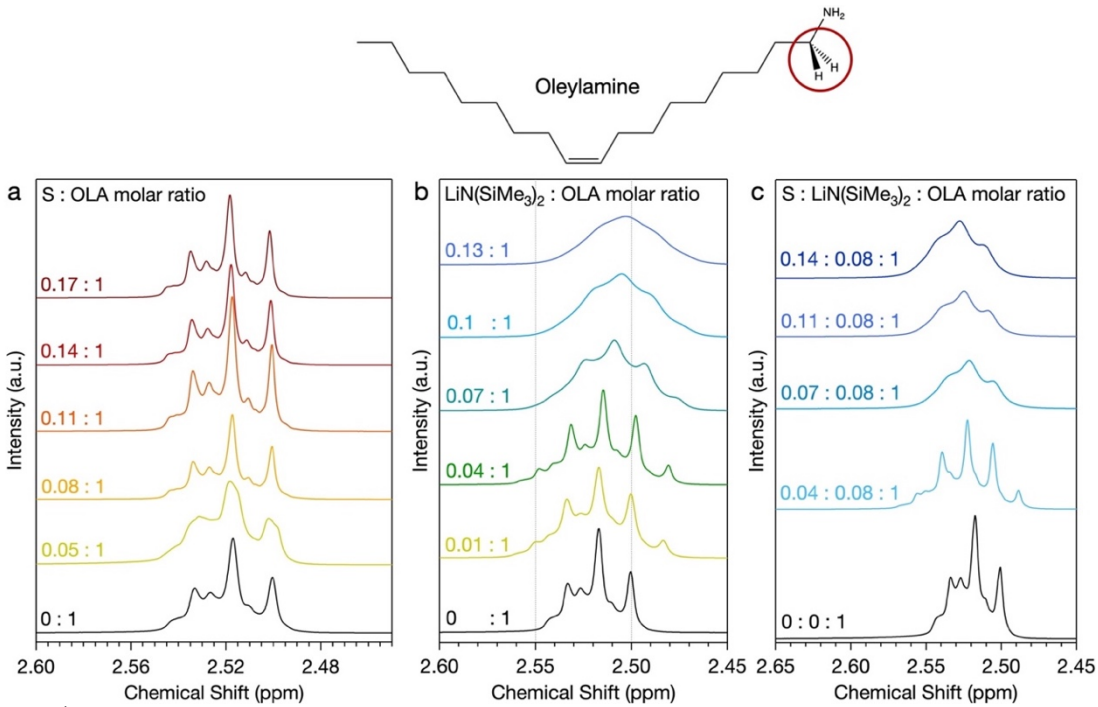

Fig. S2.22. ^{1}H NMR spectra of the **a,** S in OLA, **b,** $LiN(SiMe_3)_2$ in OLA, and **c,** injection solutions with both S and $LiN(SiMe_3)_2$ in OLA to highlight the $–C\underline{H}_2–NH_2$ resonance in each of the data sets. The S in OLA solutions show no significant changes to the peak character with increasing S concentration in OLA. However, the peak exhibits increasing broadening with increasing concentration of $LiN(SiMe_3)_2$ in OLA. This increasing broadness is also observed in the injection solutions in which both S and $LiN(SiMe_3)_2$ were dissolved in OLA. Therefore, the presence of S did not inhibit the underlying cause of this broadening, which is presumably due to the interaction of $LiN(SiMe_3)_2$ and OLA. We speculate this is related to the possible deprotonation of OLA by $LiN(SiMe_3)_2$ to form oleylamide; however, amides are known to form oligomers, and the presence of which may also contribute to peak broadening.

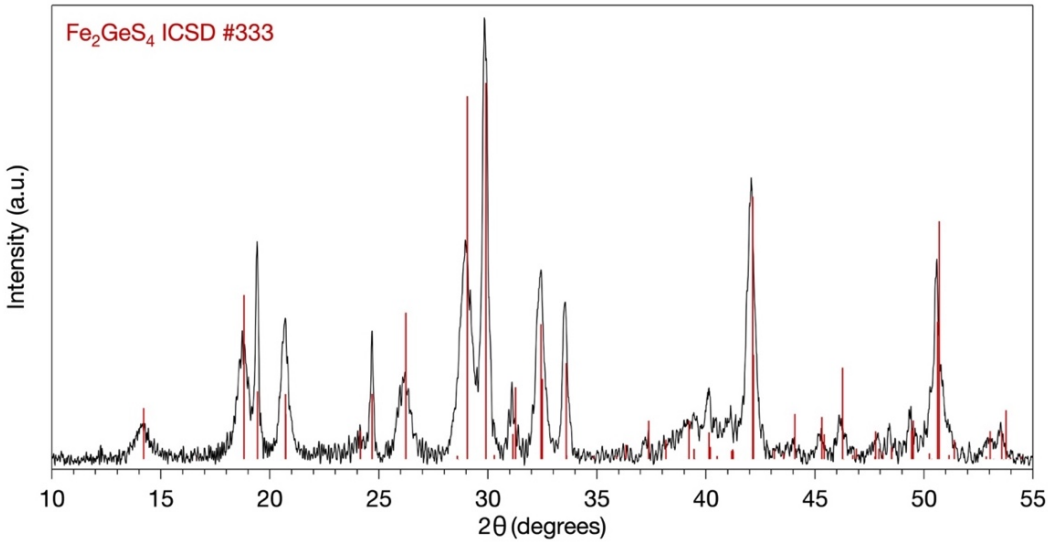

Fig. S2.23. PXRD pattern from the products of the Fe_2GeS_4 NP reaction adapted to have S and $LiN(SiMe_3)_2$ injected simultaneously but in separate solutions. Each were prepared in 1 mL of OLA instead of the typical 2 mL solution with both dissolved together. The PXRD pattern indicated only the presence of Fe_2GeS_4.

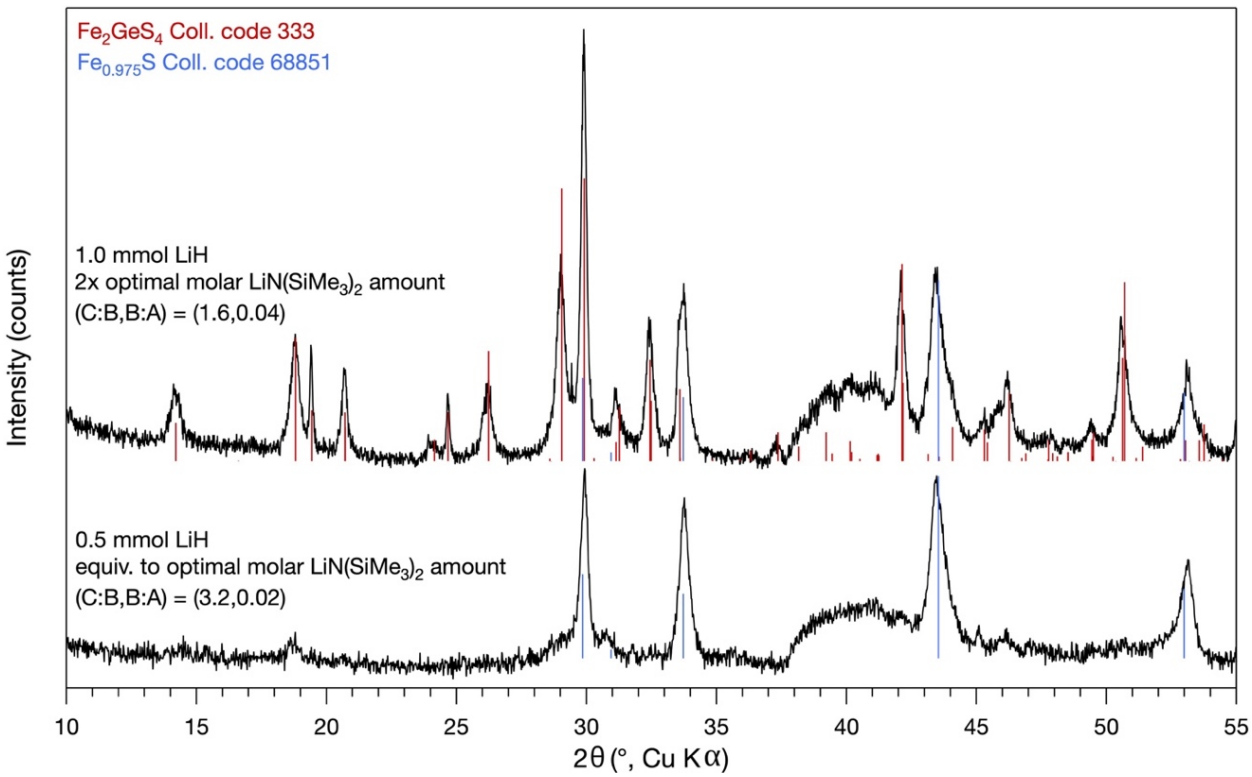

Fig. S2.24. PXRD patterns of the products from Fe_2GeS_4 NP reactions for which LiH was used instead of $LiN(SiMe_3)_2$. The bottom pattern shows the formation of $Fe_{1-x}S$ when a molar equivalent amount of LiH compared to $LiN(SiMe_3)_2$ (0.5 mmol) was used. Upon increasing the LiH amount by a factor of two, both Fe_2GeS_4 and $Fe_{1-x}S$ were formed. We speculate that the different amount of base required is simply due to a difference in the pK_a values of the conjugate bases and potentially a shifted equilibrium in the reaction with OLA due to a difference in volatility of the products, specifically H_2 versus $HN(SiMe_3)_2$.

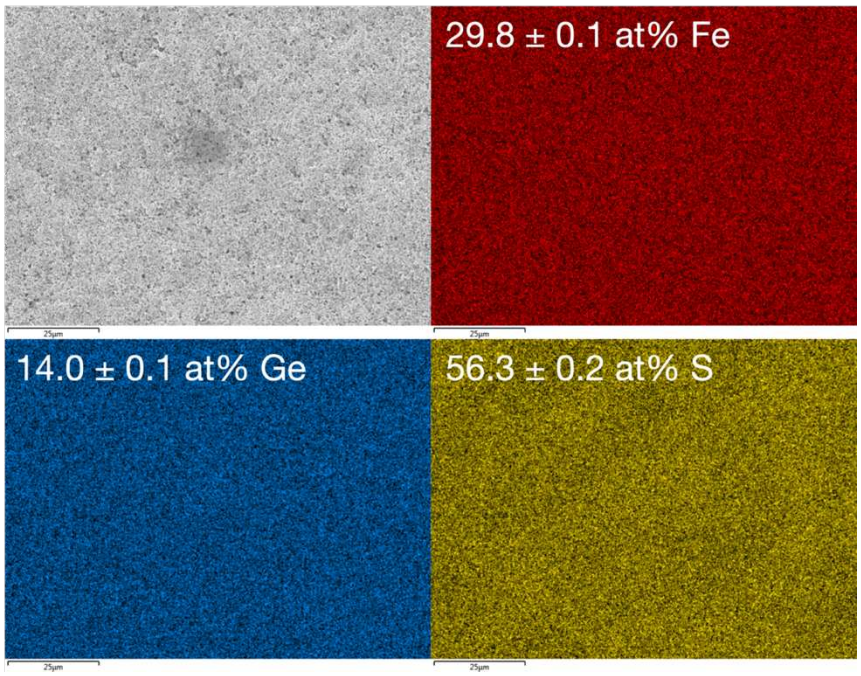

Fig. S2.25. SEM EDS elemental mapping of the products from the scaled up Fe_2GeS_4 NP reaction.

Table S2.2. Rietveld Refinement of Fe_2GeS_4 NPs

Phase	Fe_2GeS_4
Crystal system, space group	Orthorhombic, *Pnma*
a, Å	12.4888(6)
b, Å	7.2212(3)
c, Å	5.9130(2)
α, ˚	90
β, ˚	90
γ, ˚	90
Cell Volume, $Å^3$	533.26(4)
Z height displacement	-0.054(3)
Surface Roughness (Pitschke)	0.009(5)

Atom	Site	Multiplicity	Fractional Coordinate			Occupancy	B
			x	y	z		
S	S1	4	0.4105(10)	0.25	0.7129(12)	1	4.23(12)
S	S2	4	0.5763(10)	0.25	0.2424(8)	1	4.23(12)
S	S3	8	0.3371(9)	0.0109(7)	0.2459(8)	1	4.23(12)
Ge	Ge1	4	0.4118(3)	0.25	0.0832(5)	1	5.12(13)
Fe	Fe1	4	0.0	0.0	0.0	1	5.42(13)
Fe	Fe2	4	0.2320(3)	0.25	0.5091(7)	1	5.42(13)

Shape	R_{wp}(%)	R_{exp}(%)
Triaxial ellipsoid	7.133	5.953
Elliptic cylinder	7.356	5.953
Cuboid	7.473	5.953

A broad peak at ~40 ˚ 2q was included in the background in order to account for the signal originating from the PMMA sample holder puck (see Fig. S2.1).

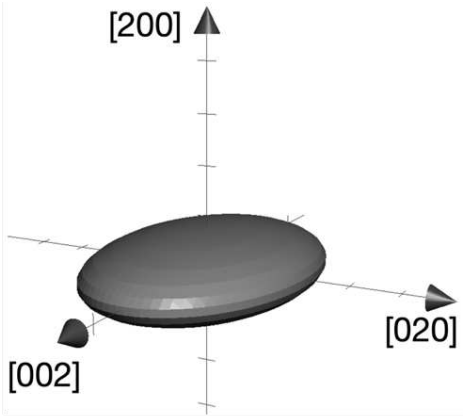

$$1 = \frac{x^2}{32^2} + \frac{y^2}{22^2} + \frac{z^2}{7.9^2}$$

Fig. S2.26. Plot of the refined triaxial ellipsoid crystallite shape, the equation that defines it, and the corresponding crystallographic directions.

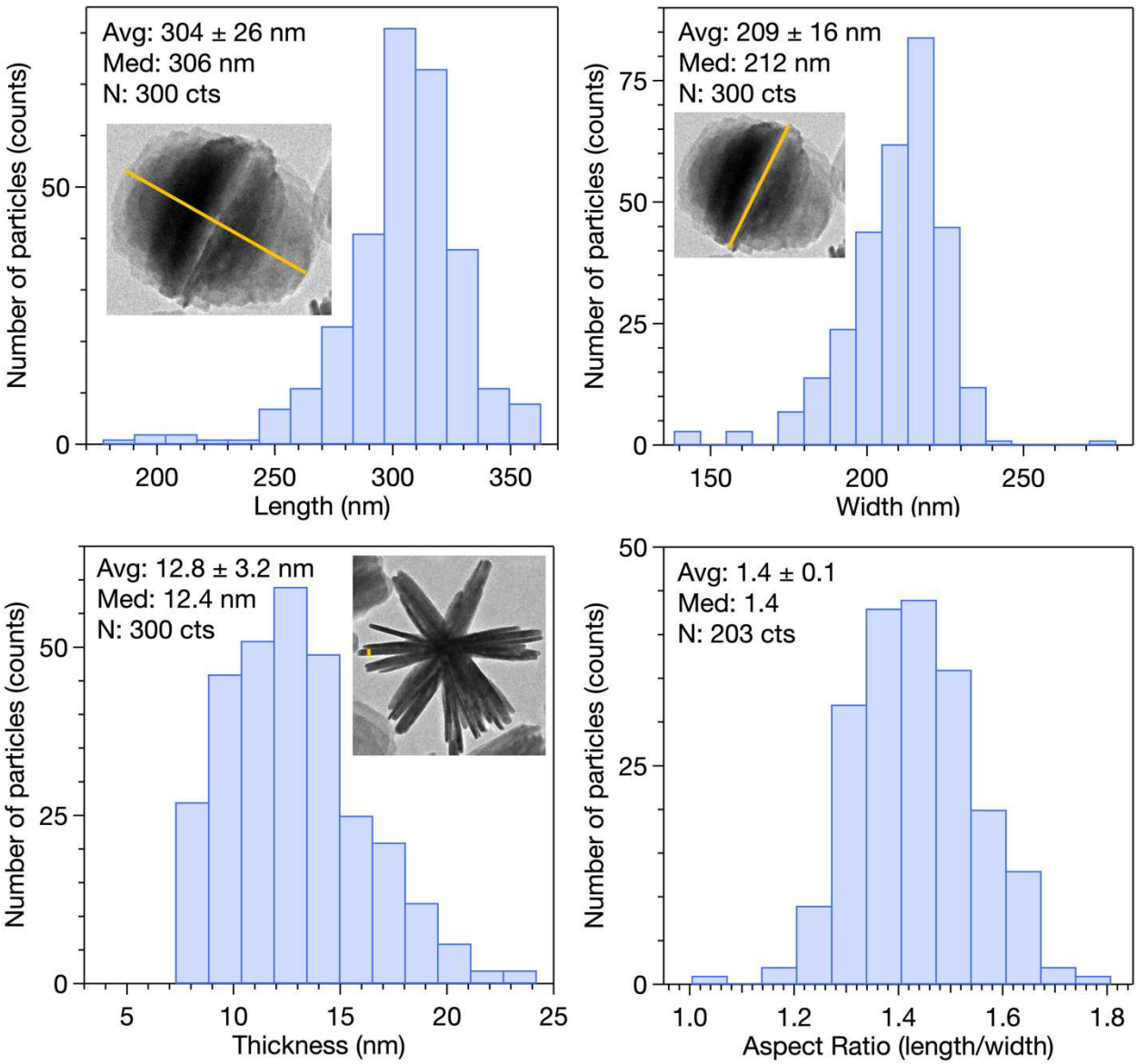

Fig. S2.27. Size distribution analysis of the NPs. Yellow lines on inset TEM images of the NPs indicate the orientation of length, width, and thickness measurements. The aspect ratio is defined as the length divided by the width. The average, standard deviation, median, and number of measurements are given for each dataset.

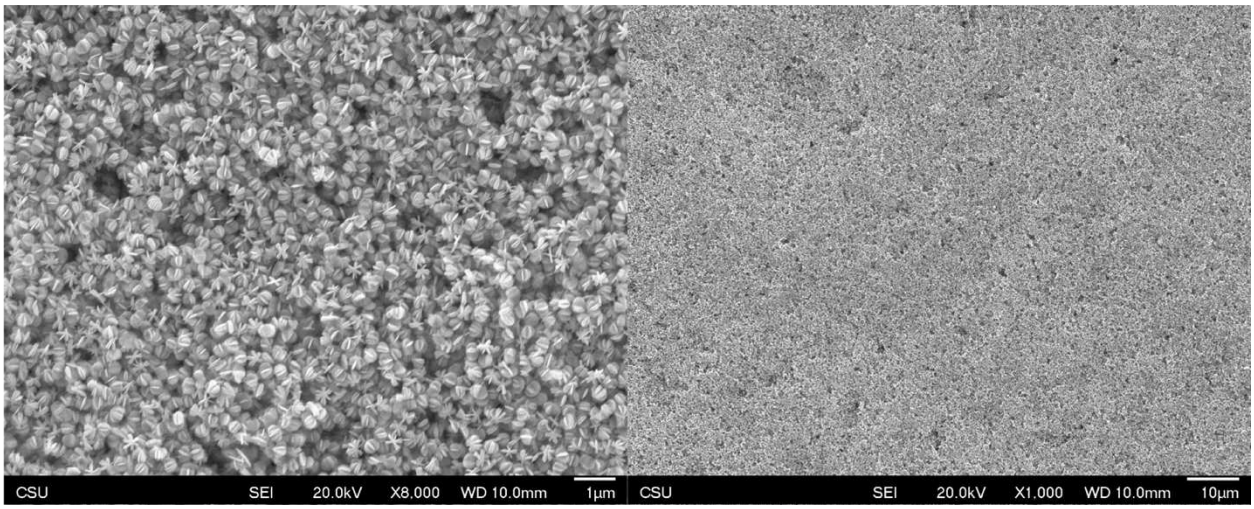

Fig. S2.28. SEM images of Fe_2GeS_4 NPs. The products show consistency in NP size and morphology.

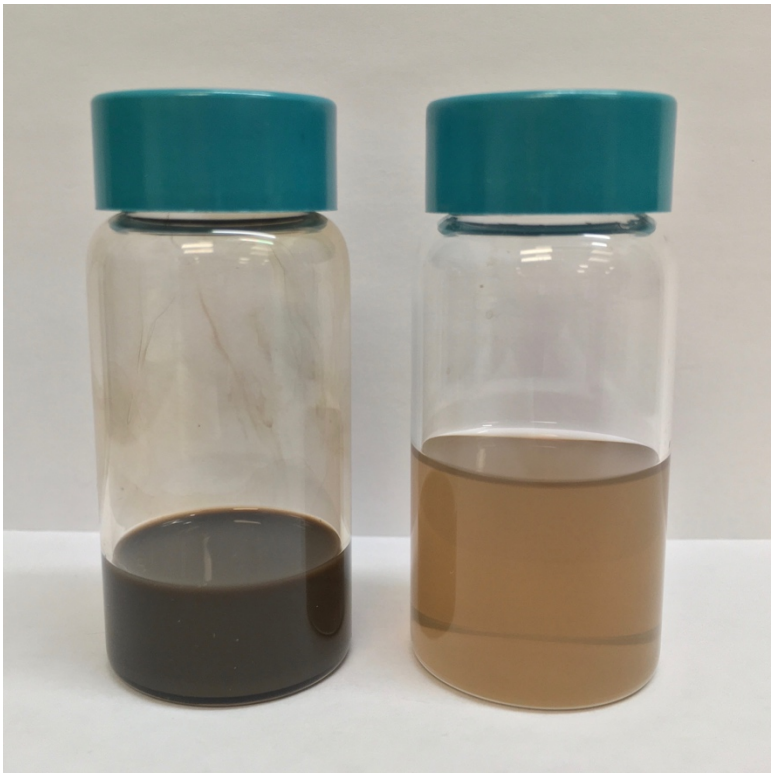

Fig. S2.29. Image of Fe_2GeS_4 NP dispersions in chloroform with a concentrated solution on the left and a dilute solution on the right. The particles are dark brown and form a turbid suspension when concentrated. The solution is not slightly more cloudy than most quantum dot suspensions, but the particles remain suspended for days, slowly precipitating out of solution. At lower concentrations, the NPs form transparent, brown solutions.

APPENDIX B

SUPPORTING INFORMATION FOR CHAPTER 3: OLIVINE CRYSTAL STRUCTURE-DIRECTED TWINNING IN IRON GERMANIUM SULFIDE (Fe_2GeS_4) NANOPARTICLES

Experimental Details

Materials Unless stated, all chemicals were used as received. Oleylamine was sparged with N_2 under heating at 70 ˚C prior to use, and dissolved gases were minimized in washing solvents (toluene, chloroform, hexanes) used in the glove box by the freeze-pump-thaw degassing process. Iron(II) chloride (anhydrous, beads, –10 mesh, 99.99% trace metals basis), germanium(IV) iodide (99.99% trace metals basis), sulfur (reagent grade, purified by sublimation, –100 mesh particle size, powder), lithium bis(trimethylsilyl)amide (97%), and oleylamine (technical grade, 70%) were purchased from Sigma-Aldrich. Technical grade toluene, hexanes (mixture of isomers), ethanol, isopropanol, and chloroform were obtained from Fisher Scientific.

Fe_2GeS_4 NP synthesis (0.16 mmol scale) In a N_2 glove box, 41 mg (0.32 mmol) $FeCl_2$, 141 mg (0.243 mmol) GeI_4, and 6.0 mL (18.2 mmol) OLA were loaded in a 50 mL three-neck round-bottom flask equipped with a magnetic stir bar, thermocouple, and condenser and sealed with rubber septa. A glass scintillation vial was loaded with 19 mg (0.59 mmol) S, 81 mg (0.49 mmol) $LiN(SiMe_3)_2$, and 2.0 mL (6.1 mmol) OLA prior to being capped by a rubber septum. The Fe:Ge:S molar ratio of 2:1.5:3.6 was used (50% excess Ge, 10% deficient S). Outside of the glove box, the Fe/Ge/OLA flask was attached to a Schlenk line under Ar and heated to 120 ˚C under vacuum with stirring. It was held under these degassing conditions for 1 h. The S/$LiN(SiMe_3)_2$/OLA vial was sonicated during the degassing hour for dissolution of the powders. The Fe/Ge/OLA solution was heated to 320 ˚C under Ar at 500 ˚C/h. At temperature, the S/$LiN(SiMe_3)_2$/OLA solution was rapidly injected into the flask using a gas-tight syringe, and a 10 min growth was carried out. To quench the reaction, the solution was removed from the reaction flask with a gas-tight syringe and injected into toluene. Workup followed immediately.

Coalesced Fe_2GeS_4 NP synthesis (0.16 mmol scale) In a N_2 glovebox, the 50 mL flask and glass scintillation vial (vial #1) described in the 0.16 mmol scale Fe_2GeS_4 NP reaction were prepare alongside a 25 mL flask containing 41 mg (0.32 mmol) $FeCl_2$, 141 mg (0.243 mmol) GeI_4, and 3 mL (9.1 mmol) OLA as well as a glass scintillation vial containing 19 mg (0.59 mmol) S, 40 mg (0.25 mmol) $LiN(SiMe_3)_2$, and 1 mL (3.1 mmol) OLA (vial #2). The 50 mL and 25 mL flasks were equipped with magnetic stir bars and thermocouples, and the 50 mL flask als had a condenser. All of the flasks were sealed with rubber septa and outside of the glove box, the 50 mL and 25 mL flasks were attached to a Schlenk line under Ar and were heated to 120 ˚C under vacuum with stirring. Both scintillation vials were sonicated during the degassing hour for dissolution of the powders. The 50 mL flask solution was then heated to 320 ˚C under Ar at 500 ˚C/hr. At temperature, the contents of vial #1 were injected. After a 10 min growth period, the solutions from both the 25 mL flask and vial #2 were simultaneously injected into the NP reaction flask. After a second 10 min growth, the reaction was quenched by extraction via a gas-tight syringe and injection into toluene. Workup followed immediately.

NP product workup and purification The reaction solution/toluene mixture (~1:1 vol) was divided among centrifuge tubes, and isopropanol was added to achieve a 1:1:2 volume ratio of reaction solution:toluene:isopropanol. The solutions were shaken to mix and centrifuged at 3500 rpm for 2 min to precipitate the solid products. The clear, red-brown supernatant was discarded. A small amount of chloroform was added to each centrifuge tube (just enough to disperse the NP pellet) and the mixture was shaken to disperse the NPs followed by addition of an excess of ethanol. The tubes were shaken once more and then centrifuged at 3500 rpm for 2 min. The supernatant was discarded prior to the addition of an excess of hexanes to each tube. The pellets were shaken to disperse followed by centrifugation at 3500 rpm for 2 min. Finally, the pellets were either dried under vacuum or dispersed in a solvent for characterization. The workup can be performed on the bench-top or in a N_2 glovebox. On the bench-top in air, ACS grade solvents that were used as received. In the glovebox, solvents that were either purchased anhydrous (ethanol) or had

dissolved gases minimized through the freeze-pump-thaw degassing process (toluene, chloroform, hexanes) were used.

Characterization of NP products All NP products were examined via powder X-ray diffraction (PXRD) for phase-purity and matched the pattern provided in our synthesis report[25]. Diffraction was performed on a Bruker D8 Discover X-ray diffractometer using a Cu Kα radiation source (λ = 1.54 Å) and a Lynxeye XE-T positron-sensitive detector. Samples were dropcast from chloroform onto zero-background Si wafer sample holders. Transmission electron microscopy (TEM) was carried out on a JEOL JEM2100F at a working voltage of 200 keV. Images and selected area electron diffraction patterns were collected and analyzed in Digital Micrograph of the Gatan Microscopy Suite and ImageJ software. Simulated electron diffraction patterns were generated using CrystalMaker and Single Crystal software, and crystal structures were modeled in VESTA software[41]. TEM samples were prepared by dip casting carbon-coated Cu grids (200 mesh, Electron Microscopy Sciences) into dilute particle dispersions in a mixture of chloroform and hexanes. Scanning electron microscopy (SEM) analysis was performed on a JEOL JSM-6500F field emission electron microscope at a working voltage of 20.0 kV.

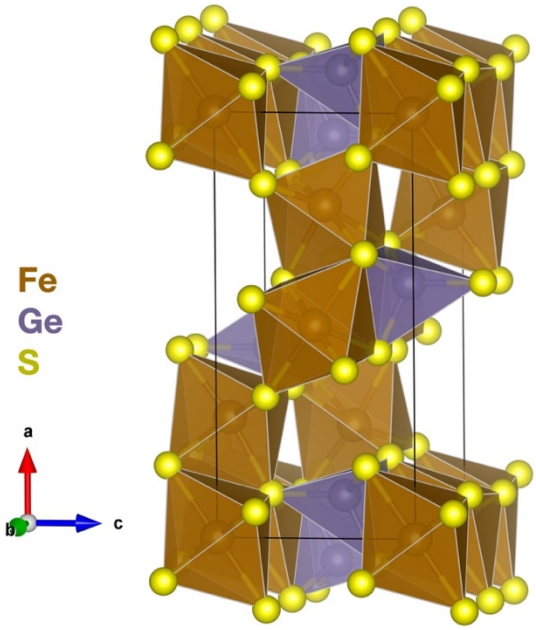

Fig. S3.1. The crystal structure of Fe_2GeS_4. Black lines outline the orthorhombic (*Pnma*) unit cell. Iron atoms and octahedra are in brown, germanium atoms and tetrahedra are in purple, and sulfur atoms are in yellow.

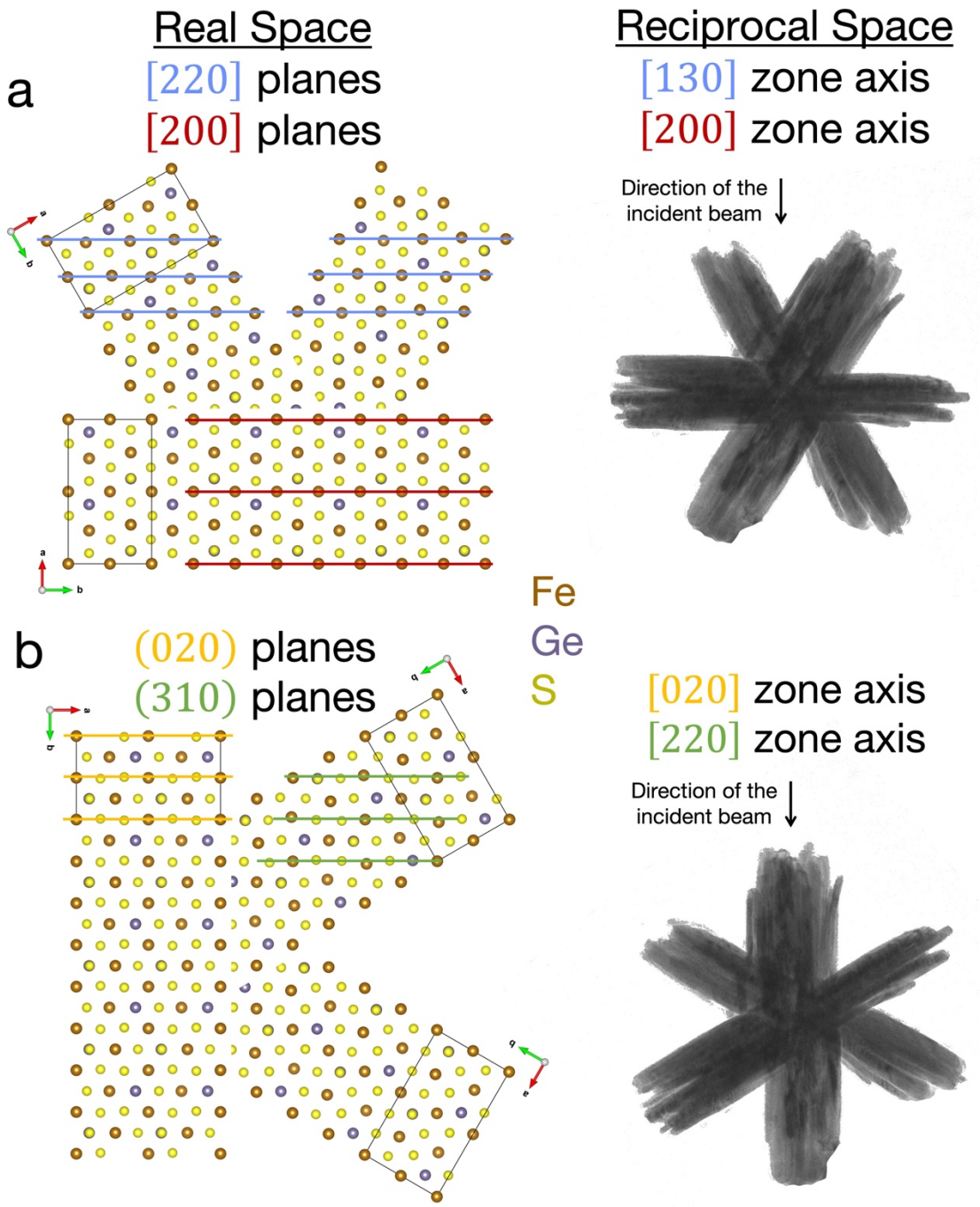

Fig. S3.2. a, The SAED pattern of a twinned NP that is oriented with one set of nanoplates parallel to the carbon substrate of the TEM grid produces the summation of the patterns from the [200] and [130] zone axes with the [200] pattern originating from the nanoplates oriented parallel to the TEM grid and the [130] pattern originating from the nanoplates at 60˚ angles relative to the TEM grid. The reciprocal space [130] zone axis corresponds to the real space (220) planes existing normal to the incident beam. **B,** The SAED pattern from a twinned NP that is oriented with one set of nanoplates perpendicular to the TEM grid produces the summation of the patterns from the[020] and [220] zone axes with the [020] pattern originating from the nanoplates perpendicular to the grid and the[220] pattern from the nanoplates at 30˚ angles relative to the TEM grid. The reciprocal space [220] zone axis corresponds to the real space (310) planes existing normal to the incident beam.

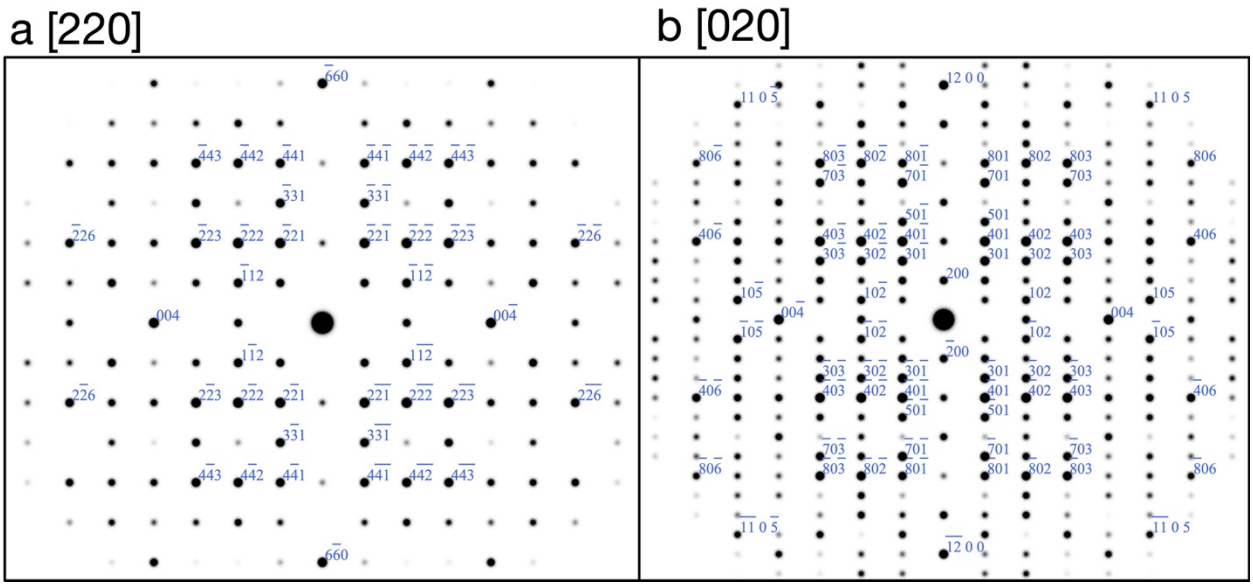

Fig. S3.3. Simulated electron diffraction patterns for the, **a**, [220] and, **b**, [020] zone axes of Fe_2GeS_4.

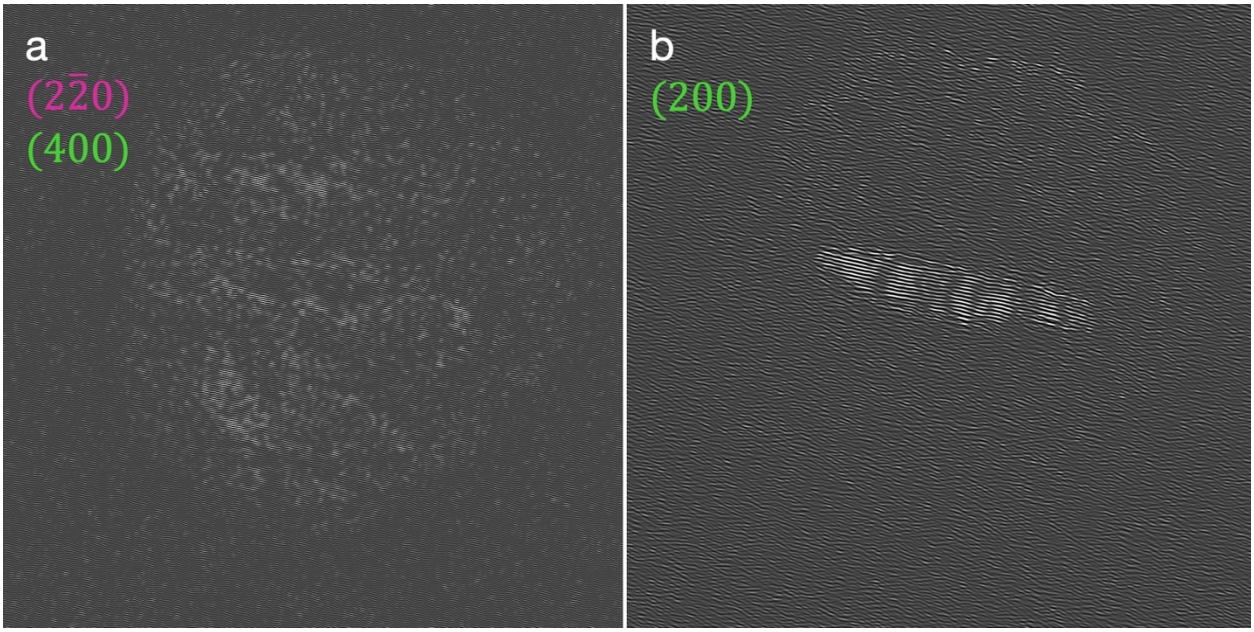

Fig. S3.4. Inverse fast Fourier transform (FFT) images. A FFT of the original TEM image was produced, and two masked versions of the FFT were created in which everything but the contents of each the green and pink circles was removed. The pink-circles-masked FFT image was converted into an inverse FFT image seen here in part **a**, and the green-circles-masked FFT image was converted into an inverse FFT image seen in part **b**. This spatially identified the lattice spacings in the TEM image. The (200) spacings are concentrated in the nanoplate that is perpendicular to the TEM grid seen along the center of the particle, and the (2$\bar{2}$0) and (400) spacings (which are nearly identical in distance at 3.122 Å and 3.117 Å, respectively) originate from the entire NP. The (2$\bar{2}$0) come from the angled nanoplates, and the (400) come from the perpendicular nanoplate.

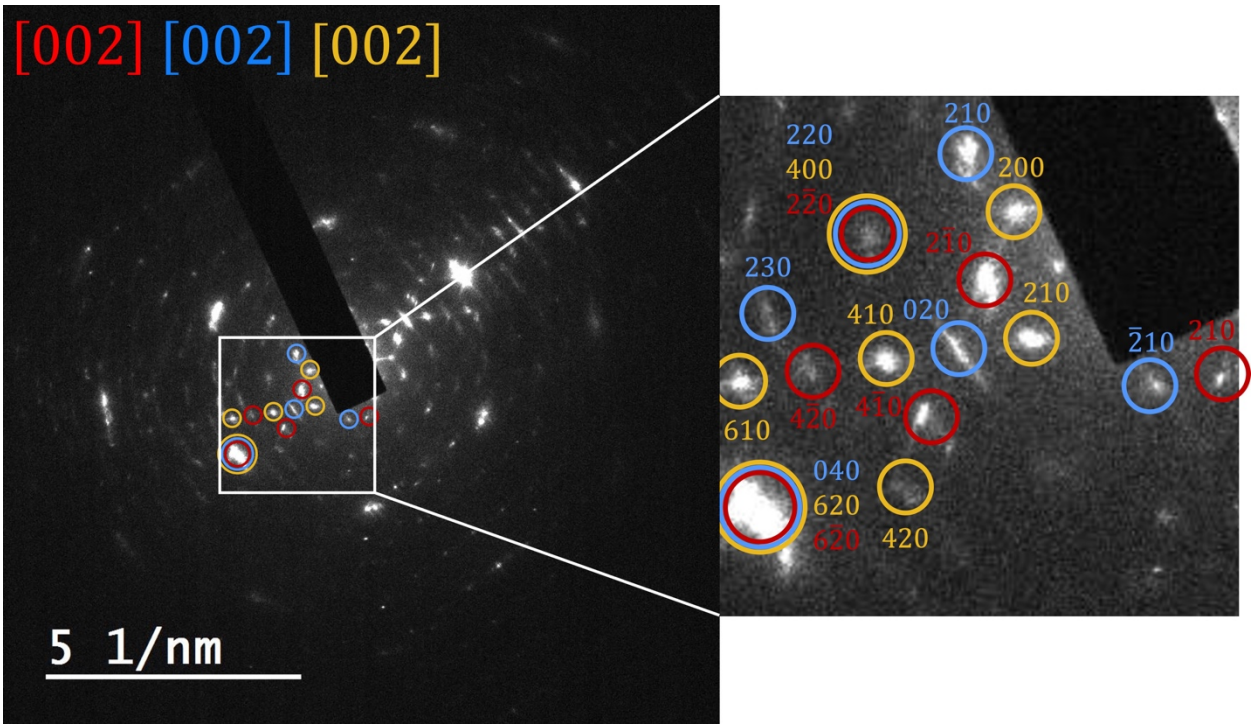

Fig. S3.5. Diffraction spot labels for the SAED pattern of Fig. 3.5d. The red, yellow, and blue labels correspond to the three sets of stacked nanoplates in the NP (see arrows in Fig. 3.5e).

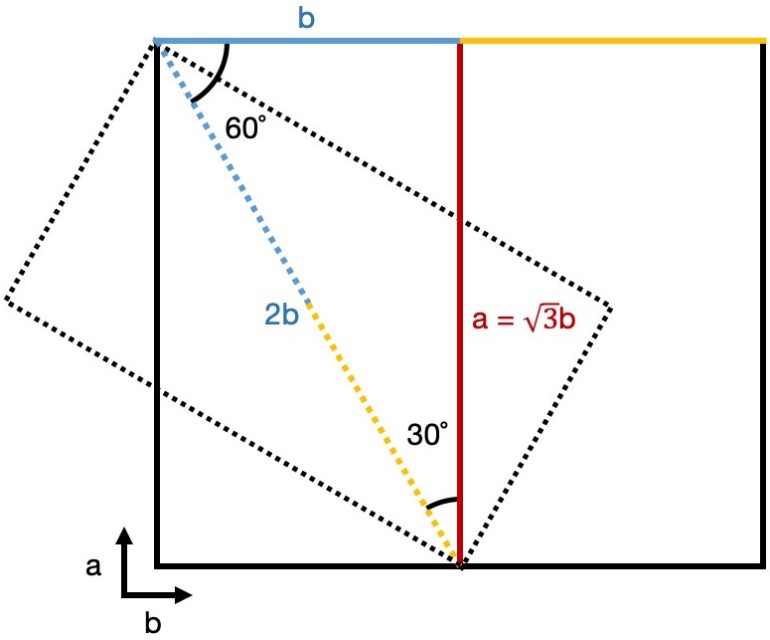

Fig. S3.6. When the unit cell dimensions of an orthorhombic crystal structure exhibit the ratio of $\sqrt{3}$: 1, shown here as $a \approx \sqrt{3} \cdot b$, hexagonal pseudosymmetry can be observed. Crystal twins or trillings can form.

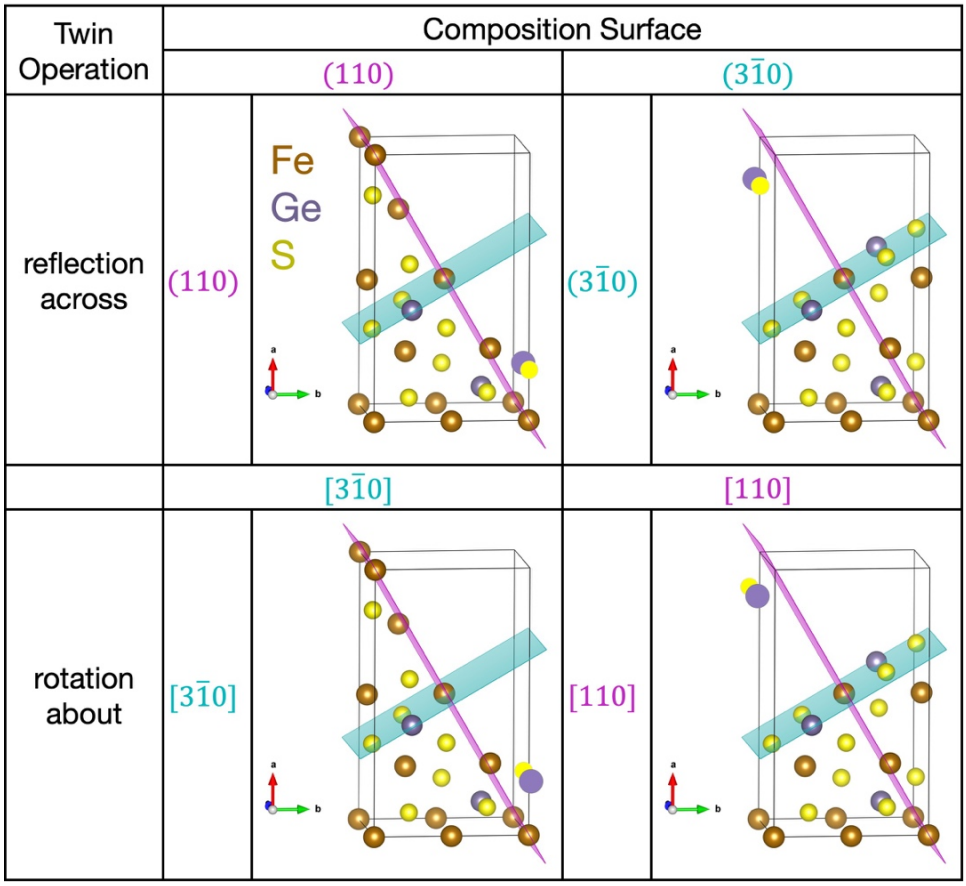

Fig. S3.7. Four twinning operations possible for Fe_2GeS_4. The reflection twins across {110} and {310} are depicted in the first row. The twin plane is also the composition surface. The reflection twins about <110> and <310> are depicted in the second row, and the composition surface is the same axis as the twin rotation axis. Because the two sets of planes are perpendicular to one another, reflection across {110} and rotation about <310> are visually similar but unique by atomic positions. In each depiction, two atoms (Ge and S) are drawn in the opposite twin domain showing that the reflection and rotation operations are distinct from one another.

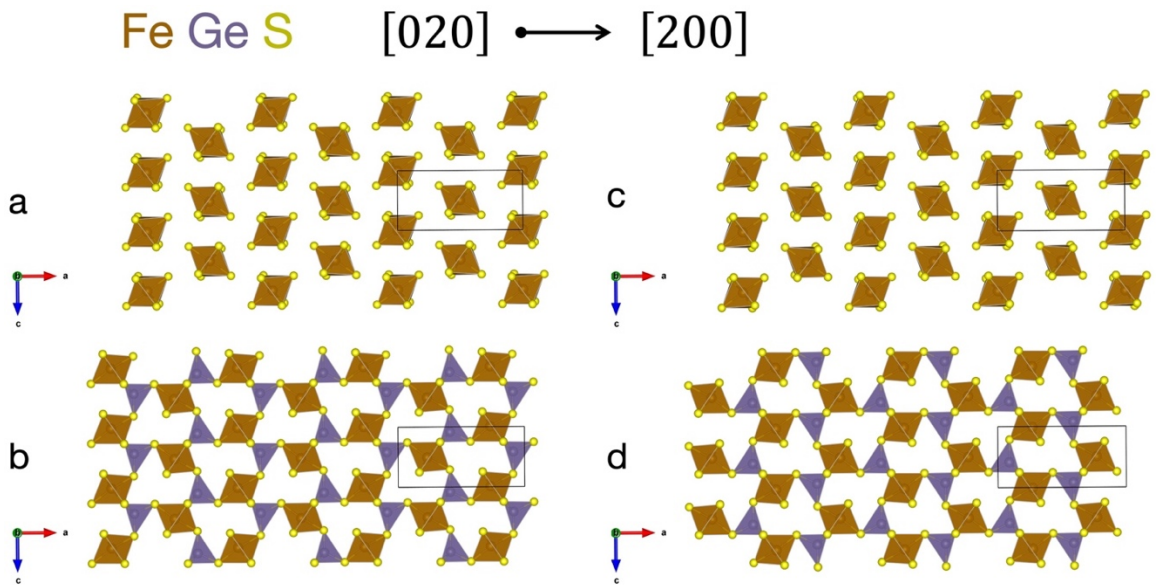

Fig. S3.8. Individual layers of the (040) lattice planes stacked in order a through d.

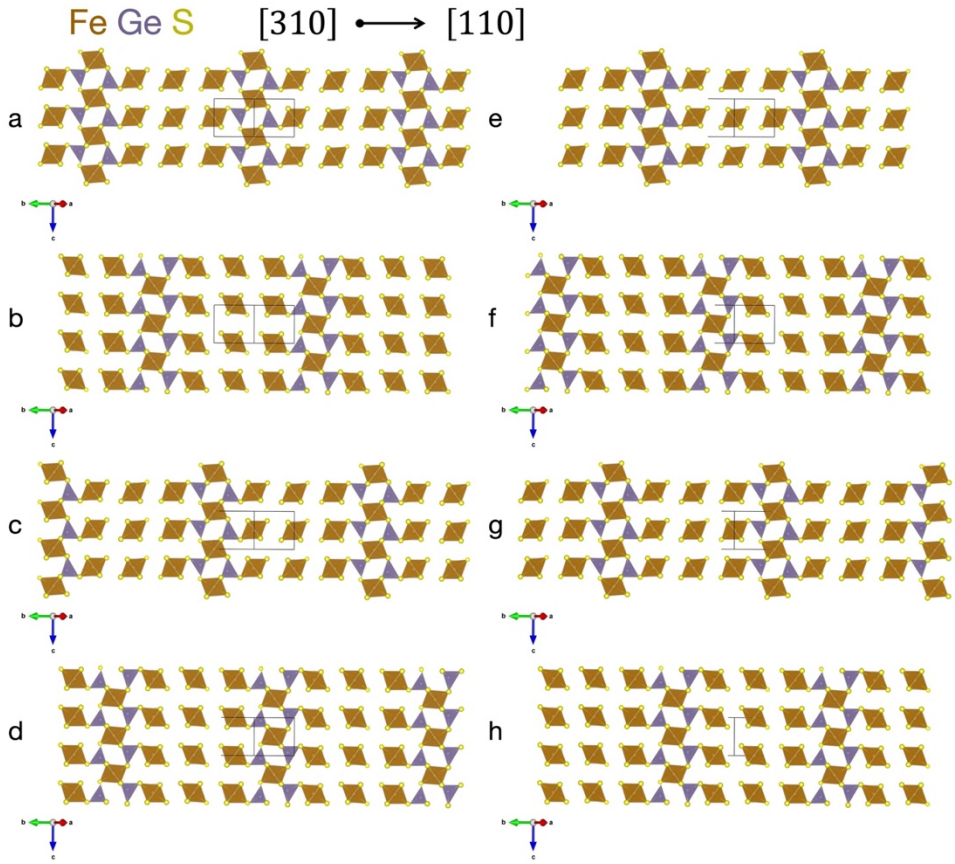

Fig. S3.9. Individual layers of the (310) lattice planes stacked in order a through h.

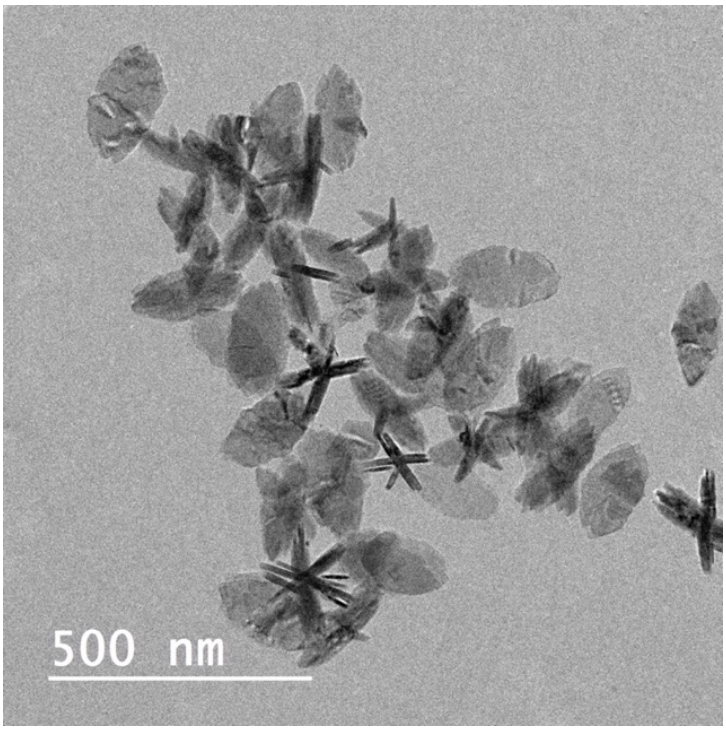

Fig. S3.10. TEM image of the Fe_2GeS_4 NP reaction carried out at one quarter the concentration of all precursors relative to the 0.16 mmol Fe_2GeS_4 NP reaction. The oval nanoplates are not twinned and encompassed 38% of the NPs (n = 554 NPs counted).

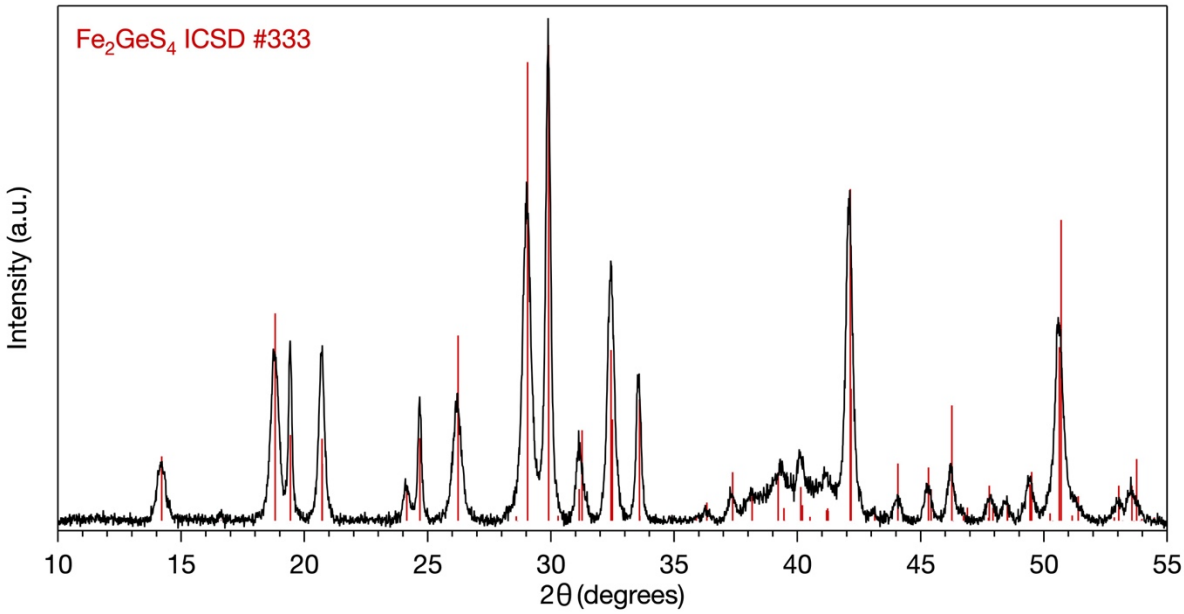

Fig. S3.11. PXRD pattern of the products from the Fe_2GeS_4 NPs carried out with a 2nd injection to form coalesced NPs. Phase-pure Fe_2GeS_4 was identified.

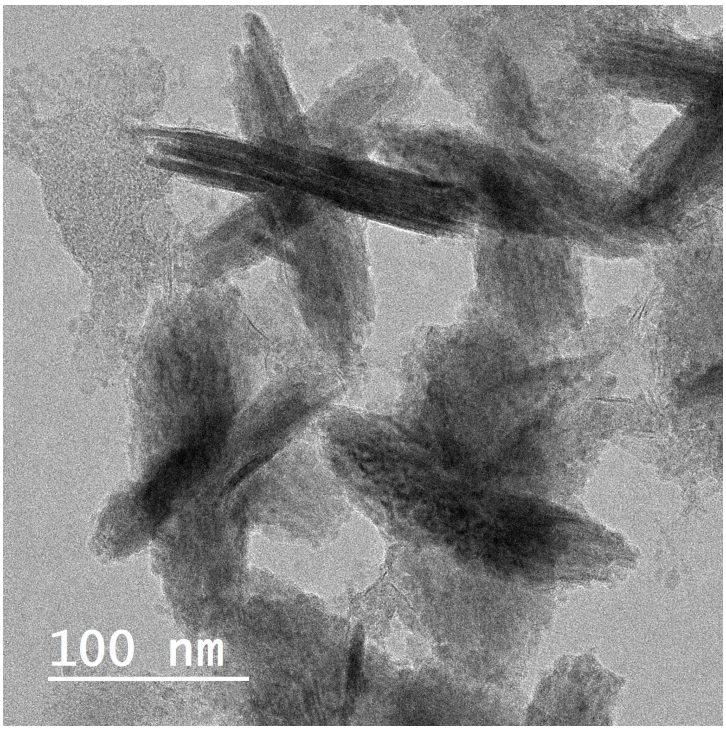

Fig. S3.12. TEM image of Fe_2GeS_4 NPs (0.16 mmol scale reaction) grown for 4 min instead of 10 min, exhibiting the large sizes attained early on during growth. The material and small particles alongside the large Fe_2GeS_4 contain some Fe, Ge, and S by STEM EDS but are mostly organic. It is hard to determine whether the small particles exist in the reaction solution and are involved in coalescence onto existing Fe_2GeS_4 NPs or whether they form upon quenching the reaction solution and exist as dissolved, unreacted monomers at the reaction temperature (320 ˚C).

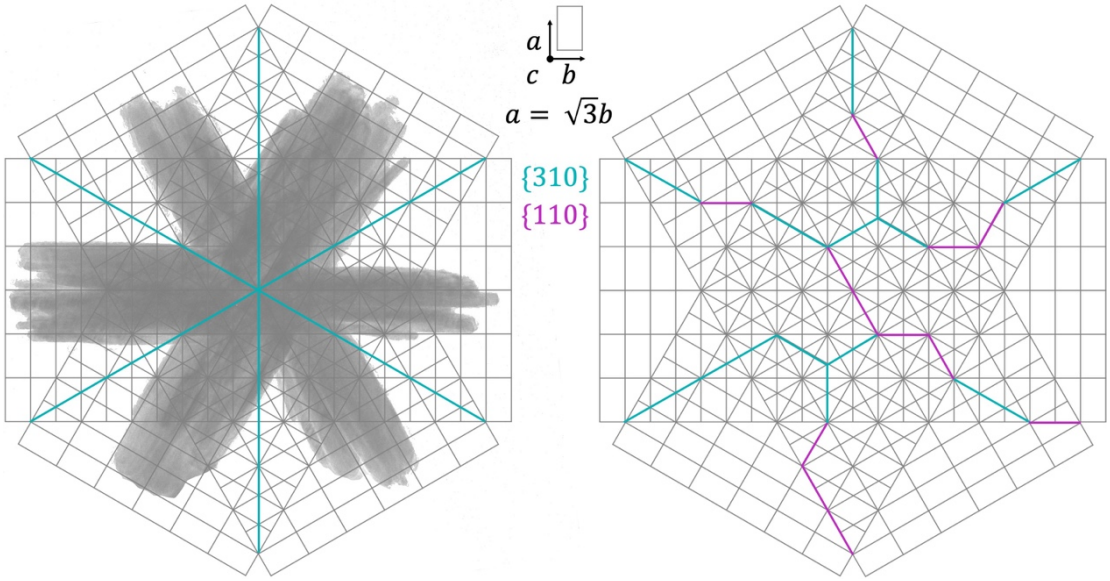

Fig. S3.13. A scheme of the twinning boundaries for trillings in olivines. The rectangular grids mimic a grid of olivine unit cells viewed along the [001] direction. The teal lines in the depiction on the left side show the twin planes (and composition surfaces) if the twinning were exclusively on the {310} planes. The right side shows the possibility for the twin boundaries to be more complex with a mixture of the {310} and {110} twin planes in teal and fuchsia, respectively.

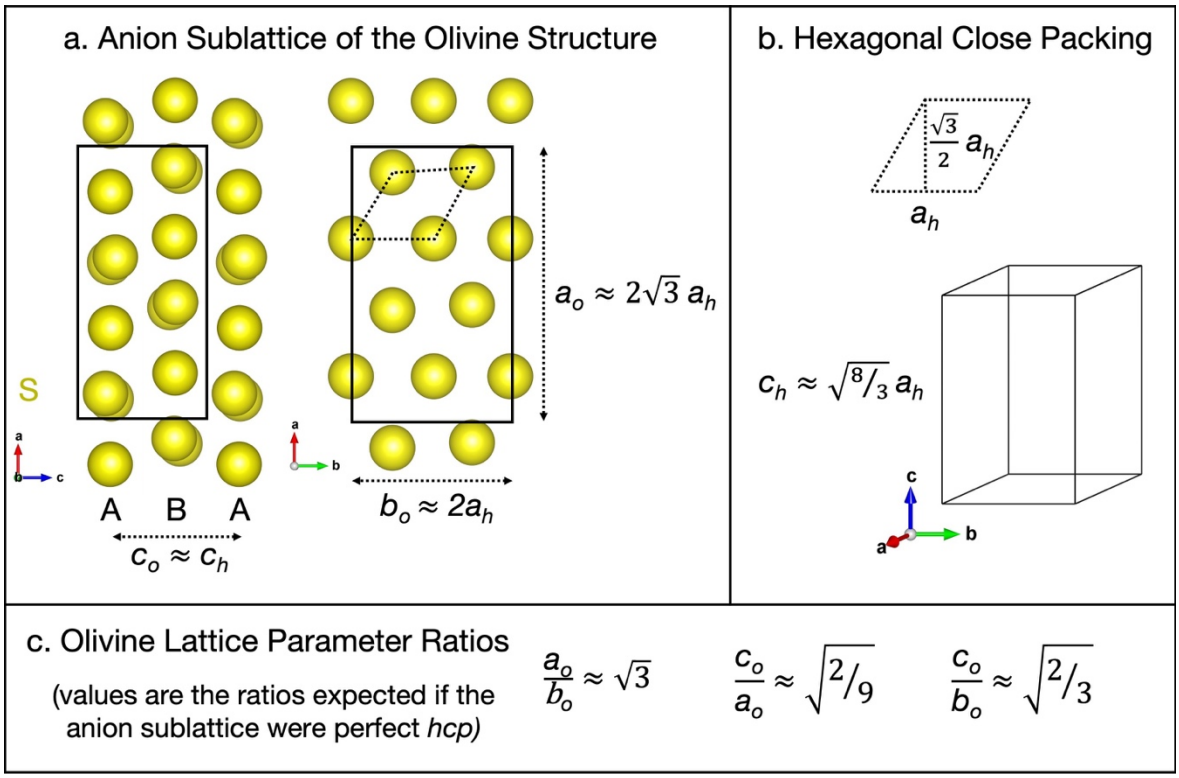

Fig. S3.14. The pseudosymmetry of the orthorhombic olivine crystal structure type. The anions form a distorted *hcp* sublattice with the *ABAB*… layers stacking in the [001] direction. **a**, Depicted are the olivine unit cell lattice parameters (a_o, b_o, c_o) defined relative to **b**, the unit cell parameters of a perfect *hcp* sublattice (a_h, c_h). **c**, The ratios between olivine lattice parameters if the anion sublattice were a perfectly *hcp* lattice.

APPENDIX C

HEXAGONAL PSEUDOSYMMETRY IN ORTHORHOMBIC OLIVINE COMPOUNDS

(Mg_2SiO_4 STRUCTURE TYPE)

This table lists all of the Mg_2SiO_4 structure type compounds from the Inorganic Crystal Structure Database (ICSD) according to the closeness of the ratios between the lattice dimensions compared to the values expected for a perfectly hexagonally close-packed anion sublattice. For the calculations used to generate this list, see Chapter 3, Fig. S3.14.

Coll Code	Molecular Formula	Space Group	R value	$\%\left\lvert\frac{Max/Med}{\sqrt{3}}\right\rvert$	$\%\left\lvert\frac{Min/Med}{\sqrt{2/3}}\right\rvert$	$\%\left\lvert\frac{Min/Max}{\sqrt{2/9}}\right\rvert$
402062	Li2(ZnI4)	Pnma	0.024	0.011	0.329	0.318
202284	CaMg(SiO4)	Pbnm	0.066	0.014	7.918	7.903
67654	CaYb(InSe4)	Pnma	0.041	0.016	0.625	0.641
83824	Ca(Fe0.77Mg0.22)(SiO4)	Pbnm	0.024	0.020	7.951	7.929
281318	LiIn(SiO4)	Pbnm	0.025	0.021	2.187	2.208
83825	Ca(Fe0.69Mg0.31)(SiO4)	Pbnm	0.023	0.023	7.979	7.954
38344	MgAl2S4	Pnma	0.055	0.045	0.437	0.393
202283	CaMg(SiO4)	Pbnm	0.055	0.113	7.948	8.069
69034	Li2(ZnI4)	Pnma	0.055	0.158	0.325	0.482
202285	CaMg(SiO4)	Pbnm	0.065	0.177	7.927	7.736
79672	MgAl2S4	Pnma	0.036	0.180	0.035	0.145
238558	Fe1.04Li0.94P0.92O4	Pnma	0.0347	0.180	3.352	3.167
87086	Fe2GeSe4	Pnma	0.094	0.180	0.513	0.692
100649	Ca(Mg0.93Fe0.07)(SiO4)	Pbnm	0.029	0.182	8.496	8.694
333	Fe2(GeS4)	Pnma	0.044	0.211	0.214	0.424
23526	Fe2GeS4	Pnma	0.11	0.211	0.214	0.424
68351	(Ca0.255Co0.745)Ca(SiO4)	Pbnm	0.021	0.241	8.279	8.018
430197	NaYbSiO4	Pnma	0.0217	0.255	1.612	1.872
100648	Ca(Mg0.93Fe0.07)(SiO4)	Pbnm	0.028	0.255	8.395	8.672
202281	CaMg(SiO4)	Pbnm	0.058	0.255	7.984	8.260
202282	CaMg(SiO4)	Pbnm	0.074	0.255	7.984	8.260
157874	(Mn1.23Fe0.77)(GeS4)	Pnma	0.021	0.305	0.246	0.059
432285	CoLi(PO4)	Pnma	0.0229	0.312	2.725	2.406
230848	Li0.8In0.8Co0.4SiO4	Pbnm	0.0824	0.316	1.947	2.270
173461	(Ca1.14Mn0.86)(GeO4)	Pnma	0.0234	0.326	4.888	4.547
243675	Mg2SnS4	Pnma	0.018	0.327	1.498	1.820
161793	(Li0.6Fe1.4)((PO4)0.6(SiO4)0.4)	Pnma	0.0199	0.350	3.666	3.304
202286	CaMg(SiO4)	Pbnm	0.056	0.355	7.925	7.543
161794	(Li0.5Fe1.5)((PO4)0.5(SiO4)0.5)	Pnma	0.0237	0.367	3.536	3.157
157875	(Mn1.53Co0.47)(GeS4)	Pnma	0.022	0.370	0.448	0.077
237898	(Fe1.07Li0.83)PO4	Pnma	0.0694	0.378	4.078	3.687
73223	Li2(ZnBr4)	Pnma	0.074	0.387	0.508	0.891
79792	Ca(Mg0.88Fe0.12)(SiO4)	Pnma	0.014	0.387	8.053	8.474
173462	(Ca1.17Mn0.83)(GeO4)	Pnma	0.021	0.389	4.891	4.484
200297	Li2(UO4)	Pnma	0.061	0.399	3.544	3.157
100647	Ca(Mg0.93Fe0.07)(SiO4)	Pbnm	0.025	0.415	8.253	8.704
161795	(Li0.29Fe1.71)((PO4)0.29(SiO4)0.71)	Pnma	0.0238	0.416	3.377	2.949
75942	(Mg0.92Fe0.015Al0.05)Al(BO4)	Pbnm	0.017	0.421	7.081	7.534
87425	(Li0.666Fe0.111)Co(PO4)	Pnma	0.035	0.427	2.249	1.814
432283	CoLi(PO4)	Pnma	0.0267	0.431	2.730	2.289
258924	LiCo(PO4)	Pnma	0.0205	0.442	2.795	2.343
291401	LiCoPO4	Pnma	0.0205	0.442	2.795	2.343

254357	CaMgSiO4	Pmnb	0.071179	0.449	7.971	8.458
262123	NaCa(AsO4)	Pnma	0.0209	0.453	3.788	3.319
258926	Li0.945Fe0.103Co0.924(PO4)	Pnma	0.0287	0.460	2.930	2.458
183756	Al(Mg0.96Fe0.04)(BO4)	Pnma	0.019	0.461	7.119	7.615
237899	Li0.87Fe1.05PO4	Pnma	0.0453	0.472	4.210	3.721
202280	CaMg(SiO4)	Pbnm	0.074	0.475	8.070	8.586
237901	Fe0.77Li0.8Mn0.3PO4	Pnma	0.0586	0.479	4.159	3.663
237903	Fe0.78Li0.86Mn0.29PO4	Pnma	0.0585	0.479	4.159	3.663
51201	LiNi(AsO4)	Pnma	0.103	0.479	0.584	0.105
432140	CoLi(PO4)	Pnma	0.0348	0.480	2.867	2.376
202287	CaMg(SiO4)	Pbnm	0.066	0.484	7.895	7.375
332	Fe2(SiS4)	Pnma	0.032	0.486	1.121	0.632
34591	MgCa(SiO4)	Pbnm	0.068	0.487	8.065	8.593
245184	LiNi(AsO4)	Pnma	0.078	0.491	0.601	0.111
34349	AlMg(BO4)	Pnma	0.11	0.492	7.061	7.591
87424	(Li0.748Fe0.084)Co(PO4)	Pnma	0.03	0.492	2.467	1.965
163524	Al(Mg0.952Fe0.048)(BO4)	Pnma	0.044	0.494	7.140	7.672
432131	CoLi(PO4)	Pnma	0.0253	0.497	2.814	2.305
100646	Ca(Mg.93Fe.07)(SiO4)	Pbnm	0.03	0.498	8.014	8.555
40736	Mg0.136Fe1.741Mn0.123(SiO4)	Pbnm	0.026	0.500	3.151	2.638
247496	LiCo(PO4)	Pnma	0.0376	0.505	2.862	2.346
258925	LiCo(PO4)	Pnma	0.025	0.509	2.852	2.331
81552	(Sc.7Mg.3)(Sc.3Mg.7)GaS4	Pnma	0.018	0.509	0.237	0.743
161792	(Li0.93Fe1.07)((PO4)0.93(SiO4)0.07)	Pnma	0.0515	0.512	4.167	3.636
68784	MnSc(GaS4)	Pnma	0.018	0.517	0.373	0.886
159317	(Li0.938Fe0.031)Fe(PO4)	Pnma	0.033	0.518	4.371	3.833
432134	CoLi(PO4)	Pnma	0.0228	0.518	2.827	2.298
247497	LiCo(PO4)	Pnma	0.0684	0.518	2.873	2.342
432132	CoLi(PO4)	Pnma	0.0209	0.521	2.847	2.314
247495	LiCo(PO4)	Pnma	0.0357	0.522	2.876	2.342
400625	LiCo(PO4)	Pnma	0.03	0.524	3.064	2.526
88517	Fe2(SiS4)	Pnma	0.016	0.526	1.136	0.607
237907	Fe0.53Li0.86Mn0.54PO4	Pnma	0.0586	0.534	4.180	3.626
237905	Fe0.51Li0.7Mn0.58PO4	Pnma	0.0588	0.534	4.180	3.626
40737	Mg0.105Fe1.741Mn0.121(SiO4)	Pbnm	0.023	0.537	3.229	2.678
290336	LiFe(PO4)	Pnma	0.0145	0.540	4.497	3.935
173773	LiCo(PO4)	Pnma	0.018	0.544	2.895	2.338
432133	CoLi(PO4)	Pnma	0.0213	0.545	2.881	2.323
87422	LiCo(PO4)	Pnma	0.049	0.552	2.884	2.319
87423	(Li0.893Fe0.036)Co(PO4)	Pnma	0.039	0.554	2.689	2.124
252398	Li(Co0.94V0.04)(PO4)	Pnma	0.237	0.557	2.823	2.254
252399	Li(Co0.91V0.06)(PO4)	Pnma	0.218	0.559	2.834	2.262
252397	Li(Co0.97V0.02)(PO4)	Pnma	0.215	0.560	2.813	2.241
252400	Li(Co0.88V0.08)(PO4)	Pnma	0.179	0.560	2.827	2.255
73222	Li2(ZnCl4)	Pnma	0.053	0.561	0.893	1.446
402399	Li2(ZnCl4)	Pnma	0.018	0.561	0.893	1.446
432139	CoLi(PO4)	Pnma	0.0291	0.562	2.930	2.354
432136	CoLi(PO4)	Pnma	0.0244	0.565	2.911	2.334
432135	CoLi(PO4)	Pnma	0.0255	0.567	2.891	2.312
252396	LiCo(PO4)	Pnma	0.212	0.567	2.828	2.249
181272	LiFe(PO4)	Pnma	0.0733	0.571	4.047	3.456
432284	CoLi(PO4)	Pnma	0.0257	0.582	2.919	2.324
40738	Mg0.075Fe1.791Mn0.134(SiO4)	Pbnm	0.023	0.590	3.236	2.631
77546	LiSc(SiO4)	Pbnm	0.063	0.592	1.496	2.100
40735	Mg0.145Fe1.742Mn0.113(SiO4)	Pbnm	0.022	0.597	3.145	2.533
258927	Li0.944Fe0.105Co0.924(PO4)	Pnma	0.0338	0.599	2.717	2.106
432138	CoLi(PO4)	Pnma	0.0303	0.600	2.971	2.357
245181	LiMn(AsO4)	Pnma	0.077	0.611	2.267	2.896
75538	LiTm(SiO4)	Pnma	0.021	0.615	4.483	3.844
26375	Fe2SiO4	Pbnm	0.0255	0.618	3.128	2.495
71814	LiMn(AsO4)	Pmnb	0.054	0.625	2.271	2.914
432137	CoLi(PO4)	Pnma	0.0302	0.628	2.998	2.356
20056	Li(Fe.67Zn.33)(PO4)	Pnma	0.1158	0.632	4.290	3.635
237902	Fe0.75Li0.88Mn0.29PO4	Pnma	0.0336	0.632	4.354	3.698
290335	LiFe(PO4)	Pnma	0.0111	0.636	4.509	3.849
237900	Fe1.02Li0.95PO4	Pnma	0.0317	0.636	4.409	3.749

54029	Fe2(SiO4)	Pbnm	0.074	0.640	3.188	2.532
193799	LiFe(PO4)	Pnma	0.018	0.645	4.489	3.819
169812	Mn2SnTe4	Pnma	0.06	0.649	0.681	0.032
64730	Fe2(SiO4)	Pbnm	0.087	0.652	3.138	2.470
67655	CaYb(InS4)	Pnma	0.023	0.654	0.484	1.130
93039	(Li0.758Fe0.081)Mg(PO4)	Pnma	0.051	0.671	2.128	1.447
4353	Fe2SiO4	Pbnm	0.047	0.671	3.138	2.451
157876	(Mn1.85Ni0.15)(GeS4)	Pnma	0.019	0.672	0.777	0.105
183800	LiFe(PO4)	Pnma	0.0366	0.674	4.527	3.827
154119	Li0.71Fe(PO4)	Pmnb	0.0213	0.677	2.267	1.579
10408	Fe2SiO4	Pbnm	0.083	0.681	3.138	2.441
237906	Fe0.5Li0.75Mn0.55PO4	Pnma	0.0354	0.689	4.391	3.677
35089	ZnLu2S4	Pnma	0.1	0.700	0.224	0.472
290339	LiFe(PO4)	Pnma	0.0323	0.701	4.458	3.730
246857	LiFe(PO4)	Pnma	0.0668	0.704	4.548	3.817
184862	LiFe(PO4)	Pnma	0.0122	0.706	4.497	3.764
260572	LiFe(PO4)	Pnma	0.0213	0.707	4.564	3.830
155305	LiCo(AsO4)	Pnma	0.0664	0.710	0.203	0.920
158572	Fe2(SiO4)	Pnma	0.0223	0.710	3.131	2.404
10116	Fe2SiO4	Pbnm	0.049	0.710	3.225	2.498
34111	Fe2(SiO4)	Pbnm	0.075	0.720	3.119	2.382
92198	LiFe(PO4)	Pnma	0.087	0.722	4.551	3.802
260571	LiFe(PO4)	Pnma	0.0225	0.723	4.559	3.808
93038	(Li0.834Fe0.055)Mg(PO4)	Pnma	0.042	0.723	2.367	1.632
160768	Li0.97Fe(PO4)	Pnma	0.023	0.724	4.184	3.435
184863	LiFe(PO4)	Pnma	0.0118	0.724	4.547	3.795
189057	LiFe(PO4)	Pnma	0.0174	0.724	4.493	3.742
245183	LiCo(AsO4)	Pnma	0.061	0.725	0.213	0.945
10409	Fe2SiO4	Pbnm	0.057	0.727	3.054	2.311
252050	Mg2GeSe4	Pnma	0.033	0.728	0.696	0.032
154117	LiFe(PO4)	Pmnb	0.0199	0.729	4.408	3.652
165000	LiFe(PO4)	Pnma	0.0046	0.729	4.522	3.766
183801	LiFe(PO4)	Pnma	0.0363	0.729	4.555	3.798
290334	LiFe(PO4)	Pnma	0.0266	0.730	4.512	3.754
260567	Li(Fe0.97Mn0.03)(PO4)	Pnma	0.021	0.731	4.581	3.822
200155	LiFe(PO4)	Pnma	0.032	0.732	4.563	3.803
194331	LiFe(PO4)	Pnma	0.0254	0.733	4.470	3.709
190772	LiFe(PO4)	Pnma	0.0398	0.742	4.492	3.722
391296	GeMn2Se4	Pnma	0.0426	0.744	0.525	0.218
68476	Mg1.4Fe0.6(SiS4)	Pnma	0.025	0.745	1.671	0.919
183799	LiFe(PO4)	Pnma	0.0305	0.747	4.511	3.737
193640	LiFe(PO4)	Pnma	0.0281	0.750	4.472	3.695
160778	(Li0.969Al0.031)Fe(PO4)	Pnma	0.0478	0.751	4.455	3.676
56291	LiFe(PO4)	Pnma	0.0163	0.751	2.510	1.745
72545	LiFe(PO4)	Pnma	0.017	0.751	4.585	3.805
260570	LiFe(PO4)	Pnma	0.0243	0.752	4.564	3.784
162282	LiFe(PO4)	Pnma	0.0974	0.753	4.499	3.717
260569	LiFe(PO4)	Pnma	0.0198	0.754	4.464	3.682
165681	Mn2(GeTe4)	Pnma	0.056	0.757	0.514	0.241
246855	LiFe(PO4)	Pnma	0.0815	0.758	4.511	3.725
161479	LiFe(PO4)	Pnma	0.0388	0.760	4.460	3.672
91452	(Fe0.839Mn0.161)(Fe0.561Mn0.439)(SiO4)	Pbnm	0.018	0.761	3.406	2.626
181341	LiFe(PO4)	Pnma	0.0456	0.761	4.515	3.726
155635	LiFe(PO4)	Pnma	0.03	0.761	4.232	3.444
154118	Li0.63Fe(PO4)	Pmnb	0.0176	0.764	2.391	1.614
193797	LiFe(PO4)	Pnma	0.0153	0.765	4.565	3.771
190771	LiFe(PO4)	Pnma	0.0651	0.768	4.510	3.714
181342	LiFe(PO4)	Pnma	0.0549	0.768	4.403	3.607
260568	Li(Fe0.91Mn0.09)(PO4)	Pnma	0.0206	0.769	4.594	3.797
66192	(Mg.26Fe1.74)(SiO4)	Pbnm	0.0367	0.769	3.112	2.325
264743	LiFePO4	Pnma	0.034	0.769	4.478	3.681
160781	(Li0.971Ni0.029)Fe(PO4)	Pnma	0.0462	0.772	4.476	3.675
54828	Li(Fe0.79Mn0.21)(PO4)	Pbnm	0.015	0.774	4.509	3.706
100650	(Ca0.98Mn0.02)(Mn0.85Mg0.10Zn0.05)(SiO4)	Pbnm	0.024	0.776	7.825	6.994
194666	Li(Fe0.984Ni0.016Co0.0001Mn0.0001)(PO4)	Pnma	0.0678	0.779	4.522	3.713
65972	Mn1.4Fe0.6(SiS4)	Pnma	0.034	0.780	1.886	1.097

100651	(Ca0.98Mn0.02)(Mn0.85Mg0.10Zn0.05)(SiO4)	Pbnm	0.024	0.781	7.849	7.014
40734	Mg.347Fe1.548Mn.105(SiO4)	Pbnm	0.025	0.790	3.204	2.395
160780	(Li0.97V0.03)Fe(PO4)	Pnma	0.0471	0.791	4.340	3.521
160779	(Li0.977Ti0.023)Fe(PO4)	Pnma	0.0463	0.793	4.422	3.600
154670	Li(Fe0.9V0.1)(PO4)	Pnma	0.0649	0.798	4.265	3.439
159107	LiFe(PO4)	Pnma	0.0448	0.799	4.396	3.568
160777	(Li0.953Mg0.047)Fe(PO4)	Pnma	0.0428	0.801	4.348	3.519
93037	(Li0.918Fe0.027)Mg(PO4)	Pnma	0.039	0.801	2.601	1.786
159108	(Li0.953Mg0.047)Fe(PO4)	Pnma	0.0428	0.801	4.352	3.522
160776	LiFe(PO4)	Pnma	0.0448	0.802	4.395	3.565
155816	Li0.89Fe(PO4)	Pnma	0.0097	0.807	4.354	3.519
260092	Co2(SiO4)	Pnma	0.033	0.814	2.303	1.477
183874	LiFe(PO4)	Pnma	0.0346	0.815	4.367	3.524
67523	LiMg(AsO4)	Pnma	0.027	0.815	0.041	0.863
62091	Al2BeO4	Pbnm	0.049	0.820	1.042	0.220
23525	Mg2GeS4	Pnma	0.13	0.820	1.093	0.271
54829	Li(Fe0.89Mn0.11)(PO4)	Pbnm	0.015	0.821	4.222	3.374
189094	Li(Fe0.78Mn0.22)(PO4)	Pbnm	0.023	0.828	4.495	3.637
77549	LiSc(SiO4)	Pbnm	0.045	0.831	1.162	2.010
62501	Al2(BeO4)	Pbnm	0.033	0.832	1.066	0.232
260091	Co2(SiO4)	Pnma	0.0291	0.838	2.340	1.490
62093	Al2BeO4	Pbnm	0.045	0.842	1.029	0.185
77548	LiSc(SiO4)	Pbnm	0.054	0.845	1.191	2.053
194290	Be(Al1.99Fe0.01)O4	Pmnb	0.0252	0.846	1.029	0.182
10117	Fe2SiO4	Pbnm	0.053	0.851	3.323	2.451
100653	(Ca0.98Mn0.02)(Mn0.85Mg0.10Zn0.05)(SiO4)	Pbnm	0.028	0.853	7.861	6.949
193641	Li(Fe0.78Mn0.22)(PO4)	Pnma	0.0511	0.853	4.527	3.643
72416	Al2(BeO4)	Pnma	0.011	0.855	0.996	0.140
34806	Al2BeO4	Pnma	0.15	0.858	0.997	0.138
62092	Al2BeO4	Pbnm	0.037	0.859	0.984	0.124
65973	Mg1.14Fe0.86(SiS4)	Pnma	0.055	0.860	1.944	1.075
201138	LiMgPO4	Pnma	0.048	0.864	2.828	1.947
66193	(Mg.26Fe1.74)(SiO4)	Pbnm	0.0438	0.865	3.278	2.392
62612	Al2BeO4	Pnma	0.0123	0.865	1.001	0.136
190125	Al2BeO4	Pnma	0.011	0.865	1.001	0.136
158391	(Al1.989Cr0.011)BeO4	Pnma	0.041	0.868	1.011	0.142
173466	(Ca1.31Mn0.69)(GeO4)	Pnma	0.0204	0.869	5.049	4.144
76654	Li(Fe0.77Mn0.23)(PO4)	Pnma	0.28	0.870	4.512	3.610
65751	Co2(SiO4)	Pbnm	0.0327	0.875	2.450	1.561
202054	Mn2GeS4	Pnma	0.038	0.878	0.705	0.171
10118	Fe2SiO4	Pbnm	0.074	0.882	3.322	2.419
62094	Al2(BeO4)	Pbnm	0.053	0.886	0.986	0.098
62505	Al2BeO4	Pbnm	0.036	0.886	0.986	0.098
183755	Al(Al0.98Fe0.02)(BeO4)	Pnma	0.019	0.888	1.062	0.173
65750	(Co.929Mg.071)2(SiO4)	Pbnm	0.0356	0.893	2.406	1.500
193800	LiFe(PO4)	Pnma	0.046	0.894	4.425	3.500
41432	(Mn1.07Co.93)(SiO4)	Pnma	0.018	0.895	3.922	3.000
35674	Co2SiO4	Pbnm	0.0277	0.896	2.472	1.562
23582	Mn2GeS4	Pnma	0.06	0.896	0.865	0.032
24142	Mn2GeS4	Pnma	0.32	0.896	0.865	0.032
100157	Li0.91(Fe0.79Mn0.21)(PO4)	Pnma	0.08	0.899	4.282	3.353
202255	Co2SiO4	Pbnm	0.021	0.902	2.434	1.518
77547	LiSc(SiO4)	Pbnm	0.061	0.903	1.159	2.081
34817	Fe2(SiO4)	Pbnm	0.05	0.905	3.401	2.474
262962	Li0.97Fe0.79Fe0.15(PO4)	Pnma	0.0284	0.906	4.465	3.526
183690	Li(Fe0.7Zn0.3)(PO4)	Pnma	0.089	0.907	4.054	3.118
100652	(Ca0.98Mn0.02)(Mn0.85Mg0.10Zn0.05)(SiO4)	Pbnm	0.03	0.908	8.028	7.057
250116	Li4Fe3.528(PO4)4	Pnma	0.062	0.908	4.621	3.680
79741	(Mg0.879Fe0.121)(Mg0.881Fe0.119)(SiO4)	Pbnm	0.062	0.909	2.665	1.740
173458	Ca1.17Co0.83GeO4	Pnma	0.0286	0.913	4.674	5.638
50072	Co2(SiO4)	Pbnm	0.0288	0.926	2.506	1.565
54827	Li(Fe0.5Mn0.5)(PO4)	Pbnm	0.015	0.926	4.793	3.831
62095	Al2BeO4	Pbnm	0.038	0.926	0.920	0.006
62506	Al2BeO4	Pbnm	0.038	0.926	0.920	0.006
6248	Co2(SiO4)	Pbnm	0.046	0.927	2.497	1.556
77544	LiSc(SiO4)	Pbnm	0.051	0.930	1.123	2.072

190124	Al2BeO4	Pnma	0.0258	0.931	1.134	0.200
260090	Co2(SiO4)	Pnma	0.0337	0.938	2.503	1.550
10412	Fe2SiO4	Pbnm	0.051	0.939	3.041	2.082
193642	Li0.96(Fe0.53Mn0.47)(PO4)	Pnma	0.0149	0.940	4.641	3.667
200705	Co2(SiO4)	Pnma	0.057	0.941	2.771	1.812
202254	(Co1.74Mg.26)SiO4	Pbnm	0.043	0.944	2.438	1.480
193957	Li(Fe0.46Mn0.46Mg0.04)(PO4)	Pnma	0.0609	0.944	4.678	3.699
200401	LiScSiO4	Pbnm	0.016	0.944	1.150	2.115
257251	LiFePO4	Pnma	0.188	0.953	4.732	3.744
77543	LiSc(SiO4)	Pbnm	0.027	0.959	1.113	2.092
193956	Li(Fe0.48Mn0.48)(PO4)	Pnma	0.0617	0.959	4.720	3.725
245182	LiFe(AsO4)	Pnma	0.023	0.960	1.014	1.993
77545	LiSc(SiO4)	Pbnm	0.05	0.963	1.183	2.167
91451	(Fe0.666Mn0.334)(Fe0.334Mn0.666)(SiO4)	Pbnm	0.014	0.967	3.610	2.619
9689	Mg.75Fe1.10Mn.15SiO4	Pbnm	0.031	0.968	3.041	2.052
83537	FeMn(SiO4)	Pbnm	0.018	0.969	3.624	2.630
66194	(Mg.26Fe1.74)(SiO4)	Pbnm	0.0568	0.978	3.388	2.387
203015	Mg0.966Ni1.034(SiO4)	Pbnm	0.028	0.981	2.393	1.398
50073	(Co0.875Mg0.125)2(SiO4)	Pbnm	0.0427	0.982	2.471	1.474
83538	FeMn(SiO4)	Pbnm	0.017	0.983	3.660	2.651
83260	(Fe0.673Mn0.327)(Fe0.327Mn0.673)(SiO4)	Pmcn	0.02	0.983	3.660	2.651
83559	FeMn(SiO4)	Pbnm	0.025	0.987	3.722	2.708
2	(Mn1.07Co.93)(SiO4)	Pnma	0.053	1.006	3.759	2.726
83539	FeMn(SiO4)	Pbnm	0.016	1.008	3.706	2.670
25834	LiMn(PO4)	Pmnb	0.076	1.009	4.988	3.940
54826	Li(Fe0.27Mn0.73)(PO4)	Pbnm	0.017	1.019	4.907	3.849
10414	Fe2SiO4	Pbnm	0.057	1.025	3.307	2.258
83540	FeMn(SiO4)	Pbnm	0.016	1.026	3.749	2.695
83558	FeMn(SiO4)	Pbnm	0.025	1.028	3.800	2.743
83557	FeMn(SiO4)	Pbnm	0.025	1.030	3.818	2.760
202253	(Co1.41Mg.59)SiO4	Pbnm	0.019	1.038	2.425	1.373
65749	(Co.745Mg.255)2(SiO4)	Pbnm	0.0331	1.041	2.425	1.370
264745	Li(Ni0.9Co0.1)PO4	Pnma	0.018	1.041	2.279	1.225
240966	Li(Ni0.66Fe0.34)(PO4)	Pnma	0.0203	1.042	2.620	1.561
50074	(Co0.75Mg0.25)2(SiO4)	Pbnm	0.0211	1.044	2.497	1.439
83542	FeMn(SiO4)	Pbnm	0.013	1.046	3.808	2.733
83541	FeMn(SiO4)	Pbnm	0.019	1.047	3.784	2.709
83556	FeMn(SiO4)	Pbnm	0.025	1.048	3.840	2.763
83543	FeMn(SiO4)	Pbnm	0.013	1.057	3.851	2.766
9691	Mg.75Fe1.10Mn.15SiO4	Pbnm	0.03	1.064	3.307	2.219
10413	Fe2SiO4	Pbnm	0.057	1.064	3.229	2.143
193643	Li0.97(Fe0.23Mn0.77)(PO4)	Pnma	0.0271	1.064	4.860	3.756
83555	FeMn(SiO4)	Pbnm	0.025	1.065	3.856	2.762
185884	LiMn((P0.845V0.155)O4)	Pnma	0.048	1.070	4.616	3.509
83544	FeMn(SiO4)	Pbnm	0.013	1.071	3.863	2.763
83554	FeMn(SiO4)	Pbnm	0.025	1.072	3.865	2.763
72929	LiNi(PO4)	Pnma	0.092	1.072	2.200	1.116
9690	Mg.75Fe1.10Mn.15SiO4	Pbnm	0.033	1.074	3.229	2.133
290182	Li0.91(Mn0.800Fe0.183)(PO4)	Pbnm	0.0235	1.081	4.958	3.836
100865	Ni(Ni0.66Mg0.34)(SiO4)	Pbnm	0.029	1.081	2.527	1.430
402760	LiNi(PO4)	Pnma	0.0369	1.083	2.121	1.026
202373	(Ni0.51Mg0.49)2(SiO4)	Pbnm	0.0274	1.086	2.396	1.296
91879	(Co0.377Ni0.396Zn0.227)2(SiO4)	Pbnm	0.025	1.089	2.476	1.372
100432	Mg1.03Mn0.97(SiO4)	Pbnm	0.029	1.090	4.285	3.160
100866	(Ni1.16Mg0.84)(SiO4)	Pbnm	0.047	1.091	2.259	1.156
264744	Li(Ni0.9Mn0.1)PO4	Pnma	0.046	1.092	2.471	1.364
83545	FeMn(SiO4)	Pbnm	0.013	1.092	3.880	2.758
290185	Li0.76(Mn0.800Fe0.180)(PO4)	Pbnm	0.0292	1.096	4.002	2.874
65748	(Co.604Mg.396)2(SiO4)	Pbnm	0.0403	1.097	2.449	1.338
203019	Mg0.62Ni1.38(SiO4)	Pbnm	0.041	1.099	2.296	1.184
247498	LiCo(PO4)	Pnma	0.0483	1.100	2.223	1.110
203016	Mg0.969Ni1.026(SiO4)	Pbnm	0.036	1.101	2.255	1.142
202375	(Ni0.75Mg0.25)2(SiO4)	Pbnm	0.032	1.102	2.271	1.156
202372	(Ni0.36Mg0.64)2(SiO4)	Pbnm	0.0228	1.102	2.427	1.310
4371	Ni1.03Mg0.97SiO4	Pbnm	0.029	1.104	2.349	1.232

60649	(Mg0.477Fe0.174Mn0.174Cr0.174)(Mg0.503Fe0.163Mn0.163Cr0.163	Pbnm	0.031	1.105	2.986	1.861
202374	(Ni0.69Mg0.31)2(SiO4)	Pbnm	0.0258	1.110	2.281	1.158
97765	LiNi(PO4)	Pnma	0.057	1.111	2.207	1.084
290184	Li0.84(Mn0.800Fe0.200)(PO4)	Pbnm	0.0292	1.113	4.732	3.580
83546	FeMn(SiO4)	Pbnm	0.012	1.113	3.896	2.753
67111	ZnTm2S4	Pnma	0.0393	1.114	0.929	0.184
73103	(Mn1.846Al0.154)((Si0.84Al0.16)S4)	Pnma	0.04	1.115	1.869	0.746
203021	Mg0.45Ni1.55(SiO4)	Pbnm	0.029	1.115	2.285	1.157
50075	(Co0.625Mg0.375)2(SiO4)	Pbnm	0.0437	1.121	2.489	1.353
31191	(Mg1.02Fe0.08Ni0.9)(SiO4)	Pbnm	0.112	1.123	2.359	1.222
203018	Mg0.66Ni1.34(SiO4)	Pbnm	0.065	1.124	2.215	1.078
157877	(Mn1.1Cd0.9)(GeS4)	Pnma	0.024	1.125	1.610	0.480
65742	(Ni.51Mg.48)2(SiO4)	Pbnm	0.0248	1.126	2.374	1.234
83547	FeMn(SiO4)	Pbnm	0.011	1.127	3.912	2.754
203013	Mg1.4Ni0.6(SiO4)	Pbnm	0.032	1.128	2.447	1.303
203022	Mg0.54Ni1.46(SiO4)	Pbnm	0.044	1.129	2.218	1.077
83548	FeMn(SiO4)	Pbnm	0.012	1.135	3.918	2.751
156792	(Fe0.935Mg1.016Mn0.04Ca0.008)(SiO4)	Pbnm	0.0115	1.138	2.928	1.770
156804	(Fe0.935Mg1.016Mn0.04Ca0.008)(SiO4)	Pbnm	0.0146	1.138	2.928	1.770
156805	(Fe0.935Mg1.016Mn0.04Ca0.008)(SiO4)	Pbnm	0.0154	1.138	2.928	1.770
156806	(Fe0.935Mg1.016Mn0.04Ca0.008)(SiO4)	Pbnm	0.0144	1.138	2.928	1.770
156807	(Fe0.935Mg1.016Mn0.04Ca0.008)(SiO4)	Pbnm	0.0196	1.138	2.928	1.770
156808	(Fe0.935Mg1.016Mn0.04Ca0.008)(SiO4)	Pbnm	0.0185	1.138	2.928	1.770
156809	(Fe0.935Mg1.016Mn0.04Ca0.008)(SiO4)	Pbnm	0.018	1.138	2.928	1.770
156810	(Fe0.935Mg1.016Mn0.04Ca0.008)(SiO4)	Pbnm	0.0193	1.138	2.928	1.770
156811	(Fe0.935Mg1.016Mn0.04Ca0.008)(SiO4)	Pbnm	0.0161	1.138	2.928	1.770
156812	(Fe0.935Mg1.016Mn0.04Ca0.008)(SiO4)	Pbnm	0.0174	1.138	2.928	1.770
156813	(Fe0.935Mg1.016Mn0.04Ca0.008)(SiO4)	Pbnm	0.0158	1.138	2.928	1.770
156814	(Fe0.935Mg1.016Mn0.04Ca0.008)(SiO4)	Pbnm	0.0165	1.138	2.928	1.770
156815	(Fe0.935Mg1.016Mn0.04Ca0.008)(SiO4)	Pbnm	0.0142	1.138	2.928	1.770
203020	Mg0.60Ni1.40(SiO4)	Pbnm	0.03	1.140	2.277	1.124
158735	(Mg1.81Fe0.19)(SiO4)	Pbnm	0.031	1.140	2.749	1.590
40733	Mg1.064Fe.902Mn.034(SiO4)	Pbnm	0.022	1.141	2.994	1.832
40732	Mg1.214Fe.786(SiO4)	Pbnm	0.015	1.144	2.882	1.718
83553	FeMn(SiO4)	Pbnm	0.023	1.147	3.930	2.751
91911	MgFe(SiO4)	Pbnm	0.032	1.149	2.908	1.739
65743	(Ni.76Mg.24)2(SiO4)	Pbnm	0.0292	1.151	2.252	1.089
167252	LiMn(PO4)	Pnma	0.0188	1.152	4.945	3.750
156793	(Fe0.935Mg1.016Mn0.04Ca0.008)(SiO4)	Pbnm	0.0111	1.155	2.961	1.785
189097	LiMn(PO4)	Pbnm	0.093	1.155	5.060	3.861
71764	Li(Mg0.5Mn0.2Fe0.3)2(PO4)2	Pbnm	0.031	1.155	1.472	0.313
83549	FeMn(SiO4)	Pbnm	0.013	1.156	3.938	2.750
202371	(Ni0.3Mg.7)2(SiO4)	Pbnm	0.0344	1.157	2.506	1.334
203010	Mg1.397Ni0.599(SiO4)	Pbnm	0.022	1.157	2.476	1.304
65747	(Co.503Mg.497)2(SiO4)	Pbnm	0.0214	1.158	2.456	1.283
69462	(Mg1.147Fe0.853)(SiO4)	Pbnm	0.027	1.160	2.929	1.748
69463	(Mg1.149Fe0.851)(SiO4)	Pbnm	0.021	1.163	2.884	1.702
243419	Fe2SiO4	Pbnm	0.0474	1.163	2.940	1.756
83550	FeMn(SiO4)	Pbnm	0.016	1.165	3.955	2.759
203017	MgNi(SiO4)	Pbnm	0.027	1.165	2.399	1.220
167251	LiMn(PO4)	Pnma	0.0289	1.166	4.968	3.758
156794	(Fe0.935Mg1.016Mn0.04Ca0.008)(SiO4)	Pbnm	0.0122	1.169	2.994	1.804
83551	FeMn(SiO4)	Pbnm	0.017	1.171	3.960	2.756
68477	Mg1.86Fe0.14(SiS4)	Pnma	0.029	1.174	2.252	1.065
69464	(Mg1.145Fe0.855)(SiO4)	Pbnm	0.024	1.174	2.848	1.654
91912	MgFe(SiO4)	Pbnm	0.032	1.175	2.959	1.763
100424	(Mg1.787Fe0.213)(SiO4)	Pbnm	0.021	1.179	2.328	1.135
54825	Li(Fe0.06Mn0.94)(PO4)	Pbnm	0.017	1.181	4.982	3.756
167253	LiMn(PO4)	Pnma	0.0303	1.183	5.003	3.776
193644	Li0.98Mn0.94(PO4)	Pnma	0.0461	1.186	5.029	3.798
203014	Mg1.4Ni0.6(SiO4)	Pbnm	0.039	1.186	2.467	1.266
264742	LiMnPO4	Pnma	0.02	1.189	5.048	3.815
189096	LiMn(PO4)	Pbnm	0.0115	1.190	5.056	3.821
156795	(Fe0.935Mg1.016Mn0.04Ca0.008)(SiO4)	Pbnm	0.0121	1.190	3.041	1.829
83552	FeMn(SiO4)	Pbnm	0.017	1.191	3.988	2.764

34208	(Mg1.04Fe0.96)(SiO4)	Pbnm	0.04	1.193	2.996	1.782
91913	MgFe(SiO4)	Pbnm	0.031	1.195	2.995	1.778
97763	LiMn(PO4)	Pnma	0.075	1.202	5.061	3.813
100362	(Mg1.727Fe0.273)(SiO4)	Pmcn	0.0202	1.203	2.818	1.595
50076	(Co0.5Mg0.5)2(SiO4)	Pbnm	0.0318	1.205	2.524	1.303
426432	Li(Mn0.95Ni0.05)(PO4)	Pnma	0.0176	1.206	5.122	3.869
173463	Ca(Ca0.16Mg0.83)(GeO4)	Pnma	0.0223	1.207	4.648	5.926
91914	MgFe(SiO4)	Pbnm	0.032	1.209	3.018	1.788
203011	Mg1.38Ni0.62(SiO4)	Pbnm	0.035	1.210	2.480	1.255
155357	CoMg(SiO4)	Pbnm	0.043	1.211	2.809	1.579
155355	CoMg(SiO4)	Pbnm	0.046	1.215	2.621	1.389
91915	MgFe(SiO4)	Pbnm	0.033	1.220	3.039	1.797
35675	Ni2SiO4	Pbnm	0.0289	1.220	2.112	0.881
100642	Ni2(SiO4)	Pbnm	0.037	1.222	2.157	0.924
79743	(Mg0.902Fe0.098)(Mg0.858Fe0.142)(SiO4)	Pbnm	0.062	1.224	3.359	2.110
173465	Ca(Ca0.11Co0.89)(GeO4)	Pnma	0.021	1.225	4.602	5.899
202376	Ni2(SiO4)	Pbnm	0.0318	1.227	2.114	0.876
155356	CoMg(SiO4)	Pbnm	0.046	1.227	2.726	1.480
100364	(Mg1.727Fe0.273)(SiO4)	Pmcn	0.0217	1.228	2.824	1.577
91916	MgFe(SiO4)	Pbnm	0.031	1.230	3.062	1.810
4370	Co1.10Mg0.90SiO4	Pbnm	0.044	1.232	2.517	1.269
155358	CoMg(SiO4)	Pbnm	0.044	1.232	2.883	1.631
34818	(Mg0.5Fe0.5)2SiO4	Pbnm	0.08	1.233	3.090	1.834
100643	Ni2(SiO4)	Pbnm	0.032	1.234	2.114	0.869
80455	CaMg(GeO4)	Pnam	0.045	1.234	4.748	6.057
100645	Ni2(SiO4)	Pbnm	0.027	1.234	2.101	0.856
202252	(Co.95Mg1.05)SiO4	Pbnm	0.021	1.235	2.477	1.227
91917	MgFe(SiO4)	Pbnm	0.031	1.238	3.085	1.824
100363	(Mg1.727Fe0.273)(SiO4)	Pmcn	0.03	1.240	2.828	1.569
9337	(Mg0.672Fe0.323)2(SiO4)	Pbnm	0.022	1.241	2.749	1.490
156798	(Fe0.935Mg1.016Mn0.04Ca0.008)(SiO4)	Pbnm	0.015	1.242	3.204	1.938
155359	CoMg(SiO4)	Pbnm	0.045	1.242	2.954	1.691
80957	Mn2(SiSe4)	Pnma	0.041	1.242	1.691	0.443
156800	(Fe0.935Mg1.016Mn0.04Ca0.008)(SiO4)	Pbnm	0.0148	1.243	3.226	1.958
156796	(Fe0.935Mg1.016Mn0.04Ca0.008)(SiO4)	Pbnm	0.0137	1.244	3.177	1.909
9336	(Mg0.637Fe0.358)2(SiO4)	Pbnm	0.022	1.245	2.855	1.591
156797	(Fe0.935Mg1.016Mn0.04Ca0.008)(SiO4)	Pbnm	0.0141	1.246	3.190	1.920
91918	MgFe(SiO4)	Pbnm	0.031	1.251	3.107	1.833
34205	(Mg1.215Fe0.785)(SiO4)	Pbnm	0.052	1.253	2.882	1.608
34206	(Mg1.36Fe0.64)(SiO4)	Pbnm	0.031	1.258	2.852	1.574
91919	MgFe(SiO4)	Pbnm	0.029	1.258	3.132	1.850
65741	(Ni.3Mg.7)2(SiO4)	Pbnm	0.0206	1.258	2.474	1.201
156799	(Fe0.935Mg1.016Mn0.04Ca0.008)(SiO4)	Pbnm	0.0155	1.259	3.222	1.938
31190	(Mg1.14Fe0.34Ni0.52)(SiO4)	Pbnm	0.085	1.262	2.688	1.408
100644	Ni2(SiO4)	Pbnm	0.027	1.262	2.079	0.807
65746	(Co.377Mg.623)2(SiO4)	Pbnm	0.0218	1.262	2.513	1.235
156803	(Fe0.935Mg1.016Mn0.04Ca0.008)(SiO4)	Pbnm	0.018	1.265	3.292	2.001
156801	(Fe0.935Mg1.016Mn0.04Ca0.008)(SiO4)	Pbnm	0.0152	1.266	3.236	1.945
156802	(Fe0.935Mg1.016Mn0.04Ca0.008)(SiO4)	Pbnm	0.0161	1.267	3.282	1.989
290183	Li0.86(Mn0.800Fe0.183)(PO4)	Pbnm	0.0219	1.268	5.106	3.791
203012	Mg1.398Ni0.62(SiO4)	Pbnm	0.021	1.268	2.523	1.240
173464	Ca(Ca0.11Co0.89)(GeO4)	Pnma	0.0199	1.269	4.600	5.944
91920	MgFe(SiO4)	Pbnm	0.028	1.270	3.172	1.878
91926	MgFe(SiO4)	Pbnm	0.049	1.273	3.391	2.091
91925	MgFe(SiO4)	Pbnm	0.052	1.274	3.373	2.072
91924	MgFe(SiO4)	Pbnm	0.058	1.276	3.329	2.028
91927	MgFe(SiO4)	Pbnm	0.047	1.276	3.395	2.092
154115	Li0.64Fe(PO4)	Pmnb	0.0506	1.278	2.988	1.689
85314	(Mg1.81Fe0.19)(SiO4)	Pbnm	0.053	1.280	2.721	1.423
91921	MgFe(SiO4)	Pbnm	0.026	1.280	3.206	1.901
9687	Mg2SiO4	Pbnm	0.057	1.280	2.823	1.523
64738	Mg2SiO4	Pbnm	0.059	1.280	2.823	1.523
91928	MgFe(SiO4)	Pbnm	0.049	1.281	3.403	2.096
91922	MgFe(SiO4)	Pbnm	0.026	1.281	3.225	1.919
91923	MgFe(SiO4)	Pbnm	0.027	1.283	3.246	1.938
79745	(Mg0.914Fe0.086)(Mg0.846Fe0.154)(SiO4)	Pbnm	0.069	1.287	3.902	2.582

10376	Ca0.01Fe0.61Mg1.38(SiO4)	Pbnm	0.031	1.289	2.935	1.625
34815	(Mg0.5Fe0.5)2(SiO4)	Pbnm	0.08	1.289	3.030	1.719
15627	Mg2SiO4	Pbnm	0.059	1.290	2.704	1.396
34112	(Mg0.9Fe0.1)2(SiO4)	Pbnm	0.059	1.290	2.704	1.396
50077	(Co0.375Mg0.625)2(SiO4)	Pbnm	0.0266	1.291	2.551	1.243
9692	Mg.75Fe1.10Mn.15SiO4	Pbnm	0.042	1.295	3.556	2.232
79744	(Mg0.907Fe0.093)(Mg0.853Fe0.147)(SiO4)	Pbnm	0.07	1.296	3.568	2.243
34207	(Mg1.46Fe0.54)(SiO4)	Pbnm	0.055	1.310	2.789	1.460
10415	Fe2SiO4	Pbnm	0.137	1.314	3.556	2.212
64739	Mg2SiO4	Pbnm	0.059	1.315	3.190	1.851
66186	(Mg1.39Fe.61)(SiO4)	Pbnm	0.0481	1.320	2.838	1.498
173467	(Ca1.07Mg0.93)(GeO4)	Pnma	0.0259	1.325	4.550	5.954
60648	(Mg0.729Fe0.09Mn0.09Cr0.09)(Mg0.734Fe0.086Mn0.086Cr0.086	Pbnm	0.059	1.326	3.230	1.878
91450	(Fe0.454Mn0.546)(Fe0.146Mn0.854)(SiO4)	Pbnm	0.012	1.329	3.837	2.475
23587	Mn2GeO4	Pnma	0.1	1.333	1.414	0.080
66188	(Mg1.41Fe.59)(SiO4)	Pbnm	0.0255	1.334	2.916	1.562
39795	(Mg1.48Fe0.52)(SiO4)	Pbnm	0.051	1.336	2.862	1.507
64894	(Mg1.64Fe.35Ca.01)(Si.99Al.01)O4	Pbnm	0.023	1.337	2.871	1.514
65745	(Co.258Mg.742)2(SiO4)	Pbnm	0.0221	1.349	2.544	1.179
66187	(Mg1.41Fe.59)(SiO4)	Pbnm	0.0222	1.351	2.868	1.497
9688	Mg2SiO4	Pbnm	0.055	1.354	3.190	1.812
72908	MgMn(GeO4)	Pbnm	0.042	1.360	1.271	0.088
64895	(Mg1.42Fe0.58)((Si0.99Al0.01)O4)	Pbnm	0.029	1.362	2.870	1.488
40730	Mg1.641Fe.359(SiO4)	Pbnm	0.017	1.368	2.851	1.463
41415	Mg2(GeO4)	Pnma	0.0751	1.371	0.248	1.108
63533	Mg2(GeO4)	Pnma	0.0485	1.371	0.248	1.108
66189	(Mg1.41Fe.59)(SiO4)	Pbnm	0.024	1.376	3.004	1.606
66190	(Mg1.41Fe.59)(SiO4)	Pbnm	0.029	1.382	3.108	1.702
50078	(Co0.25Mg0.75)2(SiO4)	Pbnm	0.0233	1.383	2.632	1.232
10375	Ca0.01Fe0.61Mg1.38(SiO4)	Pbnm	0.025	1.387	2.860	1.453
83564	MgMn(SiO4)	Pbnm	0.02	1.389	4.224	2.796
10377	Ca0.01Fe0.61Mg1.38(SiO4)	Pbnm	0.057	1.390	3.111	1.698
182588	(Mg1.854Fe0.145)(SiO4)	Pbnm	0.034	1.390	2.562	1.156
79171	(Mg0.82Fe0.18)(Mg0.902Fe0.098)(SiO4)	Pbnm	0.125	1.391	2.755	1.345
66191	(Mg1.41Fe.59)(SiO4)	Pbnm	0.0325	1.392	3.140	1.724
202251	(Co.4Mg1.6)SiO4	Pbnm	0.018	1.399	2.572	1.157
83565	MgMn(SiO4)	Pbnm	0.02	1.399	4.229	2.790
202250	(Co.26Mg1.74)SiO4	Pbnm	0.043	1.405	2.645	1.223
39796	(Mg1.44Fe0.56)(SiO4)	Pbnm	0.038	1.406	2.828	1.402
166628	ZnMn(GeO4)	Pnma	0.078	1.412	2.265	0.841
65710	Mn2(SiS4)	Pnma	0.041	1.414	2.083	0.659
83566	MgMn(SiO4)	Pbnm	0.02	1.417	4.214	2.758
69466	(Mg1.626Fe0.37)(SiO4)	Pbnm	0.021	1.428	2.803	1.356
65744	(Co.175Mg.825)2(SiO4)	Pbnm	0.0217	1.430	2.587	1.141
69467	(Mg1.627Fe0.373)(SiO4)	Pbnm	0.019	1.434	2.805	1.351
83563	MgMn(SiO4)	Pbnm	0.02	1.434	4.183	2.709
83567	MgMn(SiO4)	Pbnm	0.021	1.438	4.197	2.720
69465	(Mg1.635Fe0.365)(SiO4)	Pbnm	0.017	1.439	2.841	1.382
79742	(Mg0.868Fe0.132)(Mg0.892Fe0.108)(SiO4)	Pbnm	0.072	1.442	3.777	2.303
79173	(Mg0.854Fe0.146)(Mg0.9Fe0.1)(SiO4)	Pbnm	0.124	1.445	2.763	1.300
69468	(Mg1.62Fe0.38)(SiO4)	Pbnm	0.018	1.445	2.845	1.380
83568	MgMn(SiO4)	Pbnm	0.023	1.446	4.179	2.694
64740	Mg2SiO4	Pbnm	0.129	1.449	3.262	1.787
40731	Mg1.624Fe.376(SiO4)	Pbnm	0.021	1.451	2.918	1.446
66195	(Mg1.63Fe.37)(SiO4)	Pbnm	0.0303	1.454	2.818	1.344
29530	(Mg1.684Fe0.316)(SiO4)	Pnma	0.0303	1.455	2.829	1.354
66183	(Mg1.74Fe.26)(SiO4)	Pbnm	0.0358	1.455	2.780	1.305
100421	(Mg1.83Fe0.17)(SiO4)	Pbnm	0.019	1.457	2.554	1.082
40727	Mg1.826Fe.159Ni.015(SiO4)	Pbnm	0.023	1.457	2.740	1.264
29527	(Mg1.828Fe0.172)(SiO4)	Pnma	0.0235	1.458	2.756	1.280
66185	(Mg1.72Fe.28)(SiO4)	Pbnm	0.0412	1.459	2.774	1.295
29531	(Mg1.636Fe0.364)(SiO4)	Pnma	0.0362	1.460	2.807	1.327
79175	(Mg0.872Fe0.128)(Mg0.900Fe0.100)(SiO4)	Pbnm	0.13	1.464	2.776	1.293
54264	Mn2(SiS4)	Pnma	0.058	1.468	2.148	0.671
57422	Mn2(SiS4)	Pnma	0.058	1.468	2.148	0.671

9686	Mg2SiO4	Pbnm	0.054	1.470	2.838	1.348
64737	Mg2SiO4	Pbnm	0.056	1.470	2.838	1.348
66180	(Mg1.8Fe.2)(SiO4)	Pbnm	0.0464	1.471	2.746	1.256
29533	(Mg1.7Fe0.3)(SiO4)	Pnma	0.0435	1.473	2.876	1.383
40728	Mg1.834Fe.155Ni.011(SiO4)	Pbnm	0.023	1.473	2.715	1.224
79179	(Mg0.902Fe0.098)(Mg0.902Fe0.098)(SiO4)	Pbnm	0.103	1.473	2.780	1.288
83562	MgMn(SiO4)	Pbnm	0.029	1.474	4.141	2.628
29526	(Mg1.8Fe0.2)(SiO4)	Pnma	0.0329	1.474	2.679	1.188
39798	(Mg1.8Fe0.2)(SiO4)	Pbnm	0.061	1.474	2.722	1.230
66184	(Mg1.74Fe.26)(SiO4)	Pbnm	0.0522	1.474	2.789	1.295
83569	MgMn(SiO4)	Pbnm	0.021	1.474	4.174	2.660
79181	(Mg0.906Fe0.094)(Mg0.894Fe0.106)(SiO4)	Pbnm	0.101	1.475	2.782	1.288
9685	Mg2SiO4	Pbnm	0.048	1.476	2.663	1.170
68755	Mg2(SiO4)	Pbnm	0.048	1.476	2.663	1.170
77734	(Mg0.895Fe0.105)(Mg0.905Fe0.095)(SiO4)	Pbnm	0.021	1.476	3.015	1.516
50079	(Co0.125Mg0.875)2(SiO4)	Pbnm	0.0294	1.477	2.688	1.194
39797	(Mg1.78Fe0.22)(SiO4)	Pbnm	0.072	1.477	2.748	1.253
79185	(Mg0.910Fe0.090)(Mg0.900Fe0.100)(SiO4)	Pbnm	0.088	1.479	2.780	1.282
83570	MgMn(SiO4)	Pbnm	0.023	1.480	4.373	2.850
66176	(Mg1.77Fe.23)(SiO4)	Pbnm	0.0465	1.482	2.761	1.260
40729	Mg1.793Fe.195Ni.012(SiO4)	Pbnm	0.027	1.483	2.753	1.252
79183	(Mg0.902Fe0.098)(Mg0.898Fe0.102)(SiO4)	Pbnm	0.138	1.483	2.780	1.277
79177	(Mg0.918Fe0.082)(Mg0.898Fe0.102)(SiO4)	Pbnm	0.096	1.486	2.794	1.289
54030	Fe2(SiO4)	Pbnm	0.089	1.487	2.910	1.402
79169	(Mg0.924Fe0.076)(Mg0.898Fe0.102)(SiO4)	Pbnm	0.119	1.487	2.790	1.283
40726	Mg1.838Fe0.156Ni0.006(SiO4)	Pbnm	0.022	1.488	2.710	1.204
100360	(Mg1.784Fe0.216)(SiO4)	Pmcn	0.0279	1.491	2.801	1.291
100427	(Mg1.824Fe0.176)(SiO4)	Pbnm	0.025	1.491	2.739	1.230
93091	(Mg1.77Fe0.23)(SiO4)	Pbnm	0.03	1.494	2.776	1.263
93092	(Mg1.77Fe0.23)(SiO4)	Pbnm	0.034	1.494	2.776	1.263
39794	(Mg1.86Fe0.14)(SiO4)	Pbnm	0.074	1.494	2.710	1.198
79187	(Mg0.902Fe0.098)(Mg0.900Fe0.100)(SiO4)	Pbnm	0.098	1.495	2.776	1.263
100423	(Mg1.812Fe0.188)(SiO4)	Pbnm	0.018	1.495	2.623	1.111
85311	(Mg1.81Fe0.19)(SiO4)	Pbnm	0.033	1.495	2.740	1.226
83561	MgMn(SiO4)	Pbnm	0.021	1.496	4.119	2.585
252658	(Mg1.75Fe0.25)SiO4	Pbnm	0.011	1.498	2.787	1.270
252659	(Mg1.75Fe0.25)SiO4	Pbnm	0.01	1.498	2.787	1.270
252660	(Mg1.75Fe0.25)SiO4	Pbnm	0.01	1.498	2.787	1.270
252661	(Mg1.75Fe0.25)SiO4	Pbnm	0.011	1.498	2.787	1.270
252662	(Mg1.75Fe0.25)SiO4	Pbnm	0.012	1.498	2.787	1.270
9335	(Mg0.893Fe0.107)2(SiO4)	Pbnm	0.022	1.504	2.771	1.248
66182	(Mg1.8Fe.2)(SiO4)	Pbnm	0.0334	1.505	2.766	1.242
100429	(Mg1.82Fe0.18)(SiO4)	Pbnm	0.023	1.507	2.812	1.285
83572	MgMn(SiO4)	Pbnm	0.023	1.507	4.159	2.612
69471	(Mg1.819Fe0.181)(SiO4)	Pbnm	0.022	1.508	2.749	1.223
67429	Mg1.8Fe.2(SiO4)	Pbnm	0.038	1.508	2.777	1.250
29529	(Mg1.762Fe0.238)(SiO4)	Pnma	0.0431	1.510	2.773	1.244
83573	MgMn(SiO4)	Pbnm	0.023	1.510	4.139	2.590
69473	(Mg1.807Fe0.193)(SiO4)	Pbnm	0.021	1.511	2.756	1.227
100361	(Mg1.784Fe0.216)(SiO4)	Pmcn	0.0337	1.511	2.810	1.280
69469	(Mg1.805Fe0.195)(SiO4)	Pbnm	0.027	1.511	2.734	1.205
66179	(Mg1.8Fe.2)(SiO4)	Pbnm	0.0376	1.511	2.774	1.244
66181	(Mg1.8Fe.2)(SiO4)	Pbnm	0.0231	1.512	2.765	1.234
6219	Co6.95As3.62O16	Pnma	0.075	1.517	0.323	1.868
83574	MgMn(SiO4)	Pbnm	0.023	1.518	4.151	2.593
29528	(Mg1.774Fe0.226)(SiO4)	Pnma	0.025	1.519	2.808	1.270
83571	MgMn(SiO4)	Pbnm	0.023	1.519	4.151	2.593
69470	(Mg1.822Fe0.178)(SiO4)	Pbnm	0.025	1.521	2.716	1.177
100425	(Mg1.851Fe0.149)(SiO4)	Pbnm	0.018	1.521	2.675	1.137
66178	(Mg1.8Fe.2)(SiO4)	Pbnm	0.0496	1.521	2.771	1.232
29532	(Mg1.682Fe0.318)(SiO4)	Pnma	0.0293	1.521	2.868	1.326
69474	(Mg1.849Fe0.151)(SiO4)	Pbnm	0.027	1.521	2.717	1.178
66177	(Mg1.77Fe.23)(SiO4)	Pbnm	0.0519	1.522	2.767	1.226
77733	(Mg0.903Fe0.097)(Mg0.897Fe0.103)(SiO4)	Pbnm	0.026	1.523	2.779	1.236
65971	Mn1.4Mg0.6(SiS4)	Pnma	0.034	1.524	2.355	0.819
66197	(Mg1.83Fe.17)(SiO4)	Pbnm	0.0208	1.525	2.742	1.198

66175	(Mg1.77Fe.23)(SiO4)	Pbnm	0.0587	1.526	2.789	1.244
77736	(Mg0.888Fe0.112)(Mg0.912Fe0.088)(SiO4)	Pbnm	0.021	1.526	2.769	1.223
20779	Mg1.85Fe0.15(SiO4)	Pnma	0.021	1.527	2.773	1.227
20781	(Mg1.83Fe0.18)(SiO4)	Pnma	0.02	1.527	2.773	1.227
83560	MgMn(SiO4)	Pbnm	0.019	1.529	4.070	2.503
290186	Li0.75(Mn0.800Fe0.195)(PO4)	Pbnm	0.0218	1.531	3.840	2.275
29525	(Mg1.8Fe.2)(SiO4)	Pnma	0.0326	1.532	2.856	1.304
34816	Mg2(SiO4)	Pbnm	0.07	1.535	2.774	1.220
83575	MgMn(SiO4)	Pbnm	0.021	1.539	4.159	2.580
85312	(Mg1.81Fe0.19)(SiO4)	Pbnm	0.054	1.539	2.709	1.152
66196	(Mg1.81Fe.19)(SiO4)	Pbnm	0.0432	1.540	2.775	1.217
100426	(Mg1.814Fe0.186)(SiO4)	Pbnm	0.022	1.540	2.696	1.138
100359	(Mg1.784Fe.216)(SiO4)	Pmcn	0.0208	1.542	2.808	1.247
80089	(Fe0.12Mg0.88)2(SiO4)	Pbnm	0.0368	1.545	2.697	1.134
202370	Mg2(SiO4)	Pbnm	0.0327	1.547	2.673	1.109
85313	(Mg1.81Fe0.19)(SiO4)	Pbnm	0.057	1.550	2.697	1.130
100422	(Mg1.808Fe0.192)(SiO4)	Pbnm	0.025	1.550	2.696	1.128
68588	Mg2(SiO4)	Pbnm	0.057	1.553	2.792	1.220
69472	(Mg1.818Fe0.182)(SiO4)	Pbnm	0.025	1.554	2.807	1.234
164731	Mg1.85Fe0.12H0.06(Si0.99O4)	Pbnm	0.024	1.556	2.705	1.131
50080	Mg2(SiO4)	Pbnm	0.0323	1.556	2.792	1.217
67430	Mg1.8Fe.2(SiO4)	Pbnm	0.038	1.558	2.809	1.232
71862	LiCd(PO4)	Pnma	0.021	1.559	6.872	5.232
77117	Mg1.791Fe0.202Ni0.007(SiO4)	Pbnm	0.027	1.565	2.806	1.223
187590	Na0.68(Fe0.67Mn0.33)(PO4)	Pbnm	0.0785	1.569	1.870	0.297
20780	(Mg1.8Fe0.2)(SiO4)	Pnma	0.017	1.571	2.845	1.254
242067	Mg2(SiO4)	Pbnm	0.014	1.577	2.681	1.087
34232	Mg2(SiO4)	Pbnm	0.021	1.579	2.741	1.145
165001	Li0.6Fe(PO4)	Pnma	0.0032	1.583	2.091	0.500
163295	Mg2(SiO4)	Pbnm	0.021	1.585	2.804	1.200
163296	Mg2(SiO4)	Pbnm	0.032	1.588	2.776	1.169
171572	Mg2SiO4	Pbnm	0.0687	1.591	2.715	1.106
100430	(Mg1.818Fe0.192)(SiO4)	Pbnm	0.022	1.595	2.826	1.212
163294	Mg2(SiO4)	Pbnm	0.019	1.598	2.718	1.102
185823	NaEu(GeO4)	Pnma	0.0212	1.599	1.267	2.913
186847	NaEu(GeO4)	Pnma	0.0212	1.599	1.267	2.913
62526	Mg2(SiO4)	Pbnm	0.021	1.601	2.700	1.082
62527	Mg2(SiO4)	Pbnm	0.034	1.601	2.700	1.082
158316	Mg1.985(Si0.993O3.94(OH)0.06)	Pbnm	0.028	1.602	2.800	1.180
9334	(Mg.985Fe.015)2SiO4	Pbnm	0.023	1.609	2.757	1.130
62524	Mg2(SiO4)	Pbnm	0.0207	1.610	2.676	1.049
12124	Mg2SiO4	Pbnm	0.049	1.614	2.729	1.097
26374	Mg2SiO4	Pbnm	0.0209	1.614	2.690	1.058
243420	Fe2SiO4	Pbnm	0.0531	1.618	2.738	1.102
64744	Mg2SiO4	Pbnm	0.042	1.645	2.814	1.150
24141	Mn2(SiS4)	Pnma	0.32	1.650	2.255	0.595
100428	(Mg1.867Fe0.133)(SiO4)	Pbnm	0.026	1.682	2.627	0.929
248686	NaSm(GeO4)	Pnma	0.0138	1.687	1.663	3.408
97764	LiFe(PO4)	Pnma	0.057	1.698	4.499	2.755
79167	(Mg0.904Fe0.096)(Mg0.912Fe0.088)(SiO4)	Pbnm	0.024	1.705	2.906	1.181
54031	Fe2(SiO4)	Pbnm	0.075	1.808	3.084	1.254
242066	Mg2(SiO4)	Pbnm	0.017	1.819	2.764	0.928
30962	Mg2(SiO4)	Pbnm	0.091	1.831	0.838	0.976
30957	Mg2(SiO4)	Pbnm	0.036	1.892	2.166	0.268
154116	Li0.45Fe(PO4)	Pmnb	0.025	1.897	1.583	0.308
85496	NaGd(GeO4)	Pnma	0.016	1.907	0.752	2.710
402063	Na2(ZnCl4)	Pnma	0.021	1.908	2.678	0.756
237904	Fe0.76Li0.89Mn0.28PO4	Pnma	0.0334	1.921	4.354	6.398
429695	Ca2SnS4	Pnma	0.0245	1.942	2.096	0.151
54195	NaYb(GeO4)	Pnma	0.0366	1.942	0.420	1.552
62229	LiInGeO4	Pnma	0.027	1.946	0.722	1.248
54197	NaTb(GeO4)	Pnma	0.0305	1.968	0.637	2.657
100433	(Mg0.17Mn0.83)Mn(SiO4)	Pbnm	0.039	1.970	4.325	2.310
30958	Mg2(SiO4)	Pbnm	0.033	2.020	2.231	0.207
189095	Li0.32(Fe0.78Mn0.22)(PO4)	Pbnm	0.0282	2.030	0.227	1.767
54032	Fe2(SiO4)	Pbnm	0.091	2.101	2.727	0.613

30960	Mg2(SiO4)	Pbnm	0.038	2.127	1.866	0.255
30956	Mg2(SiO4)	Pbnm	0.062	2.132	2.702	0.558
73224	Na2(ZnBr4)	Pnma	0.074	2.155	2.938	0.767
54198	NaTm(GeO4)	Pnma	0.0261	2.172	0.273	1.941
85497	NaY(GeO4)	Pnma	0.024	2.185	0.004	2.238
20224	Cd2GeO4	Pmcn	0.077	2.185	3.163	0.957
20873	Cd2(GeO4)	Pmcn	0.055	2.185	3.163	0.957
30859	Cd2(GeO4)	Pbnm	0.019	2.188	3.077	0.870
163525	Al(Mg0.982Fe0.018)(BO4)	Pnma	0.055	2.198	5.218	7.583
30959	Mg2(SiO4)	Pbnm	0.047	2.200	2.079	0.118
95964	NaHo(GeO4)	Pnma	0.018	2.202	0.115	2.135
64741	Mg2SiO4	Pbnm	0.094	2.206	2.497	0.284
54196	NaLu(GeO4)	Pnma	0.0503	2.221	1.016	1.233
88026	Mn2(SiO4)	Pnma	0.14	2.247	4.199	1.909
26376	Mn2(SiO4)	Pbnm	0.031	2.270	4.208	1.895
54199	NaEr(GeO4)	Pnma	0.0286	2.288	0.410	1.923
9369	Cd2GeO4	Pmcn	0.148	2.334	3.360	1.002
169119	Na0.71Fe(PO4)	Pnma	0.0145	2.392	0.585	1.764
85498	NaLu(GeO4)	Pnma	0.019	2.408	1.011	1.432
243421	Fe2SiO4	Pbnm	0.0519	2.455	2.719	0.258
10411	Fe2SiO4	Pbnm	0.105	2.471	3.210	0.721
10410	Fe2SiO4	Pbnm	0.109	2.516	2.874	0.349
54033	Fe2(SiO4)	Pbnm	0.081	2.594	2.594	0.000
30961	Mg2(SiO4)	Pbnm	0.071	2.601	2.080	0.508
64742	Mg2SiO4	Pbnm	0.096	2.678	2.450	0.222
62481	LiScGeO4	Pnma	0.062	2.750	1.485	1.301
173459	Ca2(GeO4)	Pnma	0.0187	3.085	5.598	2.438
173460	Ca2(GeO4)	Pnma	0.0178	3.085	5.598	2.438
173468	Ca2(GeO4)	Pnma	0.0241	3.163	5.754	2.512
250769	NaFePO4	Pnma	0.0311	3.282	2.527	0.731
18179	Ca2(SiO4)	Pbnm	0.1	3.305	8.770	5.291
64743	Mg2SiO4	Pbnm	0.123	3.454	3.188	0.257
169118	NaFe(PO4)	Pnma	0.0163	3.506	2.641	0.835
250768	NaFePO4	Pnma	0.0325	3.549	2.648	0.870
189971	Mg2(SiO4)	Pbnm	0.048	3.592	0.125	3.347
243422	Fe2SiO4	Pbnm	0.0426	3.678	2.250	1.378
6210	NaCd(PO4)	Pnma	0.078	3.840	4.893	1.014
26006	Na(Mn0.93Fe0.07)(PO4)	Pnam	0.055	3.893	3.343	0.530
12101	Na2(BeF4)	Pbnm	0.07	4.142	9.581	5.223
23416	Ca2GeS4	Pnma	0.1	4.175	6.067	1.816
27709	Na2(BeF4)	Pbnm	0.06	4.193	9.600	5.190
34113	Na2(BeF4)	Pbnm	0.075	4.241	9.534	5.078
9095	Ca2(SiO4)	Pbnm	0.07	4.309	8.695	4.205
181558	Ca2(SiO4)	Pbnm	0.0852	4.331	8.668	4.157
166637	Ca2(SiO4)	Pbnm	0.0852	4.334	8.677	4.162
417503	Ca2(SiO4)	Pbnm	0.069	4.334	8.677	4.162
82995	Ca2(SiO4)	Pbnm	0.029	4.358	8.657	4.120
81095	Ca2(SiO4)	Pbnm	0.04	4.380	8.668	4.109
82994	Ca2(SiO4)	Pbnm	0.046	4.389	8.706	4.136
243423	Fe2SiO4	Pbnm	0.0444	4.574	2.016	2.446
200707	Ca2(SiO4)	Pbnm	0.037	4.596	8.920	4.134
54034	Fe2(SiO4)	Pbnm	0.094	4.616	3.014	1.531
39005	Ca2(SiO4)	Pbnm	0.037	4.664	8.973	4.117
243424	Fe2SiO4	Pbnm	0.0473	5.421	2.387	2.878
23306	Cd3AsCl3	Pnma	0.056	6.764	6.591	12.509
202678	NaAg(MoO4)	Pnma	0.079	18.795	3.965	12.483
252779	Ag2CrO4	Pnma	0.0583	20.874	3.530	14.349
16298	Ag2CrO4	Pnma	0.064	20.984	3.595	14.373
35762	Ag2MnO4	Pnma	0.028	21.077	4.247	13.900
193218	AgMn(VO4)	Pnma	0.0307	23.707	4.341	15.655
401350	AgCd(VO4)	Pnma	0.042	23.788	4.990	15.186
246202	AgMn(VO4)	Pnma	0.0411	23.908	4.114	15.975
239747	AgMgVO4	Pnma	0.031	23.934	3.233	16.704
260949	MnNa(VO4)	Pnma	0.0304	24.647	5.702	15.199
6311	Mg2(SiO4)	Ibmm	0.19	24.834	18.231	5.289
23568	(Mg1.7Ni0.3)(SiO4)	Ibmm	0.23	24.834	18.231	5.289

419201	AgCu(VO4)	Pnma	0.0296	26.852	2.466	19.224
419202	AgCu(VO4)	Pnma	0.0321	26.984	2.529	19.258
81504	Na2(SO4)	Pbnm	0.103	30.665	9.846	15.933
431431	NaCdPO4	Pnma	0.106293	31.058	10.954	15.339
201771	NaMn(PO4)	Pmnb	0.044	31.580	10.243	16.216
85671	NaFe(PO4)	Pnma	0.026	32.206	11.012	16.031
200111	Na(Fe0.9Mn0.1)(PO4)	Pmnb	0.02	32.231	11.040	16.026
250771	NaFePO4	Pnma	0.0372	32.238	11.115	15.973
56292	NaFe(PO4)	Pnma	0.0189	32.275	11.097	16.011
20065	Na(Fe.5Zn.5)(PO4)	Pnma	0.087	32.317	11.236	15.932
237852	NaFe(PO4)	Pnma	0.0414	32.319	11.175	15.980
82752	NaCo(PO4)	Pnma	0.031	32.379	10.210	16.746
193244	NaFe(PO4)	Pmnb	0.0474	32.511	11.201	16.082
250770	NaFePO4	Pnma	0.0351	32.530	11.206	16.090